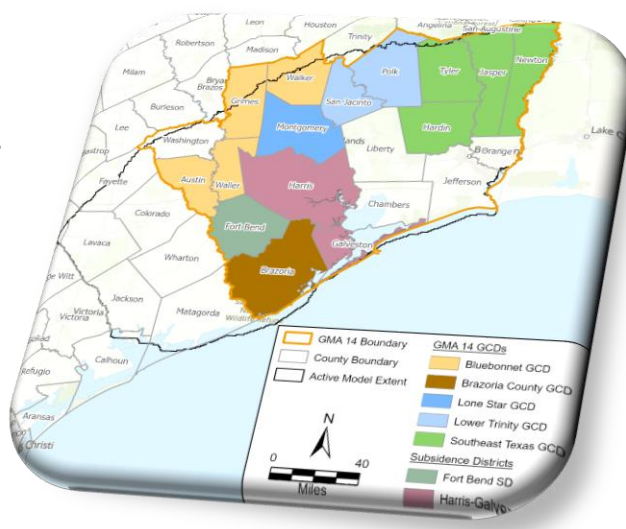


Northern Portion of the Gulf Coast Aquifer System Groundwater Availability Model for Groundwater Management Area 14 Joint Planning

Prepared For:
Groundwater Management Area 14

Prepared By:
Michael R. Keester, P.G.
Philip Webster, P.G.
James Beach, P.G.
Christopher Drabek, P.G.
Ye Hong Chen, Ph.D., EIT

In Cooperation with:
Lone Star Groundwater Conservation District



March 31, 2025

Geoscientist Seals

This report documents the work of the following professionals licensed in the State of Texas:

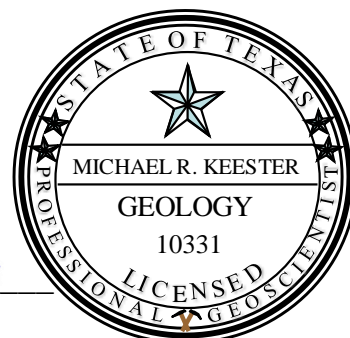
Michael R. Keester, P.G. – KT Groundwater (TBPG Firm No. 50705)

Mr. Keester was primarily responsible for the conceptual model compaction evaluations and is the primary author of report Section 2.3. He also led development of the numerical model and was responsible for the numerical model documentation.


Signature


03/31/2025

Date



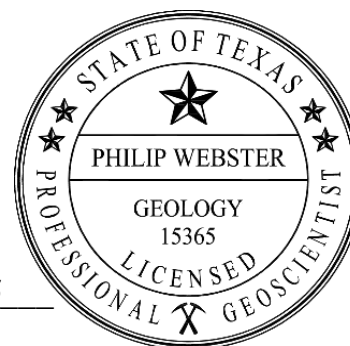
Philip Webster, P.G. – KT Groundwater (TBPG Firm No. 50705)

Mr. Webster was primarily responsible for the numerical model update and calibration. He is the primary author of report Sections 3 and 4. He also reviewed the full model documentation.


Signature

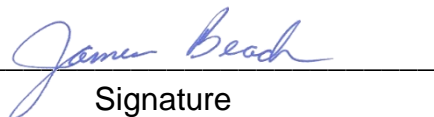
03/31/2025

Date



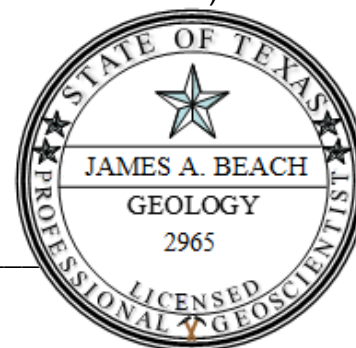
James Beach, P.G. – Advanced Groundwater Solutions (TBPG Firm No. 50639)

Mr. Beach was primarily responsible for work conducted by Advanced Groundwater Solutions staff in support of the model update.


Signature

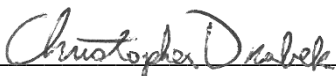
03/31/2025

Date



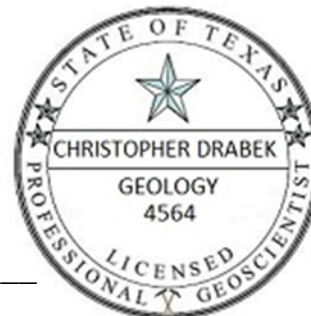
Christopher Drabek, P.G. – Advanced Groundwater Solutions (TBPG Firm No. 50639)

Mr. Drabek was primarily responsible for conceptual model hydraulic property and groundwater pumping evaluations. He is the primary author of report Sections 2.1 and 2.2. He also reviewed the full model documentation.



Signature

03/31/2025
Date



Contents

Executive Summary	1
1. Introduction	3
2. Conceptual Model Updates	6
2.1. Hydraulic Properties	6
2.2. Groundwater Pumping	11
2.2.1. GULF-2023 Model Pumping Review	11
2.2.2. Comparison with Houston Area Groundwater Model Pumping	11
2.2.3. GMA 14 Model Pumping Update	12
2.3. Compaction	16
2.3.1. Previous Investigations	16
2.3.2. Lone Star Groundwater Conservation District Porter Site	18
3. Model Overview and Packages	38
3.1. Discretization Packages	40
3.1.1. Time Discretization	40
3.1.2. Grid Discretization	42
3.2. Node Property Flow Package	51
3.3. Storage Package	51
3.4. Skeletal Storage, Compaction, and Subsidence Package	52
3.5. Well Package	66
3.6. Drain Package	71
3.7. General-Heads Boundary Package	73
3.8. Recharge Package	75
3.9. River Package	75
3.10. Output Control Package	75
3.11. Iterative Model Solution Package	75
3.12. Observations Utility	76
4. Model Calibration	78
4.1. Calibration Procedures	79
4.1.1. Calibration targets	79
4.1.2. Parameter Adjustments	85

4.1.3.	Calibration of Hydraulic (NPF and STO) Properties.....	93
4.1.4.	Calibration of Compaction (CSUB) Properties	110
4.1.5.	Calibration of Boundary Conditions	134
4.2.	Model Simulated Versus Measured Head.....	138
4.2.1.	Water levels	138
4.2.2.	Residual Distributions	142
4.2.3.	Water level hydrographs	151
4.2.4.	Simulated Water Levels	155
4.3.	Model Simulated Versus Measured Compaction and Subsidence.....	168
4.3.1.	Compaction and Subsidence	168
4.3.2.	Residual Distribution	173
4.3.3.	Compaction and Subsidence Time Series	176
4.3.4.	Simulated Compaction and Subsidence	180
4.4.	Simulated Water Budgets	185
5.	Model Limitations	199
5.1.	Jasper Aquifer as a Single Layer	199
5.2.	Compaction and Subsidence Data Availability	200
5.3.	Subsidence District Groundwater Pumping	200
6.	Summary and Conclusions	201
7.	Future Improvements	202
8.	Acknowledgements	203
9.	References.....	204

Figures

Figure 1.	Counties, subsidence districts, and member groundwater conservation districts within Groundwater Management Area 14.	4
Figure 2.	Map of locations of water wells with field data.	7
Figure 3.	Chicot Aquifer interpolated transmissivity based on pumping test data.	8
Figure 4.	Evangeline Aquifer interpolated transmissivity based on pumping test data.....	9
Figure 5.	Jasper Aquifer interpolated transmissivity based on pumping test data. .	10
Figure 6.	Comparison of the GMA 14 Model and GULF-2023 pumping in Montgomery County.	14
Figure 7.	Locations where core samples of the Gulf Coast Aquifer System have been collected for analysis of compaction properties.	17
Figure 8.	Porter Site geostatic stress.....	20
Figure 9.	Shale resistivity and calculated normal shale resistivity trend.....	22
Figure 10.	Calculated fine-grained sediment pore pressure gradient.....	23
Figure 11.	Effective vertical stress versus void ratio for core sample C8T1.....	26
Figure 12.	Porosity results from the compaction testing.	27
Figure 13.	Example of compression and recompression index determination.	29
Figure 14.	Calculated inelastic specific storage (S_{skv}) results from the compaction testing.	33
Figure 15.	Calculated elastic specific storage (S_{ske}) results from the compaction testing.	34
Figure 16.	Illustration of compaction as a function of the compaction time constant..	36
Figure 17.	Vertical hydraulic conductivity results from the compaction testing. G.....	37
Figure 18.	Layer 1 (shallow aquifer system) active model cells.	43
Figure 19.	Layer 2 (Chicot Aquifer) active model cells.....	44
Figure 20.	Layer 3 (Evangeline Aquifer) active model cells.	45
Figure 21.	Layer 4 (Burkeville) active model cells.....	46
Figure 22.	Layer 5 (Jasper Aquifer) active model cells.	47
Figure 23.	Layer 6 (Catahoula Aquifer) active model cells.....	48
Figure 24.	Model grid cross sections.	49

Figure 25.	Sections lines for cross sections in Figure 24.	50
Figure 26.	Interbed delay designations for Layer 2 (Chicot Aquifer).	54
Figure 27.	Interbed delay designations for Layer 3 (Evangeline Aquifer).....	55
Figure 28.	Interbed delay designations for Layer 4 (Burkeville).	56
Figure 29.	Interbed delay designations for Layer 5 (Jasper Aquifer).....	57
Figure 30.	Interbed thickness values for Layer 2 (Chicot Aquifer).	58
Figure 31.	Interbed thickness values for Layer 3 (Evangeline Aquifer).	59
Figure 32.	Interbed thickness values for Layer 4 (Burkeville).	60
Figure 33.	Interbed thickness values for Layer 5 (Jasper Aquifer).	61
Figure 34.	Equivalent number of interbeds for Layer 2 (Chicot Aquifer).	62
Figure 35.	Equivalent number of interbeds for Layer 3 (Evangeline Aquifer).....	63
Figure 36.	Equivalent number of interbeds for Layer 4 (Burkeville).	64
Figure 37.	Equivalent number of interbeds for Layer 5 (Jasper Aquifer).....	65
Figure 38.	2018 total pumping values for Layer 2 (Chicot Aquifer).	67
Figure 39.	2018 total pumping values for Layer 3 (Evangeline Aquifer).....	68
Figure 40.	2018 total pumping values for Layer 5 (Jasper Aquifer).....	69
Figure 41.	2018 total pumping values for Layer 6 (Catahoula Aquifer).....	70
Figure 42.	Layer 1 (shallow aquifer system) drain cell locations.	72
Figure 43.	General head boundary cell locations for all layers.	74
Figure 44.	Layer 1 (shallow aquifer system) river cell locations.	77
Figure 45.	Wells with water level measurements used during calibration.	80
Figure 46.	Compaction and subsidence station locations used during calibration. ...	81
Figure 47.	Example of the Theil-Sen and turning points applied to water level measurements.	83
Figure 48.	Example of the Theil-Sen and turning points trends applied to an extensometer station.....	84
Figure 49.	Pilot points for Layer 1 (shallow aquifer system).....	87
Figure 50.	Pilot points for Layer 2 (Chicot Aquifer).	88
Figure 51.	Pilot points for Layer 3 (Evangeline Aquifer).....	89
Figure 52.	Pilot points for Layer 4 (Burkeville).	90
Figure 53.	Pilot points for Layer 5 (Jasper Aquifer).....	91

Figure 54.	Pilot points for Layer 6 (Catahoula Aquifer).	92
Figure 55.	Calibrated layer 2 (Chicot Aquifer) hydraulic conductivity.	95
Figure 56.	Calibrated layer 3 (Evangeline Aquifer) hydraulic conductivity.	96
Figure 57.	Calibrated layer 5 (Jasper Aquifer) hydraulic conductivity.	97
Figure 58.	Calibrated layer 6 (Catahoula Aquifer) hydraulic conductivity.	98
Figure 59.	Observed versus calibrated transmissivity for Layer 2 (Chicot Aquifer). ..	99
Figure 60.	Observed versus calibrated transmissivity for Layer 3 (Evangeline Aquifer).	100
Figure 61.	Observed versus calibrated transmissivity for Layer 5 (Jasper Aquifer). ..	101
Figure 62.	Calibrated layer 2 (Chicot Aquifer) vertical hydraulic conductivity.	102
Figure 63.	Calibrated layer 3 (Evangeline Aquifer) vertical hydraulic conductivity. ..	103
Figure 64.	Calibrated layer 5 (Jasper Aquifer) vertical hydraulic conductivity.	104
Figure 65.	Calibrated layer 6 (Catahoula Aquifer) vertical hydraulic conductivity. ..	105
Figure 66.	Layer 2 (Chicot Aquifer) calibrated specific yield.	106
Figure 67.	Layer 3 (Evangeline Aquifer) calibrated specific yield.	107
Figure 68.	Layer 5 (Jasper Aquifer) calibrated specific yield.	108
Figure 69.	Layer 6 (Catahoula Aquifer) calibrated specific yield.	109
Figure 70.	Layer 2 (Chicot Aquifer) calibrated interbed porosity.	112
Figure 71.	Layer 3 (Evangeline Aquifer) calibrated interbed porosity.	113
Figure 72.	Layer 5 (Jasper Aquifer) calibrated interbed porosity.	114
Figure 73.	Layer 2 (Chicot Aquifer) calibrated interbed elastic specific storage.	115
Figure 74.	Layer 3 (Evangeline Aquifer) calibrated interbed elastic specific storage.	116
Figure 75.	Layer 5 (Jasper Aquifer) calibrated interbed elastic specific storage.	117
Figure 76.	Layer 2 (Chicot Aquifer) calibrated interbed inelastic specific storage. ..	118
Figure 77.	Layer 3 (Evangeline Aquifer) calibrated interbed inelastic specific storage.	119
Figure 78.	Layer 5 (Jasper Aquifer) calibrated interbed inelastic specific storage. .	120
Figure 79.	Layer 2 (Chicot Aquifer) calibrated interbed vertical hydraulic conductivity.	121
Figure 80.	Layer 3 (Evangeline Aquifer) calibrated interbed vertical hydraulic conductivity.	122

Figure 81.	Layer 5 (Jasper Aquifer) calibrated interbed vertical hydraulic conductivity.	123
Figure 82.	Layer 2 (Chicot Aquifer) calibrated coarse-grained elastic specific storage.....	126
Figure 83.	Layer 3 (Evangeline Aquifer) calibrated coarse-grained elastic specific storage.....	127
Figure 84.	Layer 5 (Jasper Aquifer) calibrated coarse-grained elastic specific storage.....	128
Figure 85.	Layer 6 (Catahoula Aquifer) calibrated coarse-grained elastic specific storage.....	129
Figure 86.	Layer 2 (Chicot Aquifer) calibrated coarse-grained porosity.	130
Figure 87.	Layer 3 (Evangeline Aquifer) calibrated coarse-grained porosity.....	131
Figure 88.	Layer 5 (Jasper Aquifer) calibrated coarse-grained porosity.....	132
Figure 89.	Layer 6 (Catahoula Aquifer) calibrated coarse-grained porosity.....	133
Figure 90.	Calibrated river conductance.	135
Figure 91.	Layer 1 (Shallow Aquifer System) calibrated recharge.	136
Figure 92.	Calibrated recharge over time across the model.	137
Figure 93.	Measured versus modeled water level measurements for each layer. ..	140
Figure 94.	Measured versus modeled water level measurements for the Chicot, Evangeline, Jasper, and Catahoula layers.....	141
Figure 95.	Layer 2 (Chicot Aquifer) mean residual by well.....	143
Figure 96.	Layer 3 (Evangeline Aquifer) mean residual by well.	144
Figure 97.	Layer 5 (Jasper Aquifer) mean residual by well.	145
Figure 98.	Layer 6 (Catahoula Aquifer) mean residual by well.	146
Figure 99.	Layer 2 (Chicot Aquifer) residual histogram.....	147
Figure 100.	Layer 3 (Evangeline Aquifer) residual histogram.	148
Figure 101.	Layer 5 (Jasper Aquifer) residual histogram.	149
Figure 102.	Layer 6 (Catahoula Aquifer) residual histogram.....	150
Figure 103.	Layer 2 (Chicot Aquifer) simulated and observed hydrographs.	152
Figure 104.	Layer 3 (Evangeline Aquifer) simulated and observed hydrographs.....	153
Figure 105.	Layer 5 (Jasper Aquifer) simulated and observed hydrographs.....	154
Figure 106.	Layer 2 (Chicot Aquifer) simulated potentiometric surface for 2018.	156

Figure 107.	Layer 3 (Evangeline Aquifer) simulated potentiometric surface for 2018.	157
Figure 108.	Layer 5 (Jasper Aquifer) simulated potentiometric surface for 2018.	158
Figure 109.	Layer 6 (Catahoula Aquifer) simulated potentiometric surface for 2018.	159
Figure 110.	Layer 2 (Chicot Aquifer) simulated drawdown between predevelopment and 2018.	160
Figure 111.	Layer 3 (Evangeline Aquifer) simulated drawdown between predevelopment and 2018.	161
Figure 112.	Layer 5 (Jasper Aquifer) simulated drawdown between predevelopment and 2018.	162
Figure 113.	Layer 6 (Catahoula Aquifer) simulated drawdown between predevelopment and 2018.	163
Figure 114.	Layer 2 (Chicot Aquifer) simulated versus observed water levels.	164
Figure 115.	Layer 3 (Evangeline Aquifer) simulated versus observed water levels.	165
Figure 116.	Layer 5 (Jasper Aquifer) simulated vs observed water levels.	166
Figure 117.	Layer 6 (Catahoula Aquifer) simulated vs observed water levels.	167
Figure 118.	Observed versus simulated subsidence for global positioning system stations.	169
Figure 119.	Observed versus simulated compaction for extensometer stations.	170
Figure 120.	Observed versus simulated subsidence for benchmark locations.	171
Figure 121.	Observed versus simulated subsidence for all station types.	172
Figure 122.	Compaction or subsidence mean residual by station.	174
Figure 123.	Residual histogram for compaction or subsidence targets.	175
Figure 124.	Compaction and subsidence simulated versus observed time series.	177
Figure 125.	Subsidence simulated versus observed time series.	178
Figure 126.	Compaction and Subsidence simulated versus observed time series.	179
Figure 127.	Simulated compaction from Layer 2 (Chicot Aquifer) between the end of predevelopment and the end of the calibration period (2018).	181
Figure 128.	Simulated compaction from Layer 3 (Evangeline Aquifer) between the predevelopment period and the end of the calibration period (2018).	182
Figure 129.	Simulated compaction from Layer 5 (Jasper Aquifer) between the predevelopment period and the end of the calibration period (2018).	183

Figure 130.	Simulated subsidence between the predevelopment period (1896) and the end of the calibration period (2018).	184
Figure 131.	Layer 2 (Chicot) transient simulated water budget for the calibration period (1896 – 2018).	191
Figure 132.	Layer 2 (Chicot) transient simulated net water budget for the calibration period (1896 – 2018).....	192
Figure 133.	Layer 3 (Evangeline Aquifer) transient simulated water budget for the calibration period (1896 – 2018).	193
Figure 134.	Layer 3 (Evangeline Aquifer) transient simulated net water budget for the calibration period (1896 – 2018).	194
Figure 135.	Layer 5 (Jasper Aquifer) transient simulated water budget for the calibration period (1896 – 2018).	195
Figure 136.	Layer 5 (Jasper Aquifer) transient simulated net water budget for the calibration period (1896 – 2018).	196
Figure 137.	Layer 6 (Catahoula Aquifer) transient simulated water budget for the calibration period (1896 – 2018).	197
Figure 138.	Layer 6 (Catahoula Aquifer) transient simulated water budget for the calibration period (1896 – 2018).	198

Tables

Table 1.	Subsurface core samples collected at the Porter Site.	18
Table 2.	Porter Site calculated geostatic stress, pore pressure (hydrostatic stress), and effective stress.	24
Table 3.	Typical compression and recompression index value ranges for clays. ..	29
Table 4.	Compression and recompression index for each core sample.	30
Table 5.	Average compression and recompression indices by aquifer.	31
Table 6.	Summary of MODFLOW input files.	39
Table 7.	Time Discretization Summary.	40
Table 8.	Model layers and corresponding hydrogeologic unit.	42
Table 9.	Parameters adjusted during history matching.	86
Table 10.	Initial and calibrated hydraulic property statistics by layer.	94
Table 11.	Initial and calibrated interbed compaction properties statistics by layer.	111
Table 12.	Initial and calibrated coarse-grained storage properties by layer.	125
Table 13.	Water Level calibration statistics.	139
Table 14.	Calibration statistics for compaction and subsidence targets.	168
Table 15.	Steady state simulated water budget by layer	186
Table 16.	Steady state net simulated water budget by layer.	187
Table 17.	Stress Period 59 (2018) simulated water budget by layer.	188
Table 18.	Stress period 59 (2018) net simulated water budget by layer	189

Appendices

Appendix 1 — Previously Unpublished Pumping Test Results

Appendix 2 — Comparison of Prior and Posterior GULF-2023 Pumping Input

Appendix 3 — Comparison of GULF-2023 and Houston-Area Groundwater Model
Pumping Inputs

Appendix 4 — GMA 14 Model Pumping Inputs

Appendix 5 — Comparison of GULF-2023 Pumping Inputs and Reported Groundwater
Conservation District Permitted Production Data

Appendix 6 — Comparison of Reported Production Data for the City of Conroe and The
Woodlands to GULF-2023 and GMA 14 Model Inputs

Appendix 7 — Comparison of GULF-2023 and GMA 14 Model Simulated Water Levels
to Measured Water Levels

Appendix 8 — Comparison of GMA 14 Model Simulated Compaction and Subsidence to
Measured Values

Appendix 9 — GMA 14 Model Net Water Budgets for Year 2018 for each County by
Aquifer

Appendix 10 — GMA 14 Model Net Water Budgets for Year 2018 for each Groundwater
Conservation District by Aquifer

Executive Summary

Groundwater Management Area 14 members manage the groundwater resources in the Gulf Coast Aquifer System from the western borders of Austin, Brazoria, Fort Bend, and Washington counties to the Texas border with Louisiana. In October 2019, the Harris-Galveston Subsidence District contracted the U.S. Geological Survey to update and refine the Houston-Area Groundwater Model, resulting in the GULF-2023 model, released in February 2024 by the Texas Water Development Board.

Prior to finalizing GULF-2023, stakeholders identified issues with the model affecting its utility for joint planning activities within Groundwater Management Area 14. To address these concerns, Groundwater Management Area 14 members initiated an update of GULF-2023, focusing on the skeletal storage, compaction, and subsidence package, hydraulic properties, and historical and predictive pumping data. Additionally, the model was converted from International System of Units to U.S. Customary Units and underwent recalibration to incorporate new data.

The purpose of the update was to rectify the identified issues and enhance the model for Groundwater Management Area 14's joint planning use. This model update was officially supported by Groundwater Management Area 14 members through a resolution adopted on May 14, 2024. The updated model, referred to as the GMA 14 Model, incorporates corrections based on new data collected by Lone Star Groundwater Conservation District, addressing compaction of fine-grained beds within the Gulf Coast Aquifer System, parameterization errors in GULF-2023, and other issues highlighted in stakeholder comments. Additionally, the model and report conform to Texas Water Development Board groundwater availability model and documentation standards.

We updated the conceptual model of GULF-2023 in three areas: (1) aquifer transmissivity, (2) groundwater pumping, and (3) aquifer compaction. We incorporated previously unpublished transmissivity results to enhance the available data. We then honored the transmissivity data for initializing the hydraulic properties in the model input files. For the pumping, we honored the estimated historical pumping values developed for the area by the Texas Water Development Board and others. While GULF-2023 allowed pumping to be reduced during calibration, we set up the GMA 14 Model to maintain the historical pumping estimates.

We updated the depth-dependent compaction property equations using Lone Star Groundwater Conservation District's newly acquired data from their 2024 coring program. For porosity, inelastic specific storage, and elastic specific storage, results from the new core samples were similar to the results from nearly 50 years ago in southern Harris and Galveston counties. (Gabrysch and Bonnet, 1974; 1976a; 1976b).

However, vertical hydraulic conductivity of the samples was about 10 times less than the earlier results. The lower vertical hydraulic conductivity indicates compaction may be about 10 times slower than the earlier data suggests.

Consistent with GULF-2023, we used MODFLOW 6, specifically MODFLOW 6.6.1 (Langevin and others, 2025), for the GMA 14 Model. We incorporated the updated conceptual model information into the input files for the model and converted other GULF-2023 input files as needed from length units of meters to feet. In addition, the shortest stress period in the model is one year, which reduced the total stress periods in the history matching period from 1896 through 2018 from 268 in GULF-2023 to 59 in the GMA 14 Model.

We calibrated the model using an ensemble approach to develop a base model and variations of the base model reflecting uncertainty in the model parameters. Calibration results indicated a good match between water level and subsidence simulated and measured values. The updated groundwater availability model provides improved utility for assessing regional groundwater management and joint planning by Groundwater Management Area 14 members.

1. Introduction

The Texas Water Development Board (“TWDB”) delineates the Gulf Coast Aquifer System as a band of relatively young geologic formations that parallel the Gulf of Mexico coastline, stretching from the southern Texas border with Mexico to the eastern Texas border with Louisiana (George and Mace, 2011). Groundwater Management Area 14 members manage the groundwater resources in the Gulf Coast Aquifer System from the western borders of Austin, Brazoria, Fort Bend, and Washington counties to the Texas border with Louisiana. Figure 1 illustrates the administrative boundary of Groundwater Management Area 14.

In October 2019, the Harris-Galveston Subsidence District contracted with the U.S. Geological Survey to update and refine the Houston-Area Groundwater Model. The problem presented in the U.S. Geological Survey proposal is that the subsidence districts require an updated groundwater flow model incorporating new data that can then be used for regional planning. One of the U.S. Geological Survey’s objectives was to coordinate work with the TWDB so that the updated model could be utilized by others for regional planning. Ellis and others (2023) documented the model update and in February 2024, the TWDB released the model known as GULF-2023 as the groundwater availability model for the northern portion of the Gulf Coast Aquifer System.

Prior to the TWDB’s finalization and release of GULF-2023, they published a draft model and documentation for stakeholder comments. Comments submitted jointly on behalf of Groundwater Management Area 14 members and by Lone Star Groundwater Conservation District identified several issues with the model that made it difficult to, and potentially incapable for, use in the joint planning activities of Groundwater Management Area 14. To address some of the issues with the model, to improve its use for joint planning, and to incorporate new data for the aquifer system, Lone Star Groundwater Conservation District commissioned an update of GULF-2023 on behalf of Groundwater Management Area 14 members. As discussed in the comments on the draft GULF-2023 and through subsequent findings while working with the model files, our three areas of focus for the GULF-2023 update were:

- The skeletal storage, compaction, and subsidence package used simulate aquifer compaction and land subsidence
- The hydraulic properties as included in the node property flow package to more reasonably reflect observed data
- The historical pumping and predictive pumping as included in the well package

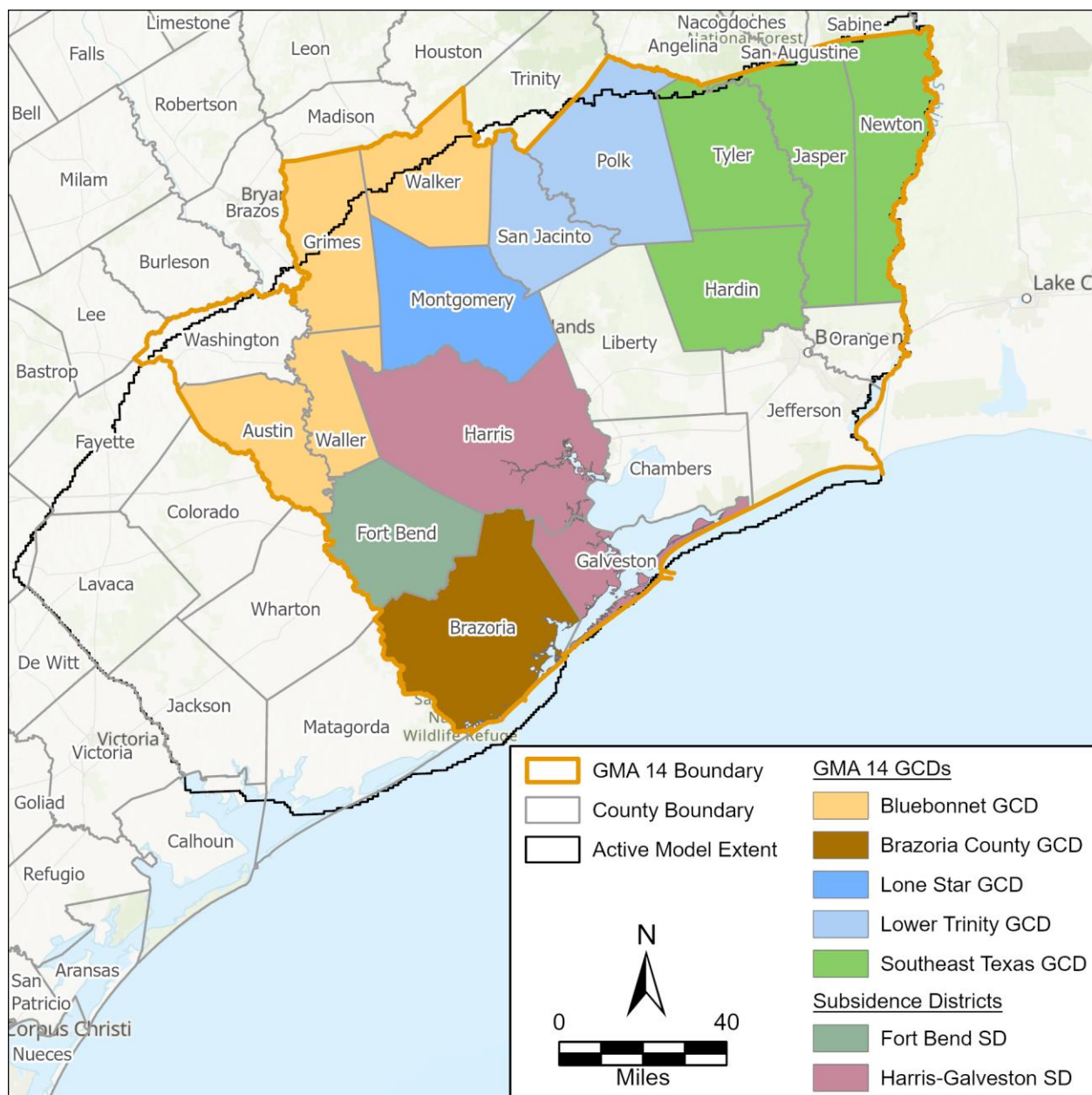


Figure 1. Counties, subsidence districts, and member groundwater conservation districts within Groundwater Management Area 14.

While we focused on the three areas above, we also reduced the number of stress periods in the model and converted the model from the International System of Units to U.S. Customary Units. In addition, our work on the model packages necessitated recalibration of the model. By correcting the above packages to better reflect the conceptual model and to incorporate new data, the existing calibration of GULF-2023 was not sufficient. Our work included updating the calibration using observed water levels, compaction, and subsidence, along with temporal trends in these observations.

The purpose of the model update was to address identified issues with GULF-2023, as presented in stakeholder comments on the model, and to improve the model for joint planning use by Groundwater Management Area 14. Groundwater Management Area 14 members recognized the need to update GULF-2023 for joint planning purposes and adopted a resolution during their May 14, 2024 meeting supporting the model update. The new data collected by Lone Star Groundwater Conservation District regarding compaction of the fine-grained beds within the Gulf Coast Aquifer System, parameterization errors in GULF-2023 (Keester, 2024), and issues identified by Groundwater Management Area 14 members in their comments on the draft GULF-2023 justify the groundwater availability model update. As an update to GULF-2023 specifically for Groundwater Management Area 14 joint planning purposes, throughout this report we refer to the updated model as the GMA 14 Model.

2. Conceptual Model Updates

As discussed below, our updates to the conceptual model focused on three areas:

1. Hydraulic properties, specifically transmissivity, of the aquifer layers
2. Groundwater pumping
3. Fine-grained material compaction

2.1. Hydraulic Properties

Aquifer transmissivity is the rate at which water is transmitted through a unit width of an aquifer over its entire thickness under a unit hydraulic gradient. It is a relative measurement of aquifer productivity that is most commonly derived from analysis of pumping test data. Transmissivity is equal to the hydraulic conductivity of an aquifer multiplied by its thickness.

Aquifer transmissivity is fundamental to groundwater flow modeling using MODFLOW. One of the basic equations applying Darcy's Law for groundwater flow to a mathematical expression of flow between model cells includes the calculation of transmissivity from hydraulic conductivity and the height of the model cell [see equation 2-3 in Langevin and others (2017)]. As such, incorporating measured transmissivity into the model update to the greatest extent possible was a priority.

We reviewed data from unpublished pumping tests for the Evangeline, Jasper, and Catahoula Aquifers to assist with filling in data gaps in the published pumping test datasets in the greater Houston and surrounding areas (that is, Montgomery, Harris, Fort Bend, Grimes, Waller, and Walker counties). Figure 2 shows the locations of wells with published and unpublished field data in the greater Houston area. The unpublished transmissivity values are based on data collected during constant-rate well pumping tests.

The use of the previously unpublished pumping test data allows for a reference of transmissivity values in areas with increasing population projections and water demands that may be subject to groundwater regulations. As shown on Figure 2, the inclusion of previously unpublished transmissivity data increased the spatial distribution of the data. We incorporated these additional transmissivity values into our update of the GMA 14 Model through interpolation of the available transmissivity data at the well locations. Figures 3, 4, and 5 illustrate the interpolated transmissivity and pumping test locations for the Chicot, Evangeline, and Jasper aquifers, respectively.

Appendix 1 contains a list of large capacity water wells with unpublished transmissivity values. Although unpublished, most of the Evangeline and Jasper Aquifer data were provided to the U.S. Geological Survey during development of the Houston-Area Groundwater Model (Kasmarek, 2013). Data for the Catahoula Aquifer is from the development of the Lone Star Groundwater Conservation District Catahoula Groundwater model (LBG-Guyton Associates and Intera, 2012) and the Lone Star Groundwater Conservation District Strategic Planning Study Task 3 (Seifert, Jr., 2017).

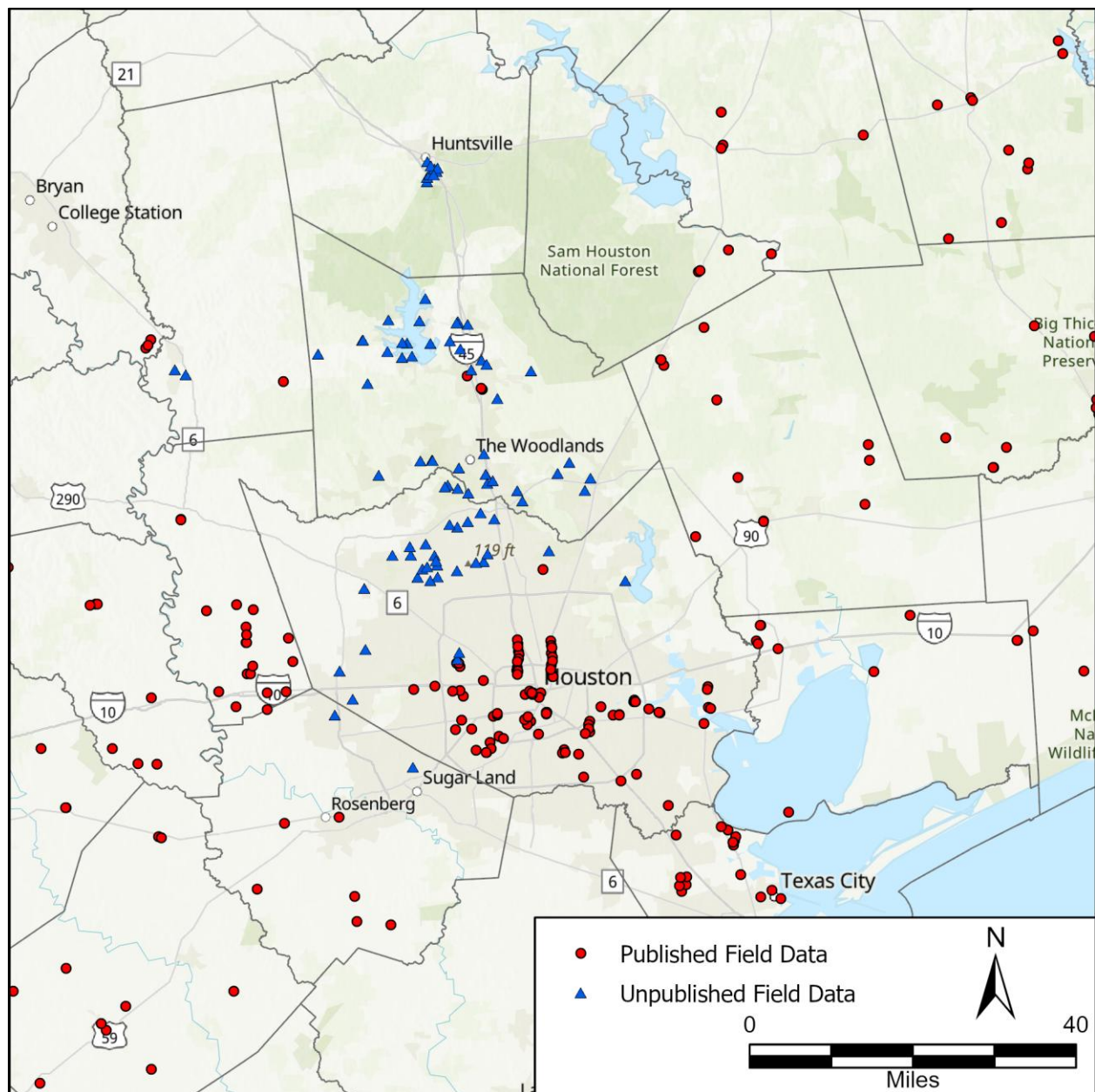


Figure 2. Map of locations of water wells with field data.

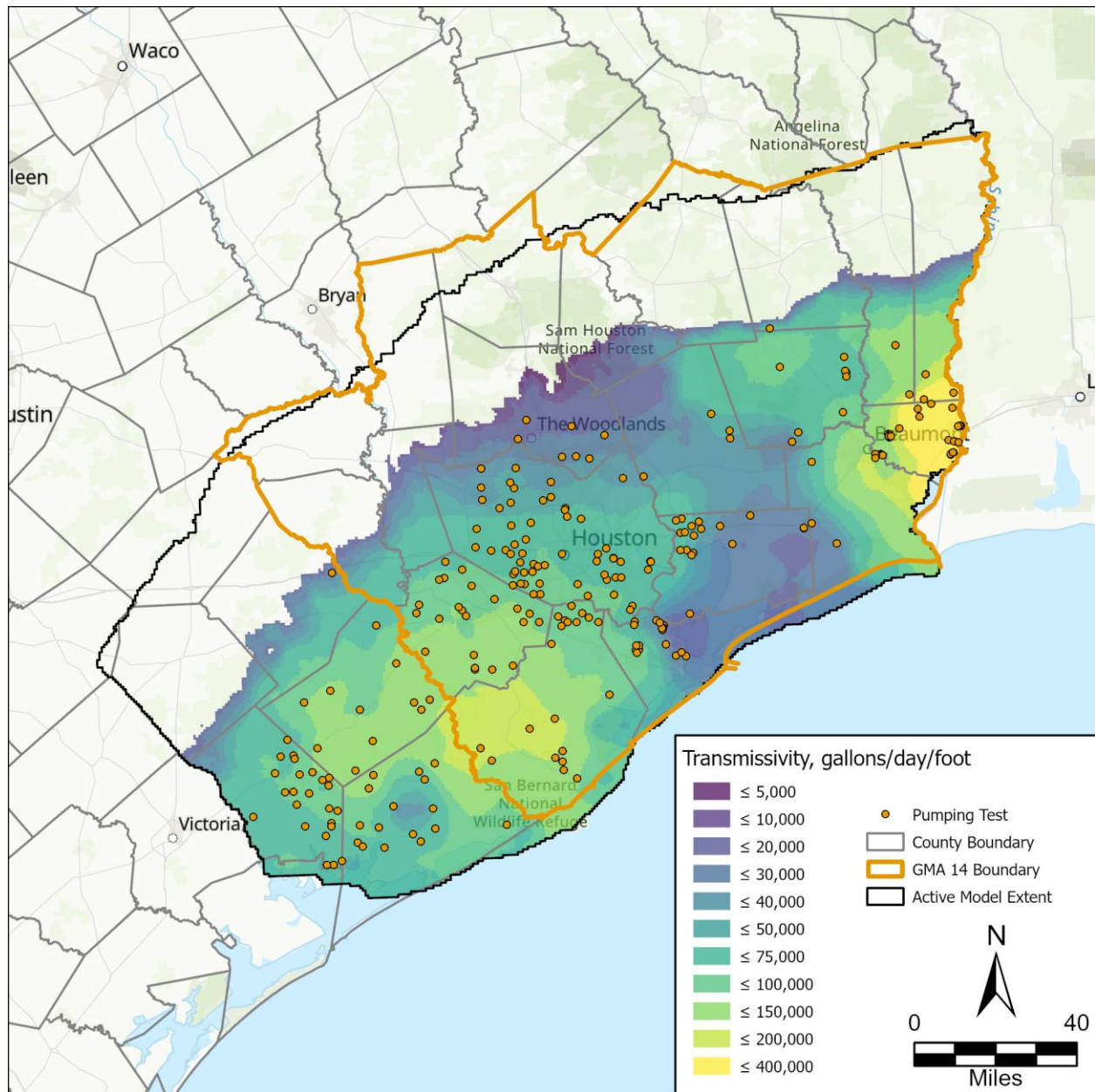


Figure 3. Chicot Aquifer interpolated transmissivity based on pumping test data.

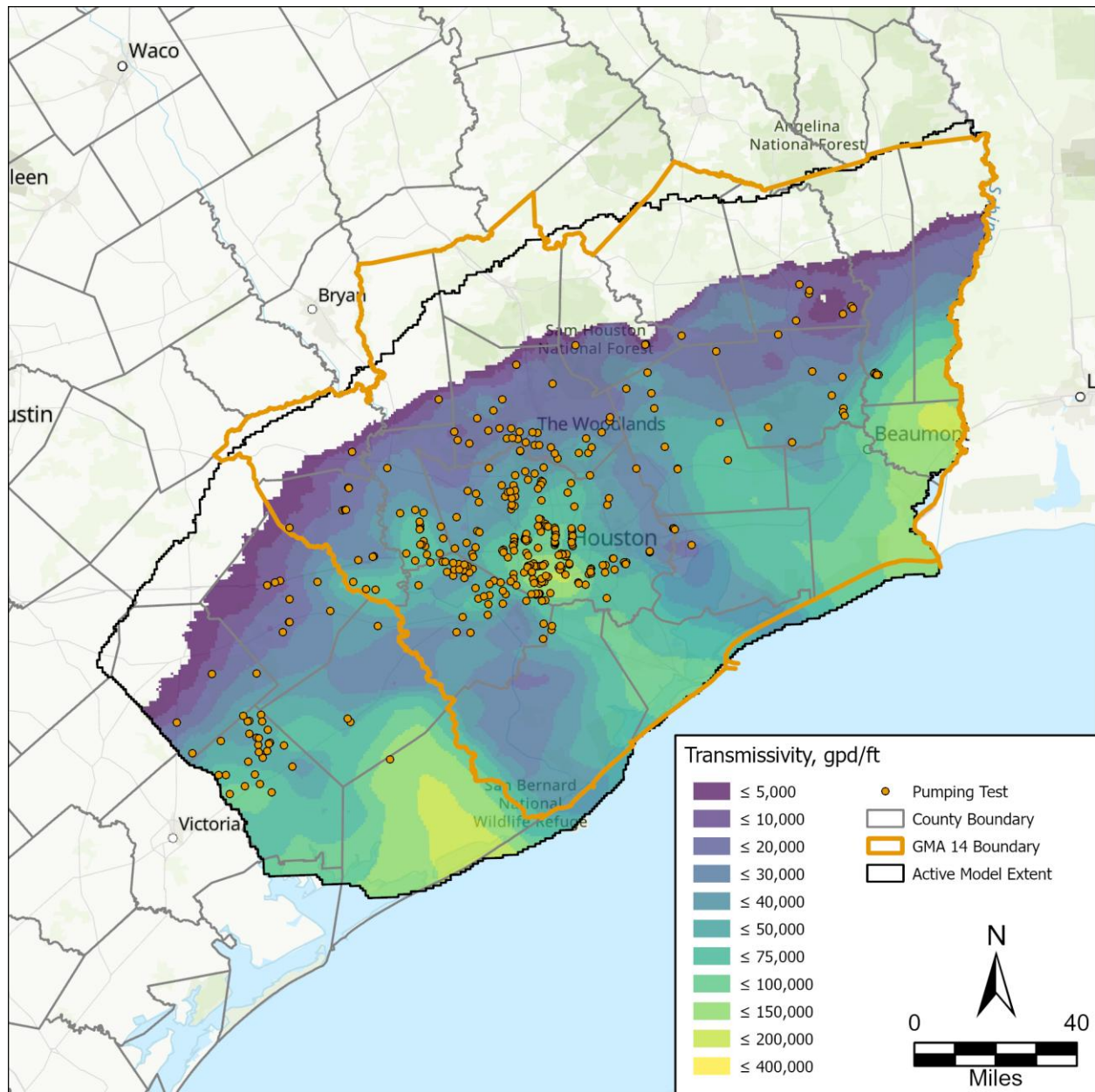


Figure 4. Evangeline Aquifer interpolated transmissivity based on pumping test data.

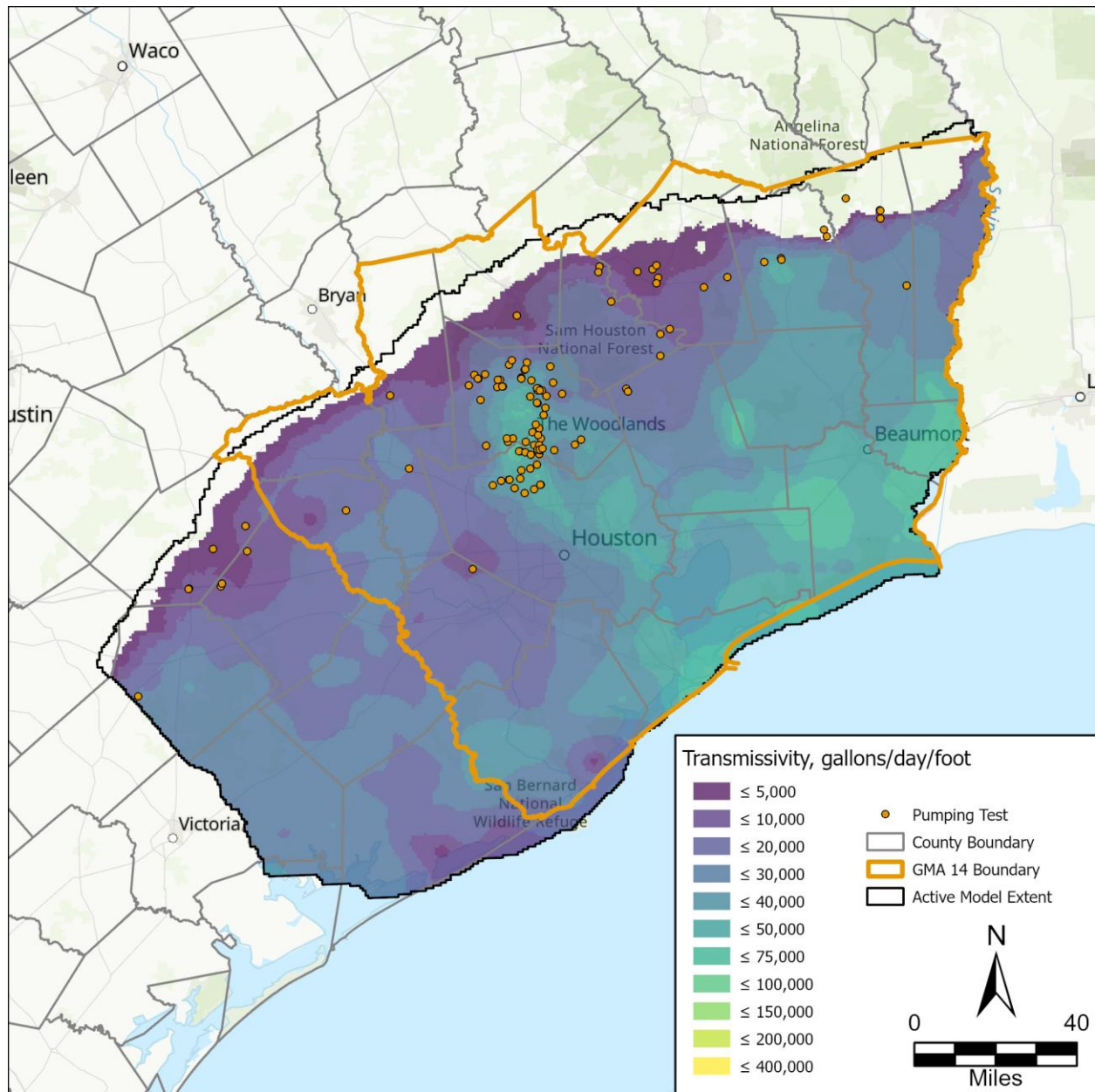


Figure 5. Jasper Aquifer interpolated transmissivity based on pumping test data.

2.2. Groundwater Pumping

As part of our development of the GMA 14 Model, we reviewed the pumping rates applied in GULF-2023. The following summarizes our review and updates applied as part of our work.

2.2.1. GULF-2023 Model Pumping Review

GULF-2023 uses two separate input files for the MODFLOW Well package during the calibration period. The “.irr” file contains irrigation pumping and the “.wel” file contains non-irrigation pumping. Two versions of each file are included with the model, namely, a “prior” version with initial pumping inputs and a “posterior” version representing calibrated values.

Ellis and others (2023) used PEST++ (White and others, 2020) to calibrate the model. As part of their calibration approach for GULF-2023, they allowed the software to make changes to the input pumping over the calibration period of the model. While PEST++ modified both the prior irrigation and non-irrigation well input values over the calibration period, Ellis and others (2023) considered the irrigation pumping to be less certain and allowed greater reductions in the estimated historical pumping.

Appendix 2 includes a series of graphs showing the GULF-2023 pumping by county. The graphs show a comparison of the GULF-2023 prior and posterior versions of the irrigation and non-irrigation pumping. The graphs in Appendix 2 show very minor differences in the non-irrigation prior and posterior pumping. However, some of the figures illustrate relatively large differences in irrigation prior and posterior pumping, such as is in Colorado, Jackson, Lavaca, Liberty, Matagorda, Waller, and Wharton counties.

2.2.2. Comparison with Houston Area Groundwater Model Pumping

As part of the GMA 14 Model update, we also compared pumping between GULF-2023 and the Houston-Area Groundwater Model. The GULF-2023 calibration period extended through 2018 (Ellis and others, 2023) while the Houston-Area Groundwater Model calibration period was through 2009 (Kasmarek, 2013). Therefore, there are no model pumping input values available for comparison from 2010 through 2018. Appendix 3 includes graphs comparing the GULF-2023 and Houston-Area Groundwater Model pumping on a county basis.

Overall, the total pumping per county between the GULF-2023 and Houston-Area Groundwater Model models are similar for most counties. There can be differences in the totals between the GULF-2023 and Houston-Area Groundwater Model based on available pumping data at certain points in time. There are larger differences in the GULF-2023 and Houston-Area Groundwater Model total pumping in the counties where

calibration reductions in irrigation pumping occurred. Austin, Brazoria, Fort Bend, and Harris counties also have notable differences in total county pumping between the GULF-2023 and Houston-Area Groundwater Model.

We also observe notable changes in the vertical distribution of pumping between the GULF-2023 and Houston-Area Groundwater Model in Fort Bend, Hardin, Harris, Jasper, Liberty, and Montgomery counties. Some of the differences in vertical distribution are likely due to a redefinition of the base of the Chicot Aquifer for the model. Young and Draper (2020) used a chronostratigraphic approach to redefine the base of the Chicot Aquifer (model layer 2). Their approach resulted in thickening of the Chicot Aquifer and thinning of the Evangeline Aquifer relative to the traditional hydrostratigraphic approach applied to the delineation of the contact between the two aquifers. This change in approach to delineating the base of the Chicot Aquifer may be responsible for part of the vertical pumping differences between GULF-2023 and the Houston-Area Groundwater Model in parts of Fort Bend, Harris, and Liberty counties. We discuss differences in Montgomery County in detail in Section 2.2.3.3.

2.2.3. GMA 14 Model Pumping Update

Appendix 4 includes a series of graphs that shows the GMA 14 Model pumping inputs by county. There are three graphs per county that include the total pumping by layer, the irrigation pumping by layer, and the non-irrigation pumping by layer.

2.2.3.1. GMA 14 Model Irrigation Pumping

Our approach for the GMA 14 Model calibration was to not allow changes to the pumping input during the calibration process. The TWDB has developed estimates of water use in the state since 1955. While the process has changed over time, TWDB staff make significant efforts to obtain the best estimates possible for water use including irrigation pumping. Their estimates for irrigation use include crop histories, land use, and water use per crop which, since 2001, are then adjusted for precipitation and various other considerations (Furnans and others, 2022). Our approach for the GMA 14 Model is that the TWDB and others used reliable methods to develop irrigation estimates for counties in the greater Houston and surrounding areas. Irrigation survey maps combined with knowledge of crop irrigation requirements support the irrigation pumping included in the prior irrigation pumping file.

The only change we made to the GULF-2023 prior irrigation pumping file during the development of the GMA 14 Model pumping files was for Montgomery County. We found the prior irrigation file to contain minimal pumping for Montgomery County in the later stress periods of the model, so we set these values to zero. Within Lone Star Groundwater Conservation District, this irrigation pumping is permitted and reported by

golf courses, nurseries, and others. We included this reported pumping within the non-irrigation pumping amounts discussed in the following section.

No additional changes were made to any of the prior irrigation well files for the other counties included in the model area. The pumping in the GMA 14 Model irrigation file is consistent with what is shown as prior amounts on the graphs in Appendix 2 with the exception of Montgomery County.

2.2.3.2. GMA 14 Model Non-irrigation Pumping

Four of the five groundwater conservation districts within Groundwater Management Area 14 reported varying degrees of historical non-exempt permitted groundwater production data for review. We compared reported non-exempt groundwater production from Bluebonnet Groundwater Conservation District, Brazoria County Groundwater Conservation District, Lower Trinity Groundwater Conservation District, and Lone Star Groundwater Conservation District with the prior GULF-2023 non-irrigation pumping. Appendix 5 includes graphs comparing the available non-exempt permitted production data and the GULF-2023 prior non-irrigation pumping data. Each groundwater conservation district has years where the GULF-2023 prior non-irrigation pumping and the total reported non-exempt pumping have some differences, but overall the pumping between the two data sources is similar.

We reviewed the spatial distribution of the historical permitted production data when possible. We found that many of the wells with permitted production data provided by Bluebonnet Groundwater Conservation District, Brazoria County Groundwater Conservation District, and Lower Trinity Groundwater Conservation District did not include an assigned aquifer. Lone Star Groundwater Conservation District tracks pumping by aquifer and has estimated non-exempt pumping for the permitted and registered non-exempt wells.

2.2.3.3. Montgomery County Pumping Update

The only changes we made to the GULF-2023 prior non-irrigation pumping input as part of the GMA 14 Model development are in Montgomery County. Figure 6 shows a comparison of the GMA 14 Model pumping to the GULF-2023 pumping.

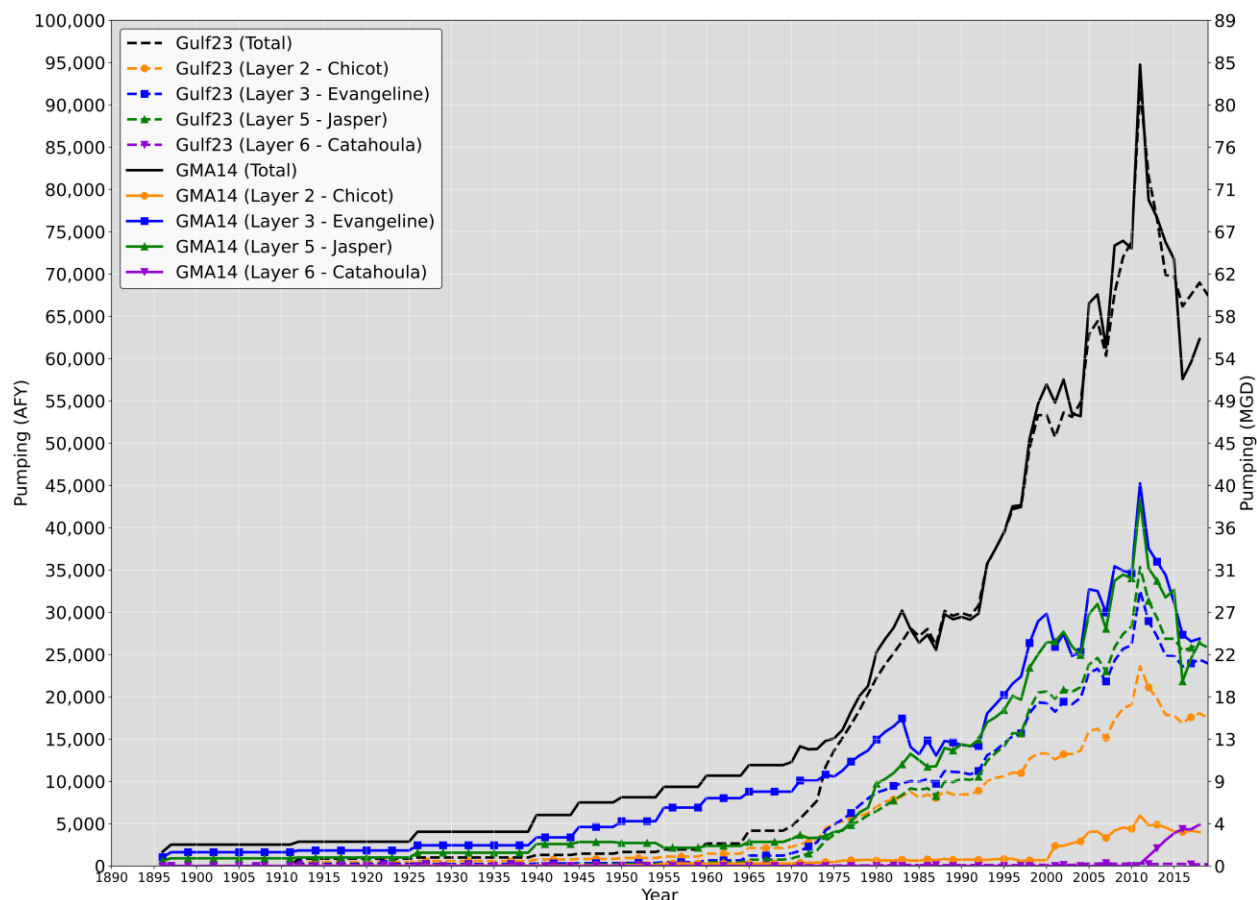


Figure 6. Comparison of the GMA 14 Model and GULF-2023 pumping in Montgomery County.

We used the total Houston-Area Groundwater Model pumping for Montgomery County from the beginning of the GMA 14 Model through 2002. We selected the use of the earlier Houston-Area Groundwater Model pumping inputs as Lone Star Groundwater Conservation District permits production by aquifer and the pumping from the Houston-Area Groundwater Model has a pumping distribution that is more representative of the current permitted pumping distribution. The Lone Star Groundwater Conservation District assigns aquifers to permitted and registered non-exempt wells based on a hydrostratigraphic understanding of the Gulf Coast Aquifer System and site-specific data.

The Montgomery County pumping in GULF-2023 is less than the Houston-Area Groundwater Model through about 1970 when the total GULF-2023 pumping starts to increase sharply. The Houston-Area Groundwater Model pumping is a better fit for the incorporation of the additional City of Conroe pumping beginning in 1955. For the GMA 14 Model, we did not change the total Montgomery County pumping with the addition of

the 1955 and beyond City of Conroe data or the 1975 and beyond San Jacinto River Authority – The Woodlands well production data. Rather, we reduced groundwater pumping evenly in other parts of Montgomery County to offset the increases in the Conroe and The Woodlands pumping. Our goal was to improve implementation of the historical pumping by Lone Star Groundwater Conservation District's two largest groundwater production permit holders.

Appendix 6 provides a comparison of the reported groundwater production for the City of Conroe and The Woodlands to the GULF-2023 and GMA 14 Model pumping. There are several utility districts located within the City of Conroe along Lake Conroe that have groundwater production wells completed in the Jasper which is why the GMA 14 Model pumping is slightly higher than the reported City of Conroe Jasper Aquifer pumping. The GMA 14 Model pumping in The Woodlands includes additional Evangeline Aquifer pumping related to irrigation for golf courses and nurseries which is not included in the pumping reported by the San Jacinto River Authority.

We used the Lone Star Groundwater Conservation District reported non-exempt permitted pumping as the basis for the 2003 to 2018 production to improve the spatial and vertical distribution of the GMA 14 Model pumping within Montgomery County. The Lone Star Groundwater Conservation District GULF-2023 comments (Drabek and Keester, 2023) submitted to the TWDB in April 2023 document the differences in the vertical distribution of pumping within Montgomery County. In Montgomery County, GULF-2023 overestimates pumping in the Chicot Aquifer and underestimates pumping in the Evangeline and Jasper aquifers.

These pumping discrepancies do not appear to be related to the change in aquifer structure based on the chronostratigraphic approach as the areas impacted by this structural change to the model layers occur in the southeast part of Montgomery County as documented in the Lone Star Phase 2 Subsidence Study (Keester and others, 2022). Review of Lone Star Groundwater Conservation District permitted pumping in the Evangeline Aquifer in the southeast part of Montgomery County indicates that the GULF-2023 Evangeline Aquifer pumping in that part of the county is similar to the reported non-exempt pumping.

Development of the Catahoula Aquifer in Montgomery County began in about 2011 and groundwater production had increased to about 4,900 acre-feet in 2018. The Montgomery County update of the non-irrigation well file includes the development of the pumping in the Catahoula Aquifer in Montgomery County.

2.3. Compaction

Ellis and others (2023) discuss how subsidence is largely dependent on the compaction properties of fine-grained sediments interbedded in the aquifer system. These compaction properties include:

- Porosity (θ) or Void Ratio (e)
- Compression Index (C_c)
- Recompression Index (C_r)
- Vertical Hydraulic Conductivity (K_v)

For these properties, Ellis and others (2023) reportedly used the depth-dependent relationships developed by Kelley and others (2018). For the compaction parameterization, Kelley and others (2018) evaluated the change in void ratio with applied stress data reported by Gabrysch and Bonnet (1974; 1976a; 1976b). Keester and others (2022) also evaluated the results from Gabrysch and Bonnet (1974; 1976a; 1976b) and found results similar to those of Kelley and others (2018) for the compaction parameterization.

A limitation of each of these studies is that they are geographically constrained to the sites where core samples were collected about 50 years ago. In addition, the core samples collected were from only the Chicot and Evangeline aquifers of the Gulf Coast Aquifer System. In 2024, to increase our conceptual understanding of the compaction parameters of the fine-grained sediments of the Chicot and Evangeline, and to get the first of its kind data for the Burkeville and Jasper, Lone Star Groundwater Conservation District conducted a drilling program to collect core samples in Montgomery County. Figure 7 illustrates locations where core samples for compaction parameter analysis have been collected.

2.3.1. Previous Investigations

It is beyond the scope of this report to detail the previous work on compaction parameterization. We discuss the data collected by Gabrysch and Bonnet (1974; 1976a; 1976b) within the context of the results from the Lone Star Groundwater Conservation District drilling program. We refer the reader to the work by Kelley and others (2018) and Keester and others (2022) for detailed analysis of the compaction data reported by Gabrysch and Bonnet (1974; 1976a; 1976b).

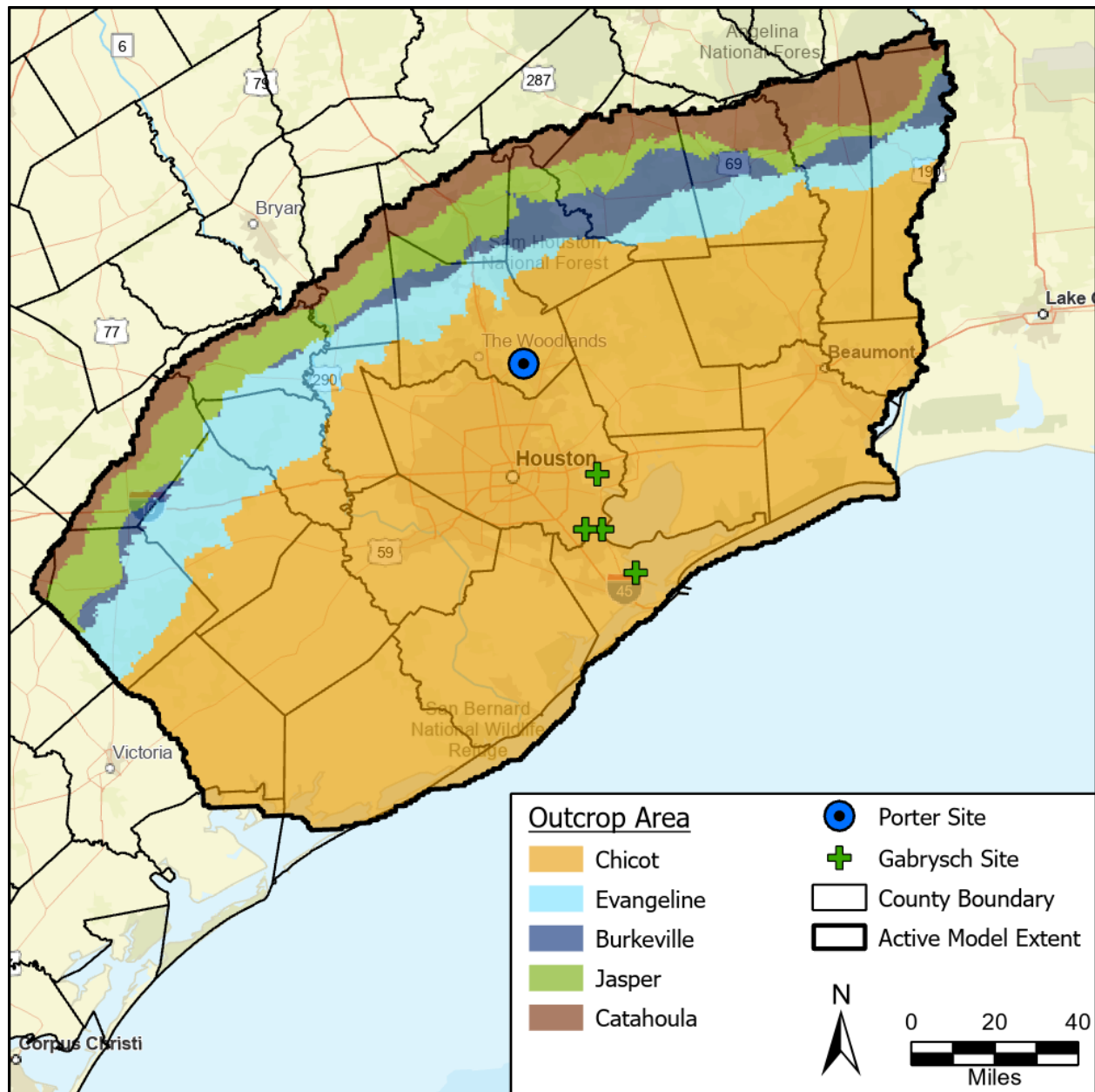


Figure 7. Locations where core samples of the Gulf Coast Aquifer System have been collected for analysis of compaction properties.

2.3.2. Lone Star Groundwater Conservation District Porter Site

At the Porter Site, Lone Star Groundwater Conservation District collected core samples from 18 distinct subsurface intervals. Table 1 provides the sample depths for collected core. Multiple tests were conducted on the samples; however, for the model update report we will focus on the tests and results related to the compaction parameter factors listed above. Additional details regarding core collection, preservation, and analyses are included in a project report in preparation as of the writing of this model report.

Table 1. Subsurface core samples collected at the Porter Site.

Core ID	Top	Bottom	Length	Aquifer	Description
1	78	84.95	6.95	Chicot	Lean Clay
2	198	206	8	Chicot	Lean Clay with Sand
3	308	319.6	11.6	Chicot	Fat Clay
4	457	463.15	6.15	Evangeline	Poorly Graded Sand with Silt
5	640	651.5	11.5	Evangeline	Fat Clay
6	833	848.35	15.35	Evangeline	Fat Clay
7	968	978.8	10.8	Evangeline	Clayey Sand
8	1,088	1,095.9	7.9	Evangeline	Fat Clay
9	1,198	1,203.4	5.4	Burkeville	Lean Clay
9B	1,208	1,217.85	9.85	Burkeville	Lean Clay
10	1,293	1,306.3	13.3	Burkeville	Fat Clay
11	1,463	1,475	12	Upper Jasper	Lean Clay
12	1,538	1,546.15	8.15	Upper Jasper	Silty Sand
13	1,633	1,644.35	11.35	Upper Jasper	Silty Sand
14	1,726	1,738	12	Upper Jasper	Lean Clay
15	1,888	1,896.1	8.1	Lower Jasper	Fat Clay
16	1,953	1,964.1	11.1	Lower Jasper	Fat Clay
17	2,058	2,065.45	7.45	Lower Jasper	Lean Clay
18	2,261	2,266.95	5.95	Lower Jasper	Fat Clay

2.3.2.1. Geostatic, Hydrostatic, and Effective Vertical Stress

Geostatic stress (σ) is a combination of the weight of sediments and fluids above a specified depth in the subsurface. The hydrostatic stress (u) is the pressure within the pore space of the sediments above a specified depth in the subsurface. Effective vertical stress (σ'_v) is the difference between geostatic stress and hydrostatic stress. Terzaghi (1925) identified this relation which allows effective stress within an aquifer to be expressed as (Leake and Galloway, 2007):

$$\sigma'_v = \sigma - u \quad \text{Eq. 1}$$

Commonly, the geostatic stress gradient (G_σ) is assumed to be 1.0 pounds per square inch per foot of burial. However, Tiab and Donaldson (2016) indicate the geostatic gradient in the Gulf Coast region increases with depth being about 0.85 pounds per square inch per foot near the surface and increasing to 1.0 pounds per square inch per foot at about 20,000 feet in depth. They indicate the reason for the trend is due to “sediments being younger and more compressible near the surface but being less compressible and more plastic with depth.” For the Porter Site we obtained a bulk density log from which we calculated the geostatic stress gradient at the site and found it increased with depth as Tiab and Donaldson (2016) described for the Gulf Coast region. Figure 8 illustrates the geostatic stress at the Porter Site.

For the hydrostatic stress, we calculated the pore pressure using the method of Eaton (1972). This method requires the normal shale (that is, clay or fine-grained sediment) resistivity (R_n) and shale resistivity when the depth equals zero (R_0). To obtain these values, we must first determine the shale intervals within the formations. To quantify the shale intervals, we used the gamma log data to calculate the volume of shale (V_{sh}) using an equation for Tertiary age unconsolidated sediments (Asquith and Gibson, 1982):

$$V_{sh} = 0.083 \left[2^{3.7 \left(\frac{GR_{log} - GR_{min}}{GR_{max} - GR_{min}} \right)} - 1 \right] \quad \text{Eq. 2}$$

Where:

GR_{log} = log response

GR_{min} = minimum log response = 26.695 API

GR_{max} = maximum log response = 94.895 API

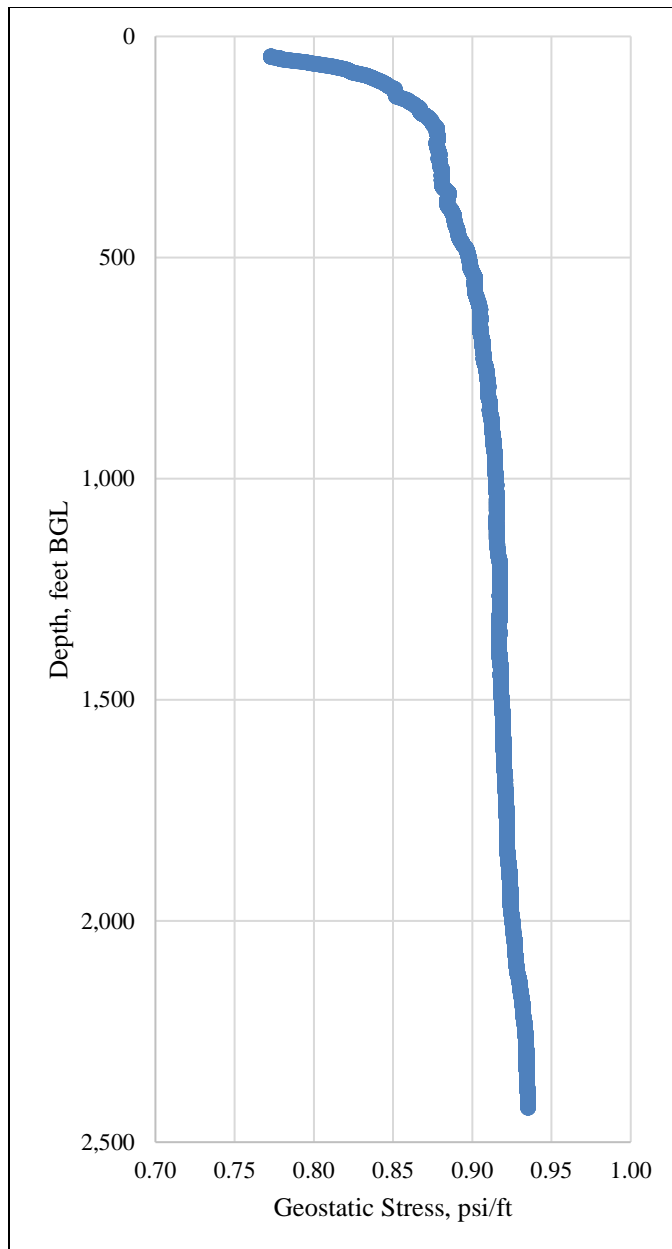


Figure 8. Porter Site geostatic stress.

We used a calculated shale volume of 30 percent as a cutoff for assigning an interval as shale. Using the volume of shale calculations, we then determined the normal shale resistivity as a best fit trend through the identified shale points at depths less than 1,000 feet below ground level with the trend line taking the form of (Zhang and Yin, 2017):

$$R_{nz} = R_0 \exp^{bz} \quad \text{Eq. 3}$$

Where:

R_{nz} = normal shale resistivity at depth Z (ohm · m)

R_0 = resistivity when $Z = 0$ (ohm · m) = 4.0 ohm · m

b = compaction parameter = $10^{-3.244}$

Z = depth below ground level (ft)

Figure 9 illustrates the shale resistivity and calculated trend for the normal shale resistivity at the Porter Site. Using the geostatic stress gradient, normal shale resistivity, and observed shale resistivity, we then calculated the pore pressure gradient (G_u) as (Eaton, 1995; Imhanzuaria and Bello, 2019):

$$G_u = G_\sigma - (G_\sigma - 0.433) \times \left(\frac{R_z}{R_{nz}} \right)^{1.2} \quad \text{Eq. 4}$$

Where:

R_z = Deep resistivity value at depth Z (ohm · m)

0.433 = normal pore pressure gradient ($\frac{psi}{ft}$)

1.2 = constant

Using the geophysical log data, we calculated the pore pressure gradient at 0.1-foot intervals for the shale intervals. As the shale intervals transition to sand layers, the calculated pore pressure decreases as the deep resistivity value increases. To account for the fluctuations, we calculated a moving median for each shale depth interval using the calculated pore pressure gradient values within 10 feet of the depth along with a running average of all calculated pore pressure values shallower than the depth of interest (Figure 10).

Using the calculated geostatic stress gradient and pore pressure (that is, hydrostatic stress) gradient, we could then calculate the in-situ effective stress for each Porter Site core sample. For most of the samples, we used the moving median pore pressure; however, three samples had a relatively high sand content, and we used the running average pore pressure value as more representative of the interval. Table 2 provides the calculated geostatic, hydrostatic, and effective stress for analyzed core samples.

The applied effective vertical stress during testing of the core samples is generally reported in units of kilopascal (“kPa”) or 1,000 pounds-force per square foot (“ksf”). Using the effective stress gradient calculated for each core sample, we converted the reported effective vertical stress during testing to an equivalent depth. We used the equivalent depths and applied the approach of Kelley and others (2018) to expand the depth-dependent relationships for compaction parameterization of the Gulf Coast Aquifer System fine-grained sediments.

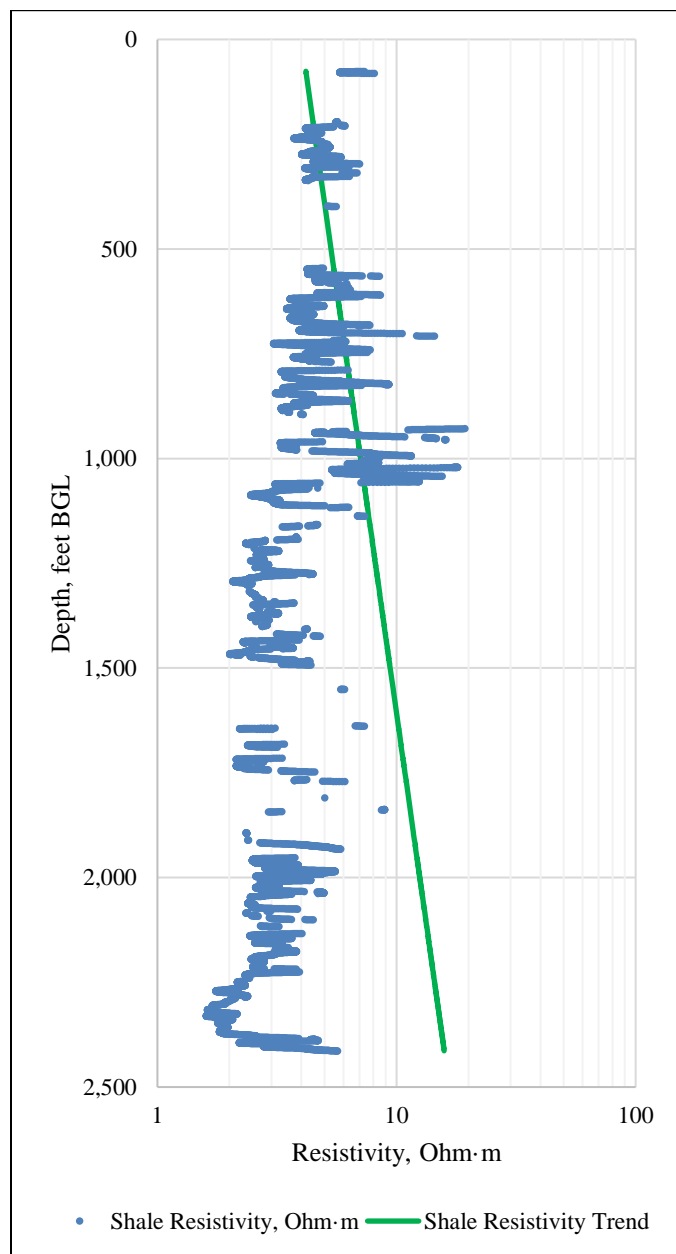


Figure 9. Shale resistivity and calculated normal shale resistivity trend.

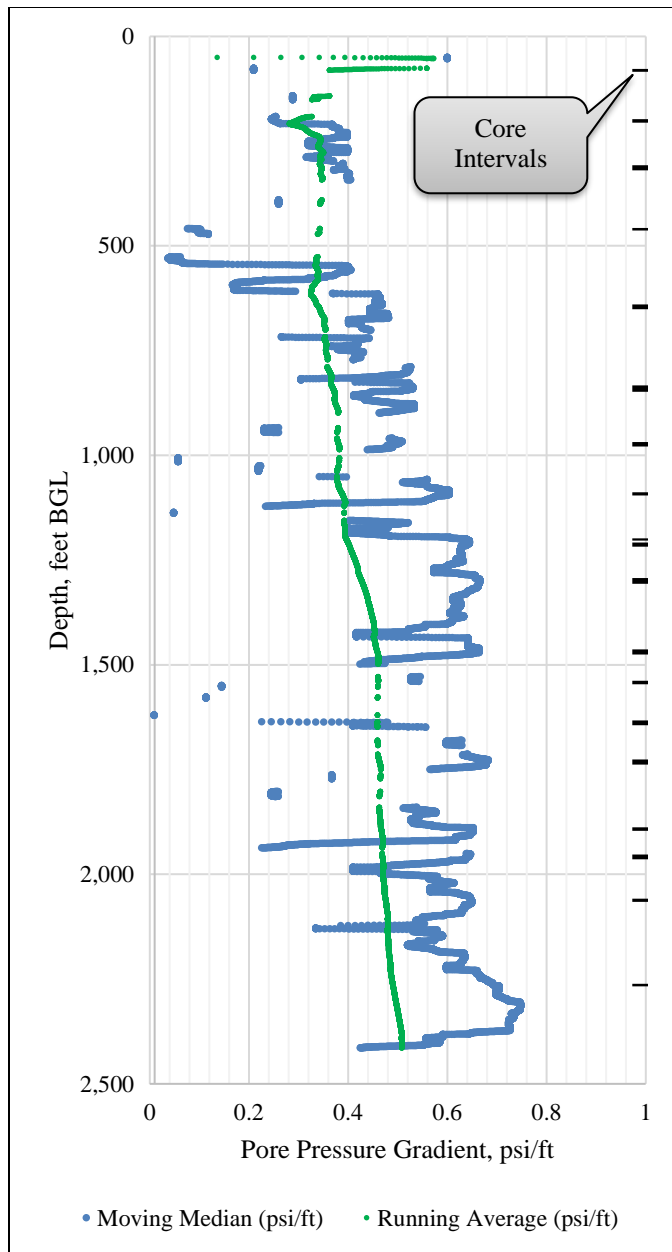


Figure 10. Calculated fine-grained sediment pore pressure gradient.

Table 2. Porter Site calculated geostatic stress, pore pressure (hydrostatic stress), and effective stress.

Core Sample [†]	Formation	Depth, feet BGL	Geostatic Stress, psi	Pore Pressure, psi	Effective Stress, psi
C1T2	Chicot	82	68	24	44
C2T4	Chicot	204	179	52	127
C3T3	Chicot	315	277	122	155
C4T2*	Evangeline	459	410	157	253
C5T5	Evangeline	648	586	293	293
C6T5	Evangeline	840	765	445	320
C6T6-TAMU	Evangeline	843	768	439	330
C6T6-SO	Evangeline	843	768	439	330
C7T3	Evangeline	974	890	478	413
C8T1	Evangeline	1,090	997	658	340
C9T1	Burkeville	1,199	1,100	755	345
C9BT1	Burkeville	1,210	1,110	779	331
C9BT4 - TAMU	Burkeville	1,199	1,100	755	345
C10T3	Burkeville	1,297	1,190	862	328
C11T3	Burkeville	1,467	1,347	973	373
C12T1*	Upper Jasper	1,540	1,415	709	706
C13T2*	Upper Jasper	1,635	1,504	751	754
C14T1	Upper Jasper	1,728	1,592	1,178	414
C15T5 - TAMU	Lower Jasper	1,897	1,752	1,236	516
C15T5 - SO	Lower Jasper	1,897	1,752	1,236	516
C15T6	Lower Jasper	1,900	1,754	1,227	527
C16T1	Lower Jasper	1,955	1,806	1,260	547
C17T1	Lower Jasper	2,059	1,909	1,332	577
C18T1	Lower Jasper	2,263	2,113	1,568	545

*Pore pressure value from running average values

† "T#" represents the tube number of the core sample.

2.3.2.2. Porosity

The porosity (θ) of a material is the amount open space within a solid volume. For example, if one cubic foot of fine-grained sediment has a porosity of 15 percent that means that 0.15 cubic feet of the sediment is open space where water or other liquid or gas can be stored. The porosity is related to the void ratio (e) as follows:

$$\theta = \frac{e}{1+e} \quad \text{Eq. 5}$$

During testing, a portion of the core sample is held within a chamber and vertical stress is applied to the sample. As effective vertical stress changes, the void ratio for the applied effective vertical stress is recorded. Figure 11 is an example of the test results for the effective vertical stress versus void ratio.

Analysis of the porosity data from the Porter Site cores showed results similar to the results from Gabrysch and Bonnet (1974; 1976a; 1976b). Figure 12 shows the measured porosity versus effective depth at the Porter Site and Gabrysch sites. While the results are similar, the porosity trend with effective depth is slightly higher. Equation 6 is the calculated best-fit trend line through all of the available porosity data from core analyses.

$$\theta = 0.3625e^{-1.00 \times 10^{-4}Z} \quad \text{Eq. 6}$$

Keester and others (2022) found a logarithmic trend best fit the Gabrysch data so a logarithmic trend was applied to the Porter Site data for comparison. However, when the data are combined, an exponential trend provides the best trend through the data. This exponential trend was applied within the model update as the initial estimate of fine-grained bed porosity prior to model calibration.

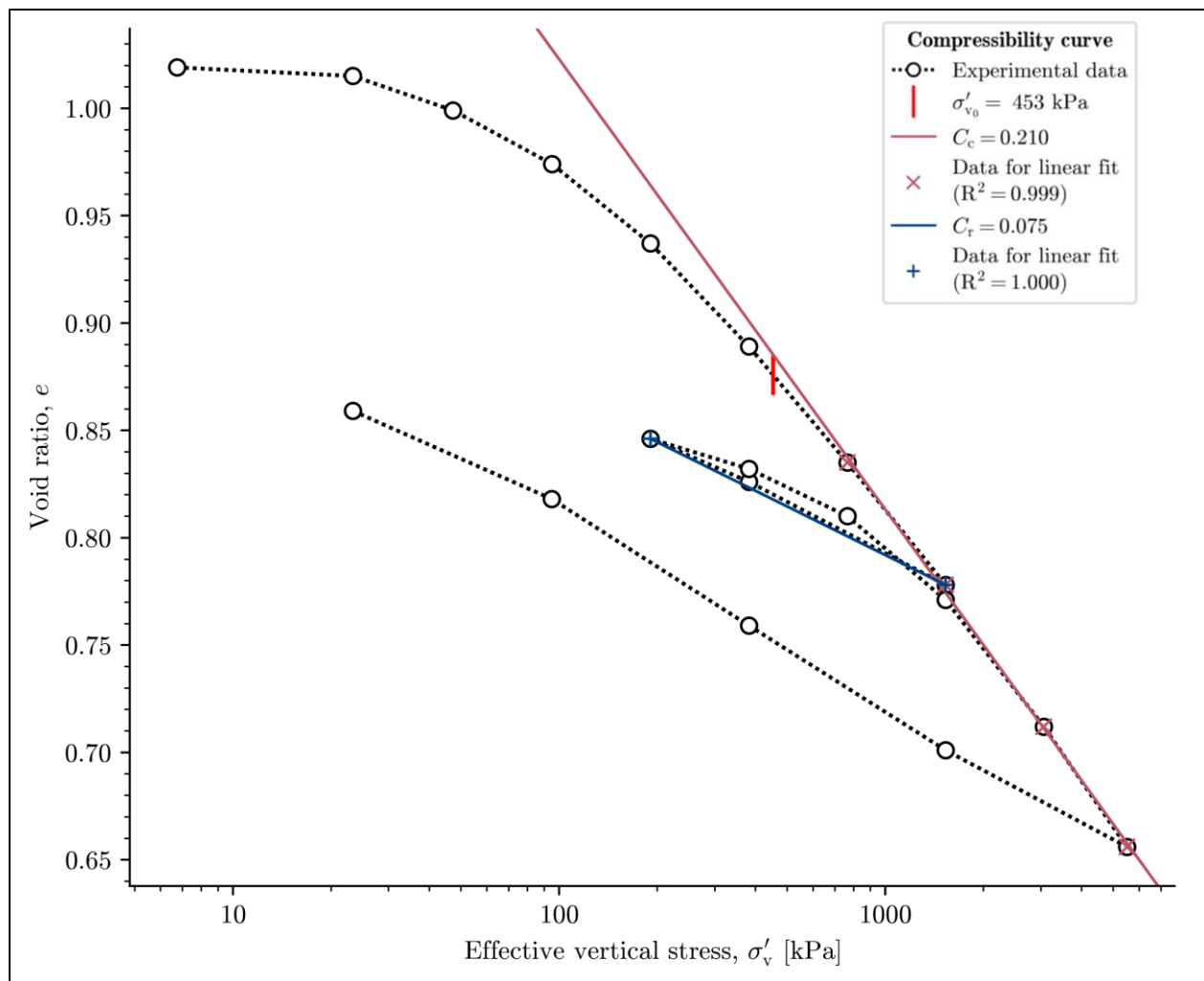


Figure 11. Effective vertical stress versus void ratio for core sample C8T1.

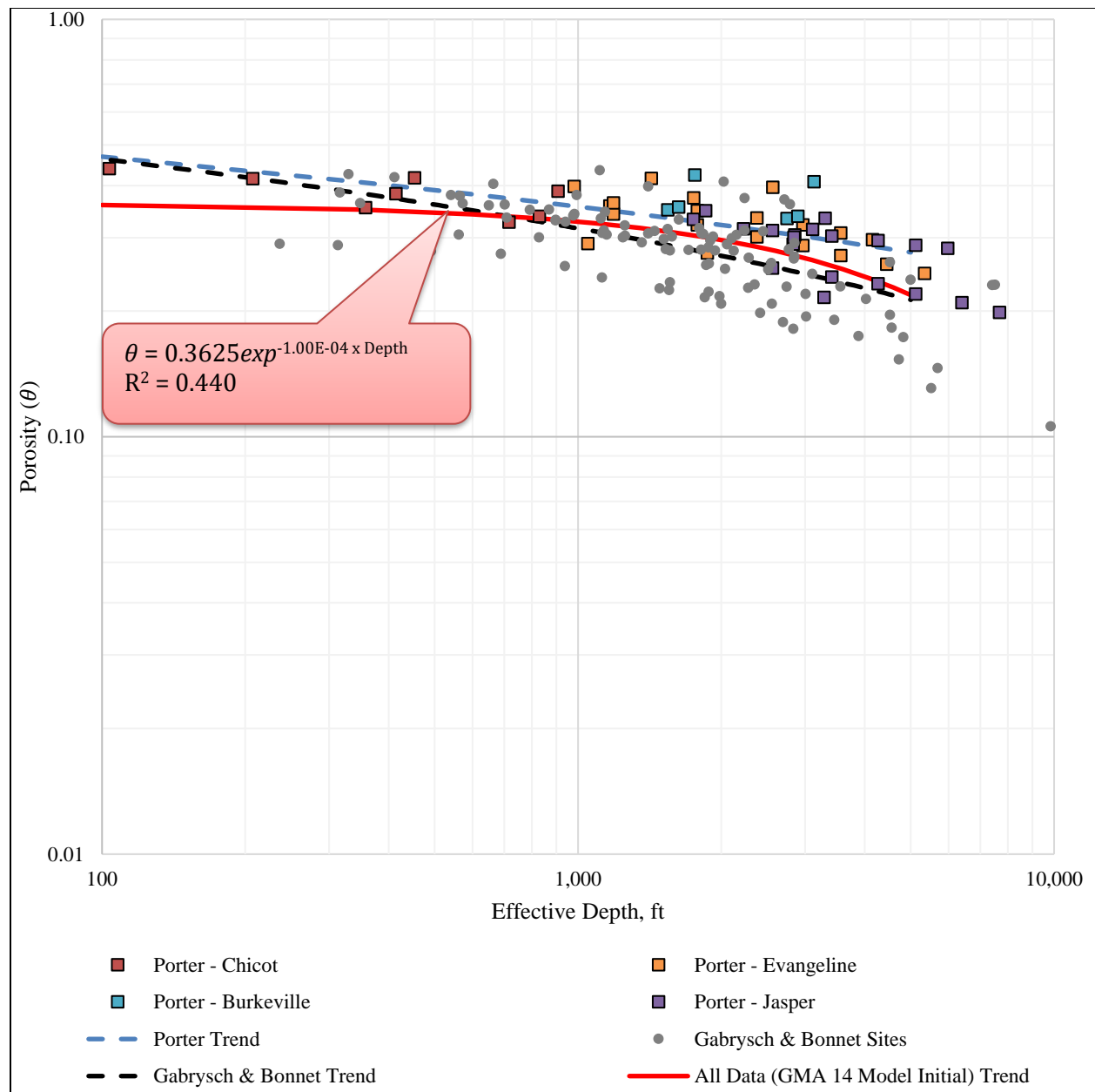


Figure 12. Porosity results from the compaction testing. Gabrysch & Bonnet trend from Keester and others (2022).

2.3.2.3. Compression and Recompression

The compression index is the change in void ratio over the logarithm of the effective stress during inelastic conditions. Similarly, the recompression index represents the same change during elastic conditions (Jorgensen, 1980). Lone Star Groundwater Conservation District worked with W.D. Von Gotten Engineering LLC and Innovative Geotechnology LLC to conduct consolidation testing on samples from each core to determine these indices for the core intervals. In addition, the Lone Star Groundwater Conservation District worked with Texas A&M University Zachry Department of Civil and Environmental Engineering to conduct consolidation testing of three samples at higher pressures than the commercial labs were capable of applying to verify results and extend analyses to greater effective depths. Using the void ratio and pressure data, the compression and recompression indices are calculated as follows (Jorgensen, 1980):

$$C_c = \frac{de}{d \log_{10} \sigma'_v} \{Loading Phase\} \quad \text{Eq. 7}$$

$$C_r = \frac{de}{d \log_{10} \sigma'_v} \{Unloading Phase\} \quad \text{Eq. 8}$$

Where:

C_c = Compression index (dimensionless)

C_r = Recompression index (dimensionless)

The compression index is determined as a slope of a fitted line of the curve defined by the plot of void ratio versus the logarithm of effective stress during the loading phase of testing which represents the inelastic range. For the recompression index, a line is fitted to the measurements during the unloading phase which represents the elastic range of the sediments. Figure 13 illustrates the calculation from the measurements using the test data for core C2T4.

Table 3 summarizes the common ranges of the indices for low to high plasticity clays. Most of the compression index results for the Porter Site data are within the low to medium plasticity range (Table 4). However, the recompression index results are generally within the typical high plasticity range. Table 5 summarizes the compression and recompression indices by aquifer.

A general range for the C_r/C_c is 0.02 to 0.2 with lower values representing highly structured and bounded soft clay and silt deposits (Terzaghi and others, 1996). The average C_r/C_c value of the Porter Site cores is 0.24 which is higher than the expected range for a clay. However, deviations from the literature values are expected due to potential variations in silt and sand content within the samples.

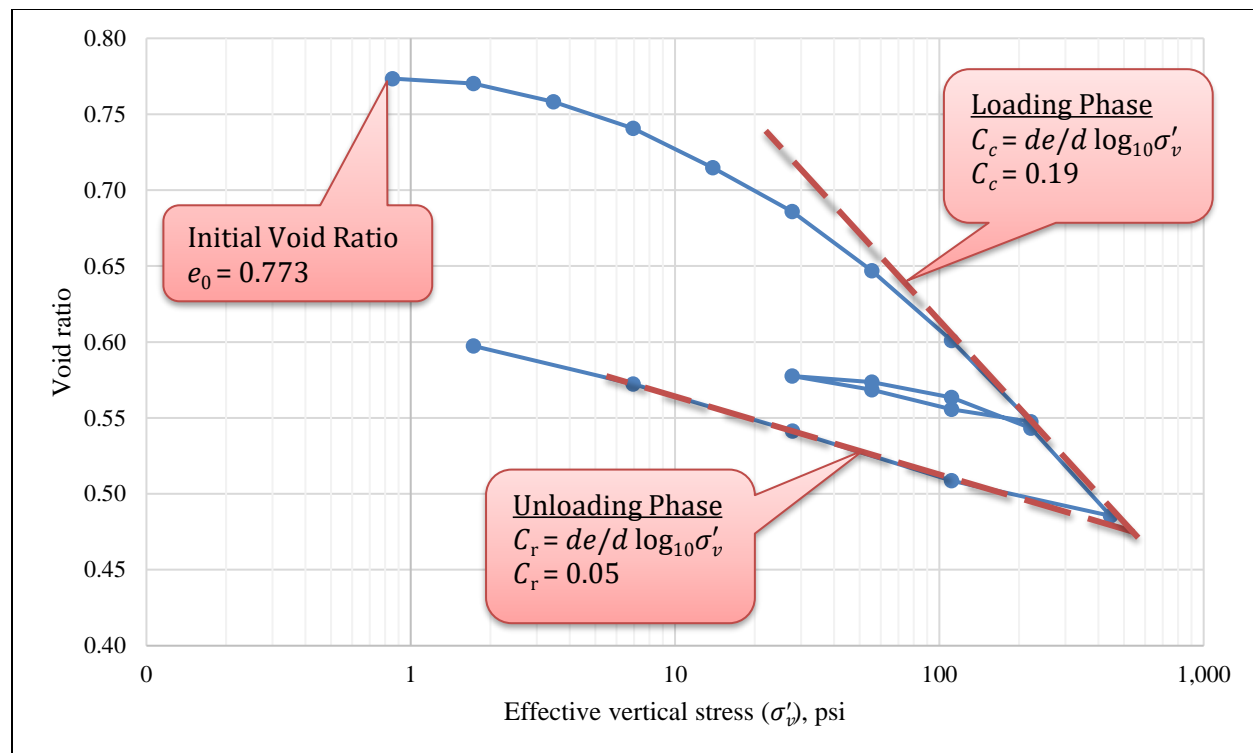


Figure 13. Example of compression and recompression index determination.

Table 3. Typical compression and recompression index value ranges for clays (Terzaghi and others, 1996; Das, 2010).

Clay Type	Compression Index	Recompression Index
Low-medium plasticity	0.1 to 0.3	0.005 to 0.015
High plasticity	0.3 to 0.6	0.01 to 0.05

Table 4. Compression and recompression index for each core sample.

Core Sample	Formation	Compression Index	Recompression Index	C_r/C_c
C1T2	Chicot	0.33	0.05	0.15
C2T4	Chicot	0.19	0.05	0.26
C3T3	Chicot	0.25	0.02	0.08
C4T2*	Evangelina	0.04	0.01	0.25
C5T5	Evangelina	0.26	0.04	0.15
C6T5	Evangelina	0.17	0.04	0.24
C6T6-TAMU	Evangelina	0.30	0.12	0.40
C6T6-SO	Evangelina	0.28	0.11	0.39
C7T3	Evangelina	0.11	0.02	0.18
C8T1	Evangelina	0.21	0.05	0.24
C9T1	Burkeville	0.15	0.02	0.13
C9BT1	Burkeville	0.16	0.03	0.19
C9BT4 - TAMU	Burkeville	0.29 [†]	0.17 [†]	0.59
C10T3	Burkeville	0.17	0.04	0.24
C11T3	Upper Jasper	0.17	0.02	0.12
C12T1*	Upper Jasper	0.05	0.002	0.04
C13T2*	Upper Jasper	0.06	0.02	0.33
C14T1	Upper Jasper	0.12	0.01	0.08
C15T5 - TAMU	Lower Jasper	0.23	0.09	0.39
C15T5 - SO	Lower Jasper	0.22	0.08	0.36
C15T6	Lower Jasper	0.2	0.1	0.50
C16T1	Lower Jasper	0.17	0.07	0.41
C17T1	Lower Jasper	0.12	0.02	0.17
C18T1	Lower Jasper	0.31	0.02	0.06

*samples with relatively high sand content that are not representative of the clay interbeds. Values not included in statistical summaries.

[†]Preliminary values as of this report. Values not included in statistical summaries.

Table 5. Average compression and recompression indices by aquifer.

Formation	Compression Index	Recompression Index	C_r/C_c
Chicot	0.26	0.04	0.16
Evangeline	0.22	0.06	0.27
Burkeville	0.16	0.03	0.19
Upper Jasper	0.15	0.02	0.10
Lower Jasper	0.21	0.06	0.32

2.3.2.4. Specific Storage

The specific storage (S_s) of aquifer sediments is the volume of water released from or added to storage in a unit volume of aquifer per unit decline or rise in water level (Bear, 1979). The specific storage value may be further defined as the sum of the elastic (S_{ske}) and inelastic (S_{skv}) components (Hoffman and others, 2003) with the inelastic component generally being approximately 100 times greater than the elastic component (Leake and Prudic, 1991; Young and others, 2006). However, other studies have found the ratio of the inelastic to elastic specific storage to be higher than 0.1 (Song and others, 2022; Jiangtao Li, 2022).

Previous investigations relied on the typical ratio of S_{skv} to S_{ske} (Kelley and others, 2018; Keester and others, 2022). However, for the Porter Site data, we applied the equations from Jorgensen (1980) relating C_c and C_r to S_{skv} and S_{ske} , respectively, as follows:

$$S_{skv} = \frac{0.434C_c\gamma_w}{(1+e_0)\sigma_v'} \quad \text{Eq. 9}$$

$$S_{ske} = \frac{0.434C_r\gamma_w}{(1+e_0)\sigma_v'} \quad \text{Eq. 10}$$

Where:

e_0 = initial void ratio

γ_w = specific weight of water $\approx 9.81 \frac{kN}{m^3} \approx 62.43 \frac{lb_f}{ft^3}$

Figure 14 and Figure 15 illustrate the calculated inelastic and elastic, respectively, specific storage values. The inelastic storage values from the Porter Site data fall along a similar trend to results from the Gabrysch and Bonnet (1974; 1976a; 1976b) data with the trend lines through each data set essentially the same. Results for the elastic specific storage are also similar though slightly higher for some samples at greater effective depths. Equations 11 and 12 are the calculated best-fit trend lines through all of the available inelastic and elastic, respectively, calculated storage coefficient values based on data from core analyses.

$$S_{skv} = 6.916 \times 10^{-5} \exp^{-2.84 \times 10^{-4}Z} \quad \text{Eq. 11}$$

$$S_{ske} = 1.244 \times 10^{-5} \exp^{-2.21 \times 10^{-4}Z} \quad \text{Eq. 12}$$

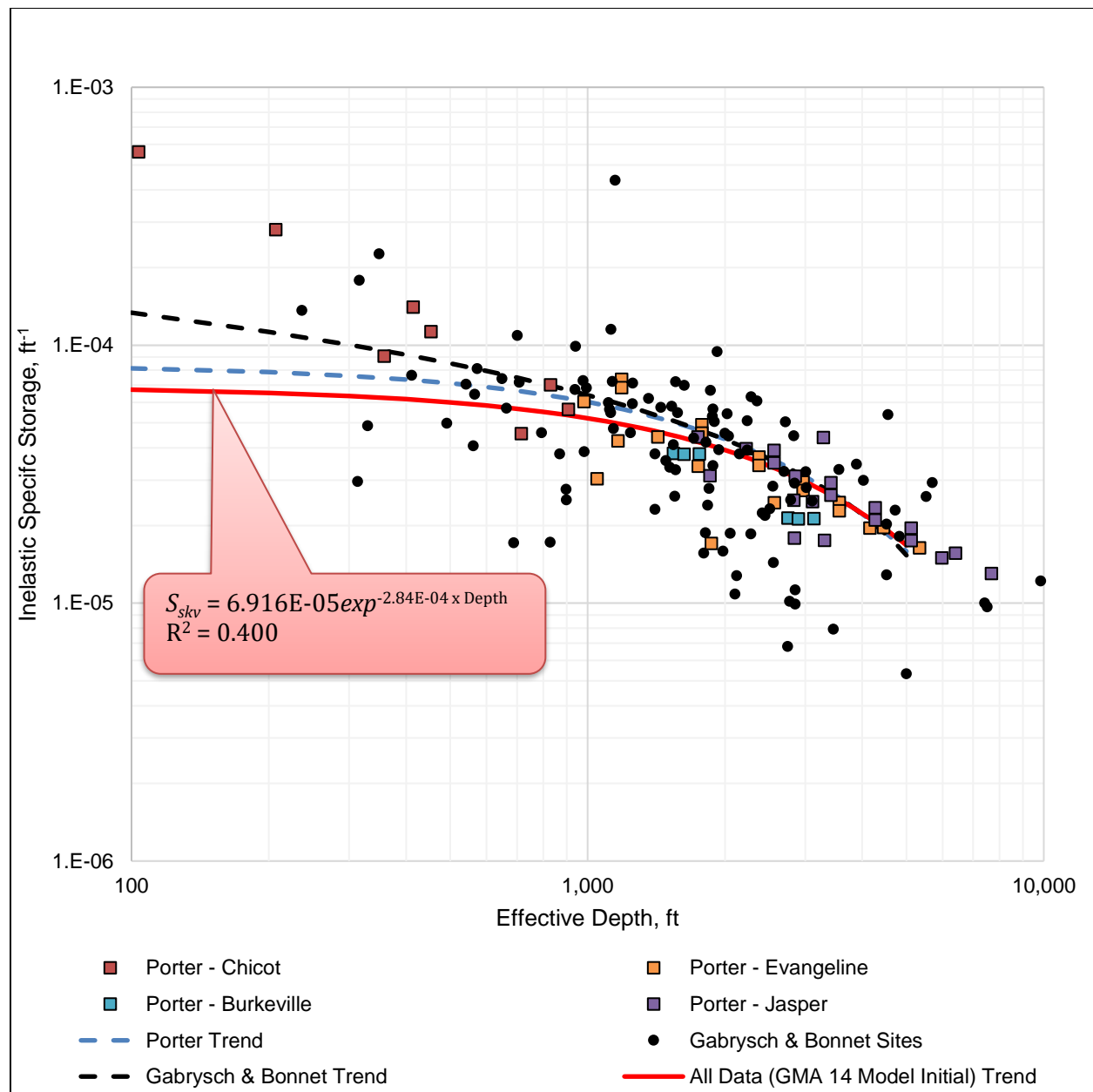


Figure 14. Calculated inelastic specific storage (S_{skv}) results from the compaction testing. Gabrysch & Bonnet trend from Keester and others (2022).

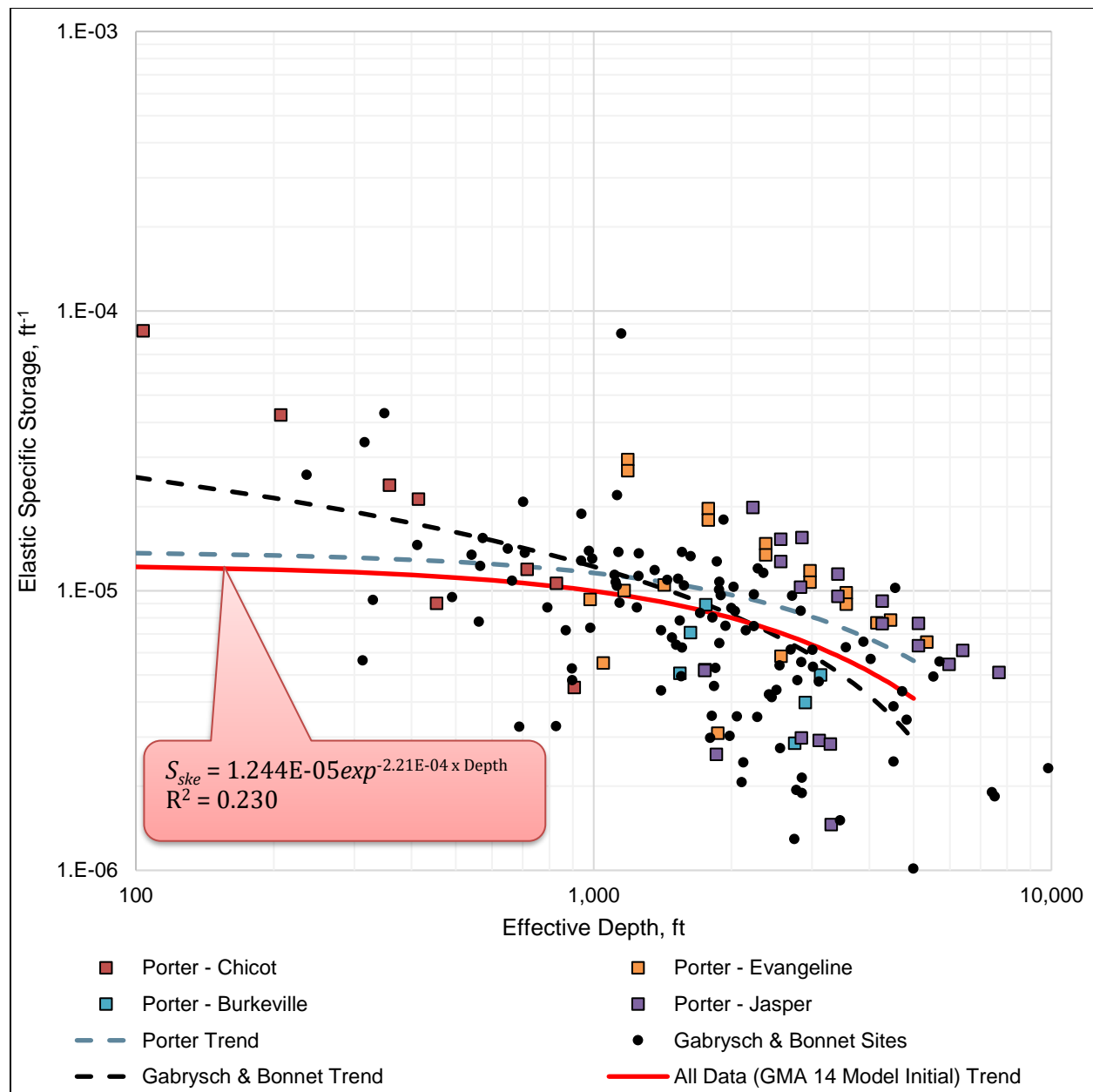


Figure 15. Calculated elastic specific storage (S_{ske}) results from the compaction testing. Gabrysch & Bonnet trend from Keester and others (2022).

2.3.2.5. Vertical Hydraulic Conductivity

The specific storage values of the clay beds control the amount of compaction that can occur under a given amount of stress. However, to determine the rate at which compaction occurs we also need to know the vertical hydraulic conductivity and thickness of the clay beds along with the specific storage.

The thickness and vertical hydraulic conductivity of individual clay beds affects the rate at which compaction may occur. When pumping from the aquifer occurs, water will preferentially move through the coarser-grained sediments (that is, sand) causing a pressure (that is, water level) decline. The decrease in pressure within the coarser-grained sediment layers creates a pressure gradient between the coarser-grained sediment layers and the finer-grained (that is, clay) sediment layers. This pressure gradient causes water to move from the finer-grained sediment layers into the coarser-grained sediment layers resulting in a decrease in pressure (and increase in effective stress) within the finer-grained sediment layers.

The decrease in pressure in a finer-grained sediment layer occurs immediately at the interface between that layer and the coarser-grained sediment layer. The decrease in pressure in the finer-grained sediment layer then propagates toward the center of the layer. Assuming consistent hydraulic properties of the layer, as the thickness of the finer-grained sediment layer increases, the time it takes for the pressure decrease to propagate to the center of the layer also increases. The amount of time it takes for full compaction to occur can be expressed as a “time constant” in compaction calculations (Hoffman and others, 2003). The time constant (τ_0) in Equation 13 represents the amount of time at which about 93 percent of the ultimate clay bed compaction will occur.

$$\tau_0 = \frac{\left(\frac{b_0}{2}\right)^2 S_s}{K_v} \quad \text{Eq. 13}$$

Where:

b_0 = *initial thickness of the clay bed*

K_v = *vertical hydraulic conductivity*

As illustrated in Figure 16, approximately 50 percent of the compaction occurs relatively rapidly (within about 20 percent of the time constant) and then gradually slows over time. To understand the timing of compaction, understanding the vertical hydraulic conductivity of compressible beds is necessary as relatively small variations can greatly affect the timing of compaction. For example, with K_v as the denominator in Equation 13, with each order of magnitude decrease in value the timing for compaction increases 10 times.

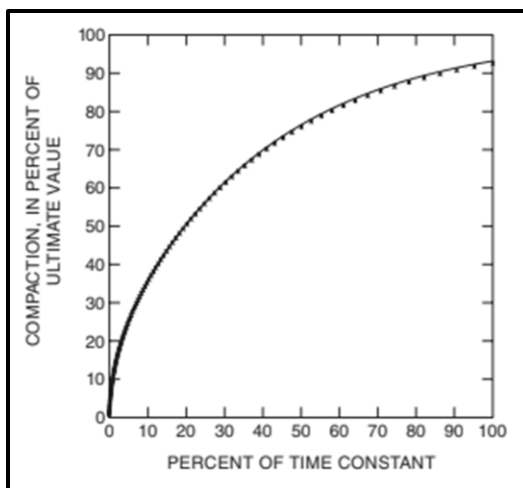


Figure 16. Illustration of compaction as a function of the compaction time constant. Reproduced from Hoffman and others (2003).

Kelley and others (2018) developed a model of vertical hydraulic conductivity with depth based on their analysis of data from Gabrysch and Bonnet (1974). To provide a lower bound on their vertical hydraulic conductivity estimates, Kelley and others (2018) also developed a depth dependent model using parameters from PRESS models (Espey, Huston, and Associates, Inc., 1982) which simulate one-dimensional compaction at sites across the Houston area.

Results from the Porter Site core analyses indicated the vertical hydraulic conductivity is generally lower than the Gabrysch and Bonnet (1974) data. The best fit trend line through the Porter Site data is an order of magnitude less than trend through the Gabrysch and Bonnet (1974) data. Figure 17 illustrates the data collected from core samples along with the trends.

The PRESS model (Espey, Huston, and Associates, Inc., 1982) input values were lower than most data points. Several of the results at greater effective depth were lower than the Porter Trend as some sample results are much higher than many of the data points. Testing narratives suggest some samples have microfractures which are allowing water to flow faster through the sample than the clay would allow, and the results are indicative of those microfractures rather than the material permeability. Nonetheless, as there are relatively few sites for the region, we used the best fit trend line through all of the data to develop a depth-dependent vertical hydraulic conductivity equation:

$$K_v = 8.774 \times 10^{-6} \exp^{-7.71 \times 10^{-4} Z} \quad \text{Eq. 14}$$

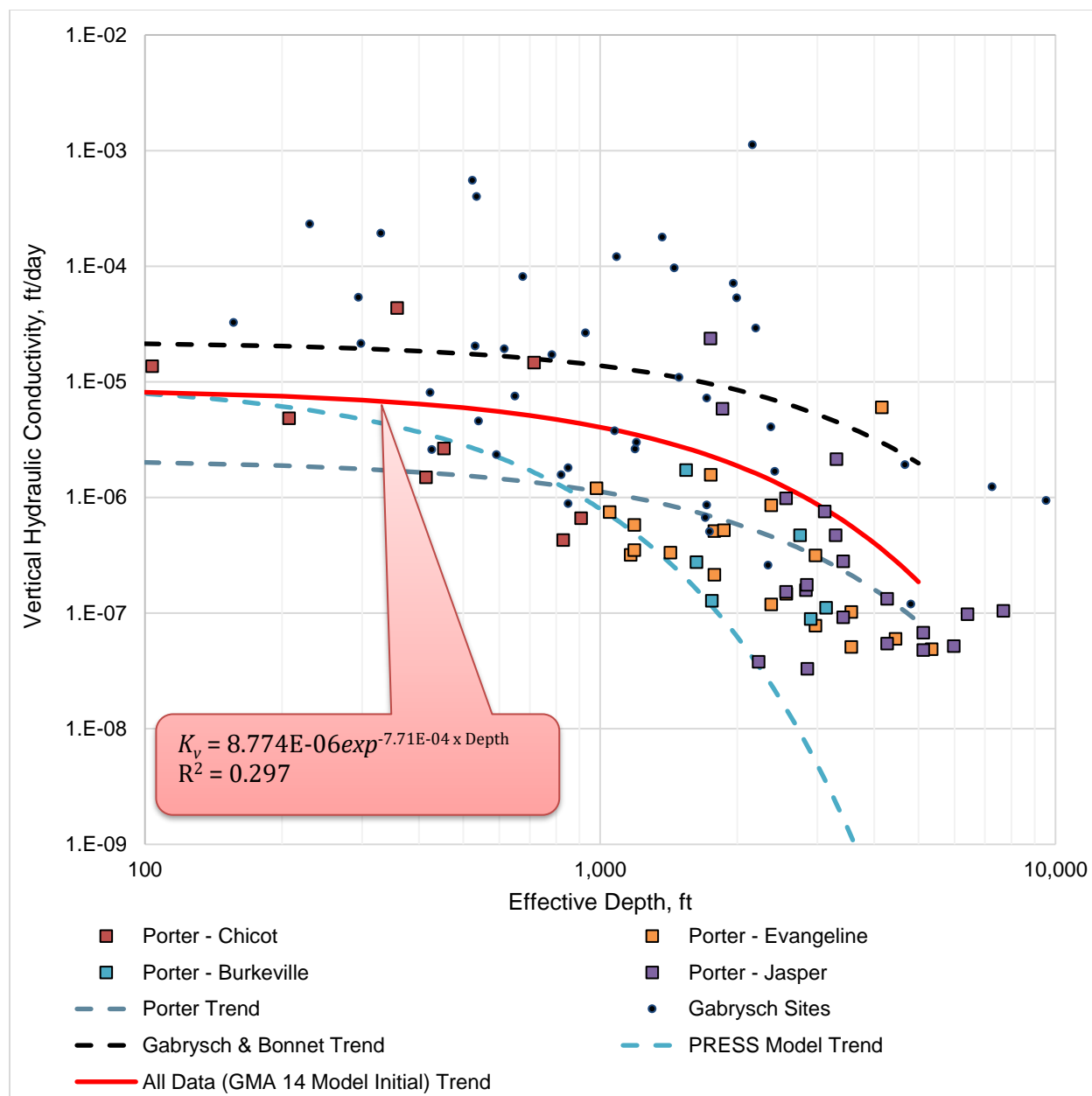


Figure 17. Vertical hydraulic conductivity results from the compaction testing. Gabrysch & Bonnet trend from Keester and others (2022).

3. Model Overview and Packages

We based the numerical model on GULF-2023 (Ellis and others, 2023) and conceptual model updates outlined in Section 2. We used the MODFLOW 6 code (Langevin and others, 2017) for the GMA 14 model. MODFLOW 6 is the latest version of the MODFLOW code developed by the U.S. Geological Survey and was originally released in 2017. The current version is MODFLOW 6.6.1 released on February 10, 2025 (Langevin and others, 2025).

A model developed using the MODFLOW 6 code consists of a combination of files that each provide information to a MODFLOW package. Each package represents a component of the groundwater flow system or output from the model. Table 6 lists the packages corresponding to file names utilized for the GMA 14 Model.

There are two Name (NAM) files for the GMA 14 Model. One NAM file is associated with simulation files that include information on the solver and time discretization. The other NAM file is for the model input and output files. Upon execution, MODFLOW 6 reads the *mfsim.nam* file to obtain the type of model, the timing of the model, and how the model is solved. In Table 6, these files are listed under the *Simulation Files* section. The *mfsim.nam* file points to the *gma14.nam* file which lists the other *Model Input Files* that define the GMA 14 Model. The GMA 14 Model provides model results as the following *Model Output Files*:

- Cell-by-Cell flows (“CBB”), which contains water budget information for each model cell per stress period
- Heads (“HDS”), which contains water levels for each model cell per stress period
- Listing (“LST”), which contains model run characteristics and water budget summaries

Along with the matrix head output file, we also used the Observation (“OBS6”) utility to output head results at specific model cells for use in our calibration processes. The following sections describe the files used in the GMA 14 Model.

Table 6. Summary of MODFLOW input files.

Package Name	File Type	Input Filename
<i>Simulation Files</i>		
Name	NAM	mfsim.nam
Time Discretization	TDIS	gma14.tdis
Iterative Model Solution	IMS	gma14.ims
<i>Model Input Files</i>		
Name	NAM	gma14.nam
Initial Conditions	IC	gma14.ic
Discretization	DIS	gma14.dis
Node Property Flow	NPF	gma14.npf
Storage	STO	gma14.sto
Skeletal Storage, Compaction, and Subsidence	CSUB	gma14.csub
Well	WEL	gma14.wel
Well	WEL	gma14.irr
Drain	DRN	gma14.drn
General Head Boundary	GHB	gma14.ghb
Recharge	RCH	gma14_rch_oc.rcha
Recharge	RCH	gma14_rch_sc.rcha
River	RIV	gma14.riv
Output Control	OC	gma14.oc
Observations	OBS	gma14.obs
<i>Model Output Files</i>		
Cell-by-Cell Flows	CBB	gma14.cbb
Heads	HDS	gma14.hds
List	LST	gma14.lst

3.1. Discretization Packages

Discretization refers to how the model domain is divided spatially and how time is represented in the model

3.1.1. Time Discretization

The Temporal Discretization (“TDIS”) Package contains information on how time is represented in the model. The package defines the model’s time units, how the total time is divided into discrete stress periods, the length of stress periods, and how each stress period is divided into time steps. Like GULF-2023, the GMA 14 Model has time units of days, starts on December 31, 1896, and continues to December 31, 2018. However, GULF-2023 used several monthly stress periods whereas the GMA 14 Model does not have any stress periods of less than one year. By eliminating the monthly stress periods, we reduced the total stress periods from 268 in GULF-2023 to a total of 59 stress periods for the history matching period.

Table 7 summarizes the details of each stress period. The first stress period is steady state to represent predevelopment conditions. The remaining stress periods are transient representing multiple years up until 1970. Starting in 1970, each stress period has a length of one year.

Table 7. Time Discretization Summary.

Stress Period	Length, days	Stress Period Start Date	Stress Period End Date	Type
1	1	12/31/1896	12/31/1896	Steady State
2	5,477	1/1/1897	12/31/1911	Transient
3	5,114	1/1/1912	12/31/1925	Transient
4	5,113	1/1/1926	12/31/1939	Transient
5	1,827	1/1/1940	12/31/1944	Transient
6	1,826	1/1/1945	12/31/1949	Transient
7	1,826	1/1/1950	12/31/1954	Transient
8	1,826	1/1/1955	12/31/1959	Transient
9	1,827	1/1/1960	12/31/1964	Transient
10	1,826	1/1/1965	12/31/1969	Transient
11	365	1/1/1970	12/31/1970	Transient
12	365	1/1/1971	12/31/1971	Transient
13	366	1/1/1972	12/31/1972	Transient
14	365	1/1/1973	12/31/1973	Transient
15	365	1/1/1974	12/31/1974	Transient
16	365	1/1/1975	12/31/1975	Transient
17	366	1/1/1976	12/31/1976	Transient
18	365	1/1/1977	12/31/1977	Transient
19	365	1/1/1978	12/31/1978	Transient

Stress Period	Length, days	Stress Period Start Date	Stress Period End Date	Type
20	365	1/1/1979	12/31/1979	Transient
21	366	1/1/1980	12/31/1980	Transient
22	365	1/1/1981	12/31/1981	Transient
23	365	1/1/1982	12/31/1982	Transient
24	365	1/1/1983	12/31/1983	Transient
25	366	1/1/1984	12/31/1984	Transient
26	365	1/1/1985	12/31/1985	Transient
27	365	1/1/1986	12/31/1986	Transient
28	365	1/1/1987	12/31/1987	Transient
29	366	1/1/1988	12/31/1988	Transient
30	365	1/1/1989	12/31/1989	Transient
31	365	1/1/1990	12/31/1990	Transient
32	365	1/1/1991	12/31/1991	Transient
33	366	1/1/1992	12/31/1992	Transient
34	365	1/1/1993	12/31/1993	Transient
35	365	1/1/1994	12/31/1994	Transient
36	365	1/1/1995	12/31/1995	Transient
37	366	1/1/1996	12/31/1996	Transient
38	365	1/1/1997	12/31/1997	Transient
39	365	1/1/1998	12/31/1998	Transient
40	365	1/1/1999	12/31/1999	Transient
41	366	1/1/2000	12/31/2000	Transient
42	365	1/1/2001	12/31/2001	Transient
43	365	1/1/2002	12/31/2002	Transient
44	365	1/1/2003	12/31/2003	Transient
45	366	1/1/2004	12/31/2004	Transient
46	365	1/1/2005	12/31/2005	Transient
47	365	1/1/2006	12/31/2006	Transient
48	365	1/1/2007	12/31/2007	Transient
49	366	1/1/2008	12/31/2008	Transient
50	365	1/1/2009	12/31/2009	Transient
51	365	1/1/2010	12/31/2010	Transient
52	365	1/1/2011	12/31/2011	Transient
53	366	1/1/2012	12/31/2012	Transient
54	365	1/1/2013	12/31/2013	Transient
55	365	1/1/2014	12/31/2014	Transient
56	365	1/1/2015	12/31/2015	Transient
57	366	1/1/2016	12/31/2016	Transient
58	365	1/1/2017	12/31/2017	Transient
59	365	1/1/2018	12/31/2018	Transient

3.1.2. Grid Discretization

The Grid Discretization (“DIS”) package defines the spatial structure of the model grid. The GMA 14 Model is a structured grid that contains 6 layers, 350 rows, and 380 columns. The lower left corner of the model grid is located at TWDB GAM coordinate system 5,770,658 easting and 18,581,706 northing. Table 8 summarizes the representative hydrogeological unit for each model layer. Figures 18 through 23 show the active cells for each model layer.

Table 8. Model layers and corresponding hydrogeologic unit.

Model Layer	Hydrogeologic Unit
1	Shallow Aquifer System
2	Chicot Aquifer
3	Evangeline Aquifer
4	Burkeville Confining System
5	Jasper Aquifer
6	Catahoula Aquifer

We developed the GMA 14 Model grid starting with the GULF-2023 grid. We reprojected the grid to the TWDB GAM coordinate system (EPSG 10481) from NAD83 Conus Albers (EPSG 5070). The reprojection of the GULF-2023 grid to the TWDB GAM system resulted in an offset and rotation of the grid. To ensure the center of the GMA 14 Model grid cells were within the GULF-2023 grid cells, we adjusted the cell row lengths and rotated the grid. The cell row lengths for the GMA 14 Model now vary from 3,276 feet to 3,293 feet while keeping a constant column length of 3,277 feet with a rotation of 2.1 degrees. The adjustments ensured all GMA 14 Model active cell centers stayed within the corresponding GULF-2023 model cells.

Layer elevations are consistent with GULF-2023 as described by Ellis and others (2023). Figure 24 illustrates the layering of the Gulf Coast Aquifer System within the GMA 14 Model. Figure 25 shows the cross-section locations.

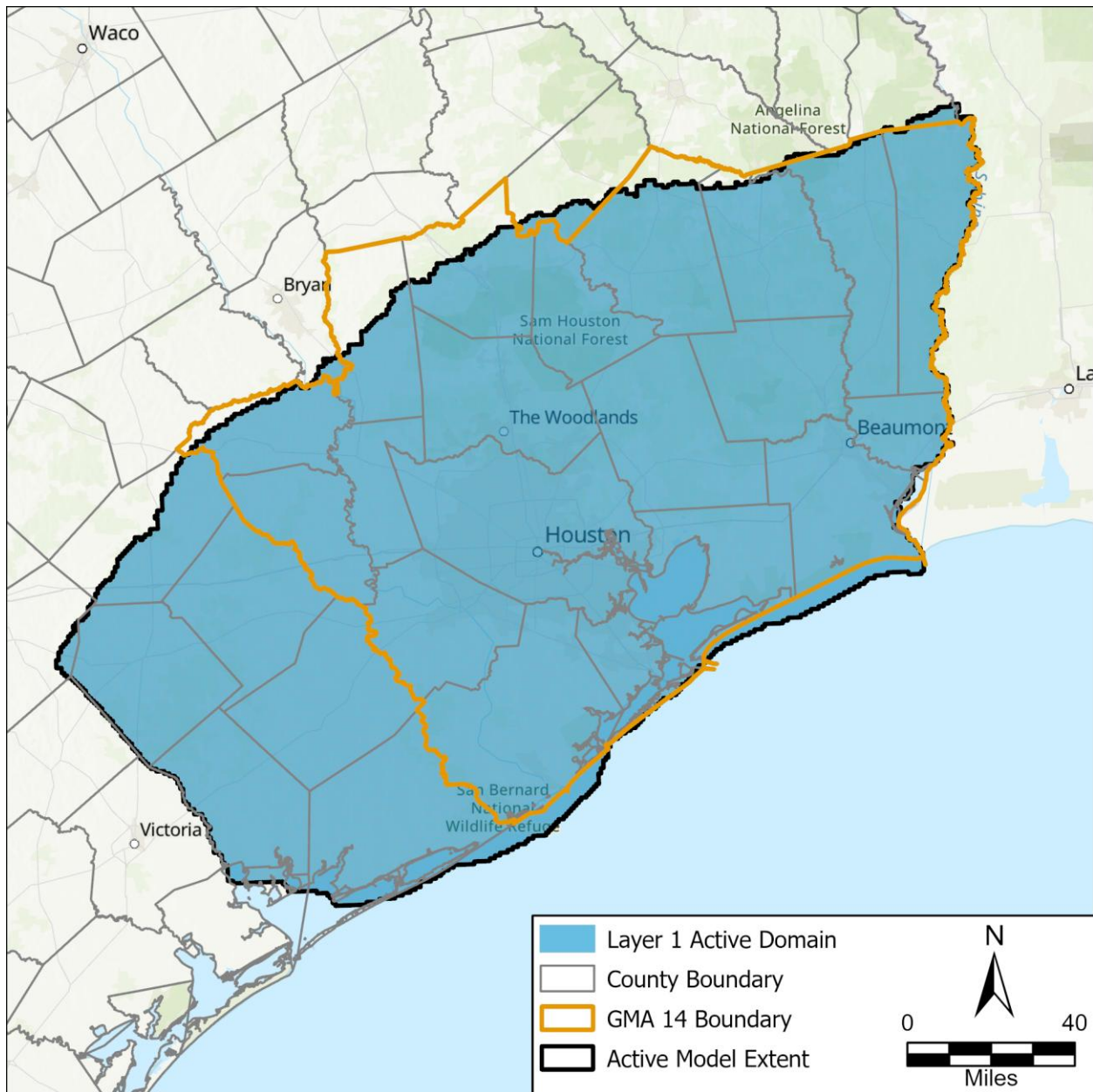


Figure 18. Layer 1 (shallow aquifer system) active model cells.

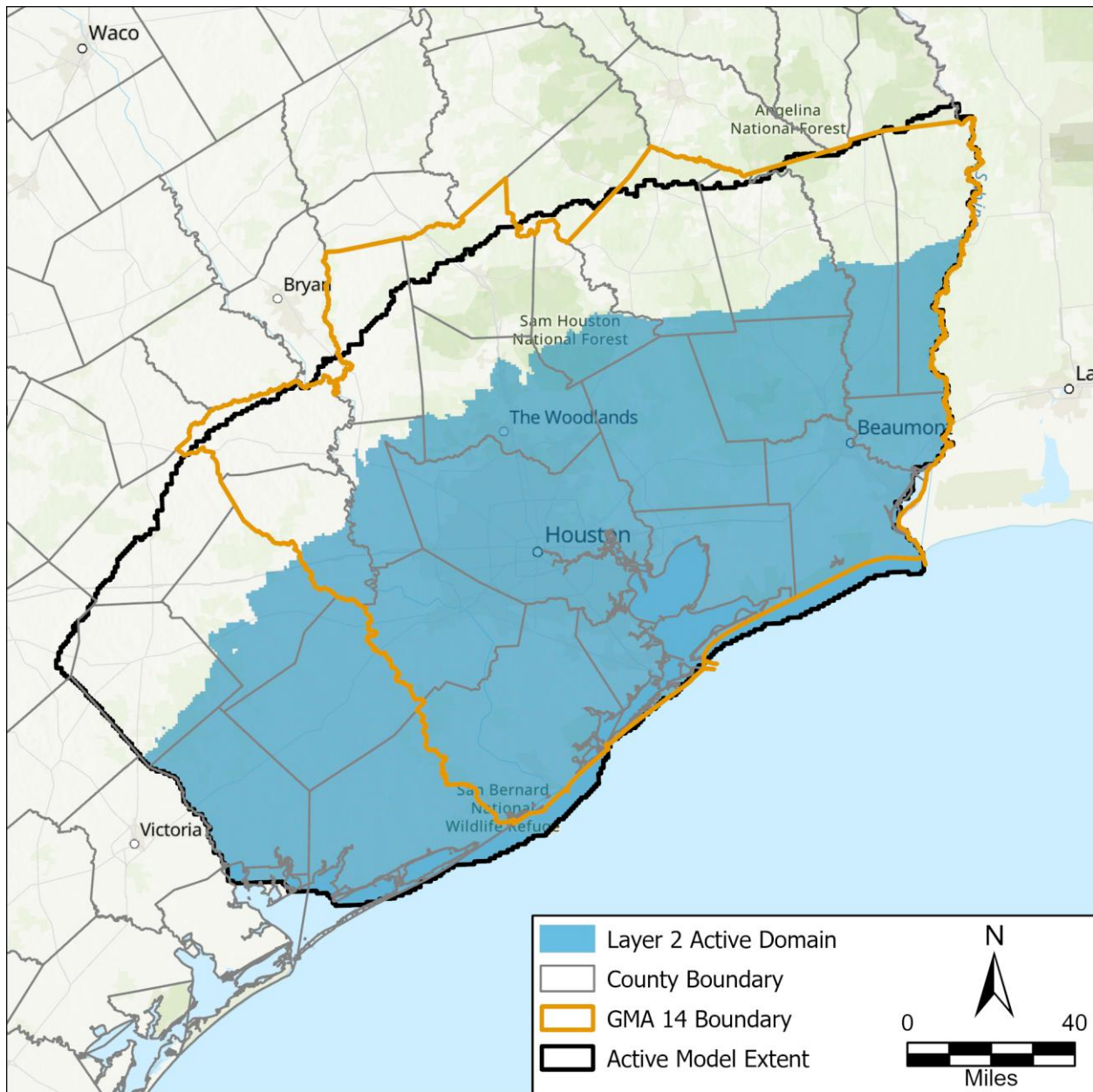


Figure 19. Layer 2 (Chicot Aquifer) active model cells.

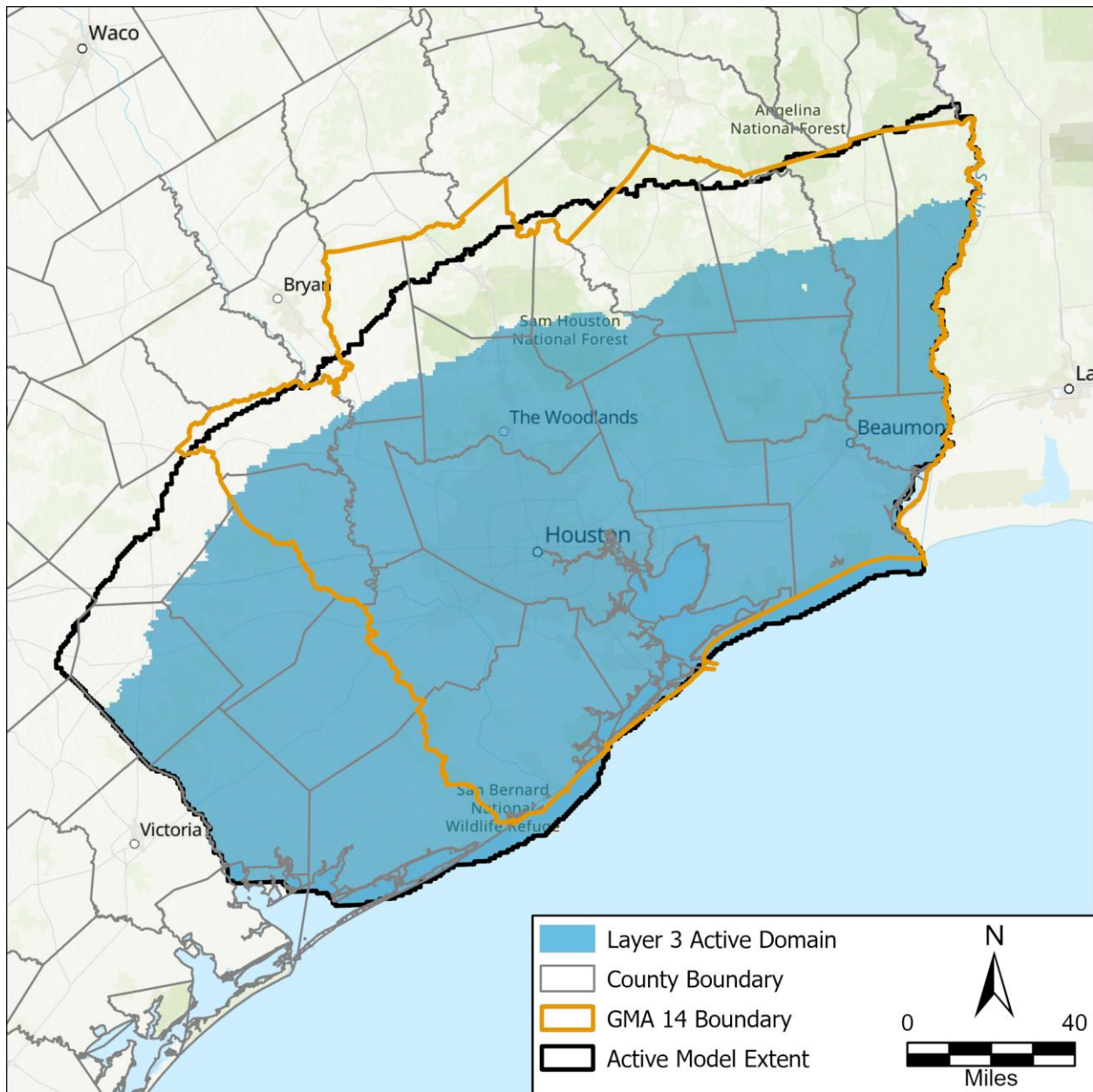


Figure 20. Layer 3 (Evangeline Aquifer) active model cells.

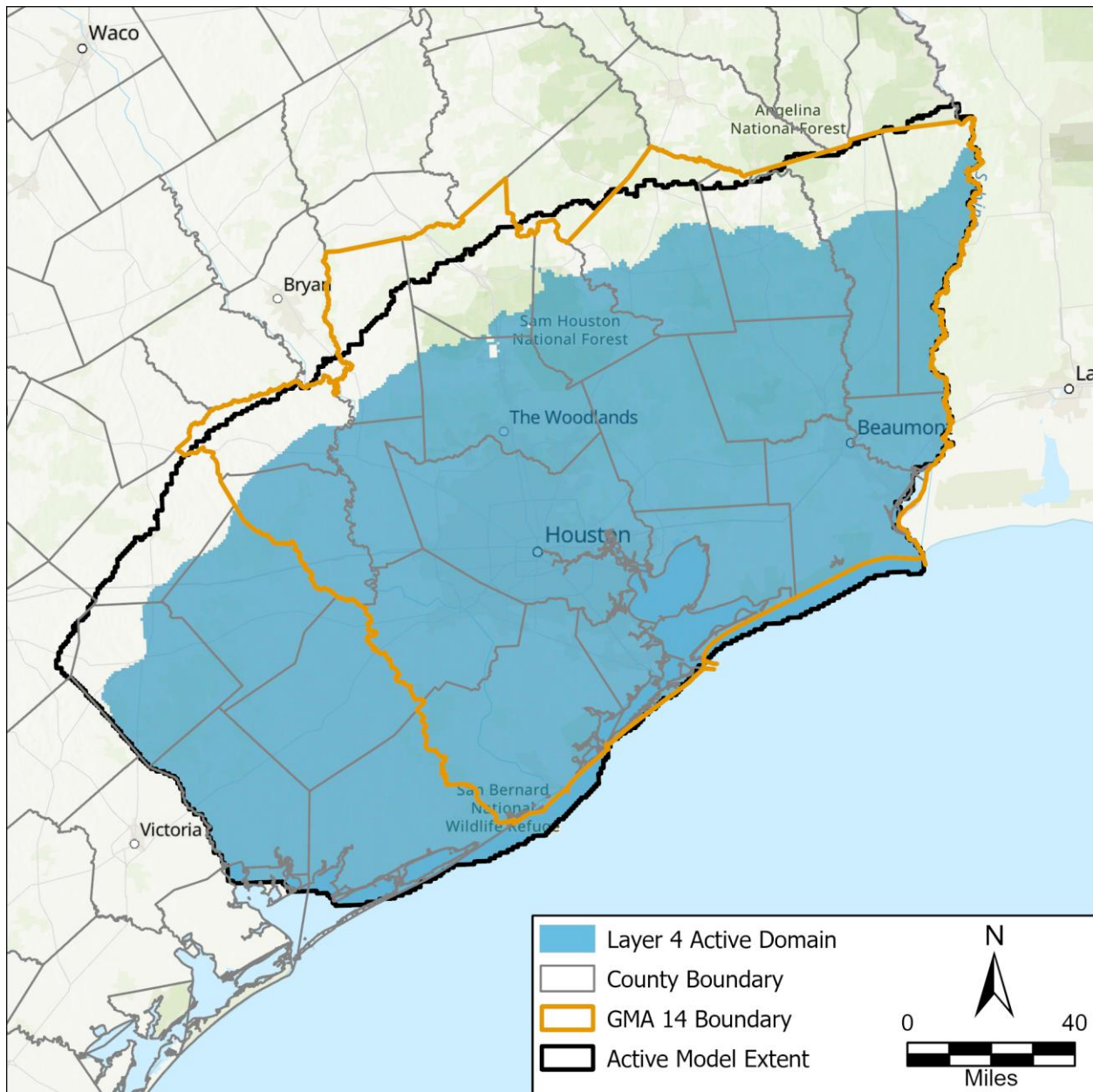


Figure 21. Layer 4 (Burkeville) active model cells.

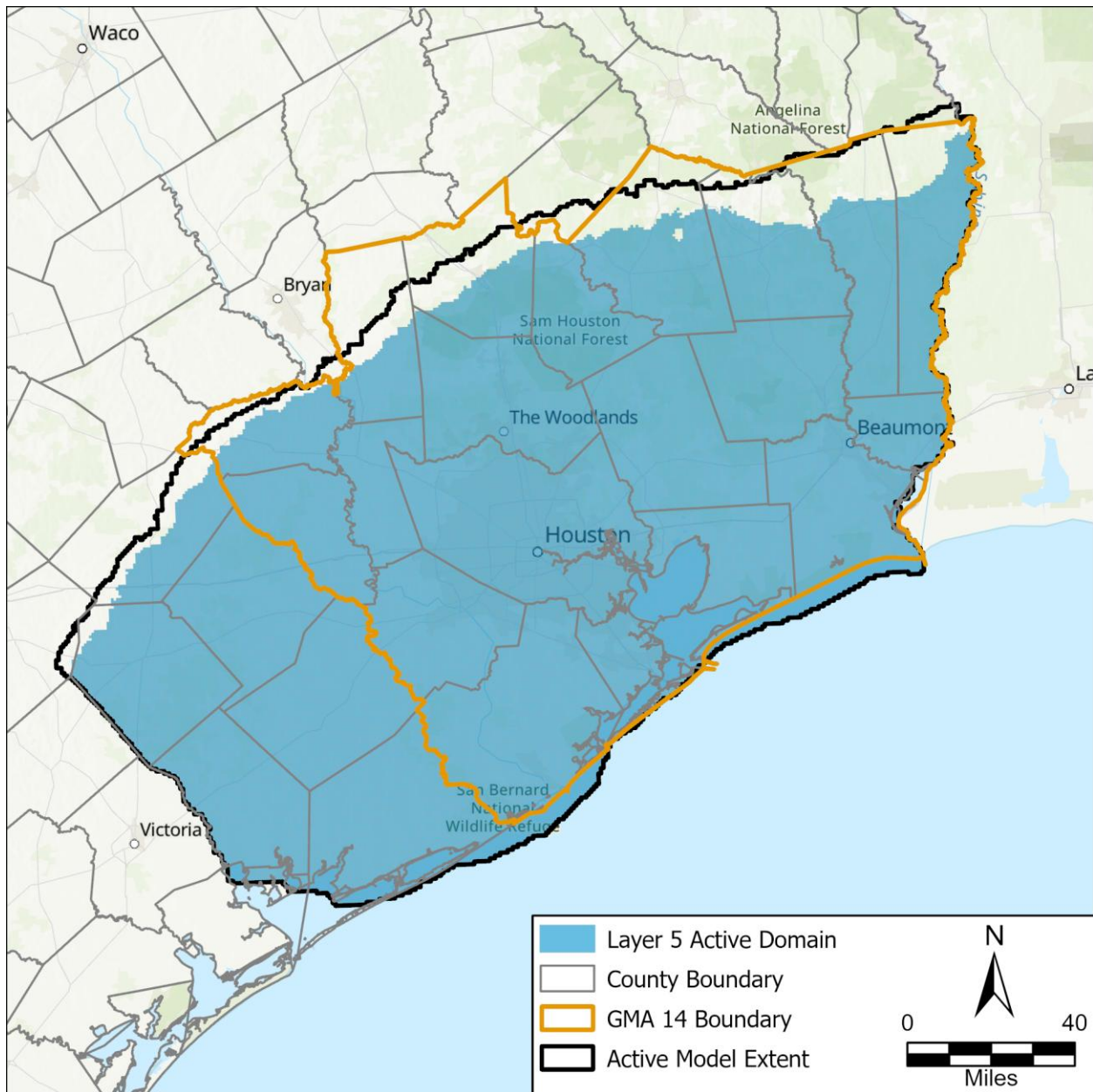


Figure 22. Layer 5 (Jasper Aquifer) active model cells.

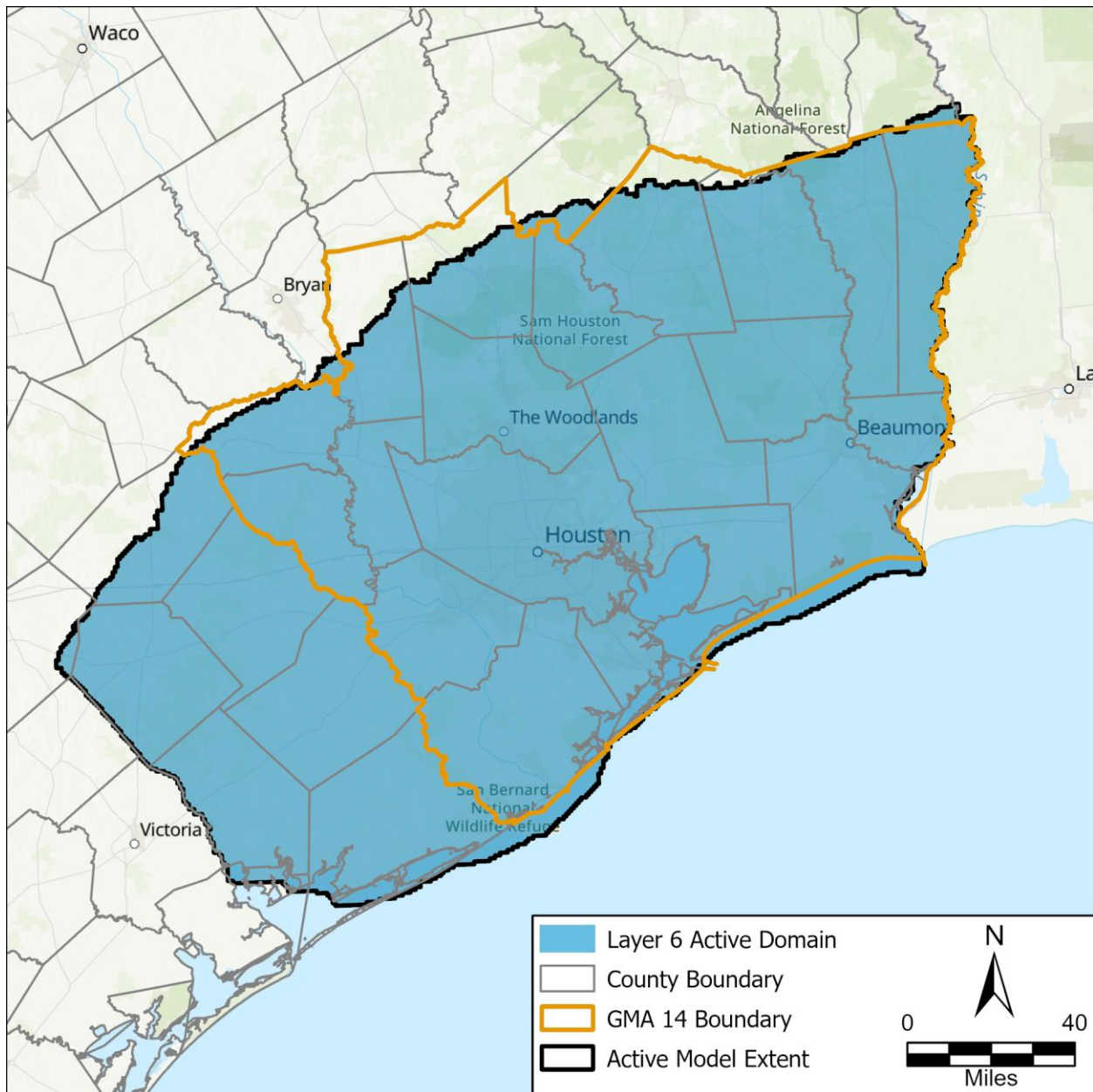


Figure 23. Layer 6 (Catahoula Aquifer) active model cells.

GMA 14 Groundwater Availability Model

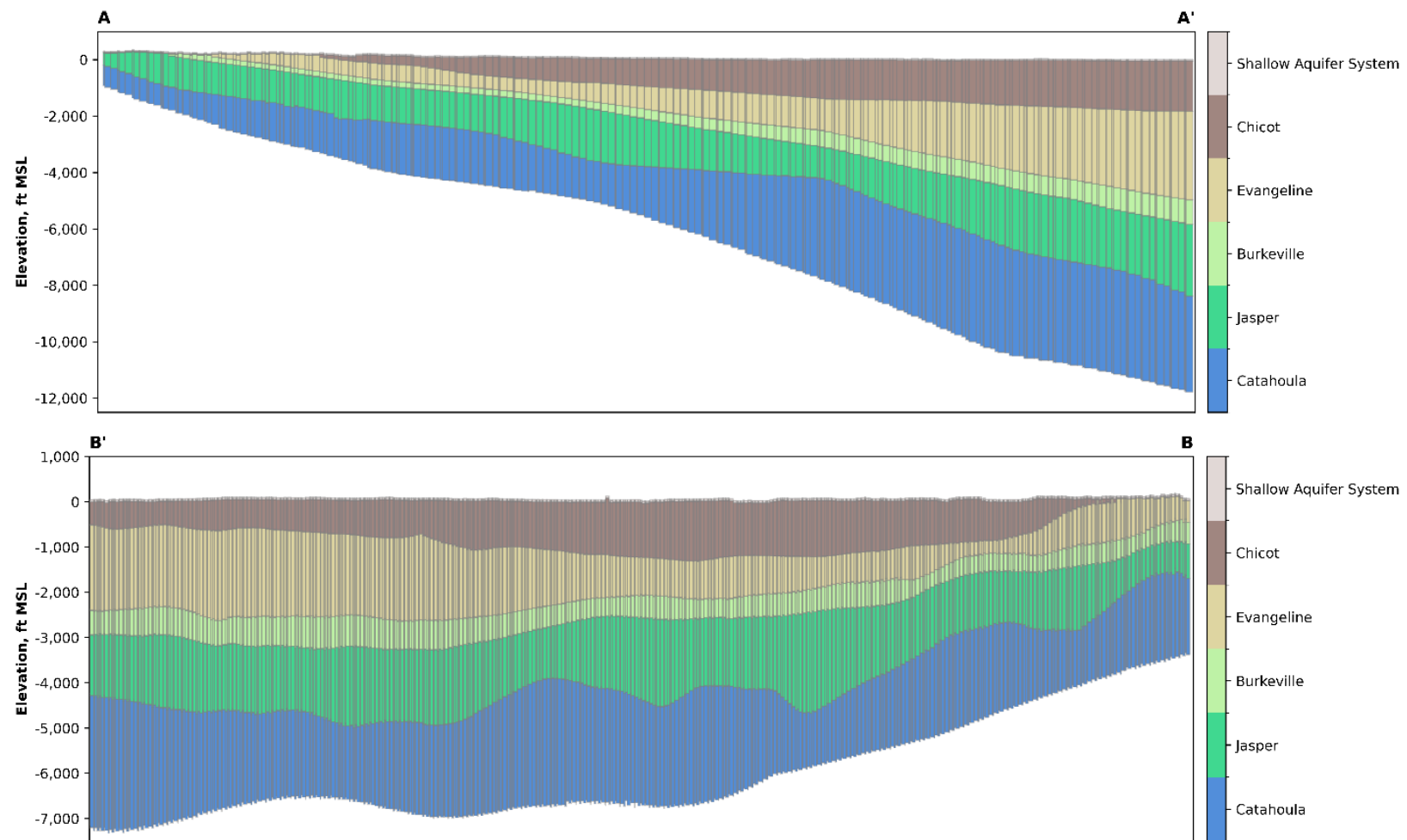


Figure 24. Model grid cross sections. Location of cross sections shown on Figure 25.

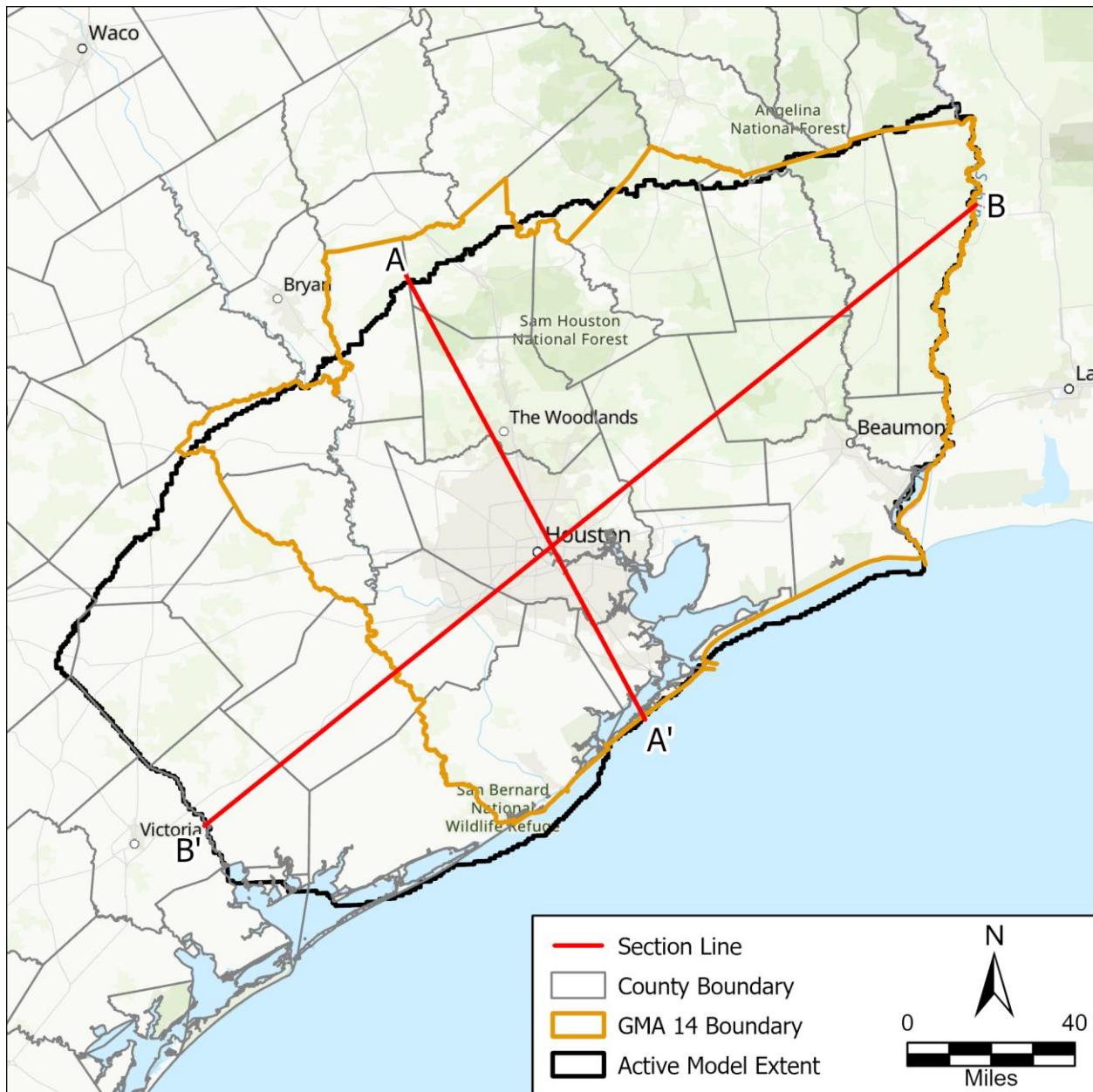


Figure 25. Sections lines for cross sections in Figure 24.

3.2. Node Property Flow Package

The Node Property Flow (“NPF”) package handles how groundwater moves through the model by calculating the hydraulic conductance between adjacent cells. The NPF package also specifies whether a cell is always confined or is convertible between confined and unconfined conditions. The NPF package also specifies values for the horizontal hydraulic conductivity and vertical hydraulic conductivity each model layer.

We specified the initial GMA 14 Model horizontal hydraulic conductivity parameterization based on pumping test data described in Section 2.1. We interpolated the transmissivity values across the model domain then divided the transmissivity by the model layer thickness to define the initial horizontal hydraulic conductivity. We selected this approach to honor the test data which represents how the aquifers are being used and where water level data are being collected. Comparison of measured and calibrated properties is in Section 4.1.3.

Our approach differs from Ellis and others (2023) who noted that the horizontal hydraulic conductivity values in GULF-2023 were consistent with reported values for the Gulf Coast Aquifer System. By focusing on the horizontal hydraulic conductivity values, GULF-2023 underrepresented the reported transmissivity of the aquifers (Drabek and Keester, 2023). One effect of underrepresenting the transmissivity is that the model will produce higher drawdown at pumping rates than would occur at the measured transmissivity. In some areas, the underrepresented transmissivity may have resulted in the reduced pumping rates during calibration as discussed in Section 2.2.1.

The vertical hydraulic conductivity represents the ease of flow between model layers. For sand layers in direct contact, the vertical hydraulic conductivity may be within an order of magnitude of the horizontal hydraulic conductivity. However, the Gulf Coast Aquifer System has several clay interbeds which inhibit vertical flow. Nonetheless, due to the lack of measured values we used the vertical hydraulic conductivity from GULF-2023 for the initial values of the GMA 14 Model.

3.3. Storage Package

The Storage (“STO”) package governs how groundwater is stored and released in the model layer due to a change in water level by considering specific storage for confined conditions and specific yield for unconfined conditions. Since specific storage is defined in the compaction package, the specific storage within the STO package is not read by MODFLOW and therefore only the specific yield is defined. There are insufficient specific yield field measurements available to compare to initial model values. We used the values developed for GULF-2023 as our initial input for the GMA 14 Model.

3.4. Skeletal Storage, Compaction, and Subsidence Package

The Skeletal Storage, Compaction, and Subsidence (“CSUB”) package simulates land subsidence caused by compaction due to groundwater extraction. It accounts for elastic and inelastic storage changes and calculates vertical displacement in response to groundwater level decline (Hughes and others, 2022). The CSUB package includes parameterization for both coarse grain and fine grained (that is, interbeds) material.

Each interbed is simulated as delay or no-delay. Simulating compaction using the no-delay approach results in the interbed head and groundwater flow cell head equilibrating instantaneously, which is often valid where the interbeds are close to the surface and thin, indicating the time it takes for the heads to equilibrate is less than the stress period length. The delay approach uses the vertical hydraulic conductivity of the interbed to allow the groundwater flow cell and interbed to equilibrate over a period of time (Hughes and others, 2022). We limited the number of interbeds simulated as no-delay to cells of the most updip limit where layer thickness and compaction was limited. Figures 26 through 29 show the cell designations for each layer with simulated interbeds. We were not able to use fewer no-delay interbeds due to an increase in numerical instability with the model for cells with relatively small saturated thicknesses.

For delay interbeds, CSUB calculates interbed thickness by multiplying the representative interbed thickness (CSUB data parameter: *thick_frac*) by the equivalent number of interbeds in the interbed system (CSUB data parameter: *rnb*). For no-delay interbeds, interbed clay thickness is only the *thick_frac* and *rnb* can be any value as it is not used in the calculation (USGS, 2025a). The values of *thick_frac* and *rnb* are equivalent to the b_{equiv} and n_{equiv} values, respectively, discussed by Hughes and others (2022).

GULF-2023 defined *thick_frac* and *rnb* values for all interbeds regardless of whether designated as delay or no-delay. As a result, no-delay interbeds were about three to four times thinner than the clay thickness should be. This mistake in parameterization is understandable, but the effect of the error makes prediction of compaction and subsidence unrealistic where no-delay beds are present.

For the GMA 14 Model, since GULF-2023 provided *thick_frac* and *rnb* for all interbeds, we kept the delay interbed cells consistent with GULF-2023 values. However, for the GMA 14 Model no-delay interbeds, we determined *thick_frac* by multiplying the GULF-2023 *thick_frac* and *rnb* values. We then set the GMA 14 Model *rnb* value to 1.0. Figures 30 through 33 illustrate the interbed (clay) thicknesses for each model layer with simulated interbeds. Figures 34 through 37 illustrate the representative number of interbeds for each model layer with simulated interbeds.

To parameterize the depth dependent interbed compaction parameters (namely, inelastic specific storage, elastic specific storage, porosity, and vertical hydraulic conductivity), we used the depth to the cell center from the top of the model along with the depth-dependent equations described in Section 2.3.

Preconsolidation stress is essentially the amount of change in effective stress before inelastic compaction begins to occur. Ellis and others (2023) conceptualized the preconsolidation stress as linearly decreasing with depth. The preconsolidation stress is 75 feet at the surface and decreases to 0 feet at a depth of 870 feet as measured from the top of the model to the middle of the cell. The initial parameterization of the GMA 14 Model CSUB package uses the same conceptualization as GULF-2023 (Ellis and others, 2023).

The CSUB package also defines the coarse grain specific storage and porosity parameters. For the GMA 14 Model initial parameters, we used the values from GULF-2023.

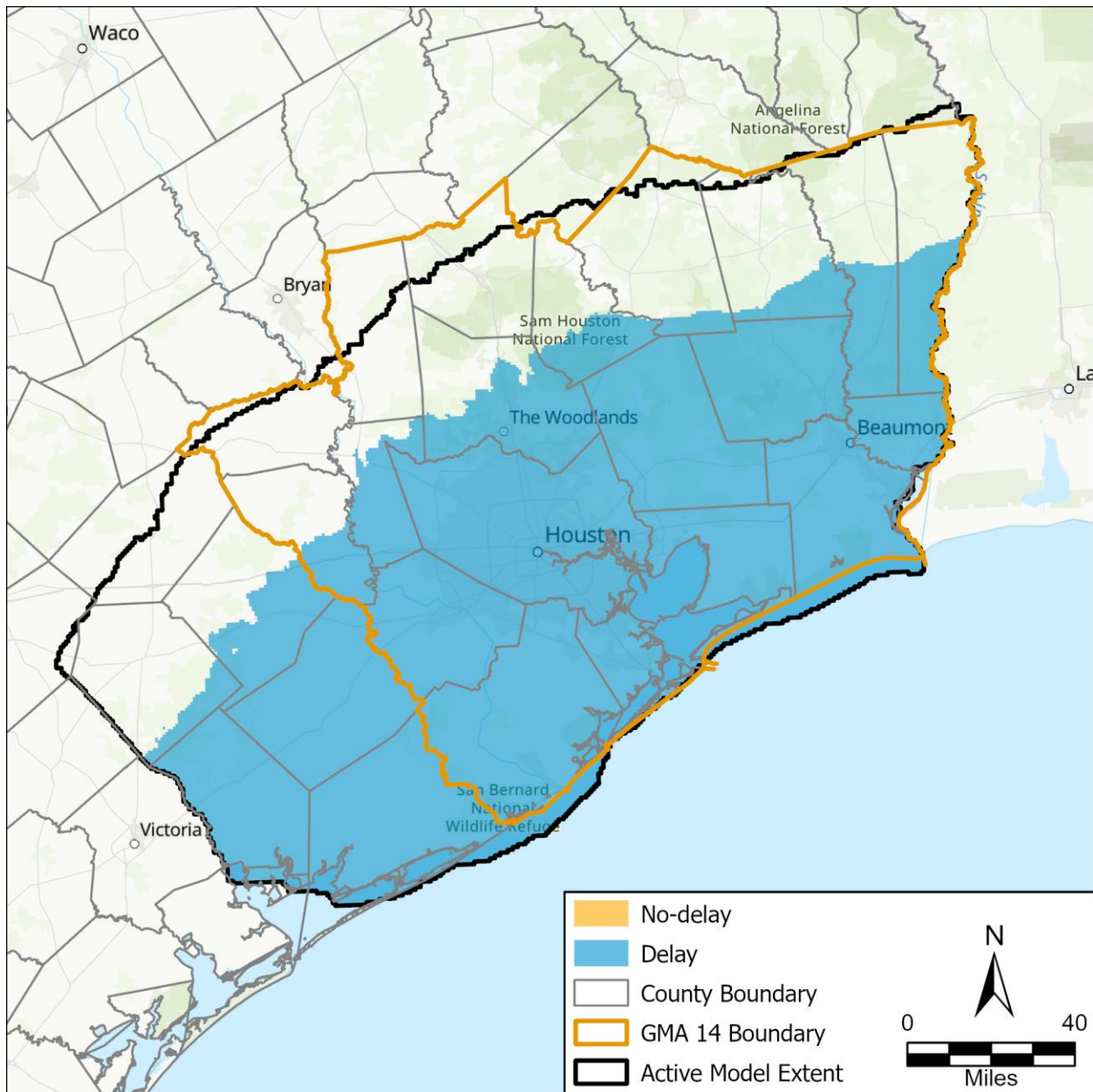


Figure 26. Interbed delay designations for Layer 2 (Chicot Aquifer).

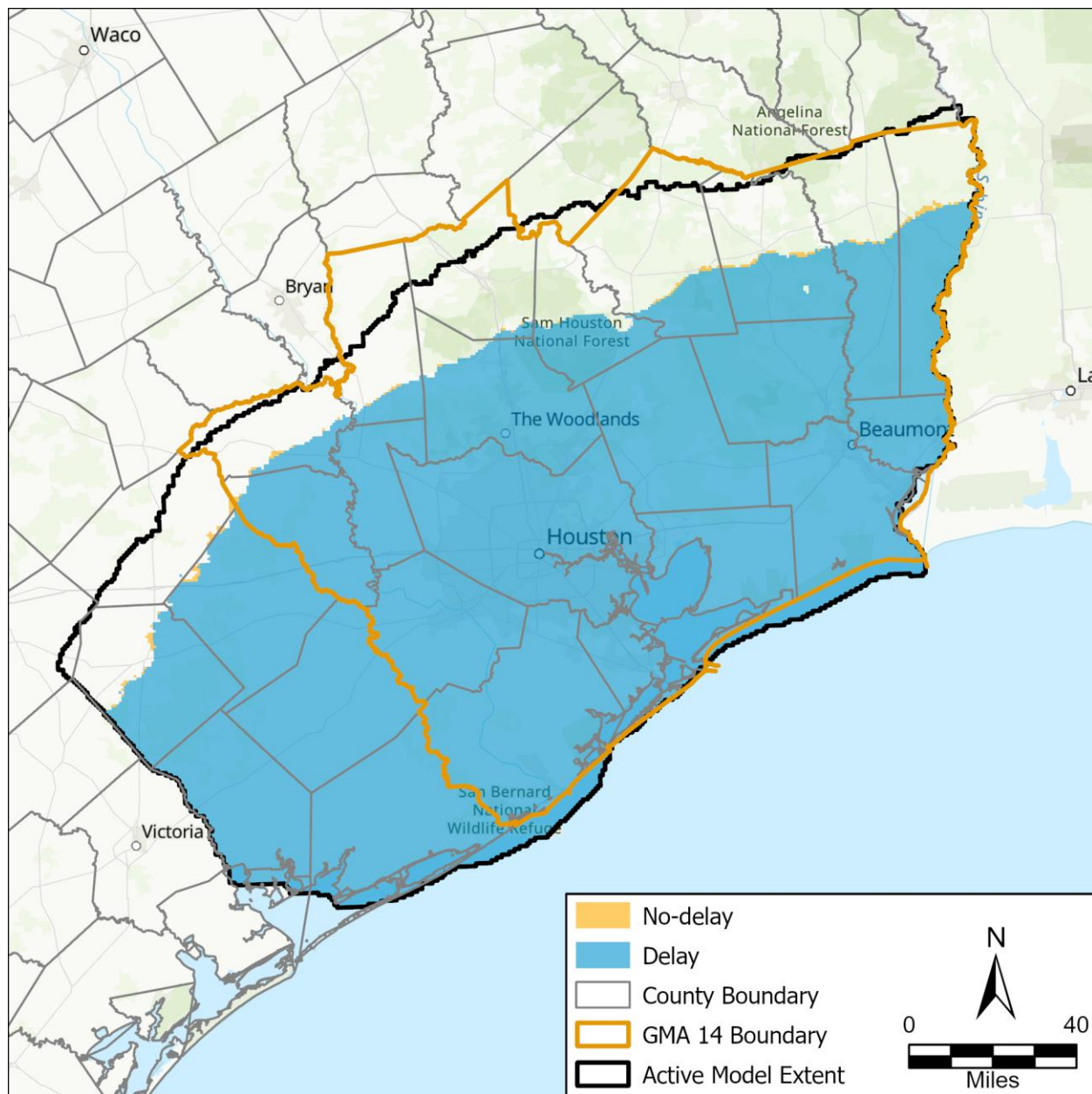


Figure 27. Interbed delay designations for Layer 3 (Evangeline Aquifer).

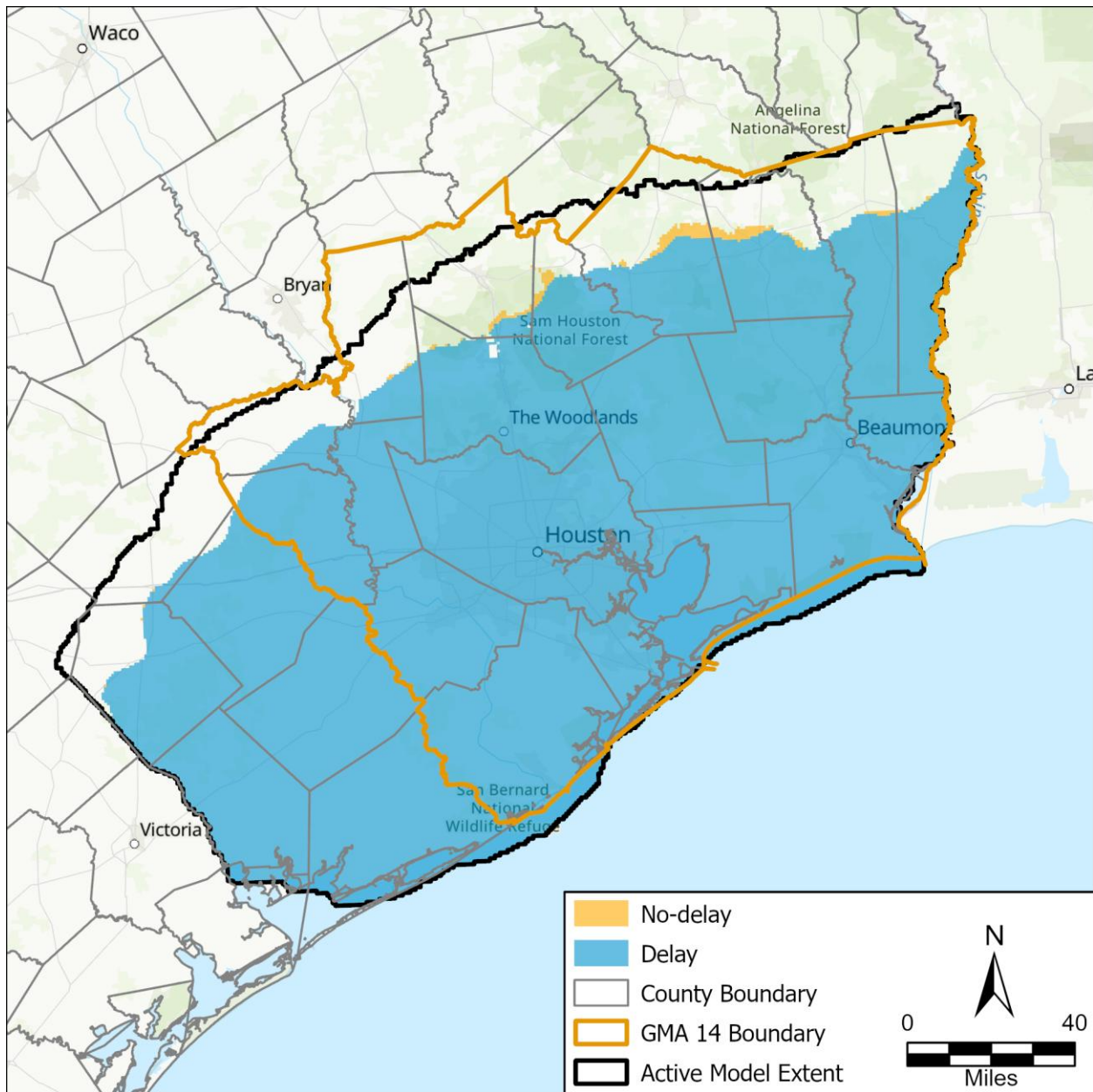


Figure 28. Interbed delay designations for Layer 4 (Burkeville).

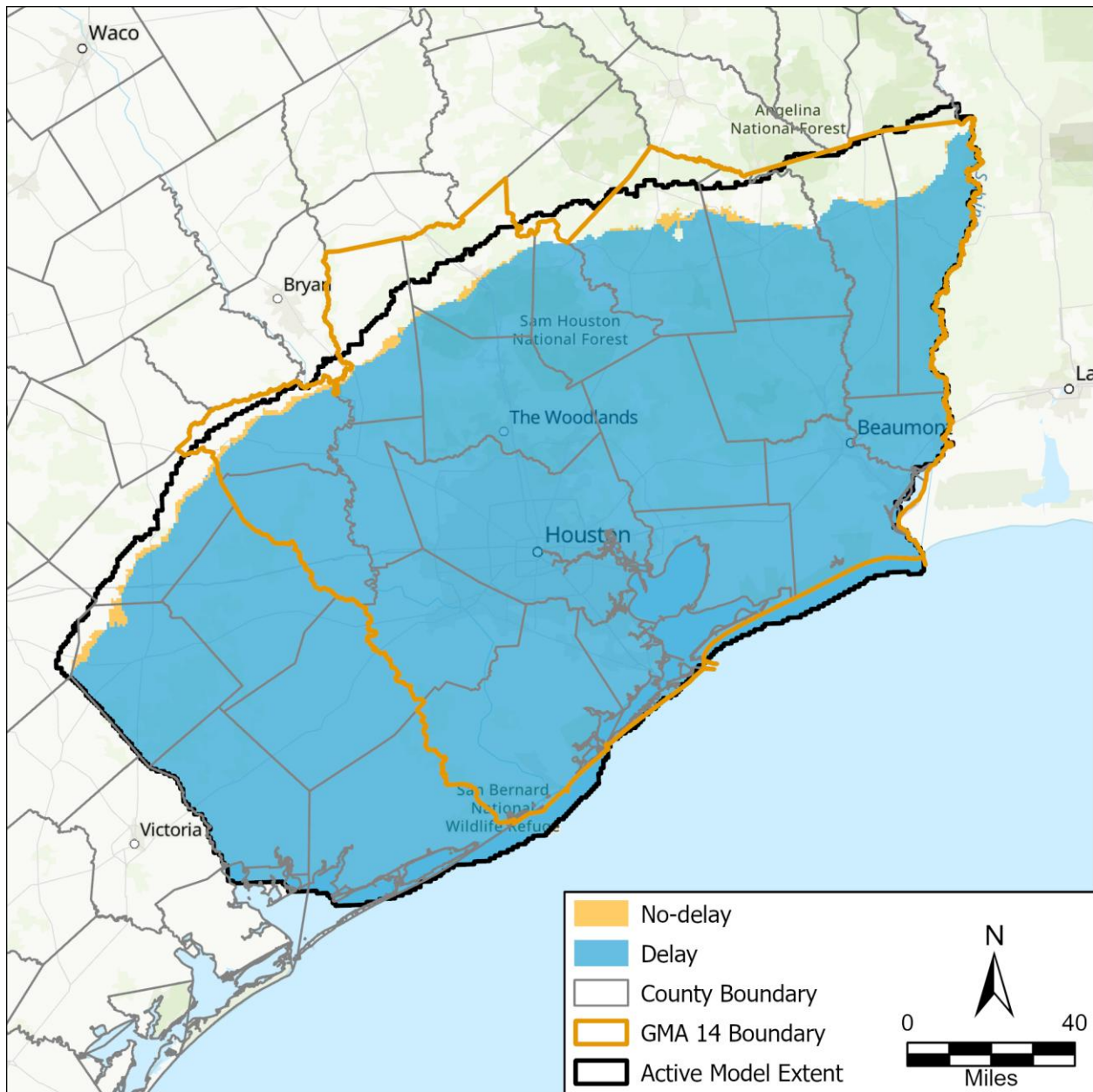


Figure 29. Interbed delay designations for Layer 5 (Jasper Aquifer).

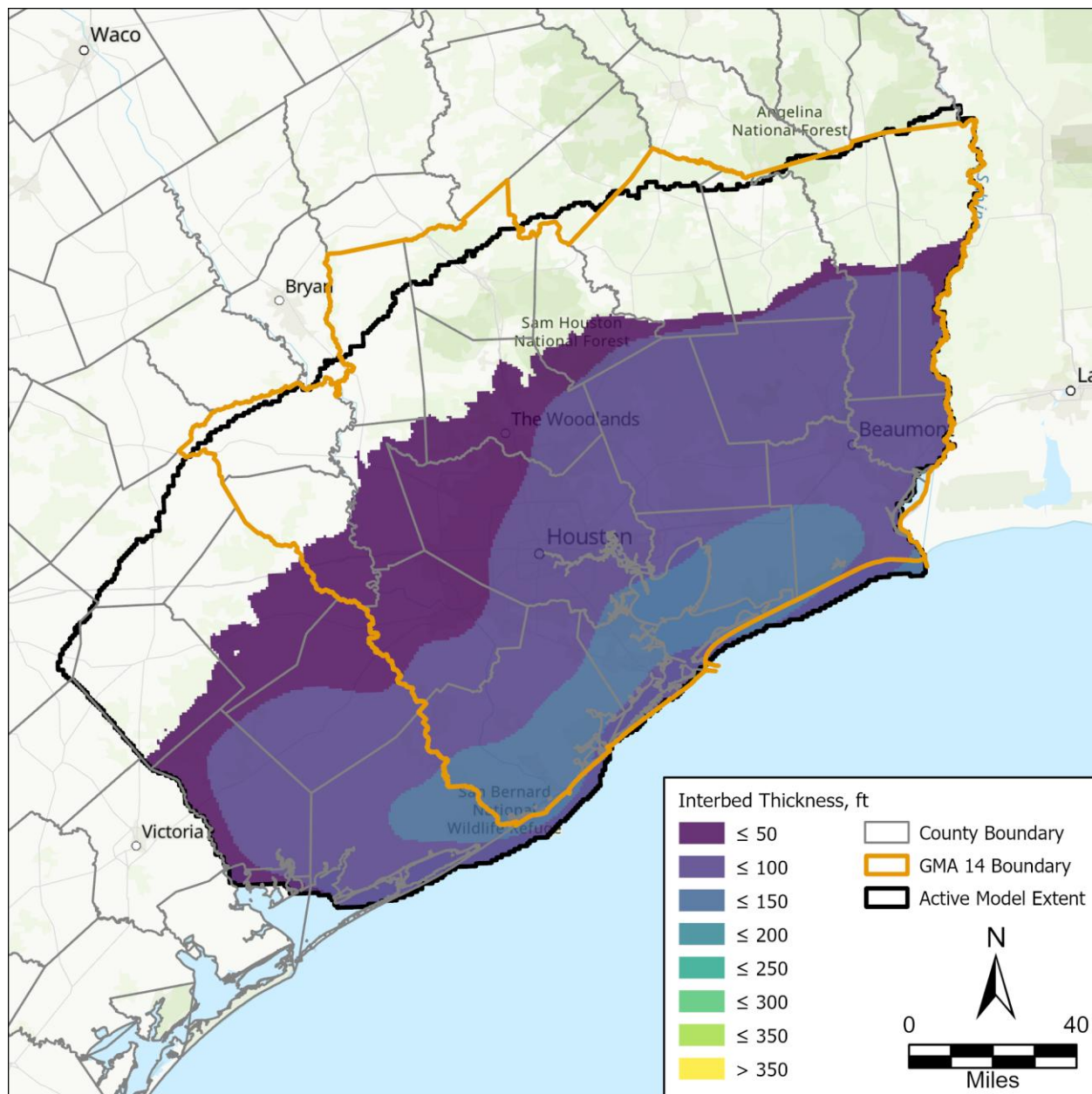


Figure 30. Interbed thickness values for Layer 2 (Chicot Aquifer).

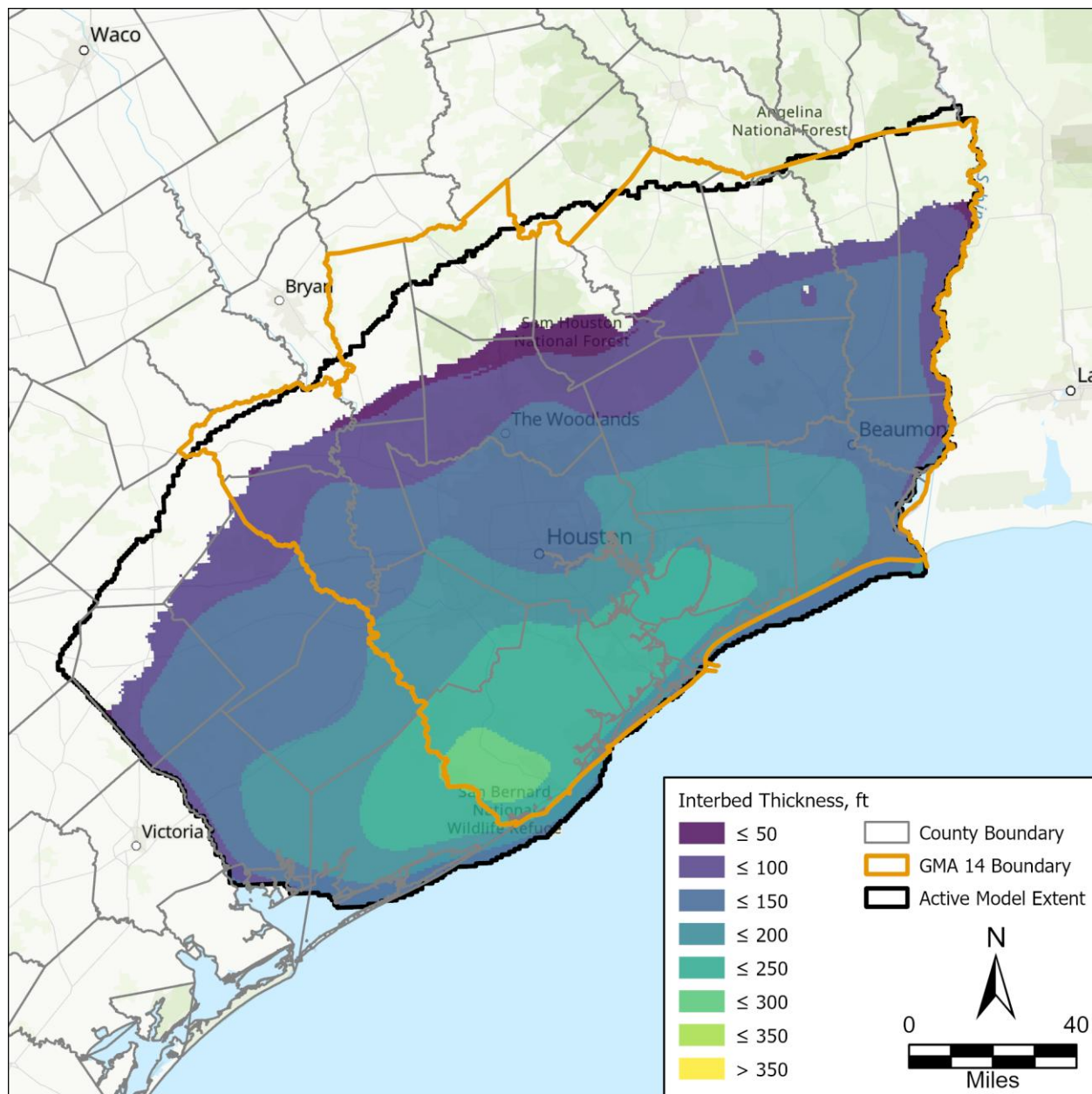


Figure 31. Interbed thickness values for Layer 3 (Evangeline Aquifer).

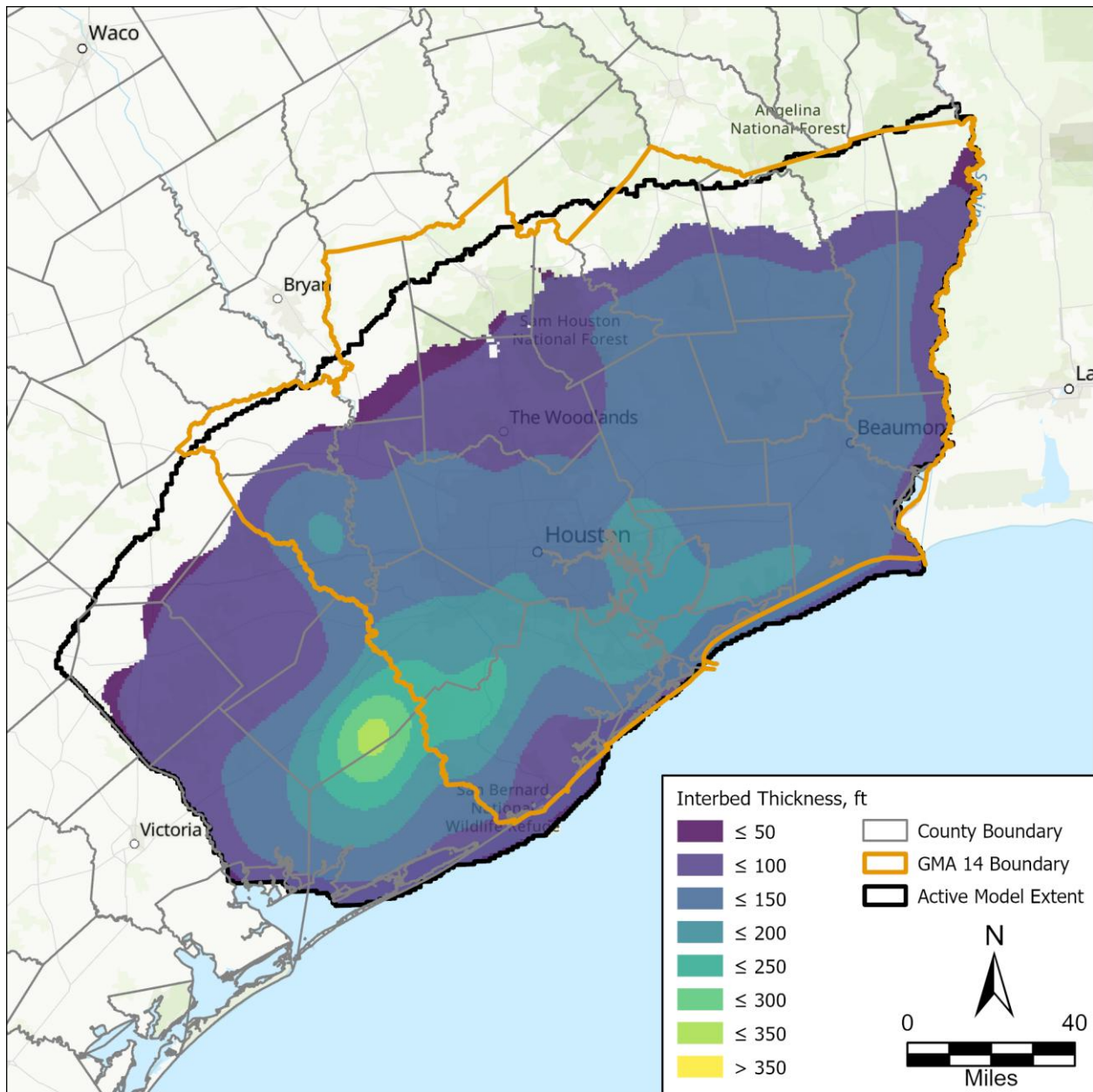


Figure 32. Interbed thickness values for Layer 4 (Burkeville).

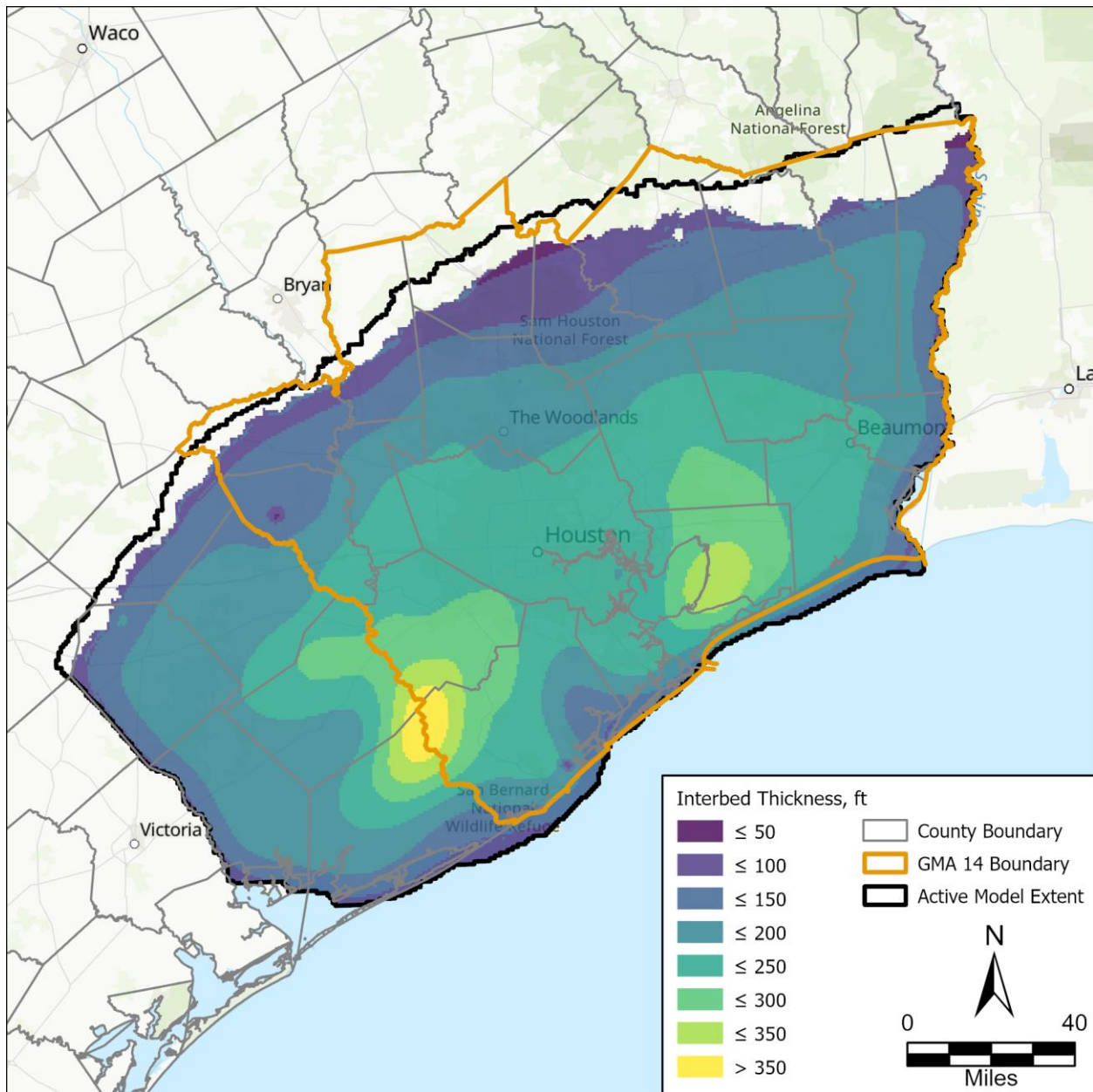


Figure 33. Interbed thickness values for Layer 5 (Jasper Aquifer).

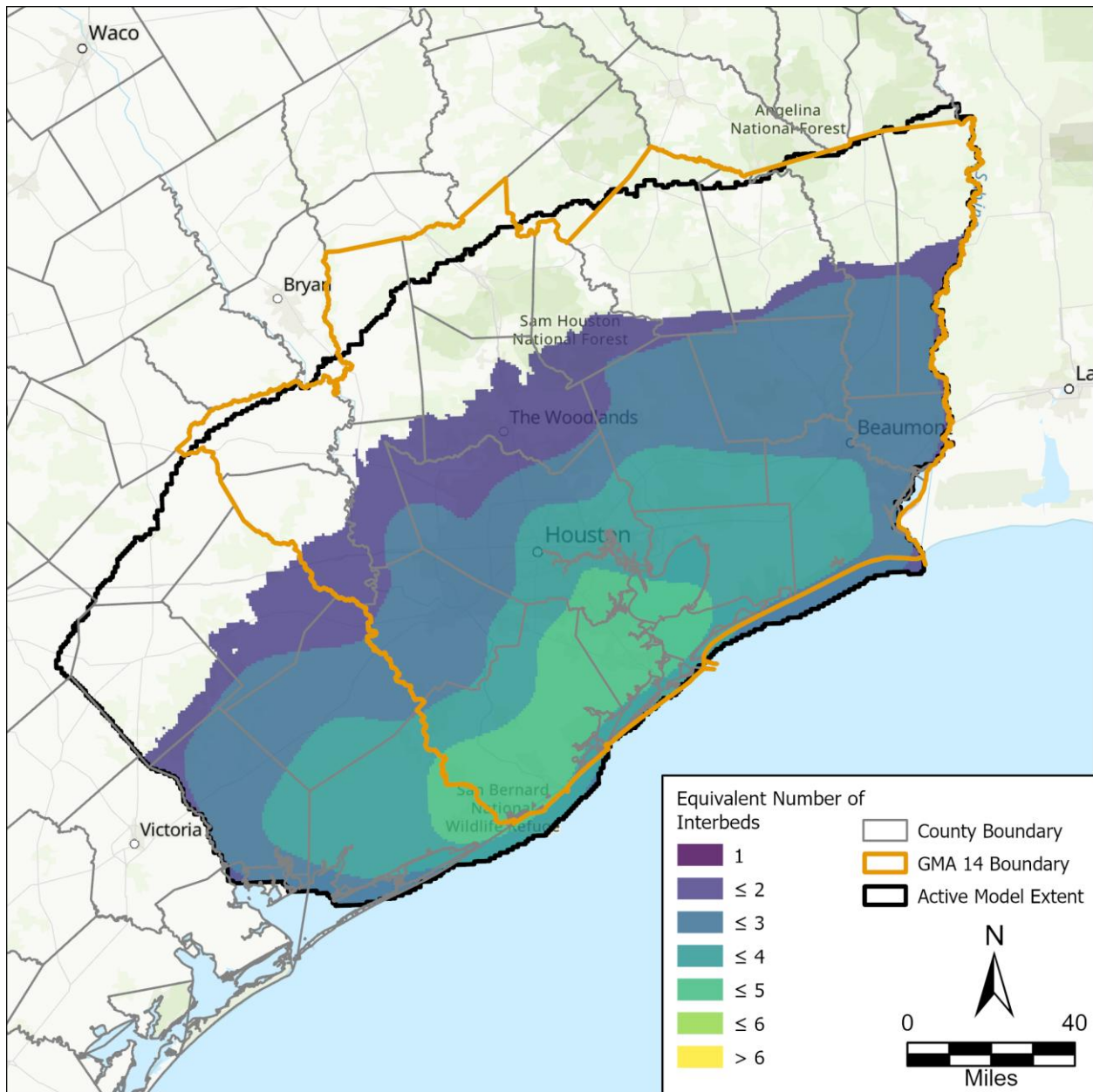


Figure 34. Equivalent number of interbeds for Layer 2 (Chicot Aquifer).

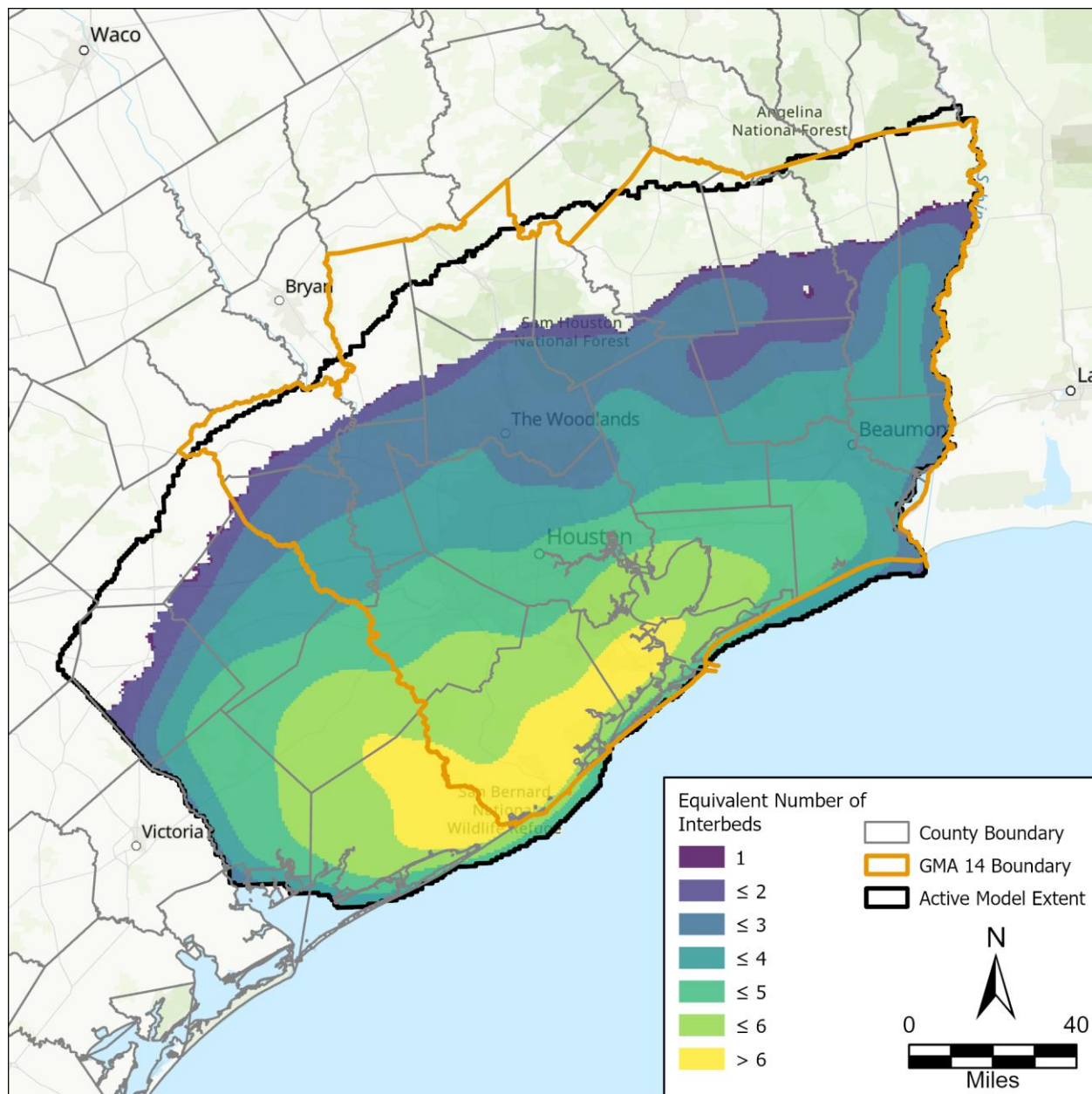


Figure 35. Equivalent number of interbeds for Layer 3 (Evangeline Aquifer).

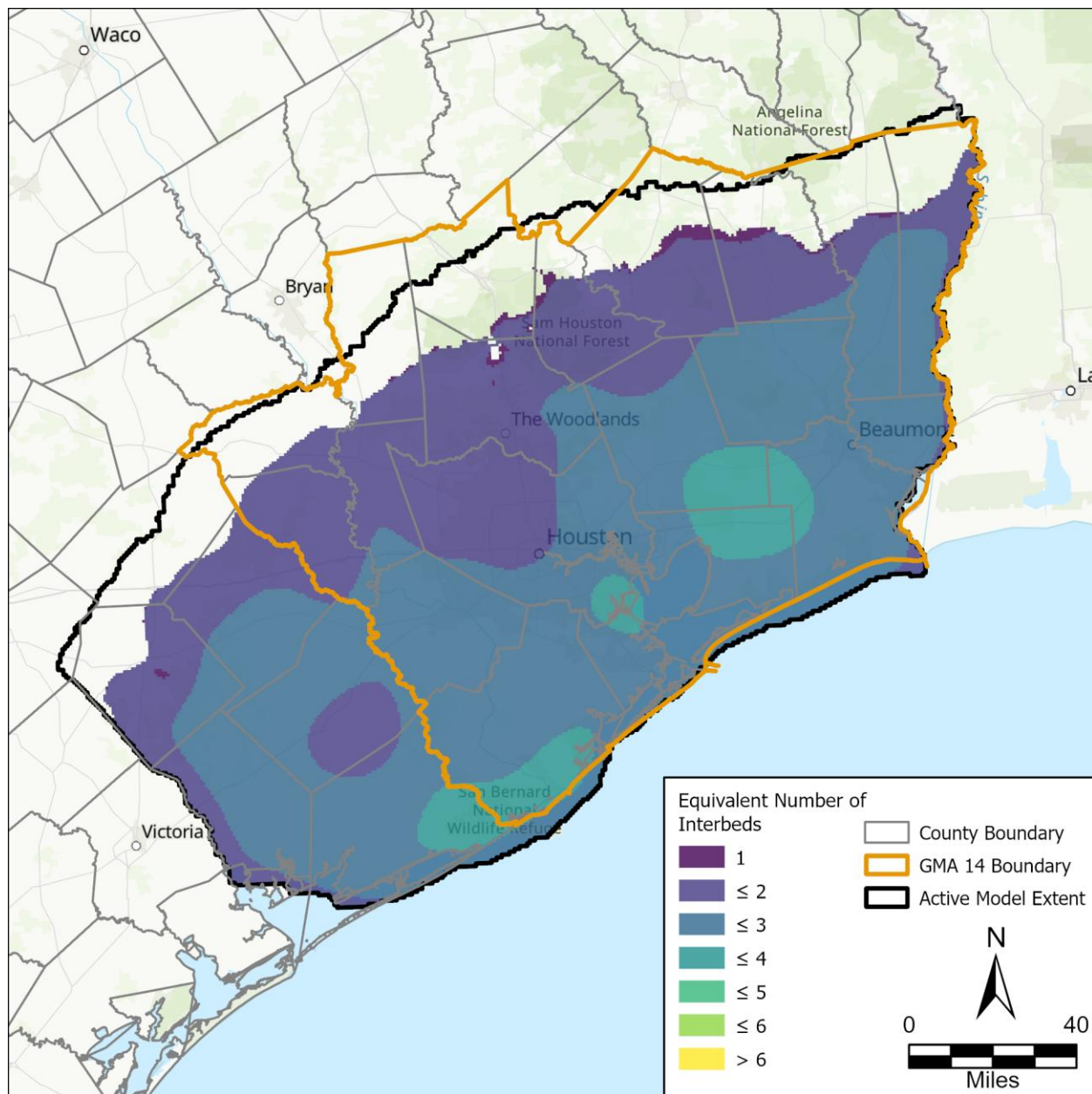


Figure 36. Equivalent number of interbeds for Layer 4 (Burkeville).

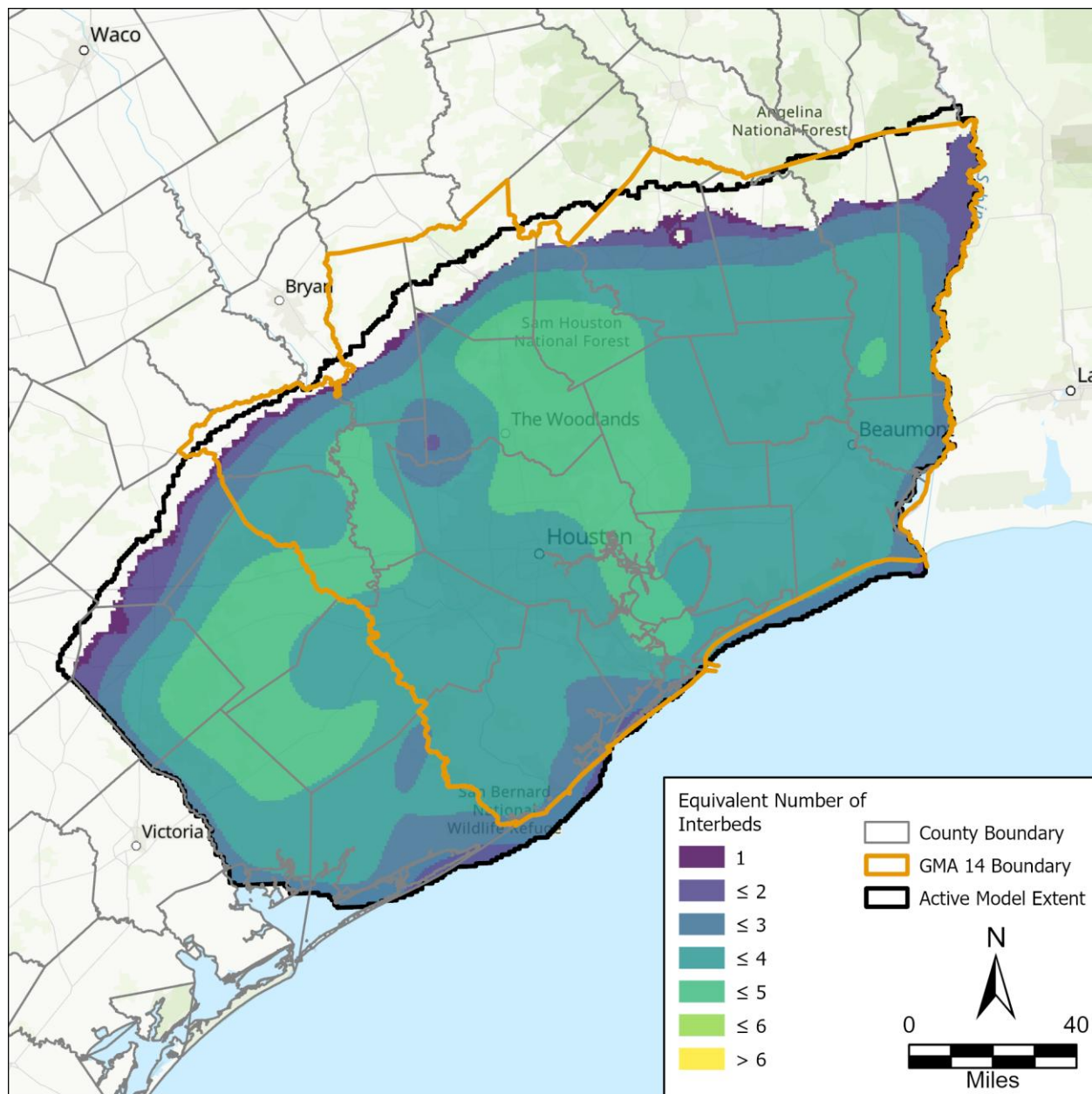


Figure 37. Equivalent number of interbeds for Layer 5 (Jasper Aquifer).

3.5. Well Package

The Well (“WEL”) package represents groundwater extraction or injection by defined well locations and pumping rates by stress period. As described in Section 2.2, we created two WEL files, one with only irrigation pumping (“gma14.irr”) and the other with all other pumping (“gma14.wel”). For both files, we set the AUTO_FLOW_REDUCE option to 0.1, causing pumping to reduce if a cell reaches 10 percent saturated thickness. The option provides numerical stability when the simulated water level approaches the bottom of the cell in convertible cells. Figures 38 through 41 illustrate the pumping distribution for each layer.

See Appendix 4 for the total pumping per county per stress period for each model layer.

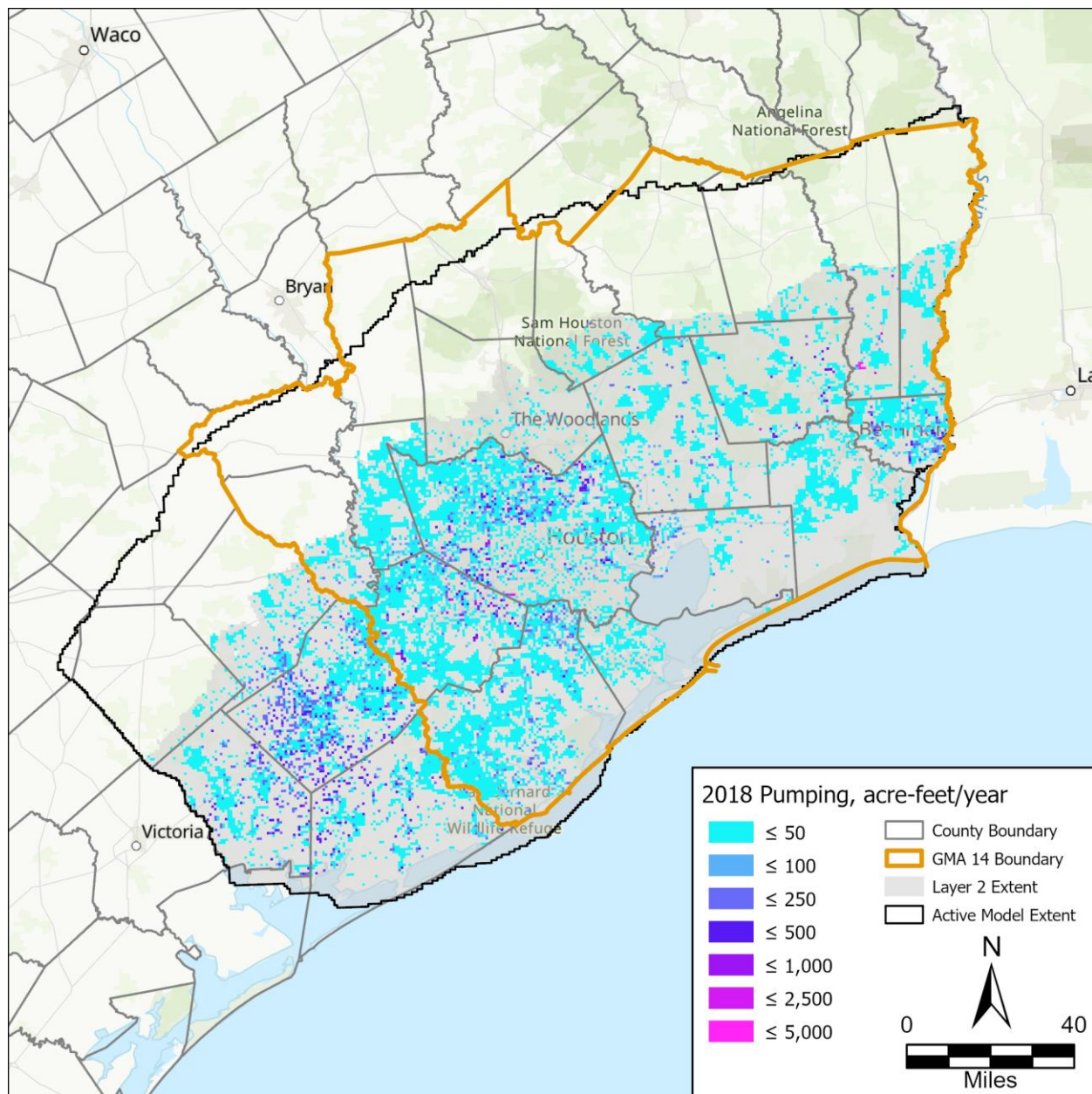


Figure 38. 2018 total pumping values for Layer 2 (Chicot Aquifer).

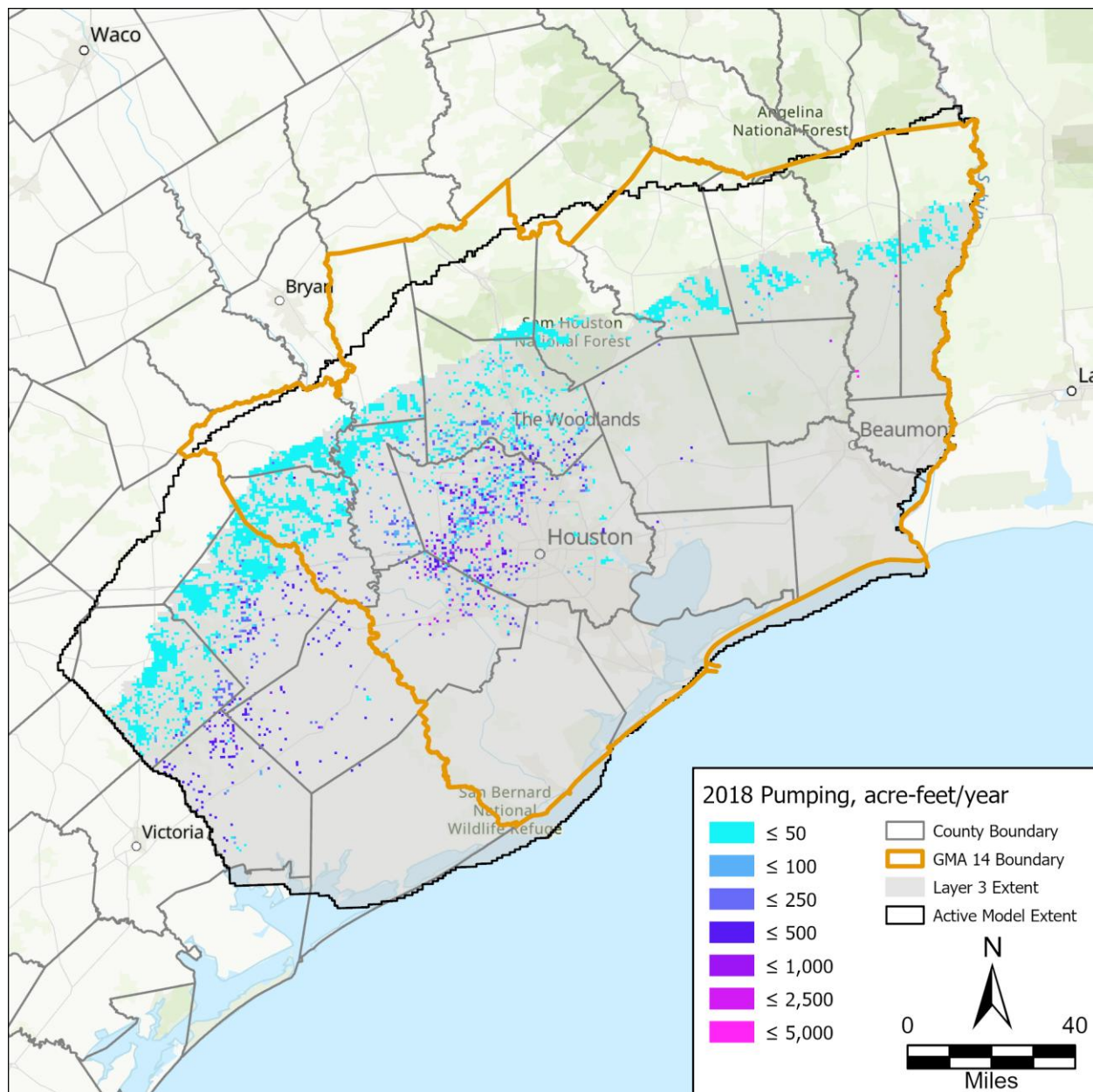


Figure 39. 2018 total pumping values for Layer 3 (Evangeline Aquifer).

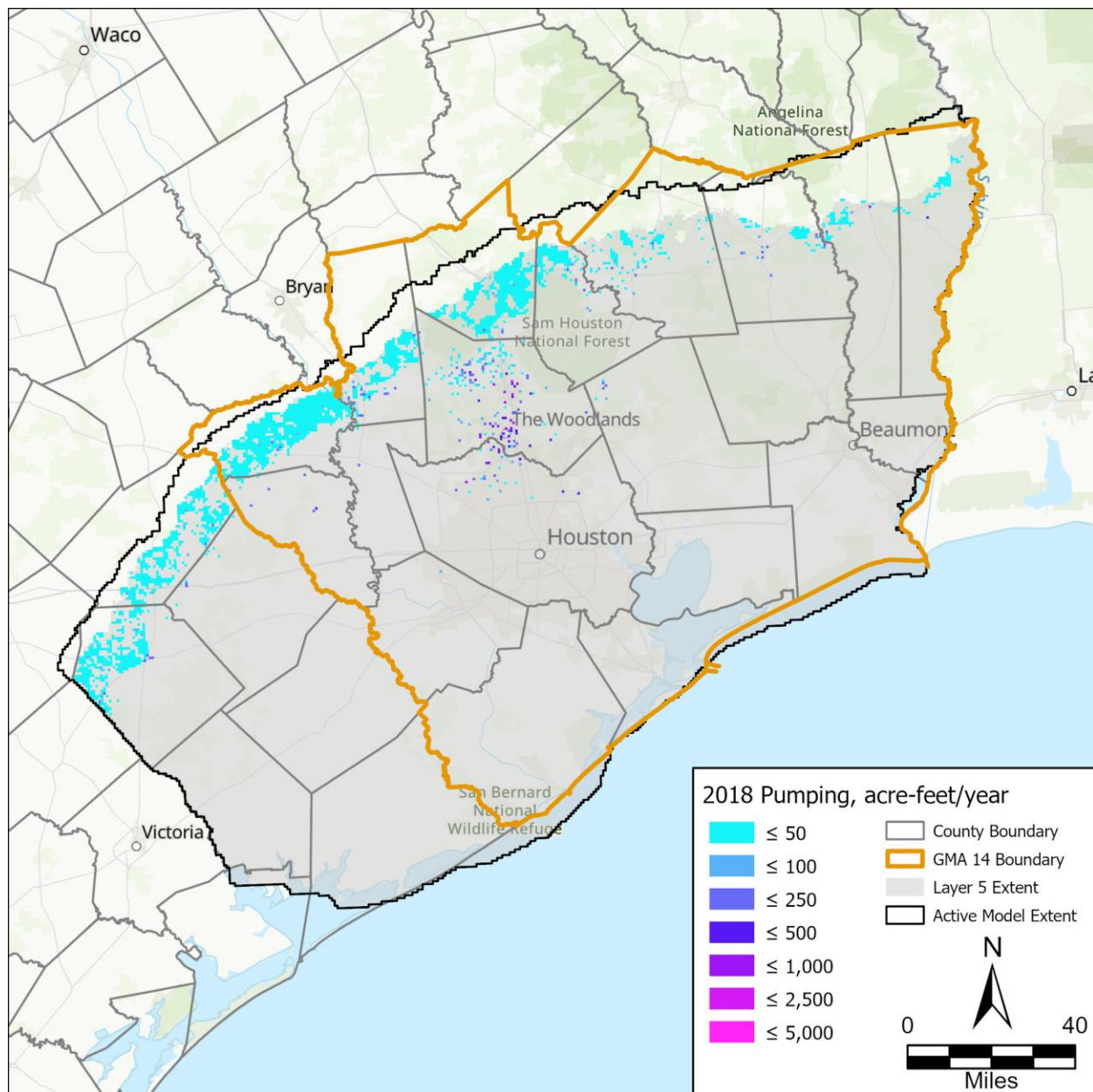


Figure 40. 2018 total pumping values for Layer 5 (Jasper Aquifer).

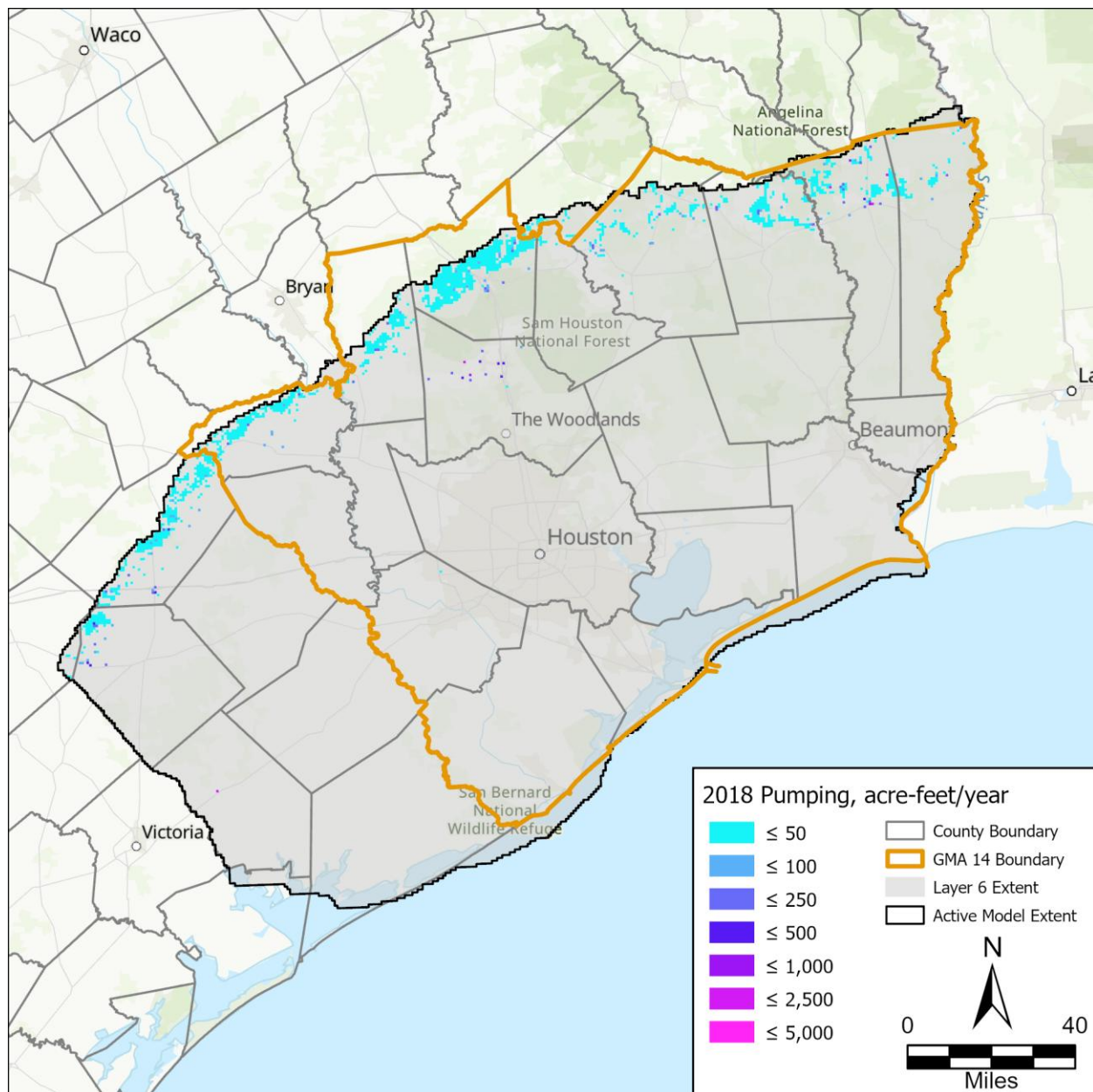


Figure 41. 2018 total pumping values for Layer 6 (Catahoula Aquifer).

3.6. Drain Package

The Drain (“DRN”) package simulates groundwater discharge through drains when the water table exceeds a specific elevation. Flow is calculated based on the difference between the water elevation and drain elevation using a conductance term to regulate flow. Once the water elevation drops below the drain elevation, flow ceases. With the GMA 14 Model, the DRN package was used to simulate springs and seeps (Figure 42).

For the GMA 14 Model, the DRN package elevations and conductance values are consistent GULF-2023 (Ellis and others, 2023) other than modifying the length units to feet.

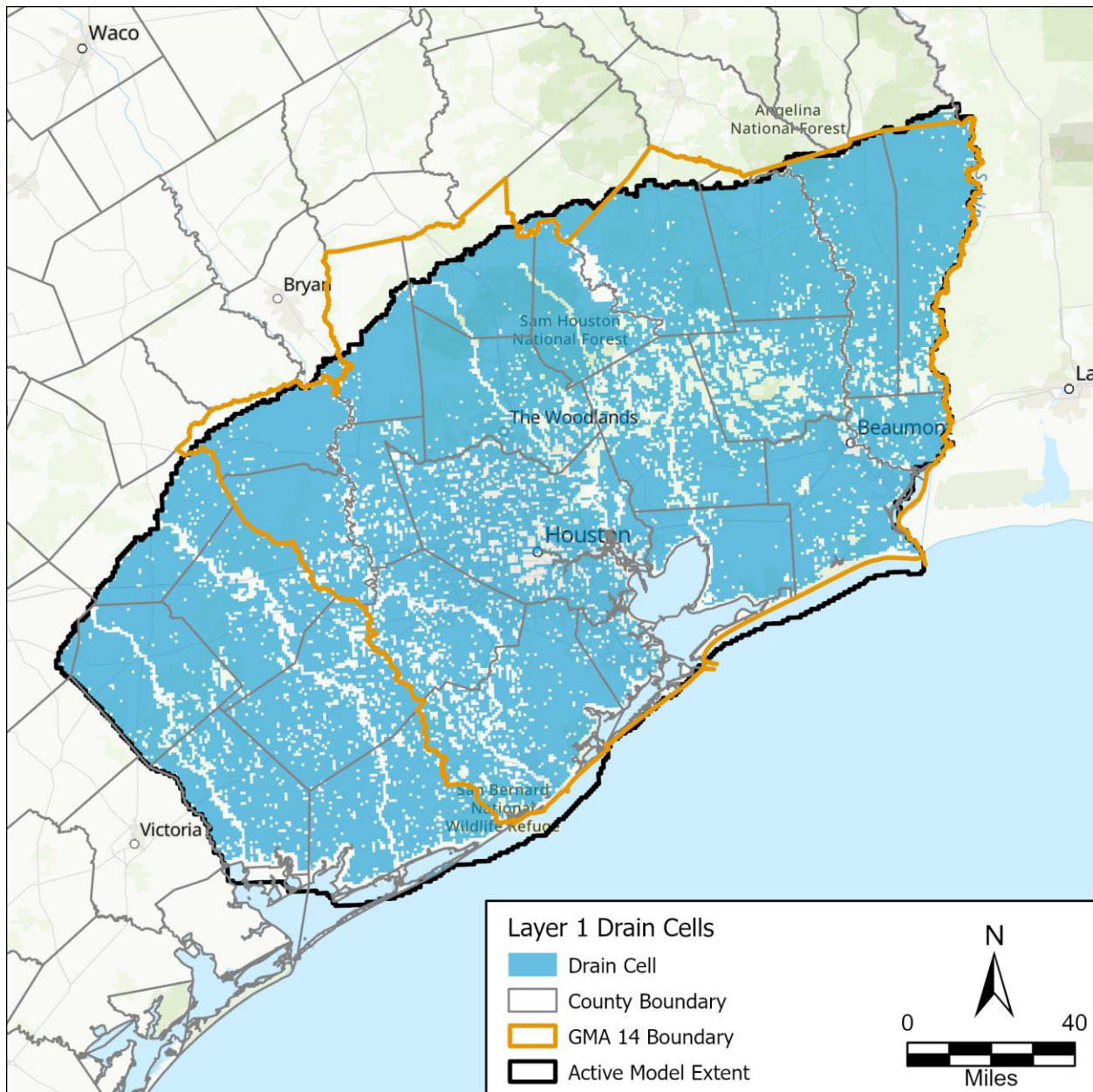


Figure 42. Layer 1 (shallow aquifer system) drain cell locations.

3.7. General-Heads Boundary Package

The General-Head Boundary (“GHB”) package provides a head-dependent boundary condition to represent groundwater flux between the water elevation at the model cell and the external water elevation. Flow is driven by the difference between the model cell water elevation and the boundary water elevation, regulated by conductance. Within the GMA 14 model, we used the GHB package to simulate flux between the groundwater system and the Gulf of Mexico (Figure 43).

For the GMA 14 Model, the GHB package is consistent GULF-2023 (Ellis and others, 2023) other than modifying the length units to feet. Calibrated conductance values are discussed in Section 4.1.5.



Figure 43. General head boundary cell locations for all layers.

3.8. Recharge Package

The Recharge (“RCH”) package simulates the addition of water to the groundwater system from precipitation, irrigation, or other sources. It applies recharge rates to the top model layer, which can vary spatially and temporally. The RCH package is essential for representing natural and artificial recharge processes affecting groundwater availability.

The GMA 14 Model contains a file for recharge to the outcrop (“gma14_rch_oc.rcha”) and a file for recharge to the subcrop (“gma14_rch_sc.rcha”). For the GMA 14 Model, the RCH package is consistent GULF-2023 (Ellis and others, 2023) other than modifying the length units to feet. We did not modify the soil-water-balance model developed for GULF-2023. Calibrated recharge values are discussed in Section 4.1.5.

3.9. River Package

The River (“RIV”) package provides a head-dependent boundary condition to represent flux between surface water and the modeled groundwater system. Flow between the river and aquifer is controlled by the head difference and riverbed properties. The RIV package is used to simulate baseflow conditions and surface water depletion due to groundwater pumping. The RIV package within the GMA 14 Model only interacts with layer 1. Figure 44 illustrates the river cell locations.

For the GMA 14 Model, the RIV package is consistent GULF-2023 (Ellis and others, 2023) other than modifying the length units to feet.

3.10. Output Control Package

The Output Control (“OC”) package informs MODFLOW of the frequency and type of model output, including heads, flows, and budget summaries. The GMA 14 Model outputs heads, flows, and the budget summary at the end of each stress period.

3.11. Iterative Model Solution Package

The Iterative Model Solution package (“IMS”) solves the system of equations governing groundwater flow using iterative numerical techniques. The IMS package describes the solver parameters that MODFLOW uses for solving the linear and nonlinear equations as part of the groundwater flow solution. We set the head change criteria for convergence of the nonlinear iterations to 0.1 feet and to 0.001 feet for the linear iterations. We set the flow residual criteria for convergence of the linear iterations to 0.1 ft³/day.

3.12. Observations Utility

The Observations (“OBS”) Utility informs MODFLOW to output specific model results for specified cells and times. We used the utility to output head values calculated during the simulation at water level observation target locations.



Figure 44. Layer 1 (shallow aquifer system) river cell locations.

4. Model Calibration

For the GMA 14 Model calibration, we adjusted parameters to improve the fit to water level, compaction, and subsidence targets during the history matching period described in Section 3.1.1. We automated calibration using the PEST++ software (White and others, 2020) for history matching. Specifically, we used the Iterative Ensemble Smoother program of the PEST++ suite known as PESTPP-IES.

The Iterative Ensemble Smoother is a calibration approach that adjusts model parameters iteratively to improve the match between model outputs and observed data. It operates by generating an ensemble of parameter sets, each representing a possible realization of the system. Each realization is run through the groundwater model to generate simulated observations. These simulated values are compared to measured field observations which inherently contain noise due to measurement errors and natural variability. To account for this noise, PESTPP-IES assumes that both observations and parameters are probabilistic treating them as random variables with associated uncertainties. This PESTPP-IES approach allows for a calibration process that does not rely solely on a single best-fit solution but rather on a distribution of calibrated parameter values (White and others, 2020).

The PESTPP-IES calibration process is iterative, meaning that it refines parameter estimates over multiple adjustment cycles. After each iteration, PESTPP-IES adjusts the parameter ensemble to minimize the discrepancy between simulated and observed data as represented by a least-squares objective function. Each ensemble update is informed by the covariance between parameters and observations ensuring that parameter adjustments remain physically meaningful. Because PESTPP-IES works with an ensemble of parameter sets rather than a single deterministic parameter set, it naturally incorporates uncertainty quantification (White and others, 2020).

Within the ensemble of parameters sets, one realization is referred to as the “base model” which represents the parameter set defined by the user. The numerical model inputs outlined in Section 3 are the “base model” PESTPP-IES.

For a deterministic calibration approach, PEST++ would undertake as many model runs as adjustable parameters to calculate the sensitivity matrix between the parameters and observations, thus the calibration run time is dependent on the number of adjustable parameters. For example, if there are 1,000 adjustable parameters PEST++ would have to run the model 1,000 times and if each run took 10 minutes it would take 10,000 minutes of run time to complete one iteration. With the PESTPP-IES approach, sensitivities are approximated using the ensemble of model runs which reduces the number of runs required to the size of the ensemble. In the example above, the 1,000 adjustable parameters could be estimated through an ensemble of 100 realizations. The

ensemble approach of PESTPP-IES makes it particularly well-suited for highly parameterized groundwater models.

4.1. Calibration Procedures

4.1.1. Calibration targets

We developed the calibration target dataset for the GMA 14 Model using data from the TWDB database, U.S. Geological Survey databases, and water level targets Ellis and others (2023) used in the GULF-2023 calibration. The calibration targets used during history matching consisted of water level, compaction, and subsidence measurements. Since the GMA 14 Model simulates groundwater flow using one year stress periods, we filtered the water level and subsidence data to only end-of-year measurements. As end-of-year measurements are rarely available, we used values from within three months of the end of the stress period to reflect end-of-year conditions. If multiple values were within the 3-month range, we used the value closest to the end of the stress period. In the case where multiple wells within the same cell, we consolidated the measured values with priority given to the well with the longest measurement period. The approach resulted in 32,105 water level measurements (17,634 for the Chicot Aquifer [Layer 2], 10,627 for the Evangeline Aquifer [Layer 3], 2,930 for the Jasper Aquifer [Layer 5], and 914 for the Catahoula Aquifer [Layer 6]) from 1,820 wells and 2,554 compaction and subsidence measurements from extensometers, GPS stations, and benchmarks. Figure 45 shows the locations of wells by aquifer utilized for history matching. Figure 46 shows the locations of compaction (extensometer) and subsidence (GPS and benchmark) stations utilized for history matching.

We included all counties within the GMA 14 Model in the calibration target dataset. Most aquifer designations for the wells in the calibration target dataset are the TWDB aquifer designation. The only exception is the water level calibration target dataset for Montgomery County where, similar to the pumping dataset, we assigned the aquifer according to the permitted aquifer.

In addition to the water level, compaction, and subsidence measurements, the following targets were applied during history matching:

1. The change in target between stress periods.
2. The absolute change in targets between stress periods.
3. Trend in targets over the measurement period.
4. Trend in targets between calculated turning points.

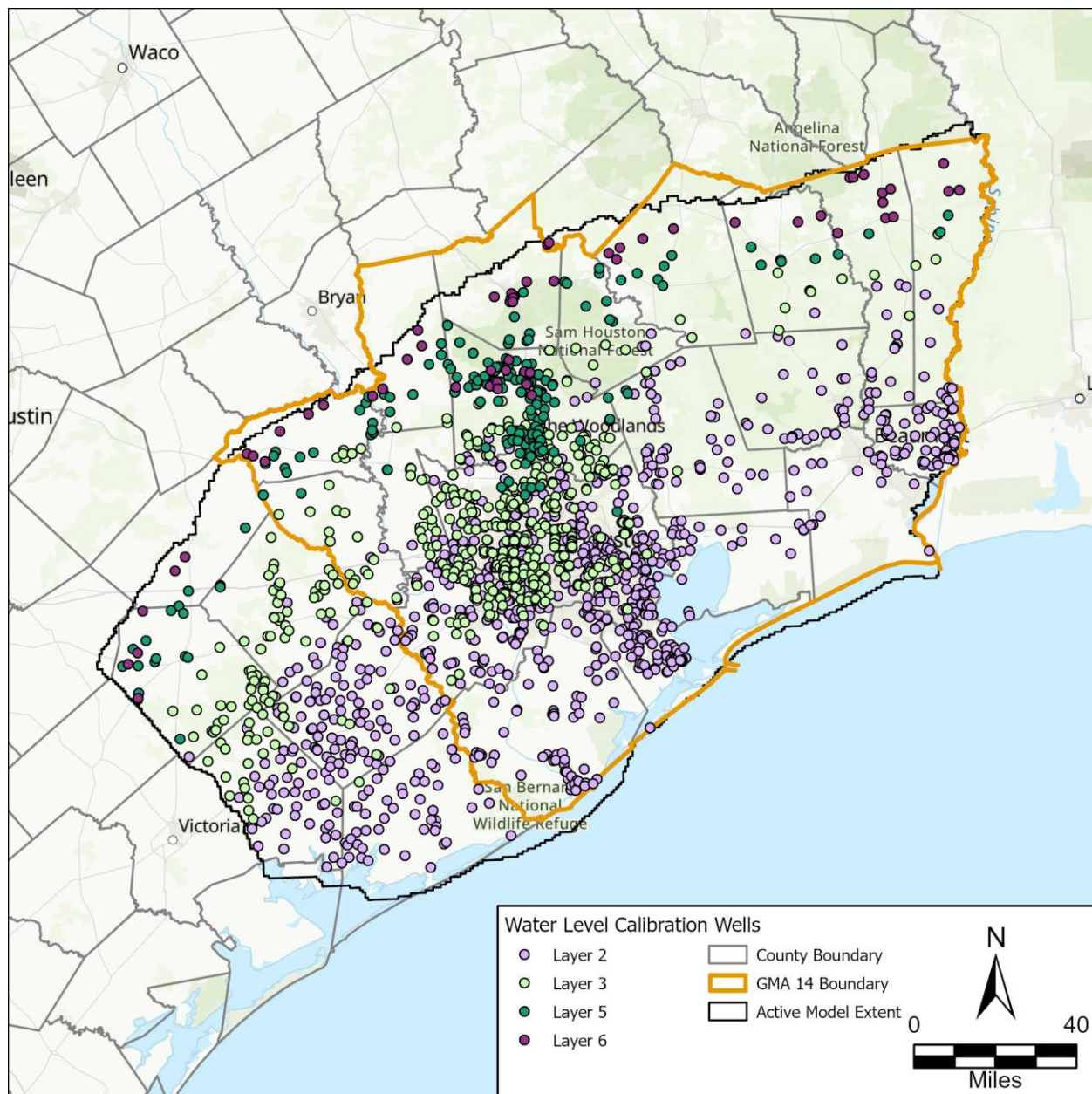


Figure 45. Wells with water level measurements used during calibration.

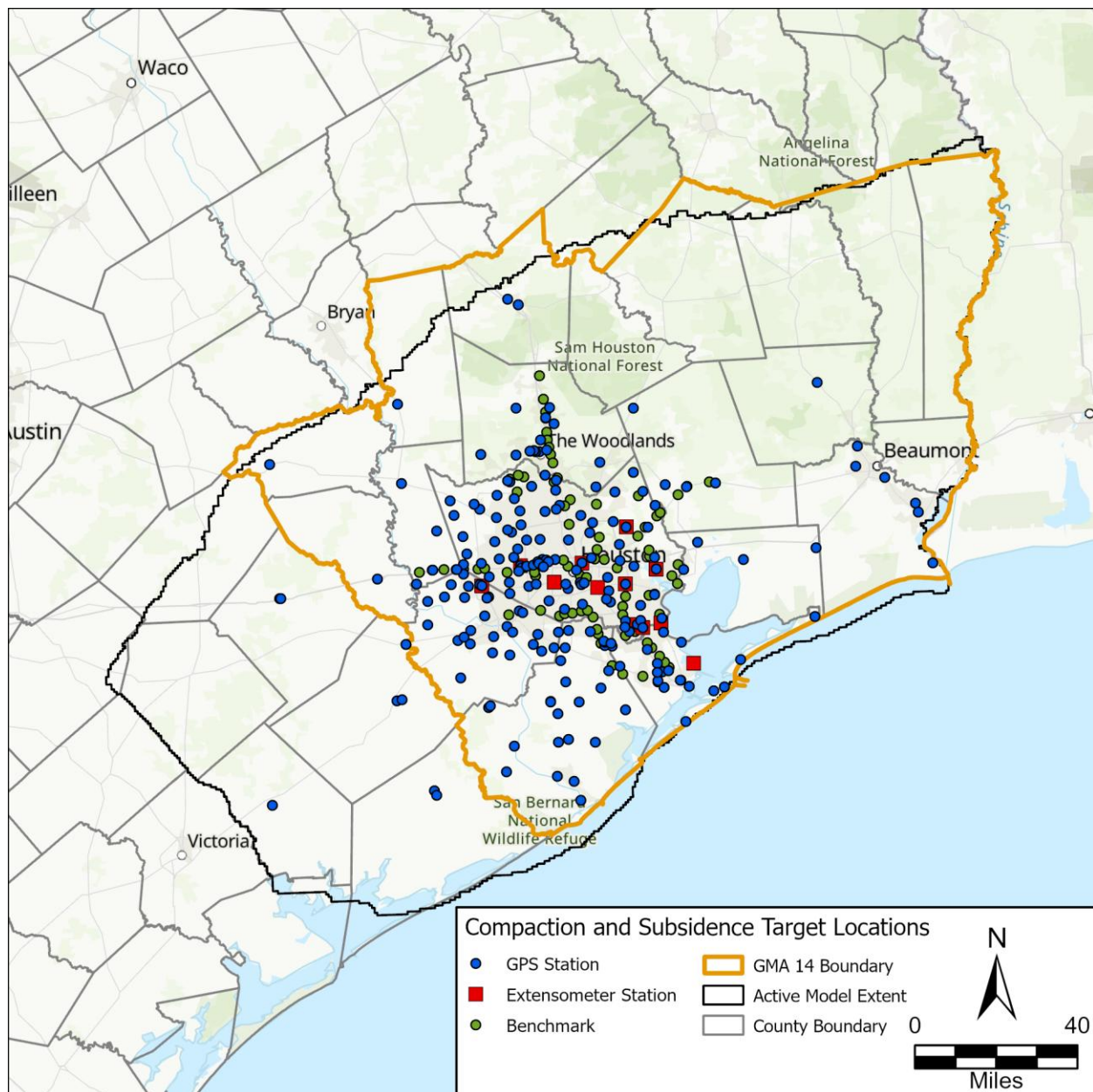


Figure 46. Compaction and subsidence station locations used during calibration.

We calculated the change in target between stress periods by subtracting the previous stress period measurement from the current stress period measurement. An increasing water level produced a negative result while a decline yielded a positive value. The absolute difference ensured all values were positive. This distinction allowed the model to capture both the magnitude and direction of measurement changes while the absolute difference emphasized the magnitude of the change. This analysis resulted in 30,287 difference-based and absolute difference-based water level targets and 2,266 difference-based and absolute difference-based compaction and subsidence targets.

The overall trend in either water level or subsidence measurements is calculated using the Kendall-Theil approach (Granato, 2006). As described by Granato (2006), this approach utilizes the available measurements to calculate a trend but is less susceptible to the influence of outliers compared to standard linear regression analysis. This analysis resulted in 1,190 overall water level trend targets and 71 compaction and subsidence trend targets. Figure 47 is an example of the calculated trend in measured water levels and Figure 48 illustrates an example of the calculated trends in an extensometer station.

Turning points in either water level or subsidence measurements refer to quantifiable changes in data trends. To conduct the analysis, we apply the Ramer-Douglas-Peucker algorithm (Ramer, 1972; Douglas and Peucker, 1973) to the data points. The algorithm simplifies data by only keeping values that indicate a change in slope. From this simplified set of points, we can identify the first and last year of a trend along with the trend between those years. Our analysis resulted in 3,328 water level targets of trend between turning points and 366 subsidence targets of the trend between turning points. Figure 47 is an example of the calculated turning points and trends between those turning points in measured water levels. Figure 48 is an example of the calculated turning points and trends between those turning points in measured subsidence.

Since PEST-IES estimates the objective function based on the summed squared residuals of targets, it is necessary to assign different weights to each target group. We grouped the water level and compaction/subsidence measurements separately and weighted each group such that it accounted for 50 percent of the total objective function. We applied this approach to minimize bias during calibration towards either measurement group. We further divided water levels by target metric and aquifer to more heavily weight water level differences and trends. Subsidence targets were also further broken down by target metric and station type.

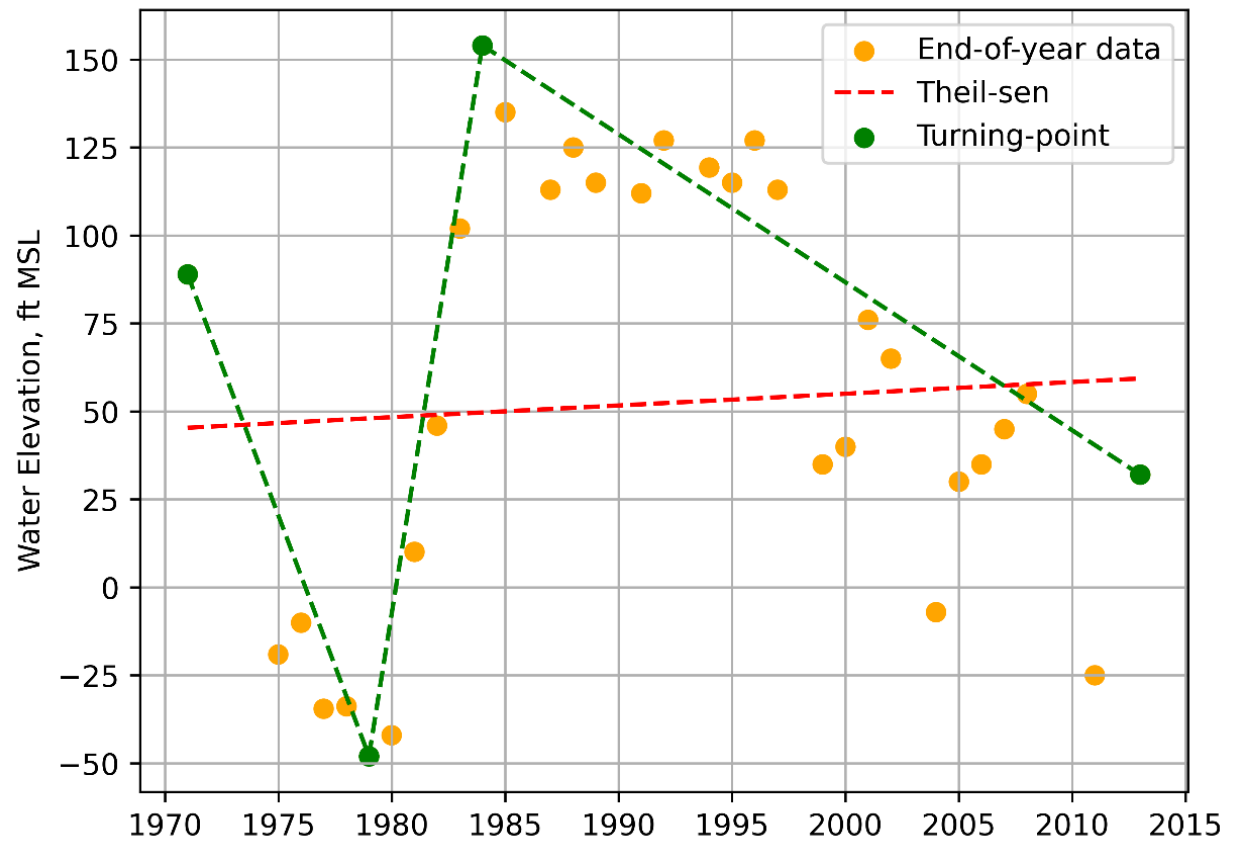


Figure 47. Example of the Theil-Sen and turning points applied to water level measurements.

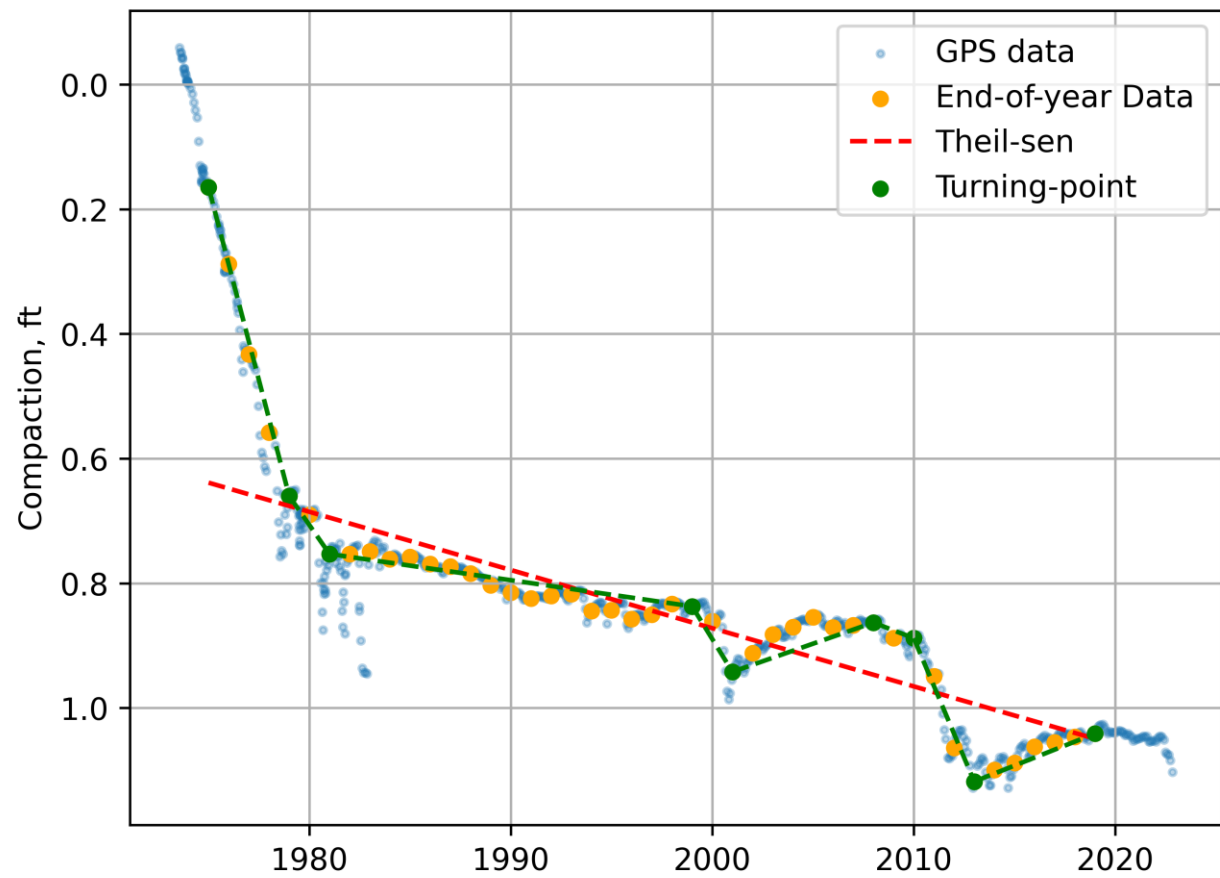


Figure 48. Example of the Theil-Sen and turning points trends applied to an extensometer station.

4.1.2. Parameter Adjustments

We adjusted parameters during history matching using multipliers on model-wide and pilot point scales. Our approach allowed calibration to fine tune parameterization at different resolutions. The multiplier scales used for each parameter along with the range of allowable values are summarized in Table 9. The multiplier upper and lower limit is the range of the allowable multipliers, and the ultimate upper and lower limit are the range of allowable model values after all multipliers. The ultimate upper and lower limits are based on reasonable expected values from the conceptual model.

Figures 49 through 54 show the locations of the pilot points for each layer. Pilot points are included in every 10 cells and are evenly spaced throughout each active layer extent.

Table 9. Parameters adjusted during history matching.

Parameter	Layers	Units	Model-wide Multiplier	Pilot Point Multiplier	Cell Multiplier	Multiplier Lower Limit	Multiplier Upper Limit	Ultimate Lower Limit	Ultimate Upper Limit
Recharge	1	ft/day	x			0.75	1.25	0	0.0012
General Head Boundary Conductance	All	ft ² /day	x			0.1	10	0.01	1000
River Conductance	1	ft ² /day	x		x	0.1	10	10	10,000
Aquifer Horizontal Hydraulic Conductivity	1, 4, & 5	ft/day	x	x		0.1	10	0.001	200
	2, 3, & 6	ft/day	x	x		0.75	1.25	0.001	200
Aquifer Vertical Hydraulic Conductivity	All	ft/day	x	x		0.1	10	1.0E-10	1
Specific Yield	1	-	x	x		0.25	1.5	0.001	0.25
	2-6	-	x	x		0.75	1.25	0.001	0.25
Coarse-Grained Elastic Specific Storage	All	ft ⁻¹	x	x		0.1	10	1E-09	1E-04
Coarse-Grained Porosity	All	-	x	x		0.75	1.25	0.05	0.4
Interbed Elastic Specific Storage	2-5	ft ⁻¹	x	x		0.15	5	1E-07	3E-03
Interbed Inelastic Specific Storage	2-5	ft ⁻¹	x	x		0.15	5	1E-07	1E-03
Interbed Vertical Hydraulic Conductivity	2-5	ft/day	x	x		0.1	10	1E-09	0.001
Interbed Porosity	2-5	-	x	x		0.5	1.5	0.05	0.6

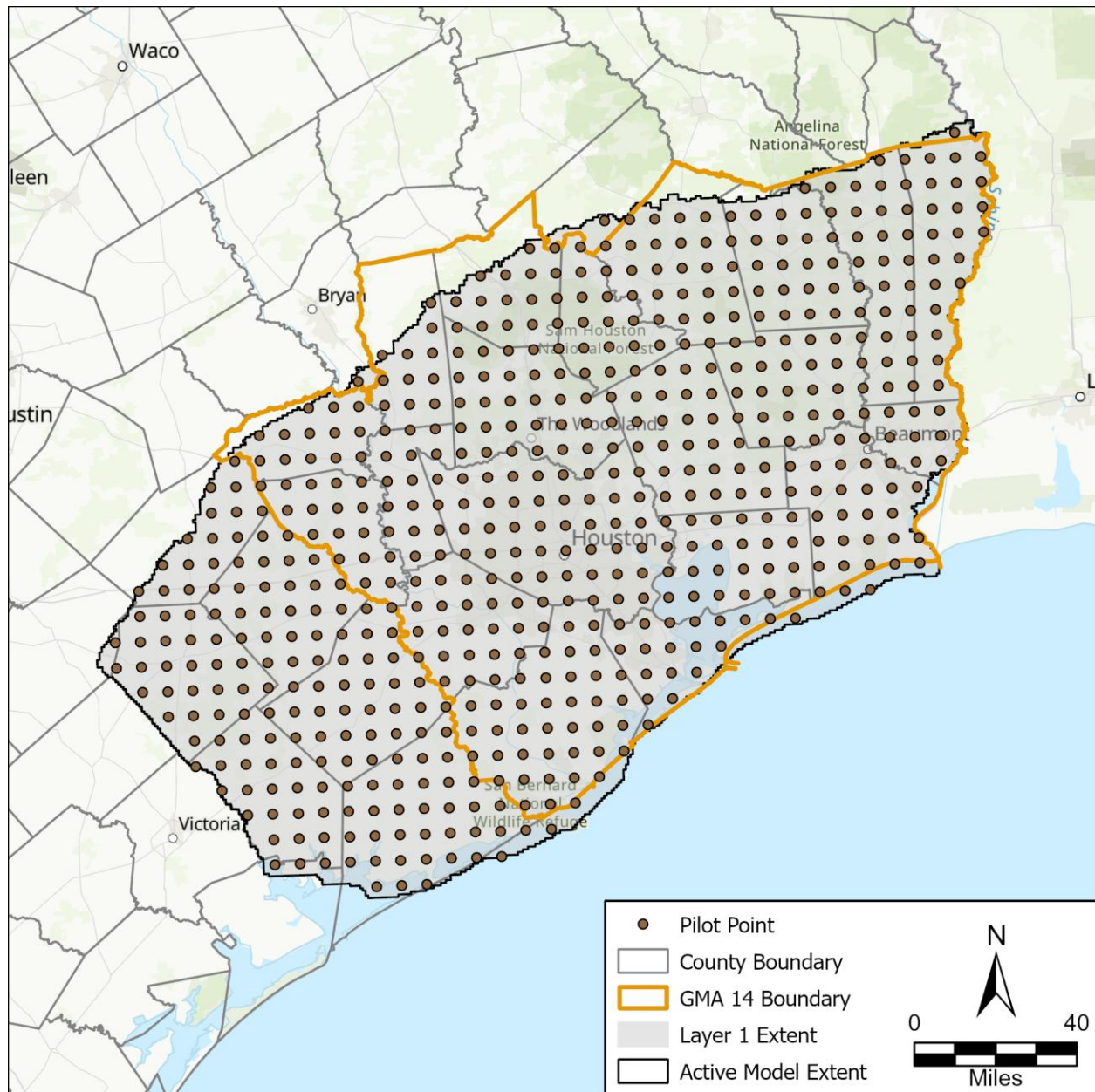


Figure 49. Pilot points for Layer 1 (shallow aquifer system).

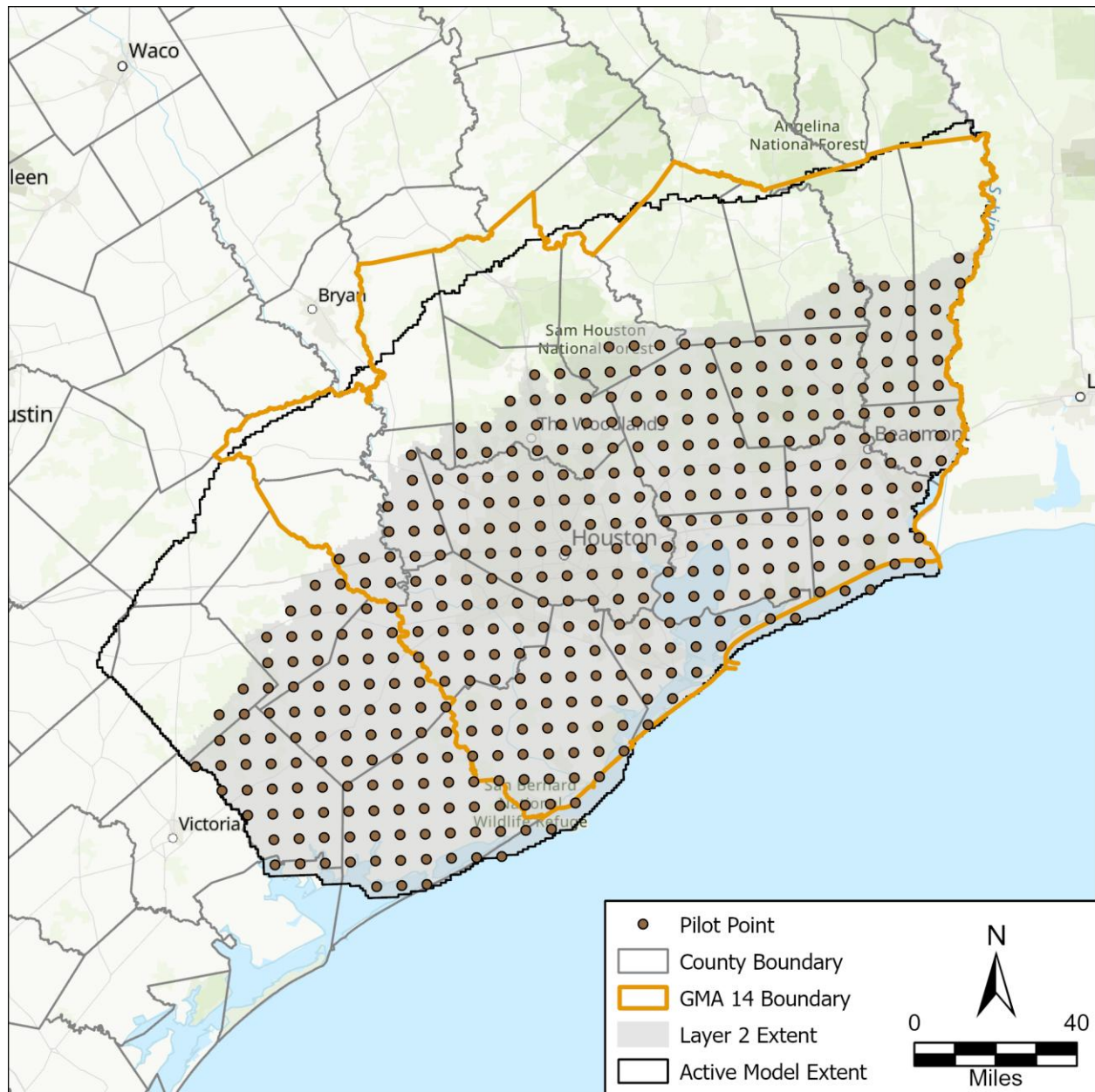


Figure 50. Pilot points for Layer 2 (Chicot Aquifer).

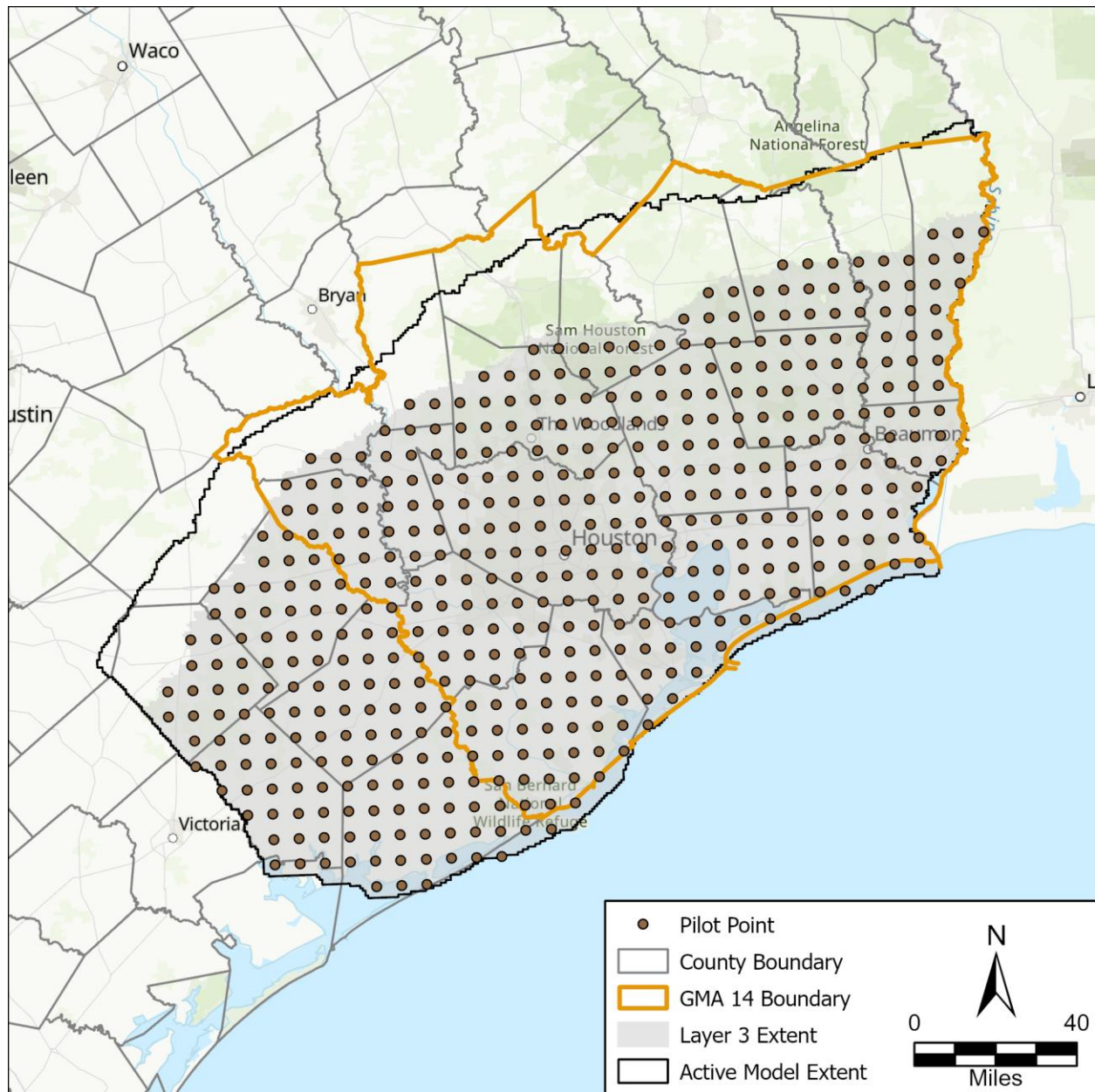


Figure 51. Pilot points for Layer 3 (Evangeline Aquifer).

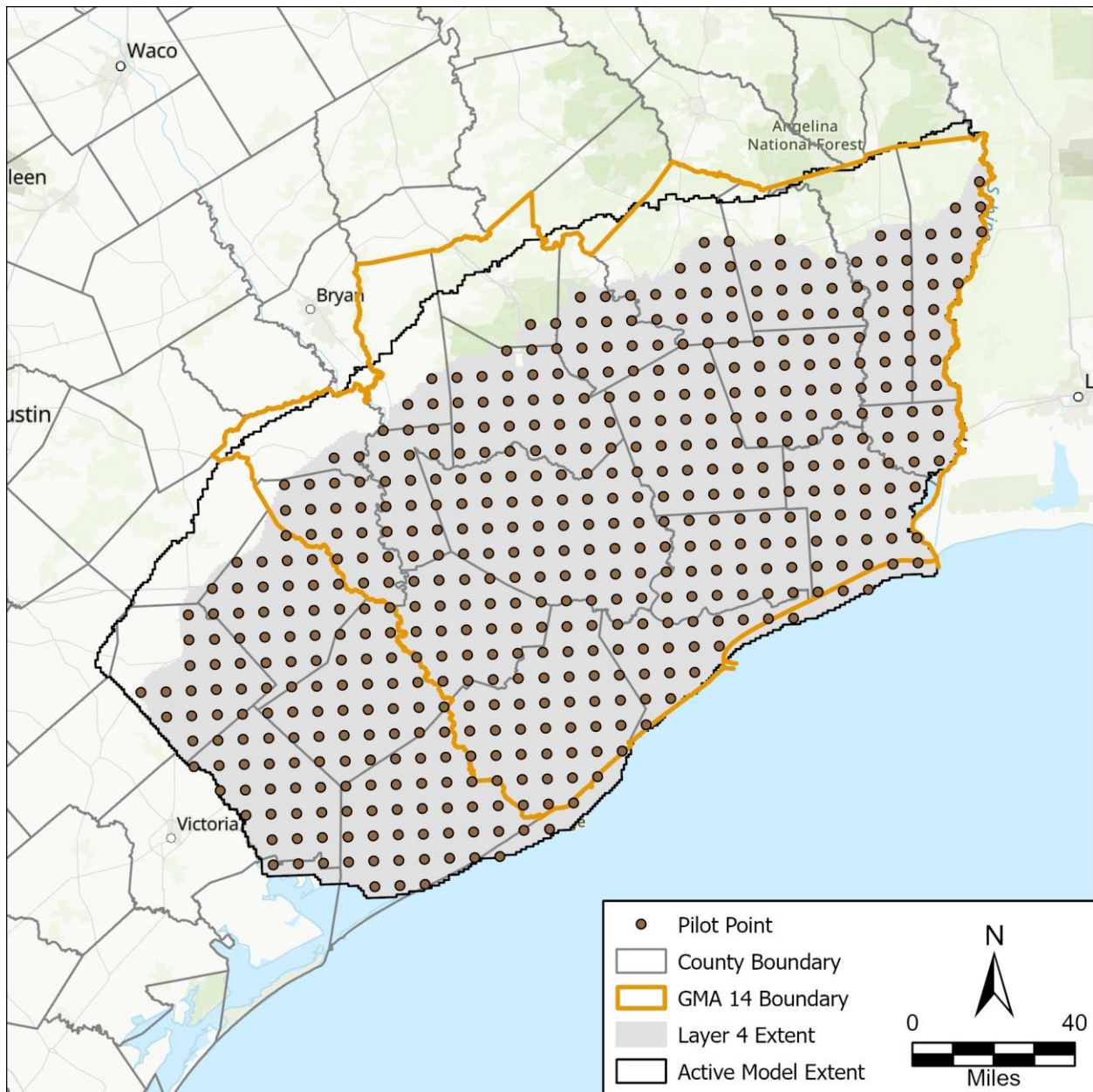


Figure 52. Pilot points for Layer 4 (Burkeville).

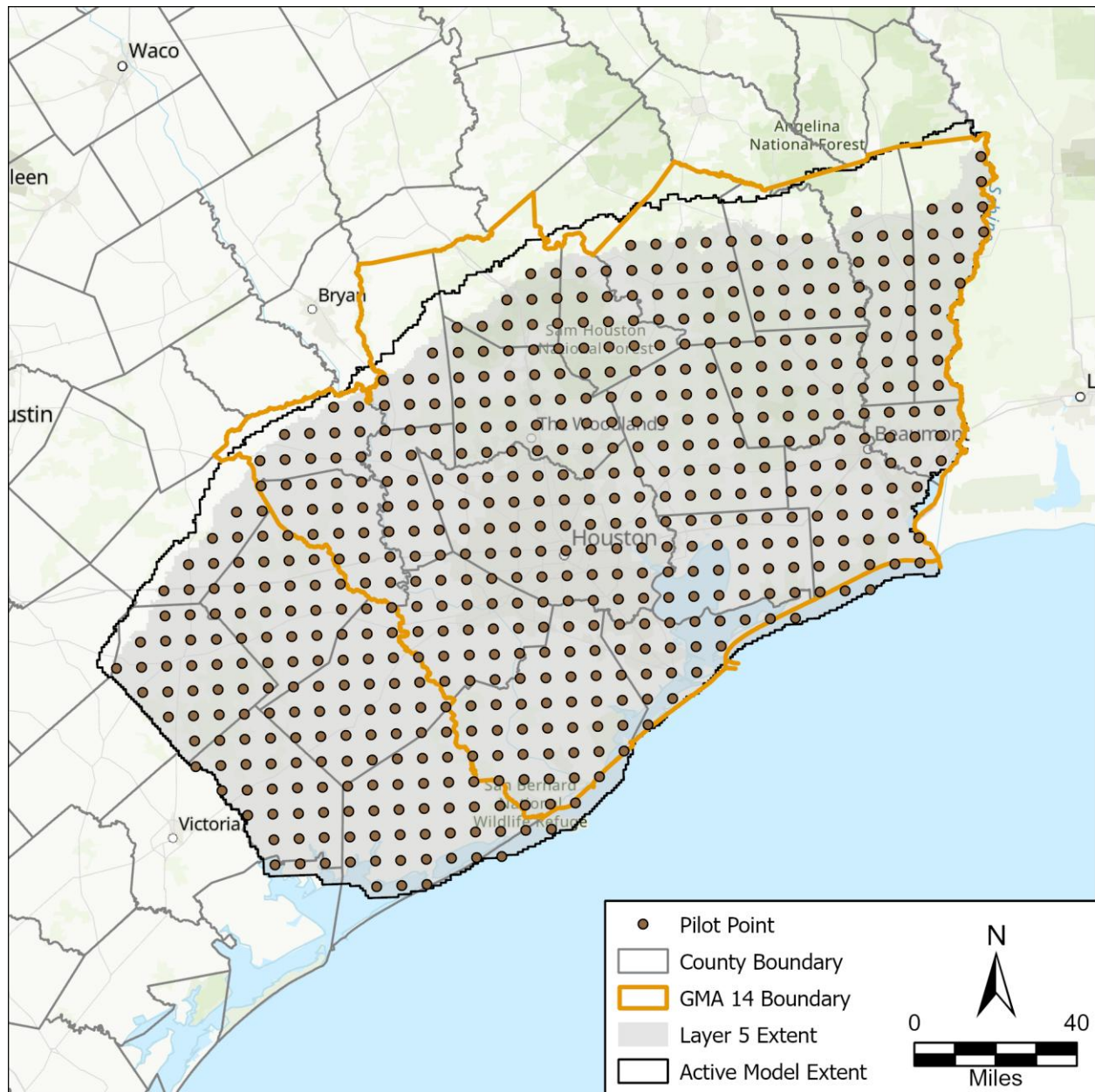


Figure 53. Pilot points for Layer 5 (Jasper Aquifer).

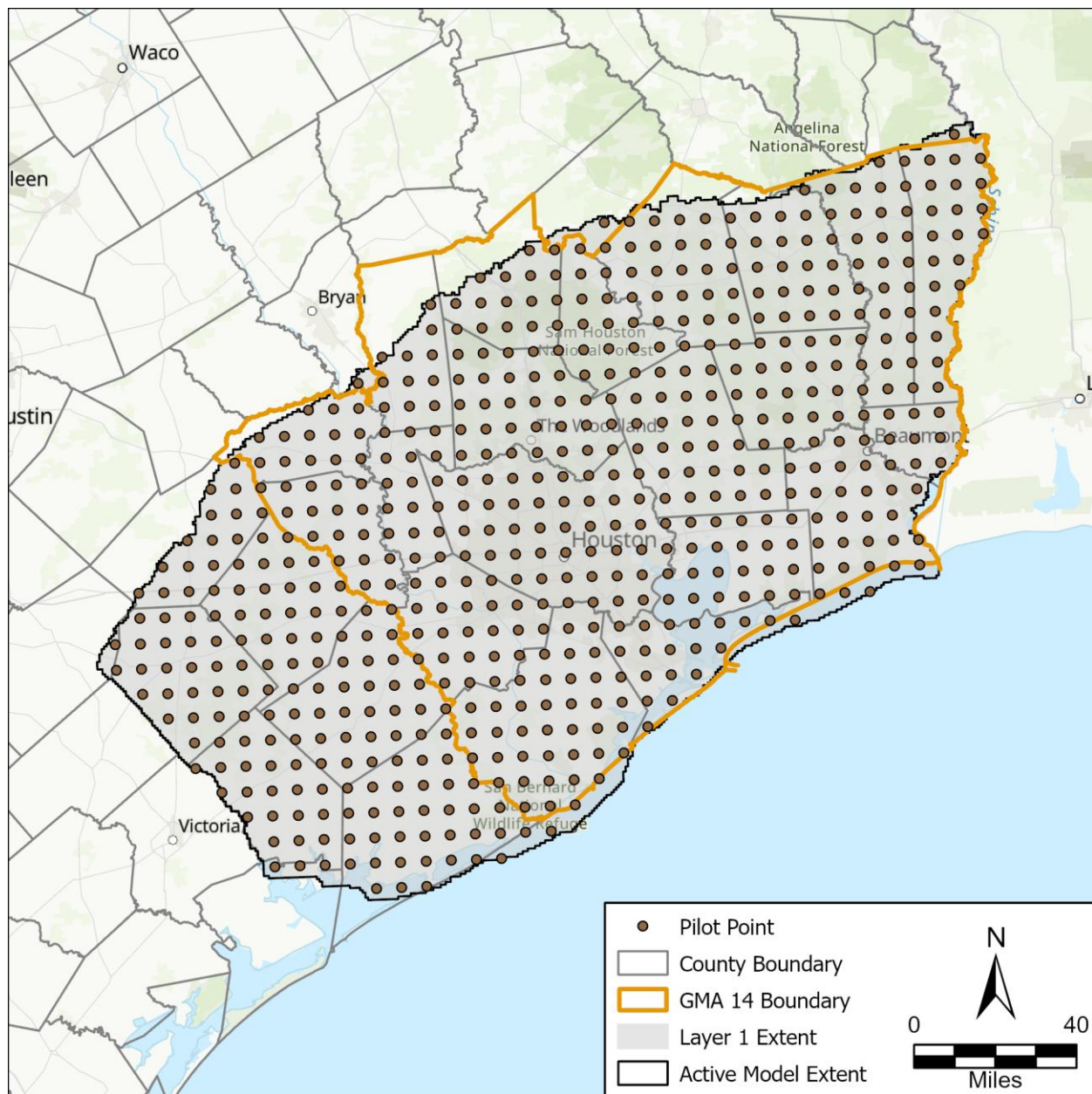


Figure 54. Pilot points for Layer 6 (Catahoula Aquifer).

4.1.3. Calibration of Hydraulic (NPF and STO) Properties

We applied model-wide and pilot-point scale multipliers to hydraulic properties for all layers during calibration. Table 10 summarizes the initial and calibrated value statistics by layer for each hydraulic property adjusted during calibration. The results of the hydraulic conductivity for the aquifer layers are illustrated in Figures 55 through 58. The model-wide mean value for the Chicot and Evangeline only slightly increased while the Jasper and Catahoula layer calibrated mean value stayed consistent with the initial value.

The modeled transmissivity is equal to the layer thickness multiplied by the hydraulic conductivity. We compared the transmissivity data from pumping tests to the calibrated transmissivity to verify the results are within the expected values. Figures 59 through 61 show the observed transmissivity from test data compared to the modeled transmissivity. The one-to-one line on each figure indicates where values would plot if the match were perfect.

The modeled transmissivity for Layer 2 (Chicot Aquifer) overall huddled around the one-to-one line, indicating a good fit between the modeled and test data. At the lower transmissivity range the modeled transmissivity was generally higher than the test data while the higher ranges the calibration under simulated the values. Similar to the Chicot, the calibration generally over simulated the transmissivity of the Evangeline at lower ranges and under simulated the higher values. The Jasper also under simulated the higher observed values. It should be noted that we used the observed values to parameterize the base model prior to calibration and the interpolation can smooth out the higher values.

We adjusted vertical hydraulic conductivity by 0.1 to 10 for each multiplier throughout all layers. The model-wide mean increased in layers 1 through 4 and decreased in the Jasper and Catahoula. Figures 62 through 65 illustrate the calibrated base model vertical hydraulic conductivity for each aquifer layer. The Chicot and Evangeline maintained higher values in the downdip regions which is consistent with the conceptual model of Ellis and others (2023).

We adjusted the specific yield multipliers by 0.25 to 1.5 in the shallow aquifer system and 0.75 to 1.25 in all other layers. Figures 66 through 69 illustrate the spatial distribution of the specific yield by layer. We applied a depth dependent function for specific yield in layer 2 (Chicot) while a constant value of 0.2 for all other layers which is consistent with the approach by Ellis and others (2023) in GULF-2023. The mean layer values changed slightly during calibration.

Table 10. Initial and calibrated hydraulic property statistics by layer.

Hydraulic Property	Layer	Initial			Calibrated Base Model		
		Min	Max	Mean	Min	Max	Mean
Aquifer Horizontal Hydraulic Conductivity	1	0.07	13.06	9.51	0.01	60.00	4.67
	2	0.71	36.20	11.30	0.63	47.59	13.29
	3	0.91	18.14	4.48	0.58	21.72	5.04
	4	0.11	0.11	0.11	0.02	1.03	0.22
	5	0.20	10.98	2.31	0.24	10.83	2.08
	6	0.48	8.53	3.01	0.43	13.82	3.30
Aquifer Vertical Hydraulic Conductivity	1	1.31E-07	2.61E-05	1.90E-05	1.72E-07	1.12E-03	1.54E-04
	2	8.77E-04	9.67E-01	8.83E-02	4.51E-04	1.00E+00	2.13E-01
	3	1.01E-04	1.31E-01	1.56E-02	5.89E-05	1.00E+00	8.47E-02
	4	9.24E-07	9.24E-07	9.24E-07	5.66E-08	5.46E-06	1.11E-06
	5	2.42E-03	1.32E-01	2.77E-02	8.61E-04	1.42E-01	1.04E-02
	6	5.28E-03	9.39E-02	3.31E-02	1.60E-04	4.27E-02	4.25E-03
Specific Yield	1	0.20	0.20	0.20	0.12	0.25	0.24
	2	1.00E-03	0.20	5.96E-02	1.04E-03	0.25	7.19E-02
	3	0.20	0.20	0.20	0.16	0.25	0.21
	4	0.20	0.20	0.20	0.20	0.25	0.24
	5	0.20	0.20	0.20	0.15	0.24	0.19
	6	0.20	0.20	0.20	0.17	0.25	0.22

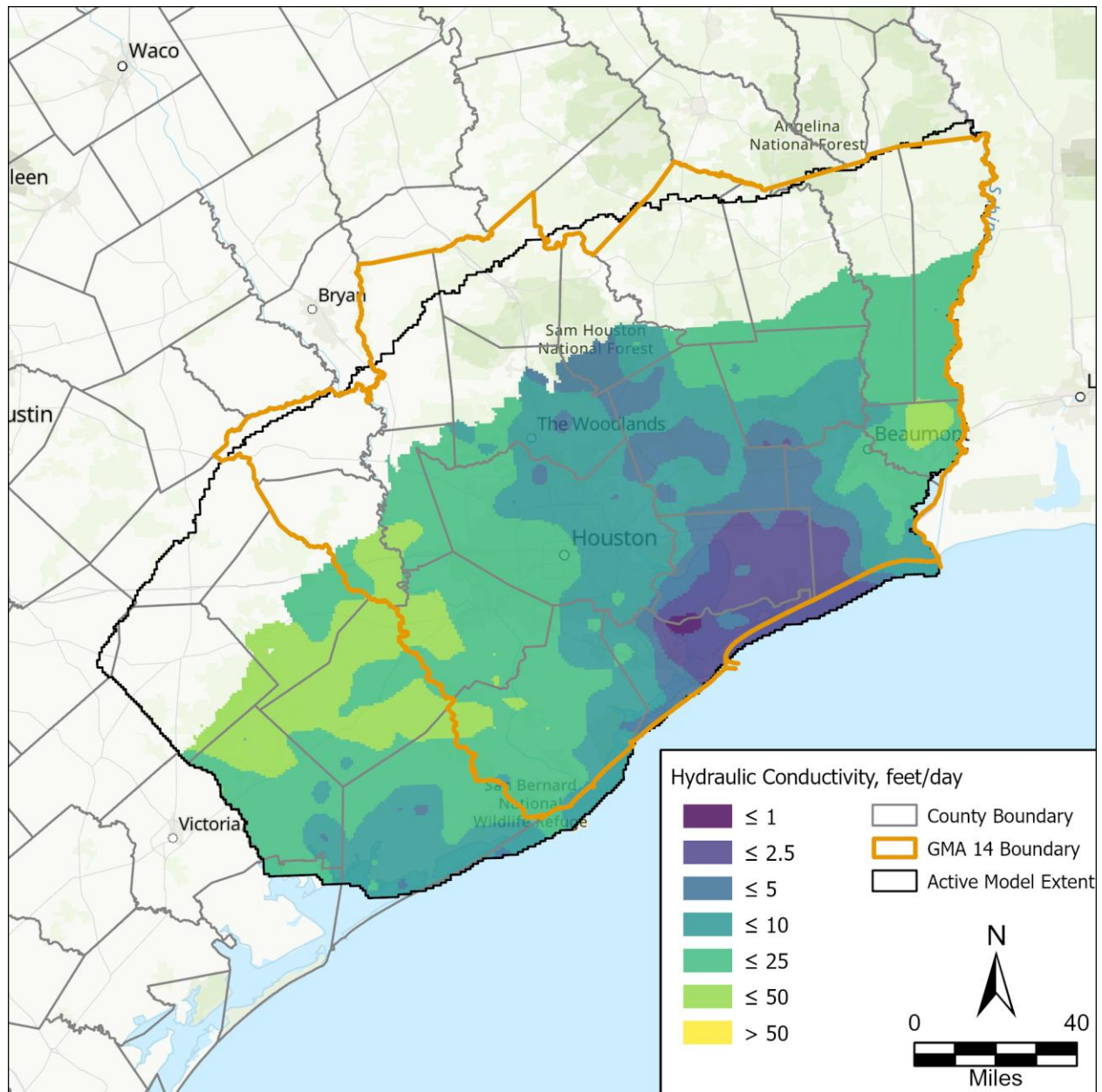


Figure 55. Calibrated layer 2 (Chicot Aquifer) hydraulic conductivity.

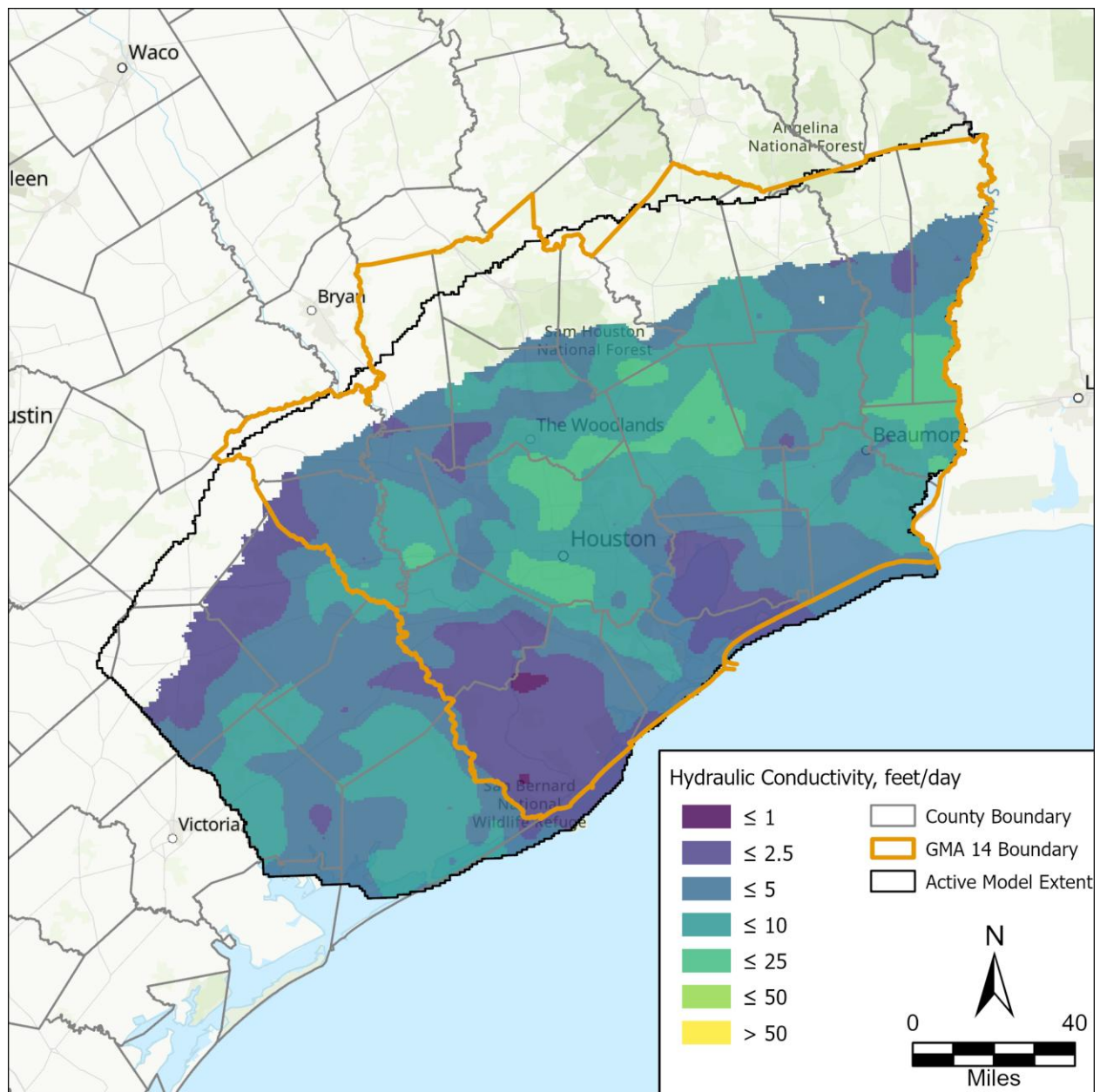


Figure 56. Calibrated layer 3 (Evangeline Aquifer) hydraulic conductivity.

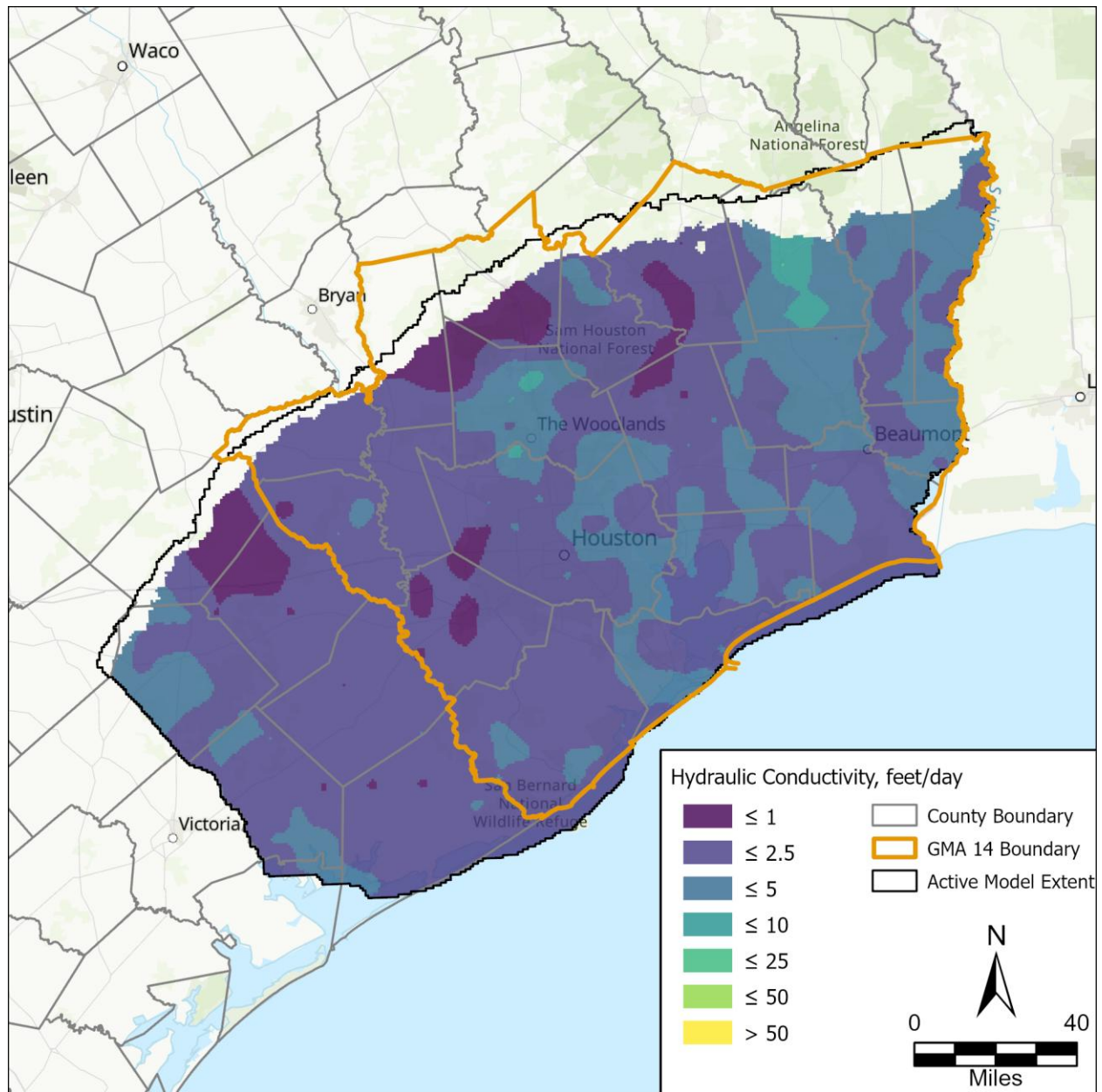


Figure 57. Calibrated layer 5 (Jasper Aquifer) hydraulic conductivity.

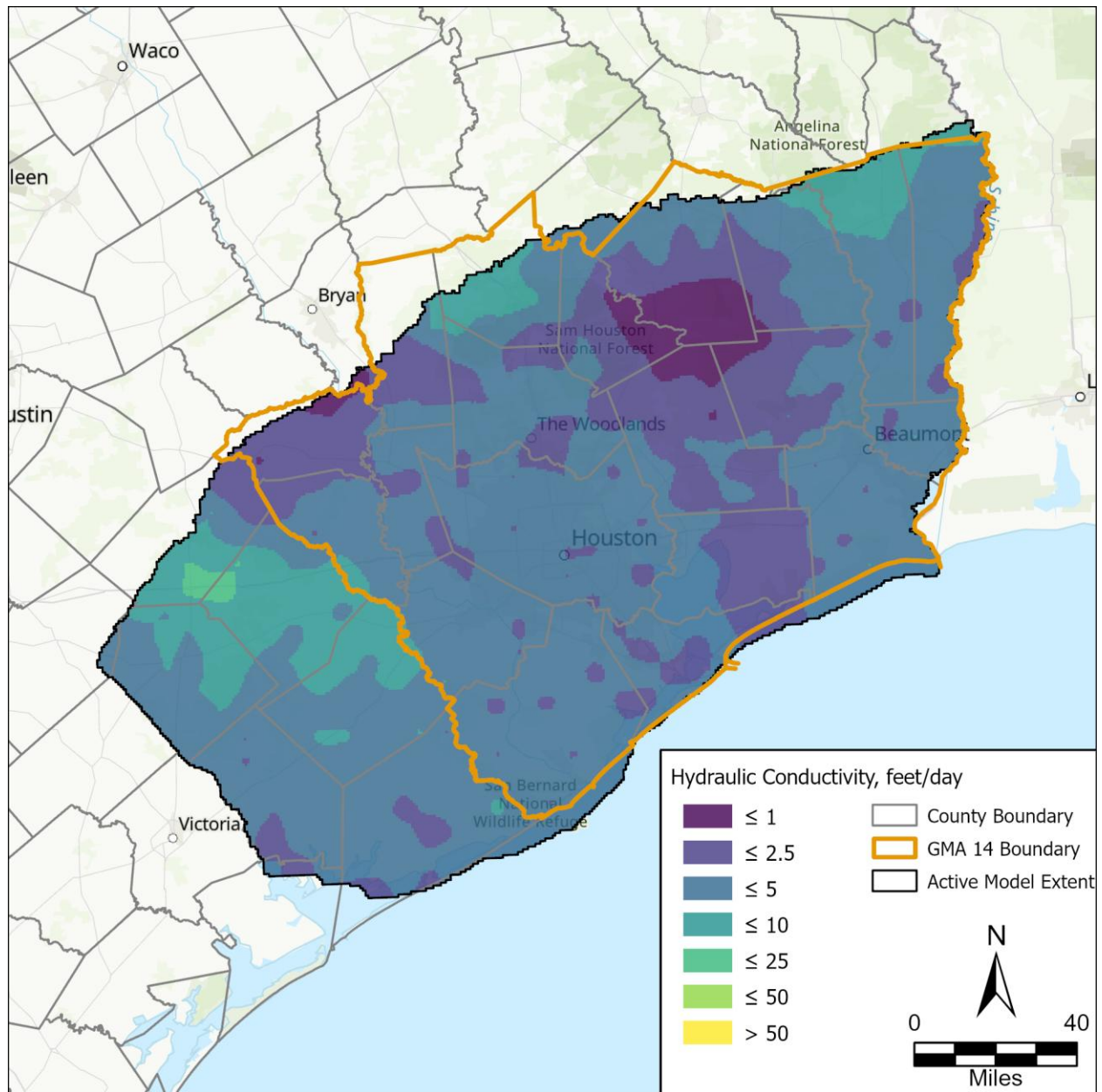


Figure 58. Calibrated layer 6 (Catahoula Aquifer) hydraulic conductivity.

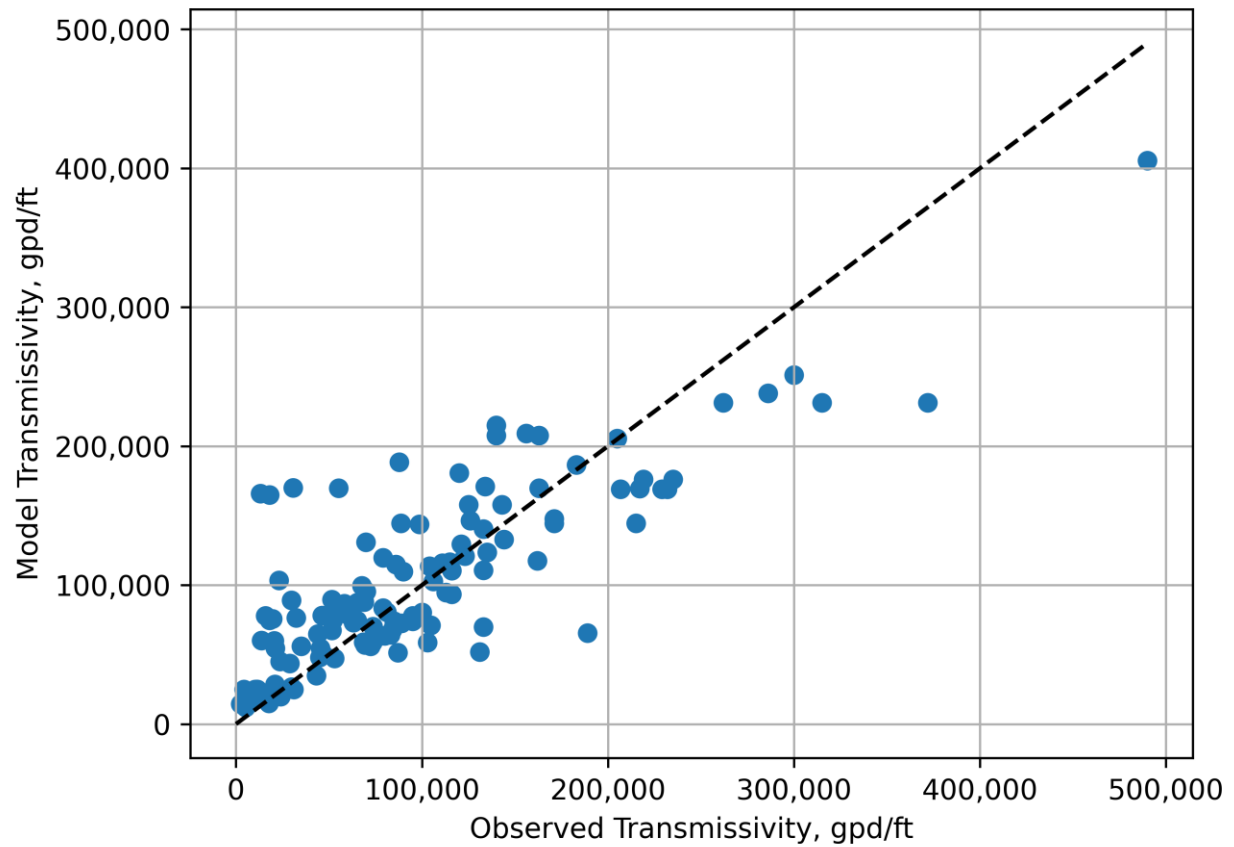


Figure 59. Observed versus calibrated transmissivity for Layer 2 (Chicot Aquifer).

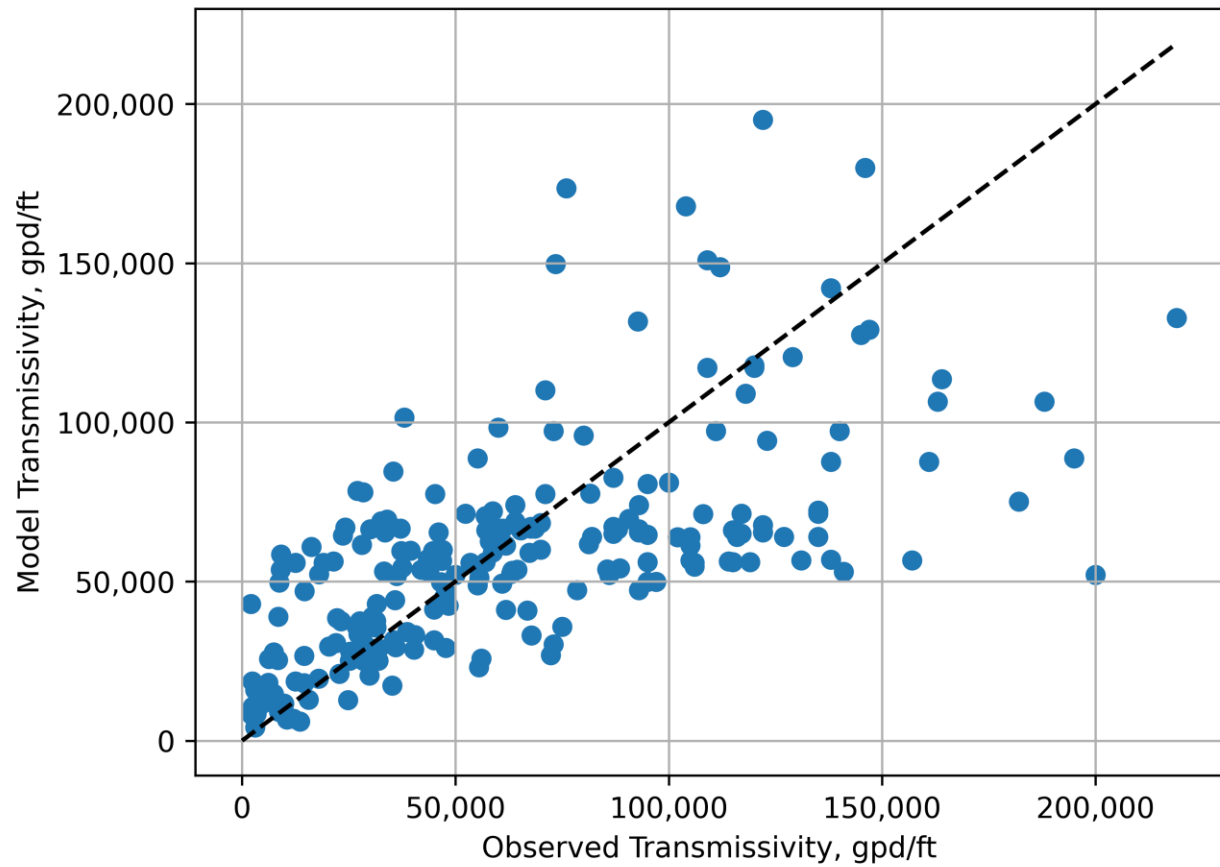


Figure 60. Observed versus calibrated transmissivity for Layer 3 (Evangeline Aquifer).

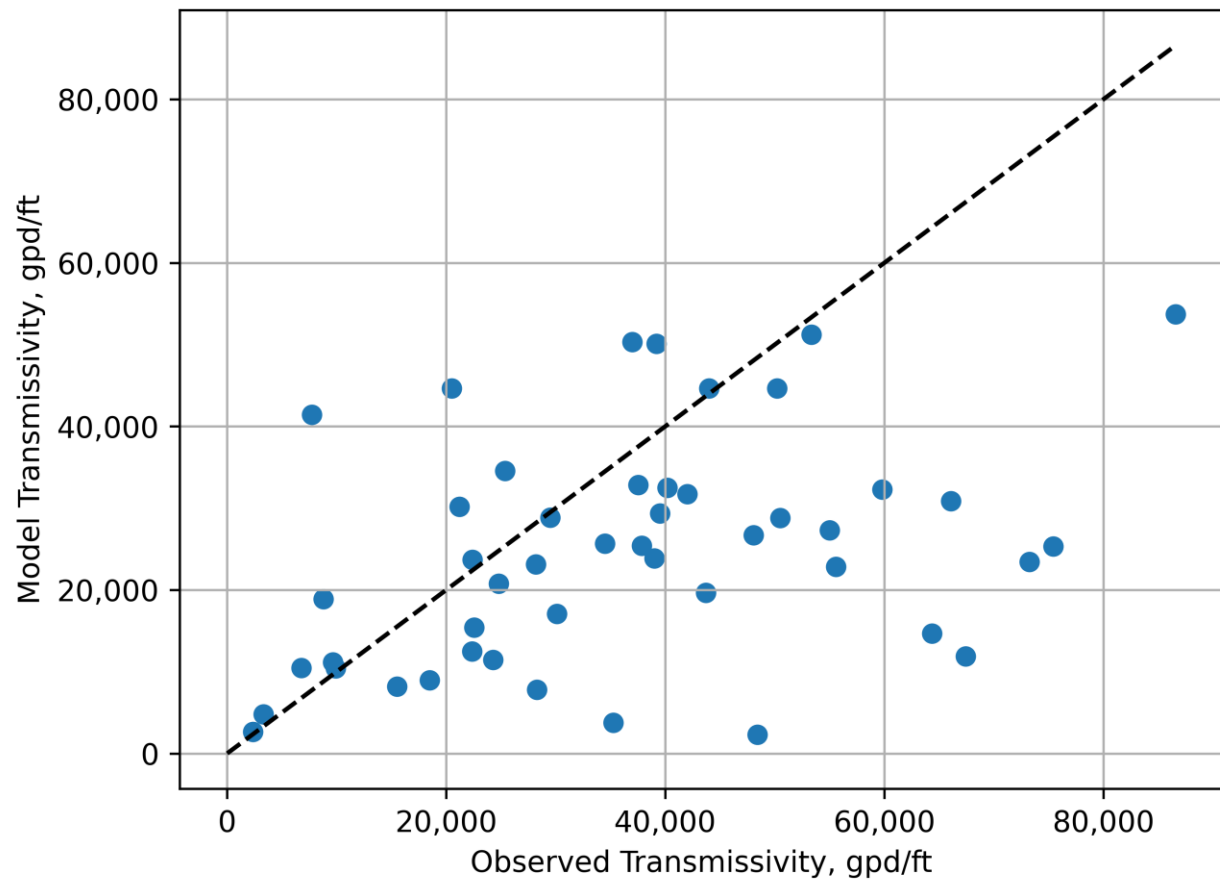


Figure 61. Observed versus calibrated transmissivity for Layer 5 (Jasper Aquifer).

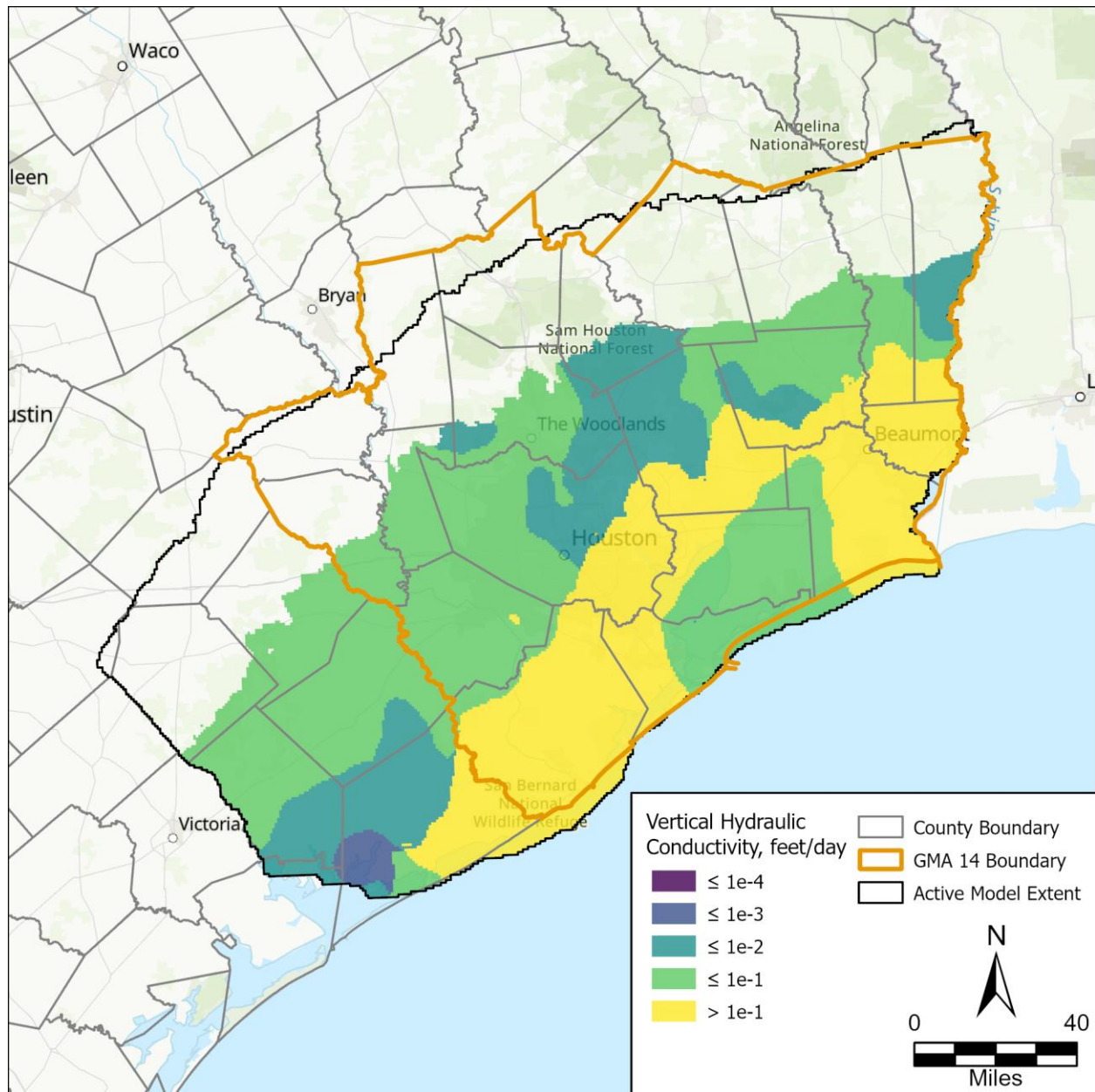


Figure 62. Calibrated layer 2 (Chicot Aquifer) vertical hydraulic conductivity.

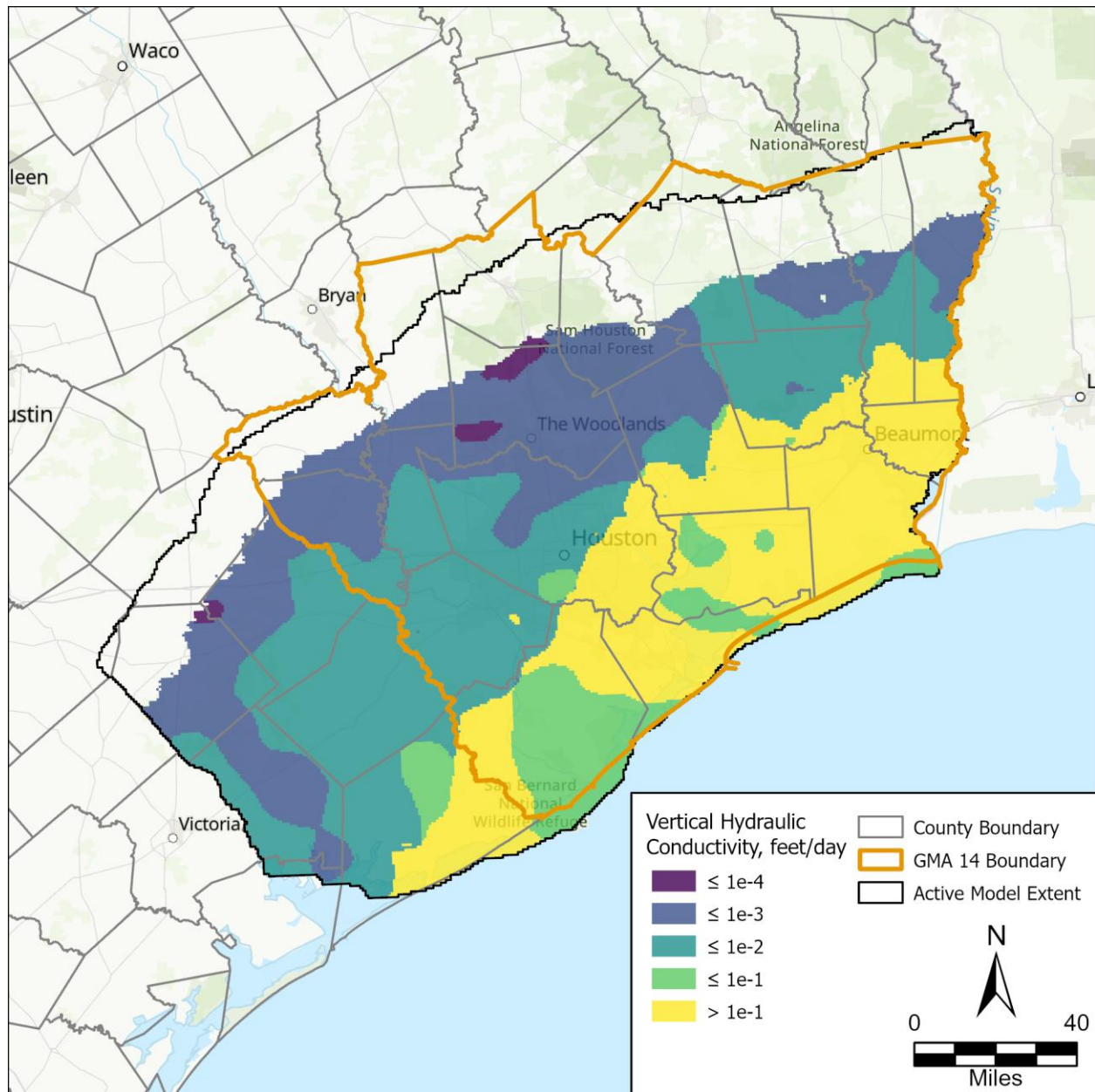


Figure 63. Calibrated layer 3 (Evangeline Aquifer) vertical hydraulic conductivity.

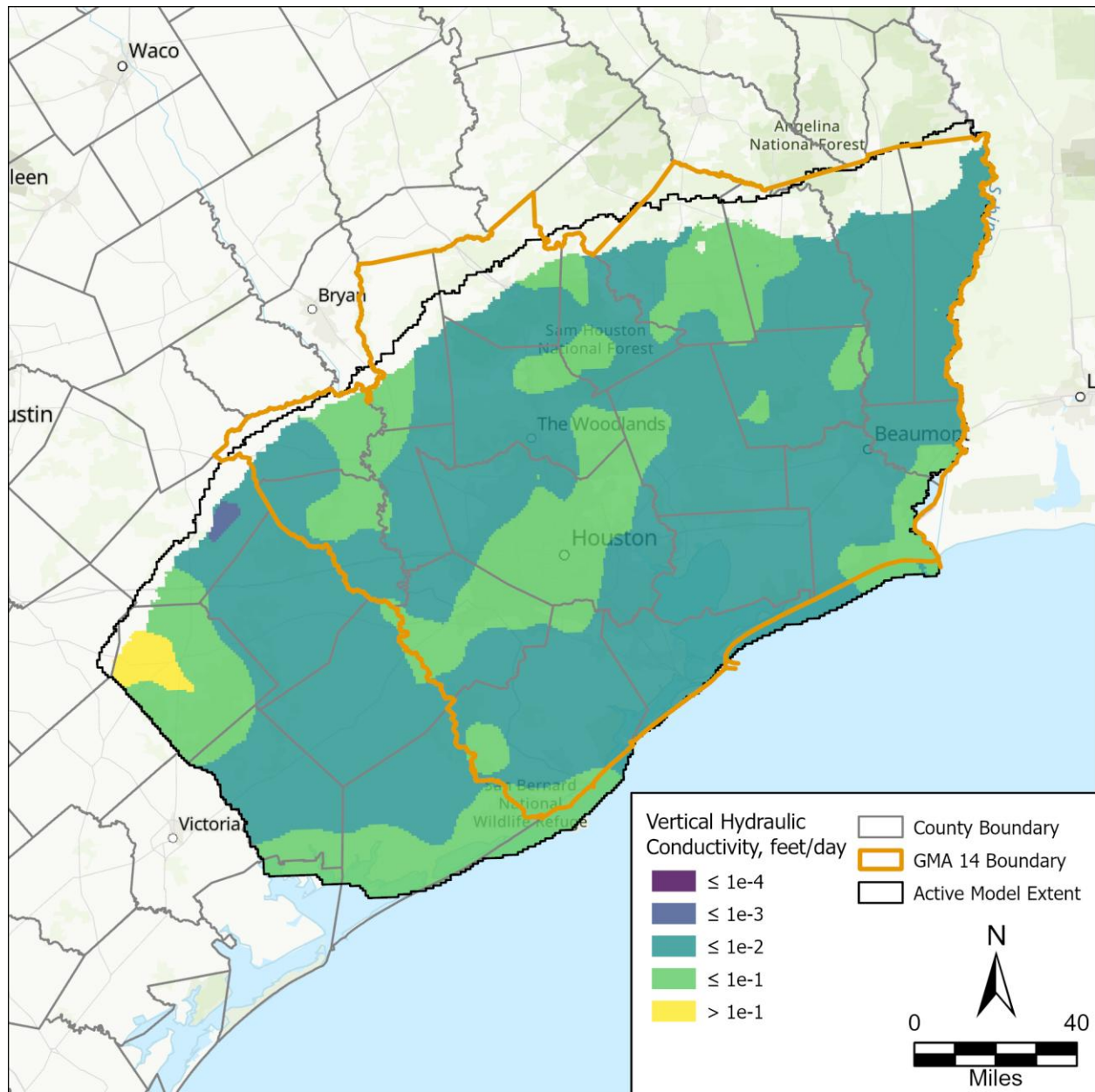


Figure 64. Calibrated layer 5 (Jasper Aquifer) vertical hydraulic conductivity.

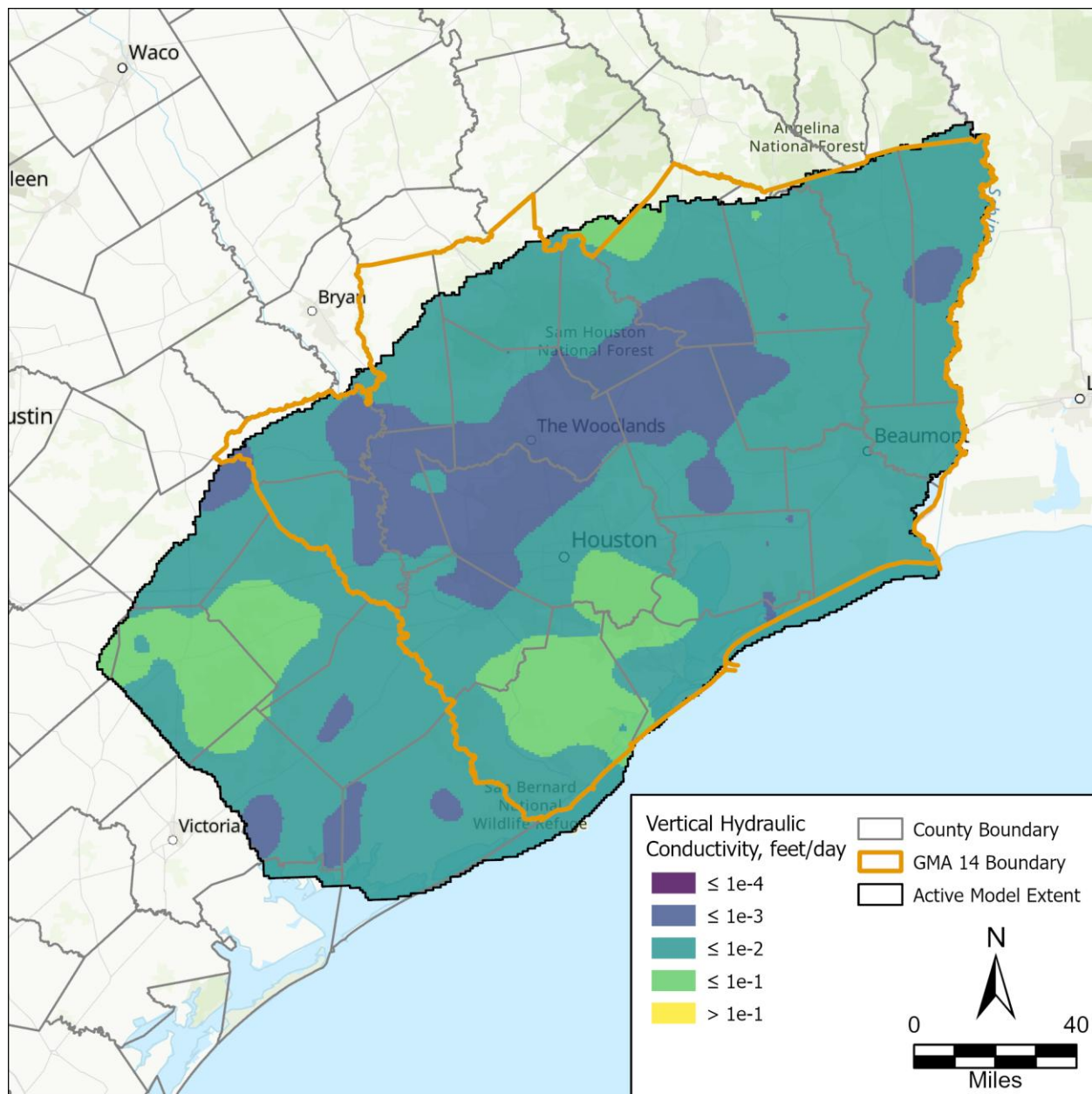


Figure 65. Calibrated layer 6 (Catahoula Aquifer) vertical hydraulic conductivity.

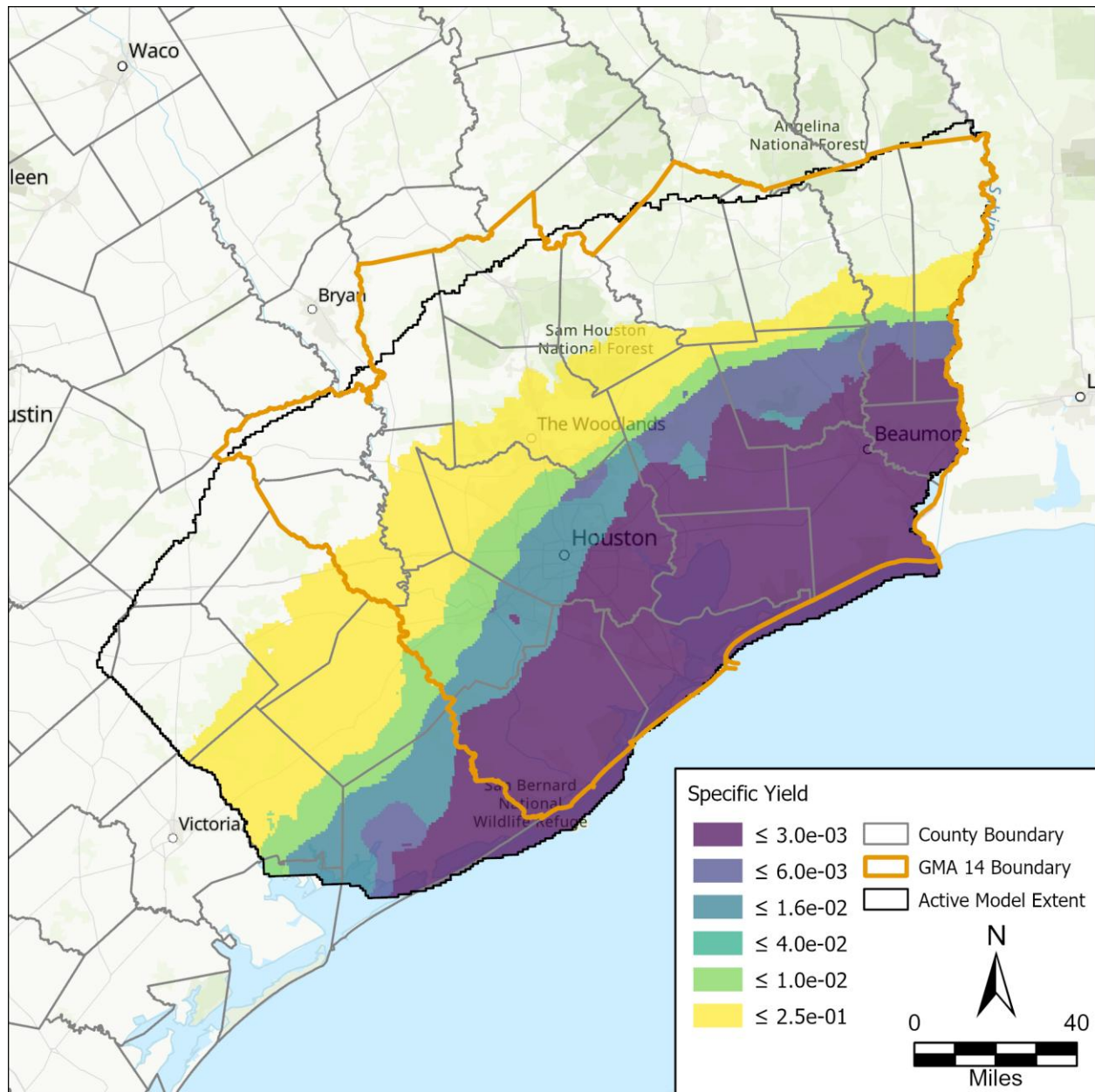


Figure 66. Layer 2 (Chicot Aquifer) calibrated specific yield.

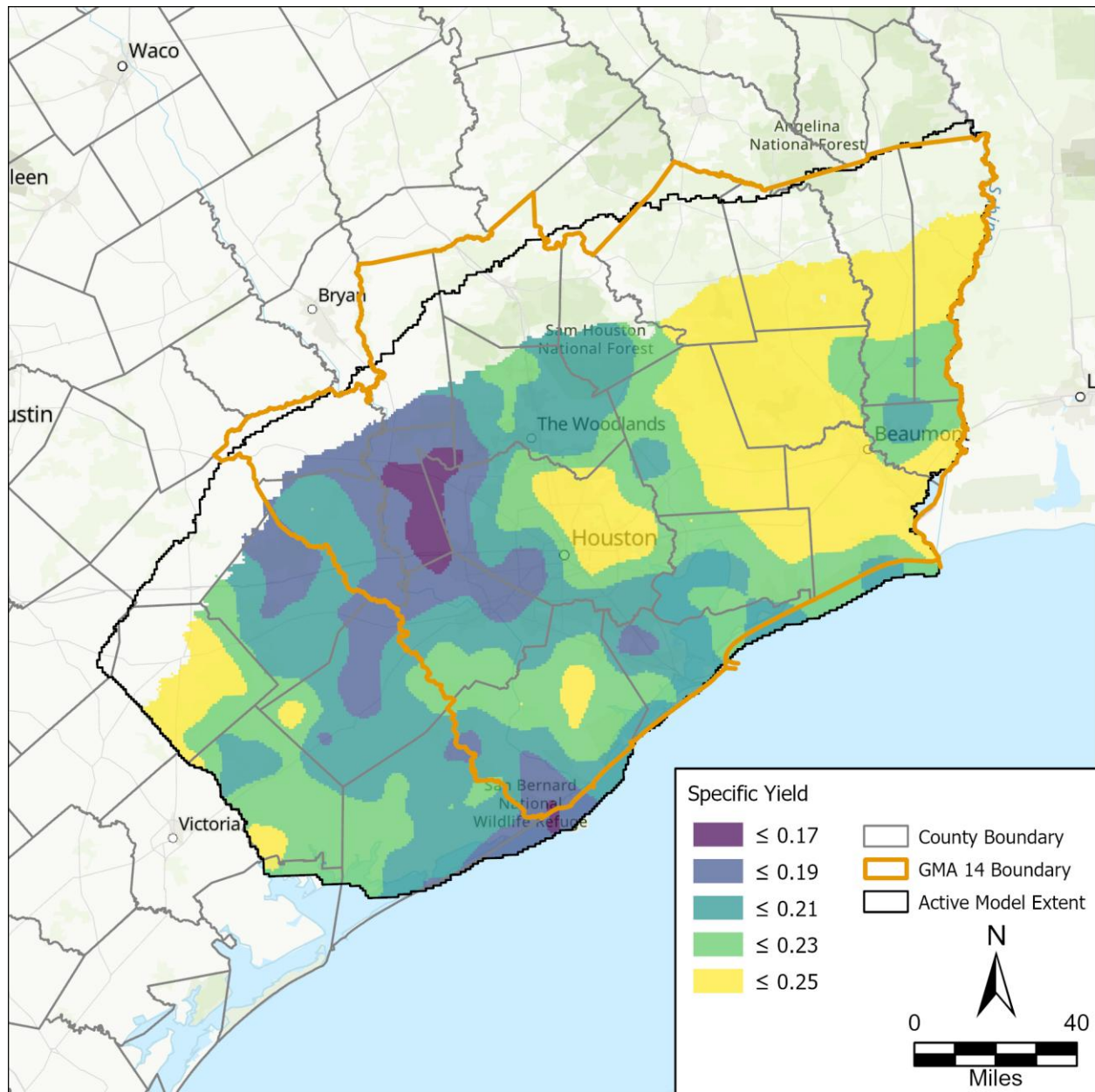


Figure 67. Layer 3 (Evangeline Aquifer) calibrated specific yield.

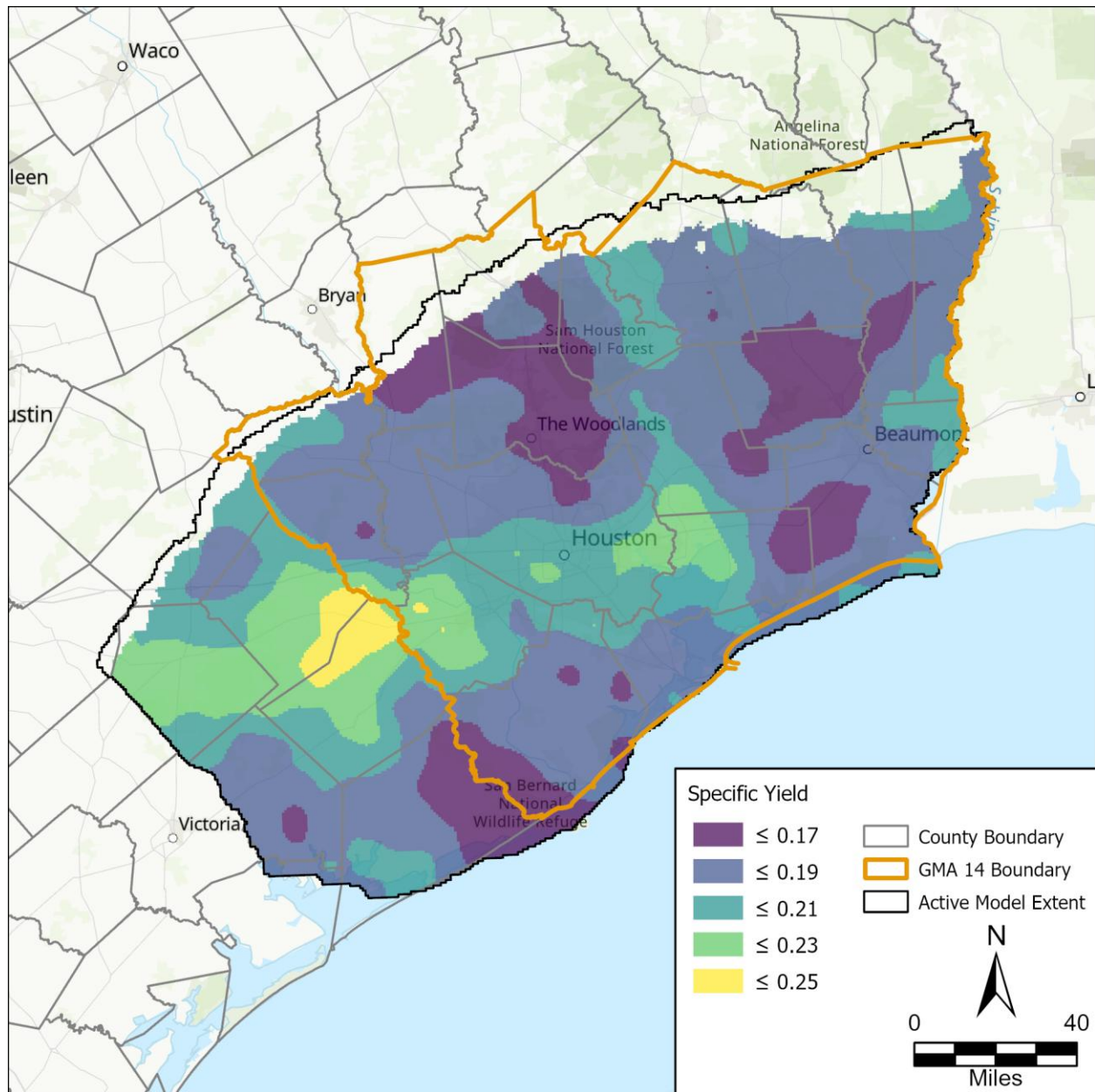


Figure 68. Layer 5 (Jasper Aquifer) calibrated specific yield.

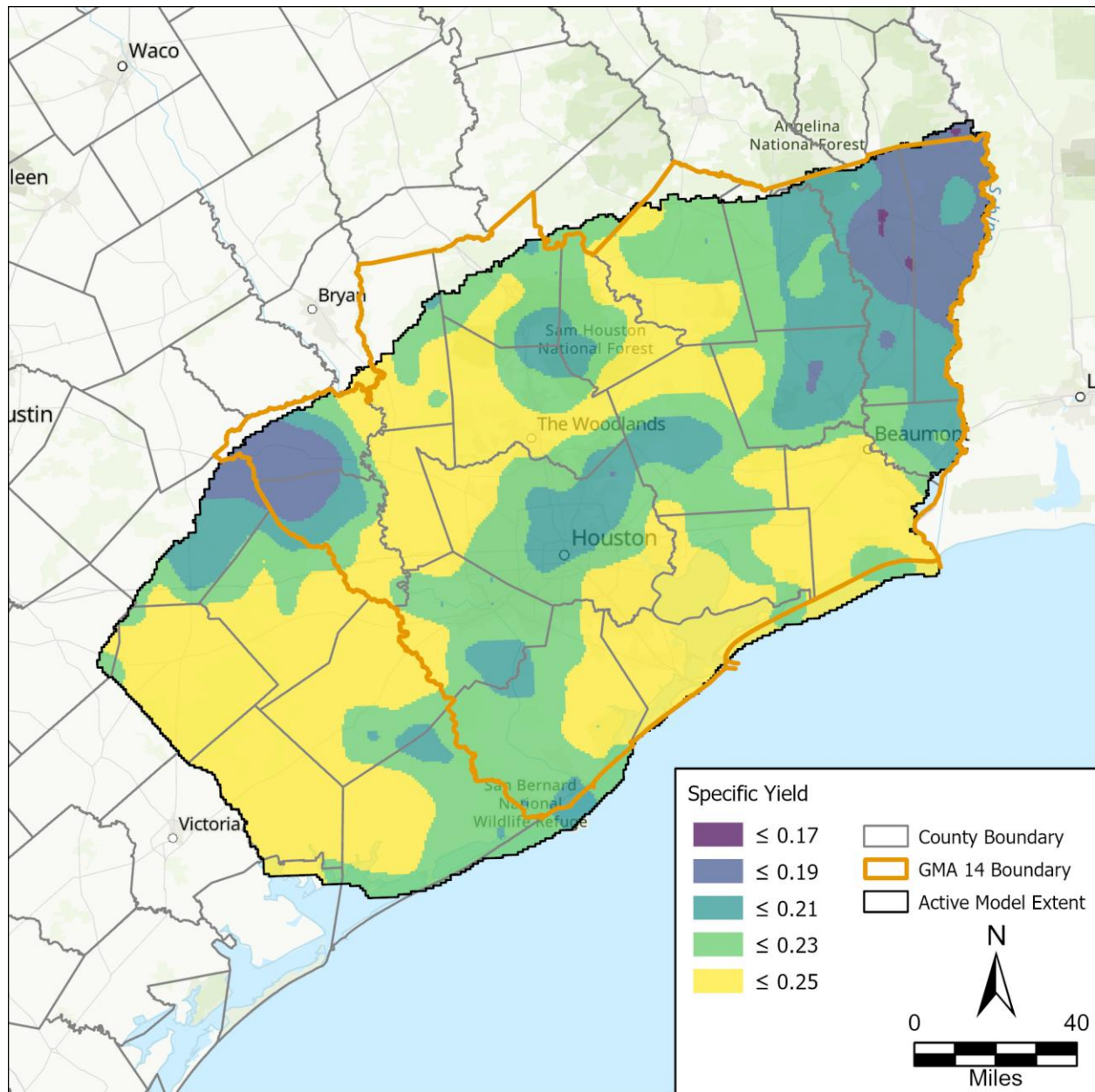


Figure 69. Layer 6 (Catahoula Aquifer) calibrated specific yield.

4.1.4. Calibration of Compaction (CSUB) Properties

We applied model-wide and pilot-point scale multipliers to interbed compaction properties for layers with interbeds. Table 11 summarizes the initial and calibrated base model statistics by layer for each interbed compaction property adjusted during calibration.

The interbed porosity varied using a multiplier range of 0.75 to 1.25. The model-wide mean increased in the Evangeline and decreased in the Chicot, Burkeville, and Jasper. Figures 70 through 72 illustrate the calibrated base model interbed porosity for each aquifer layer with interbeds. The Evangeline layer had the highest increase in areas in the northeast region, southwest regions, and Montgomery County.

The interbed elastic specific storage varied using a multiplier range of 0.15 to 5. The model-wide mean increased in the Burkeville and Jasper, decreased in the Evangeline, and the Chicot remained about the same. Figures 73 through 75 illustrate the calibrated base model interbed elastic specific storage for each aquifer layer with interbeds. The Chicot and Evangeline both had the most decrease in the shallowest depths and the most increase in the deeper depths. The Jasper layer values decreased with depth with the highest values around Montgomery and surrounding counties.

The interbed inelastic specific storage varied using a multiplier range of 0.15 to 5. The model-wide mean decreased in all layers. Figures 76 through 78 illustrate the calibrated base model interbed inelastic specific storage for each aquifer layer with interbeds. The Chicot had the highest changes in the deeper downdip regions of the model where values increased from the initial to the calibrated base model. Values within the Evangeline and Jasper aquifers predominantly decreased across the model domain during calibration. Values within the Evangeline are highest in Austin, Montgomery, and Harris counties with the lowest values in the northeastern region on the model. The Jasper had the highest values near the shallow depth and decreased with deeper depths.

The interbed vertical hydraulic conductivity varied using a multiplier range of 0.1 to 10. The model-wide mean increased in the Evangeline and Burkeville and decreased in the Chicot and Jasper. Figures 79 through 81 illustrate the calibrated base model interbed vertical hydraulic conductivity for each aquifer layer with interbeds. Values within the Chicot were highest in the eastern region of the model and were consistent across the remainder of the model area. The Evangeline had the highest values in the northeastern region of the model with the lowest values near the deeper regions near the Gulf of Mexico. The Jasper had the lowest overall mean value between the layers. Values within the Jasper were highest where the depths were shallow and increased with increased depth.

Table 11. Initial and calibrated interbed compaction properties statistics by layer.

Interbed Compaction Property	Layer	Initial			Calibrated Base Model		
		Min	Max	Mean	Min	Max	Mean
Porosity	2	0.33	0.45	0.37	0.18	0.47	0.31
	3	0.27	0.45	0.33	0.21	0.60	0.44
	4	0.26	0.45	0.31	0.10	0.44	0.24
	5	0.26	0.45	0.30	0.09	0.41	0.23
Elastic Specific Storage	2	1.33E-05	3.49E-05	2.08E-05	3.48E-06	7.53E-05	2.04E-05
	3	3.29E-06	3.49E-05	1.27E-05	8.45E-07	3.65E-05	5.79E-06
	4	3.29E-06	3.49E-05	9.93E-06	6.48E-07	5.00E-05	1.16E-05
	5	3.29E-06	3.49E-05	8.67E-06	3.69E-06	3.04E-04	5.45E-05
Inelastic Specific Storage	2	6.50E-05	1.79E-04	1.04E-04	5.79E-06	1.55E-04	5.53E-05
	3	1.21E-05	1.79E-04	6.20E-05	1.71E-06	9.42E-05	1.64E-05
	4	1.21E-05	1.79E-04	4.71E-05	1.00E-07	8.57E-06	1.43E-06
	5	1.21E-05	1.79E-04	4.05E-05	7.55E-07	9.78E-05	1.52E-05
Vertical Hydraulic Conductivity	2	7.13E-06	1.27E-05	1.00E-05	2.50E-07	2.80E-05	6.45E-06
	3	1.60E-06	1.27E-05	6.30E-06	2.27E-07	1.46E-04	1.35E-05
	4	9.92E-07	1.27E-05	4.80E-06	1.23E-07	1.88E-04	1.93E-05
	5	9.92E-07	1.27E-05	4.06E-06	8.14E-09	4.78E-06	2.95E-07

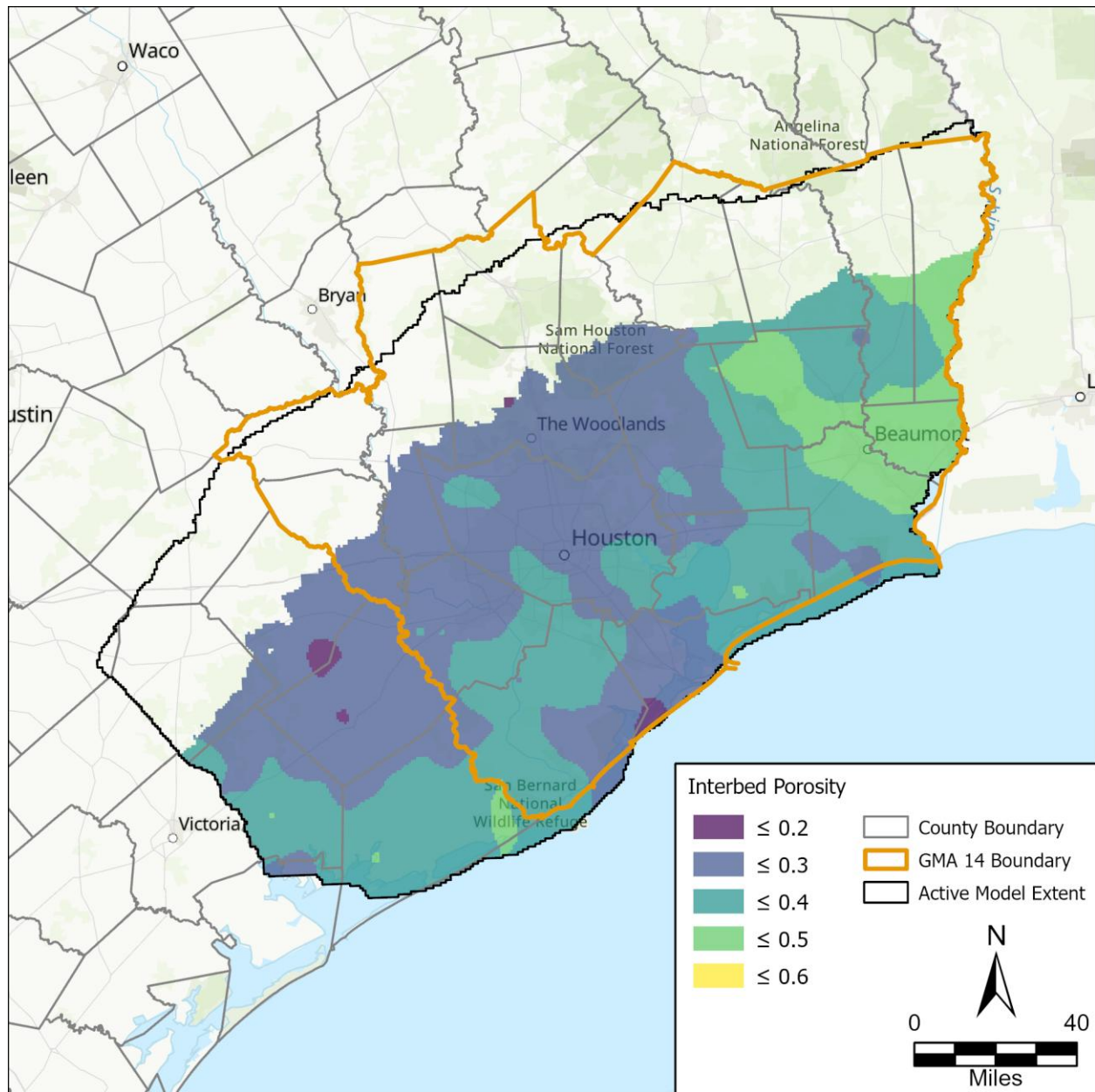


Figure 70. Layer 2 (Chicot Aquifer) calibrated interbed porosity.

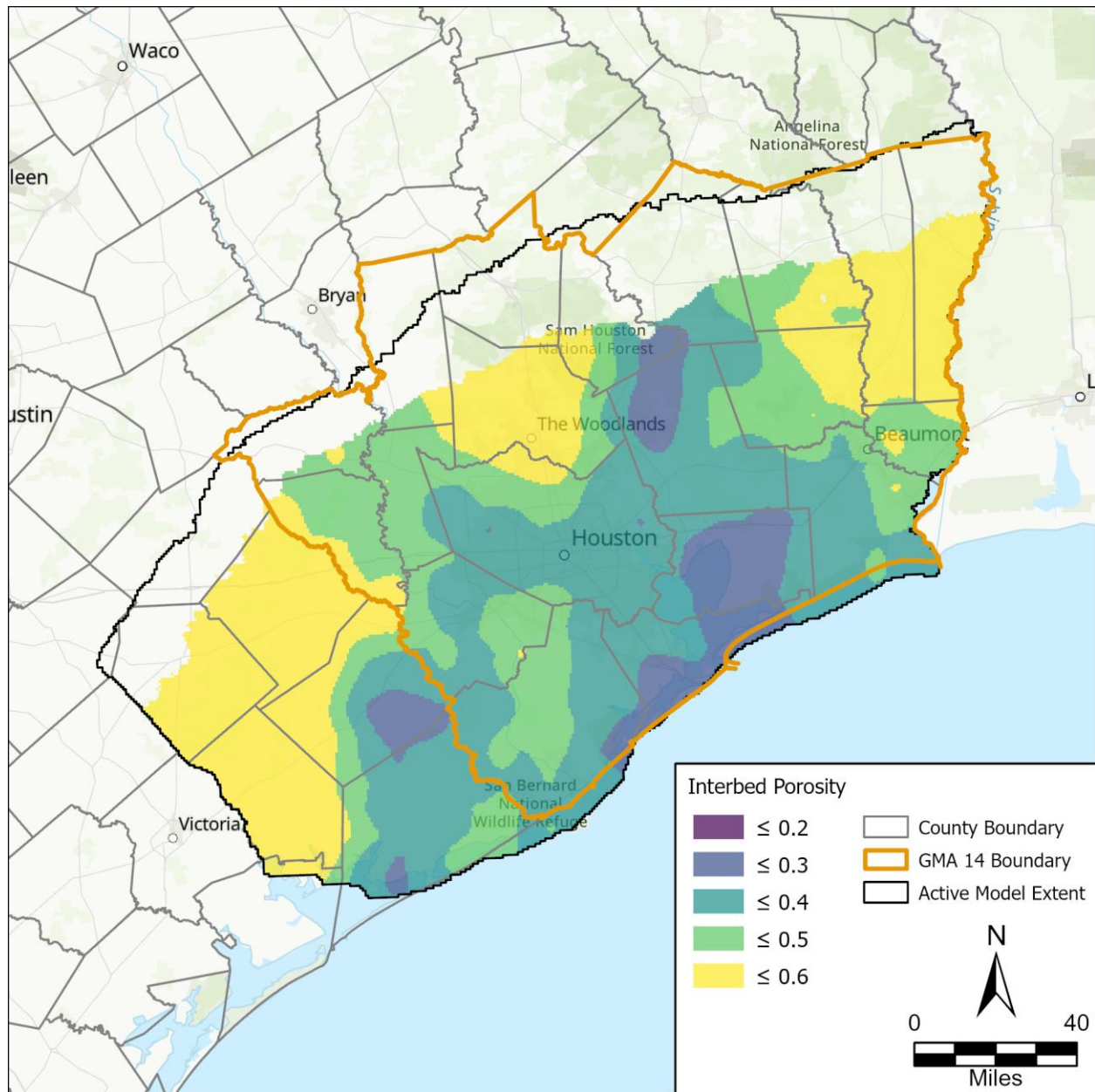


Figure 71. Layer 3 (Evangeline Aquifer) calibrated interbed porosity.

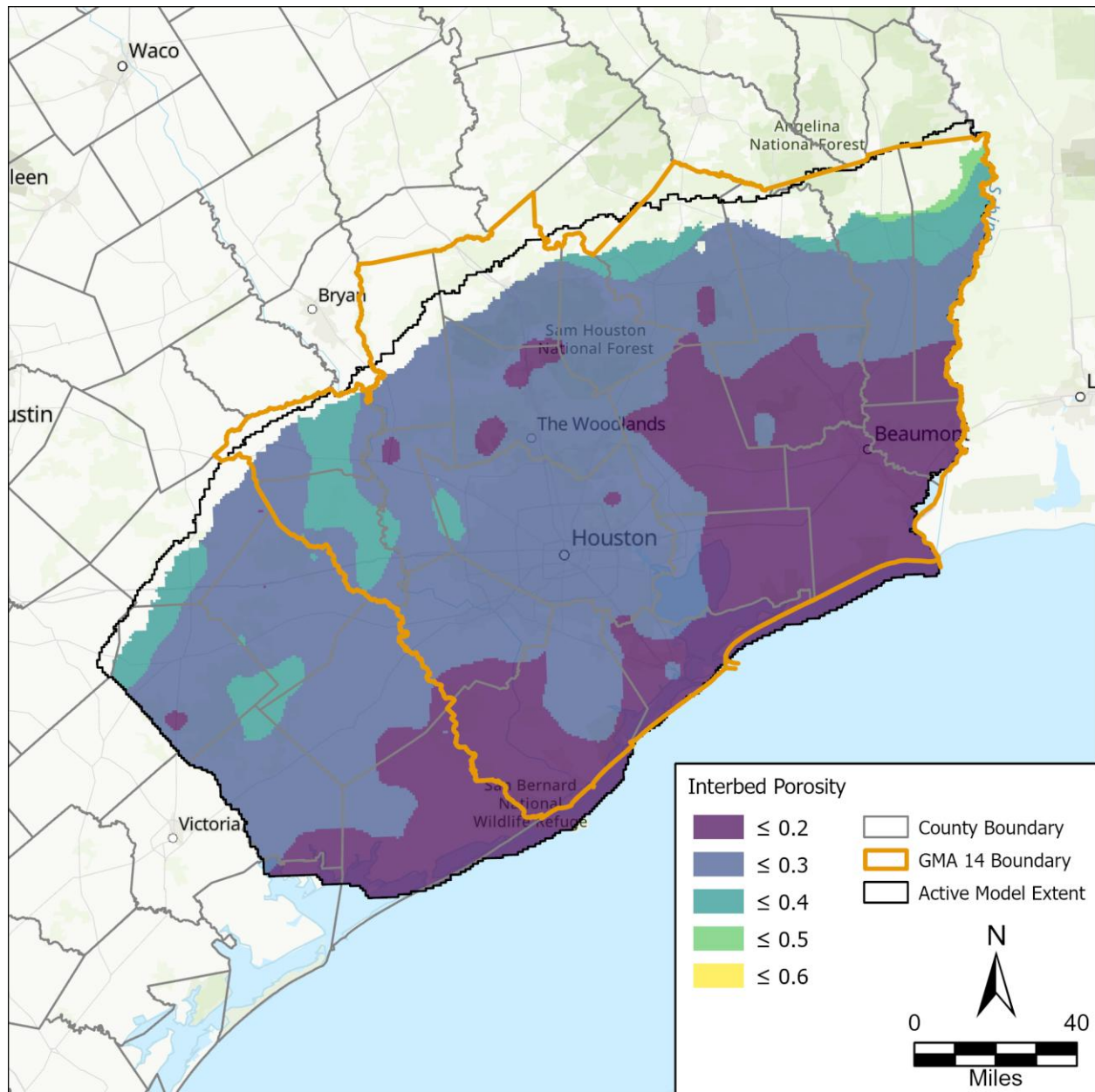


Figure 72. Layer 5 (Jasper Aquifer) calibrated interbed porosity.

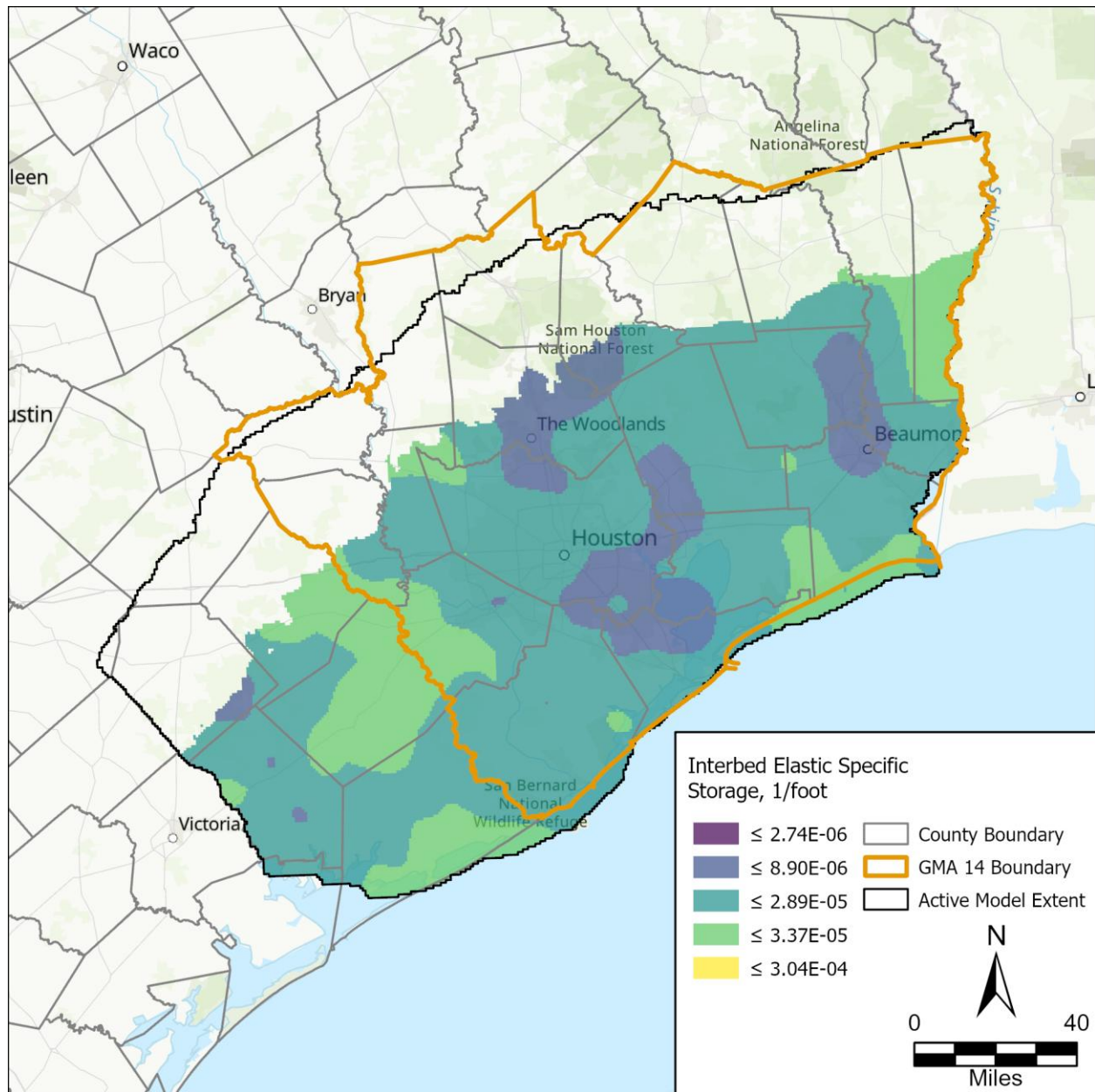


Figure 73. Layer 2 (Chicot Aquifer) calibrated interbed elastic specific storage.

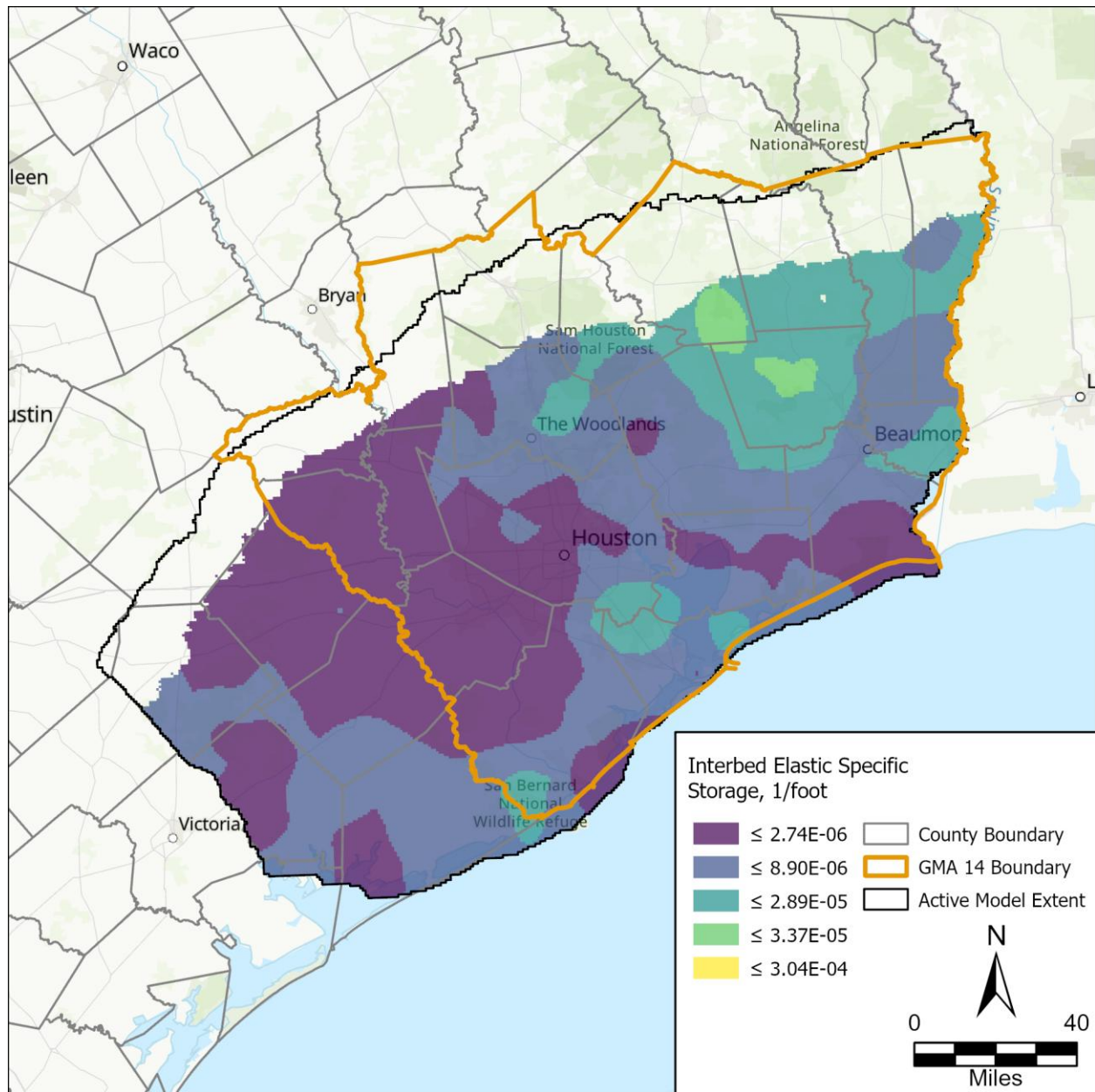


Figure 74. Layer 3 (Evangeline Aquifer) calibrated interbed elastic specific storage.

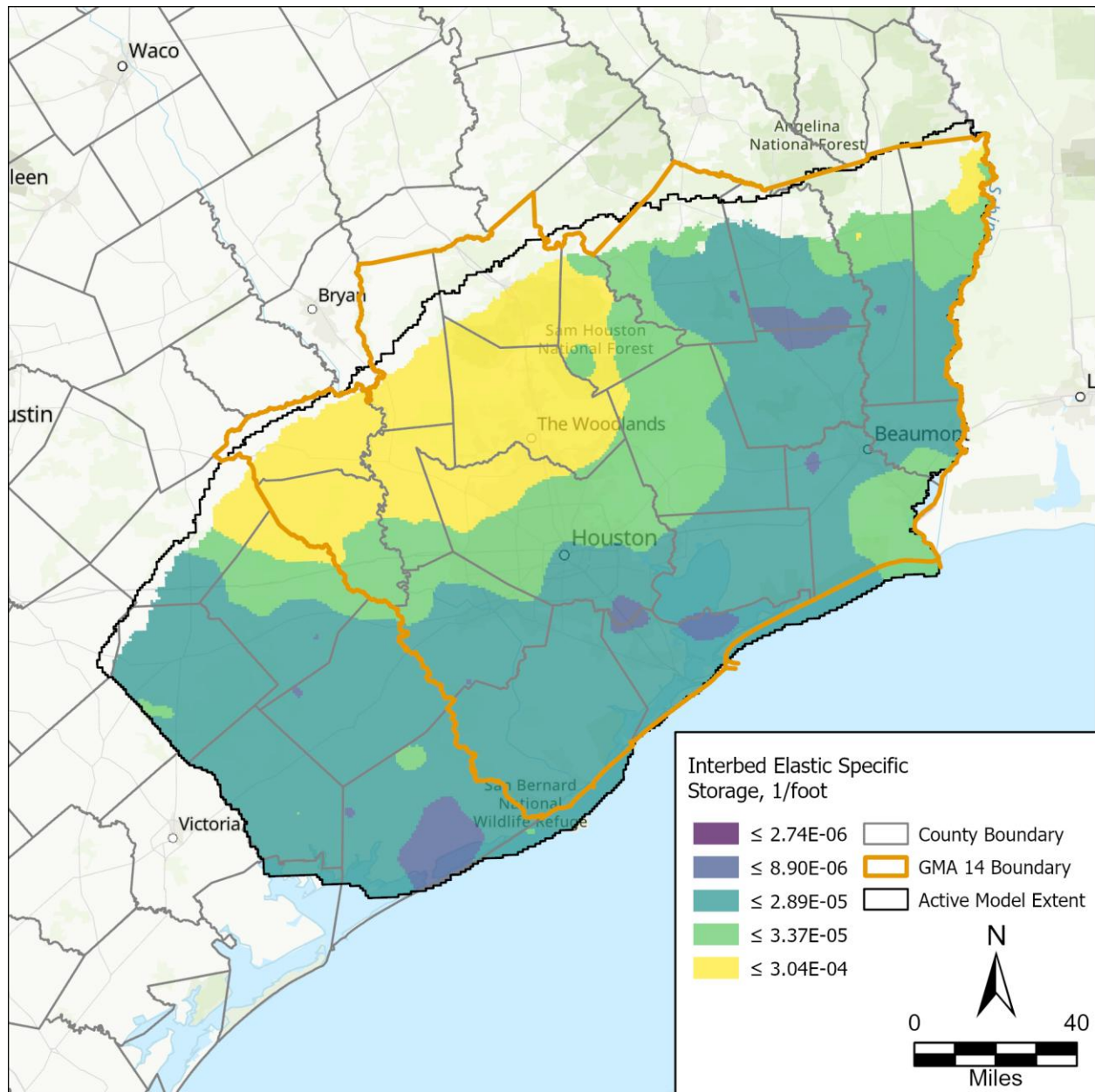


Figure 75. Layer 5 (Jasper Aquifer) calibrated interbed elastic specific storage.

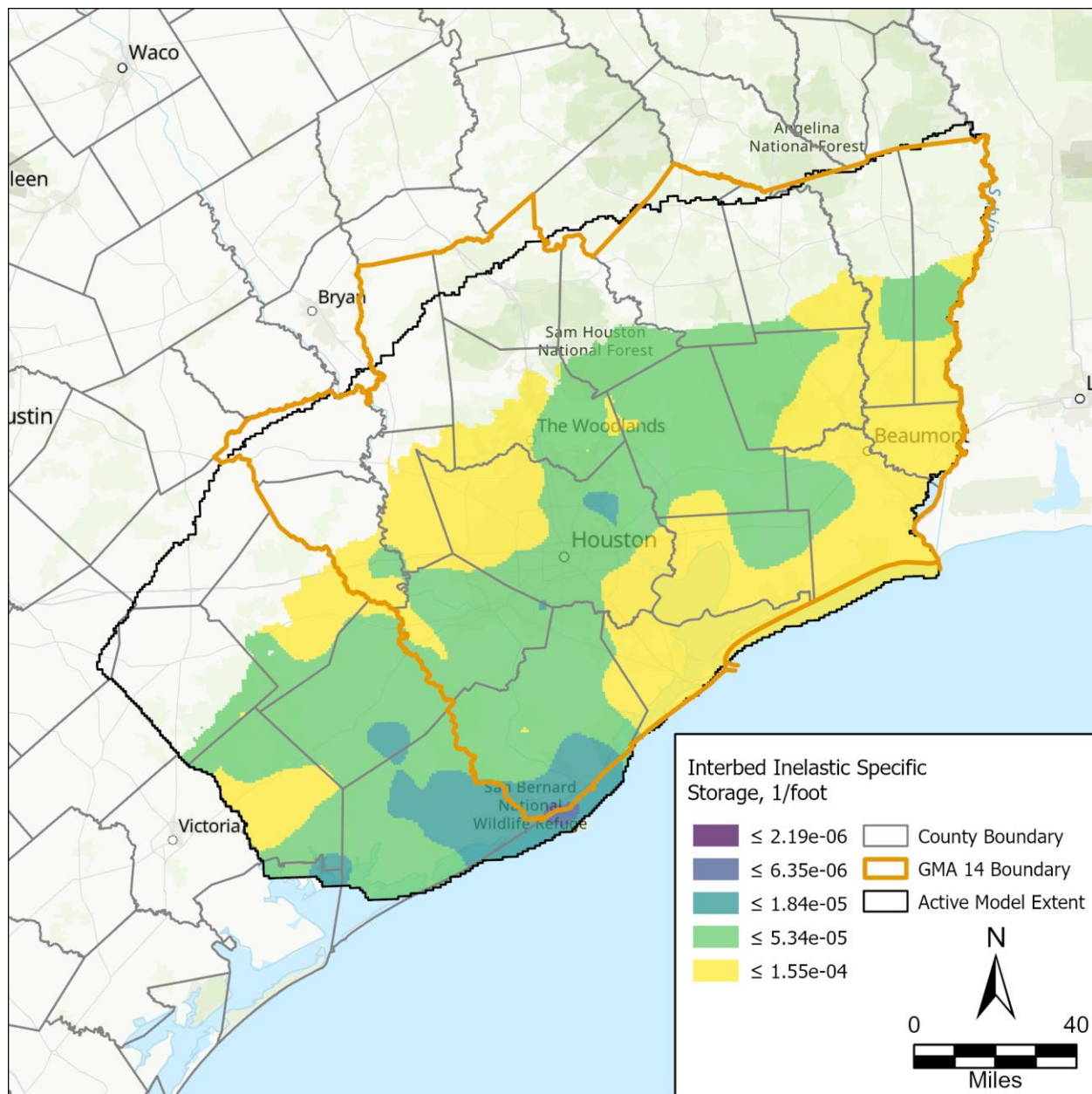


Figure 76. Layer 2 (Chicot Aquifer) calibrated interbed inelastic specific storage.

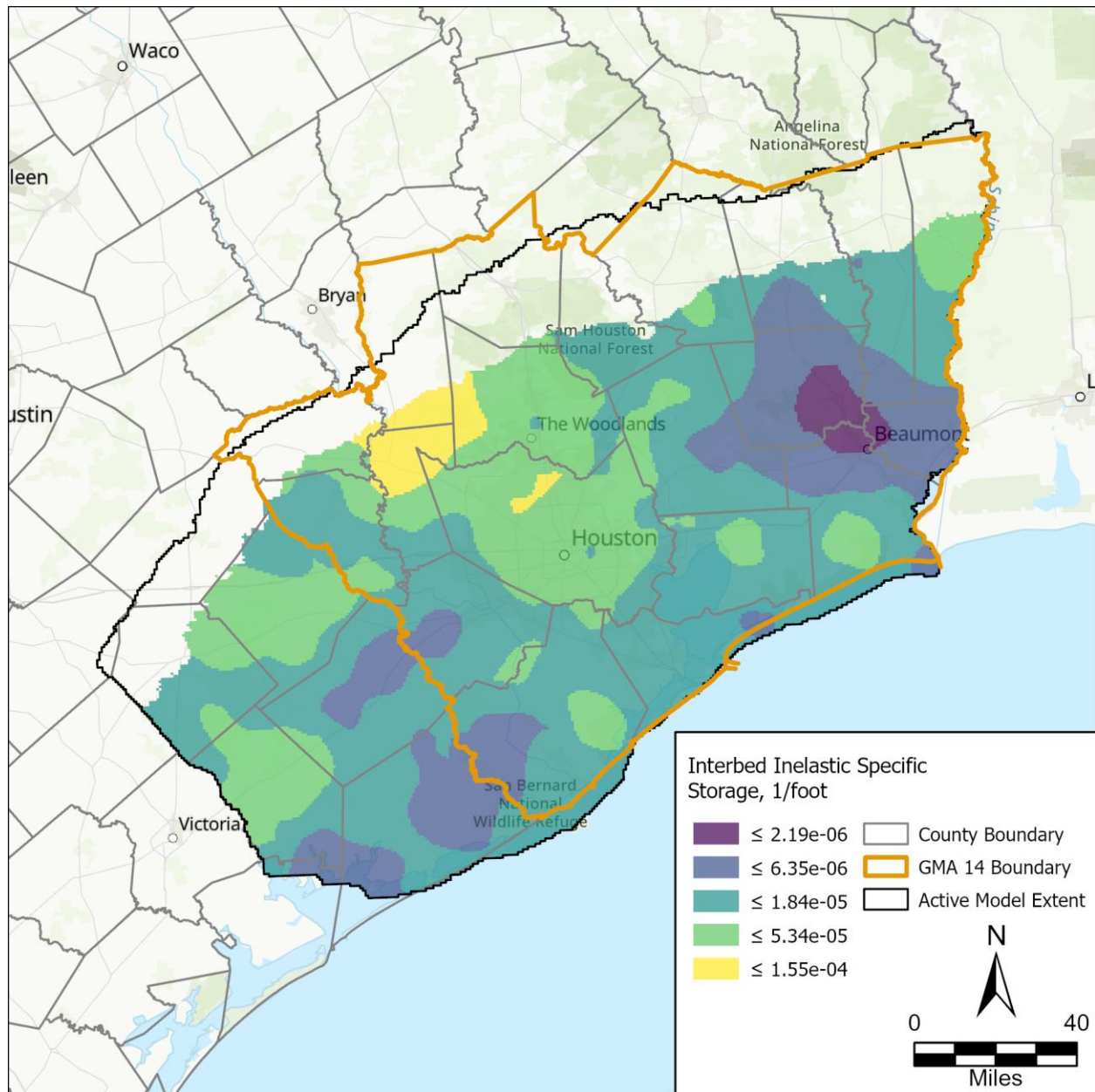


Figure 77. Layer 3 (Evangeline Aquifer) calibrated interbed inelastic specific storage.

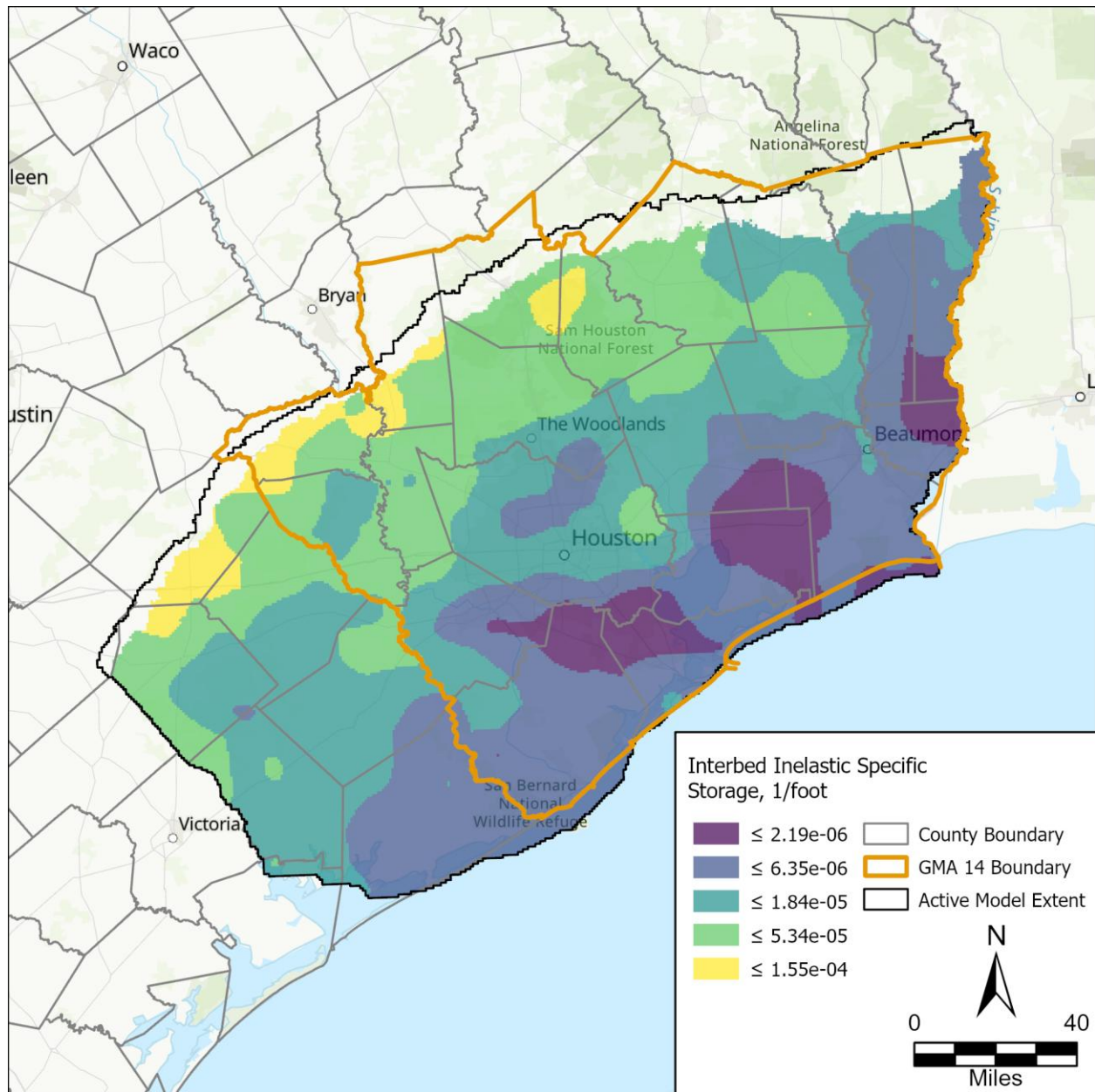


Figure 78. Layer 5 (Jasper Aquifer) calibrated interbed inelastic specific storage.

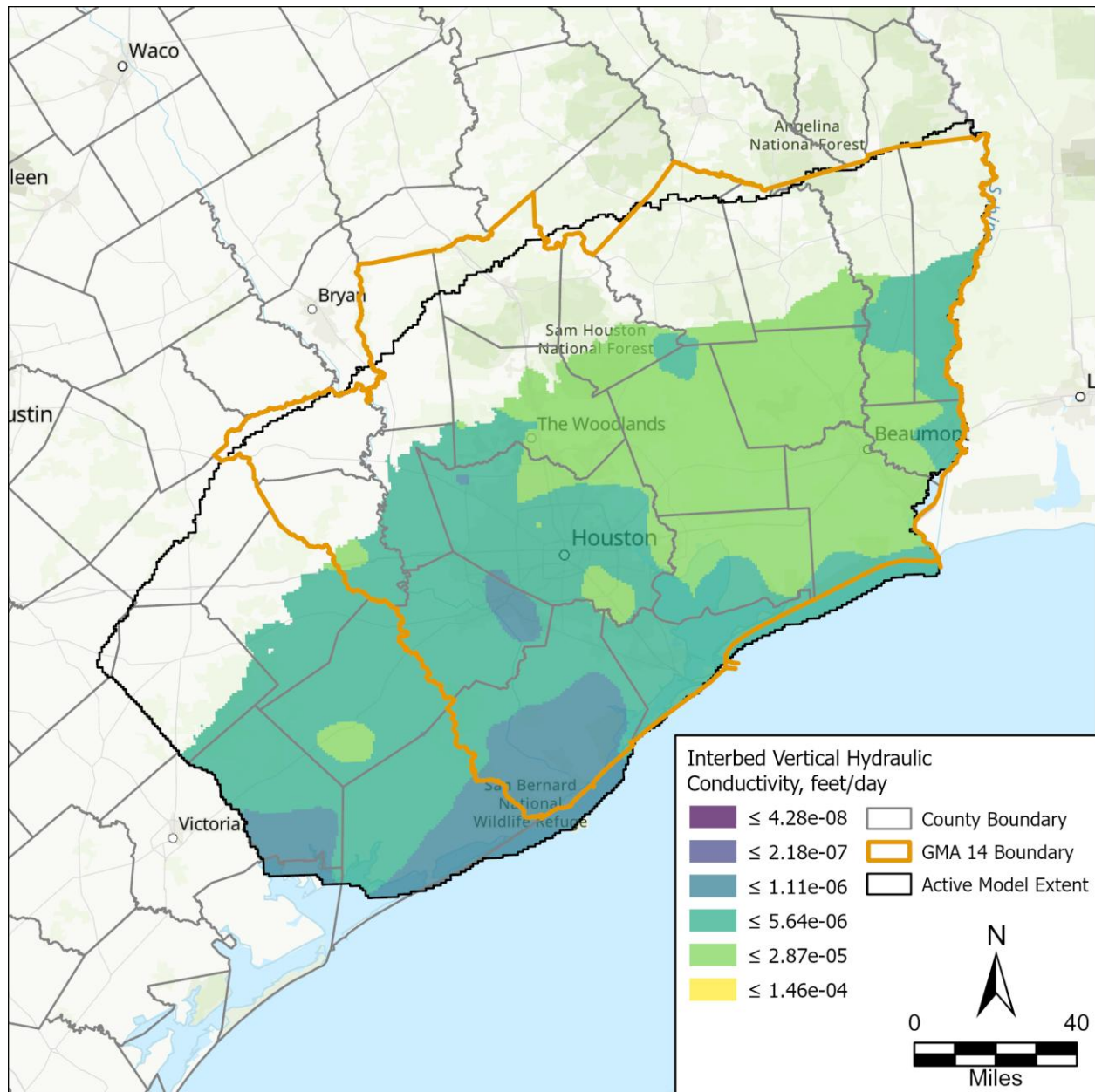


Figure 79. Layer 2 (Chicot Aquifer) calibrated interbed vertical hydraulic conductivity.

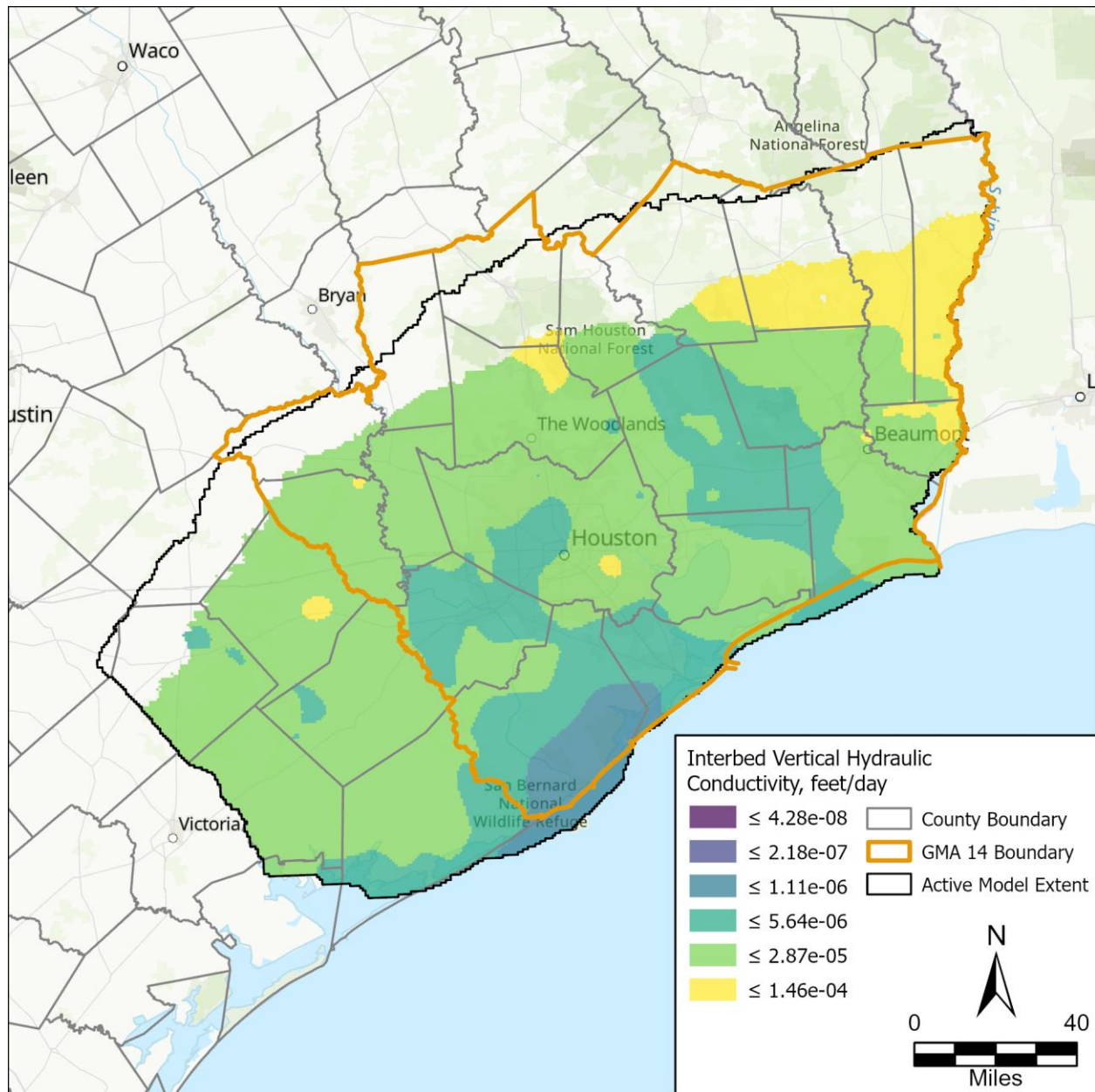


Figure 80. Layer 3 (Evangeline Aquifer) calibrated interbed vertical hydraulic conductivity.

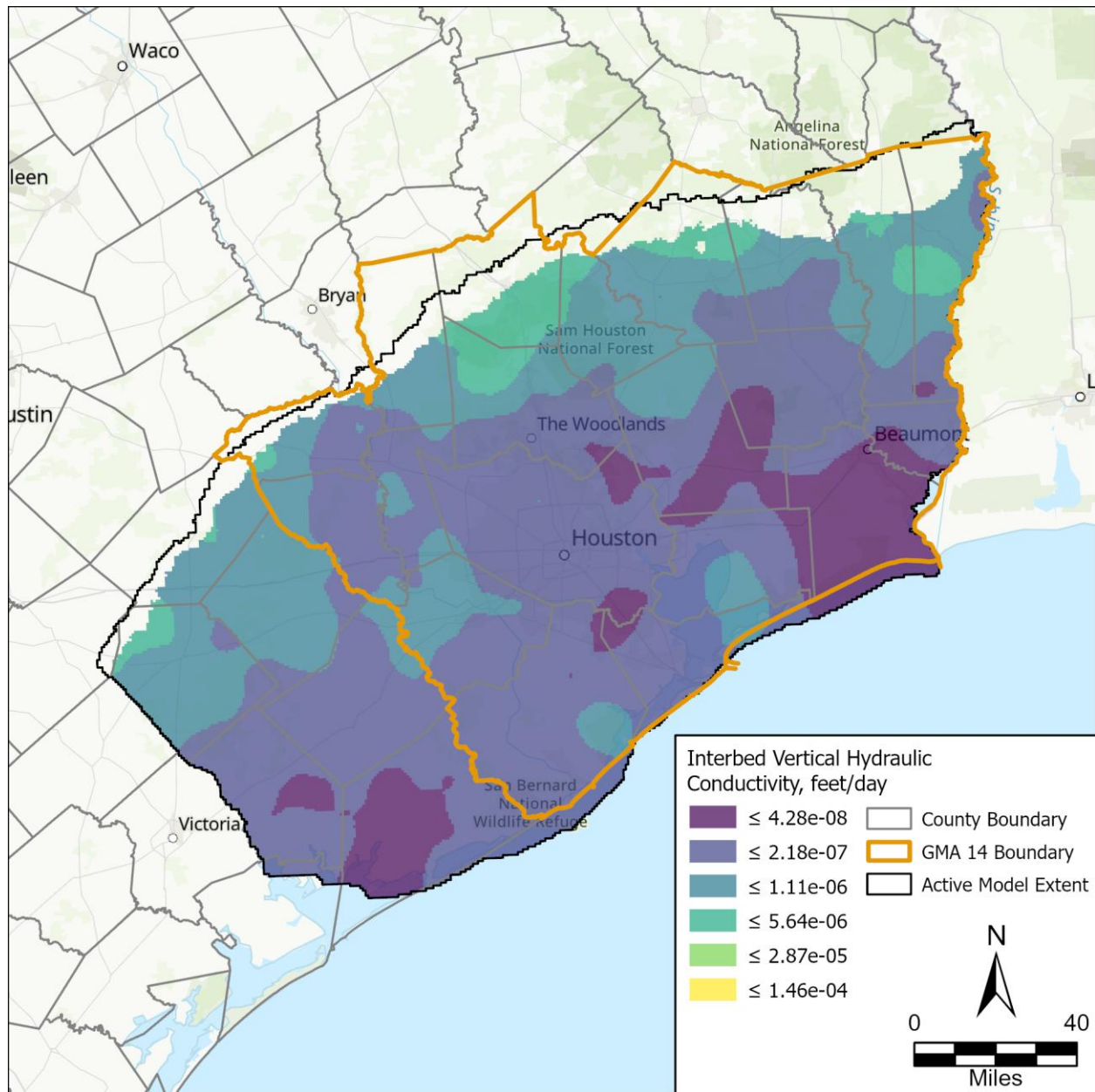


Figure 81. Layer 5 (Jasper Aquifer) calibrated interbed vertical hydraulic conductivity.

Model-wide and pilot-point scale multipliers were applied to coarse-grained storage properties for all layers during calibration. Table 12 summarizes the initial and calibrated base model statistics by layer for each coarse-grained storage property adjusted during calibration.

The coarse-grained elastic specific storage varied using a multiplier range of 0.1 to 10. The model-wide mean increased in the Chicot and Burkeville, decreased in the Evangeline, and stayed about the same as the initial values in the Jasper. Figures 82 through 85 illustrate the calibrated base model coarse-grained elastic specific storage for each aquifer. The coarse-grained elastic storage within the Chicot had the highest increase in central and southeastern Harris County.

The coarse-grained porosity varied using a multiplier range of 0.1 to 10. The model-wide mean increased in the shallow aquifer system, Burkeville, and Catahoula and decreased in the remaining layers. Overall, the mean calibrated values per layer are within 0.03 of the initial mean values. Figures 86 through 89 illustrate the calibrated base model coarse-grained porosity for each aquifer layer.

Table 12. Initial and calibrated coarse-grained storage properties by layer.

Coarse-Grained Storage Property	Layer	Initial			Calibrated Base Model		
		Min	Max	Mean	Min	Max	Mean
Elastic Specific Storage	1	9.20E-07	9.20E-07	9.20E-07	8.57E-08	7.49E-06	1.02E-06
	2	9.20E-07	9.20E-07	9.20E-07	6.45E-08	5.88E-06	1.13E-06
	3	9.20E-08	9.20E-08	9.20E-08	1.71E-09	1.68E-07	3.17E-08
	4	9.20E-07	9.20E-07	9.20E-07	4.51E-07	4.16E-05	4.52E-06
	5	9.20E-07	9.20E-07	9.20E-07	9.48E-08	5.56E-06	9.02E-07
	6	9.20E-07	9.20E-07	9.20E-07	5.57E-08	4.18E-06	4.11E-07
Porosity	1	0.15	0.15	0.15	0.10	0.16	0.12
	2	0.15	0.15	0.15	0.14	0.22	0.17
	3	0.15	0.15	0.15	0.14	0.22	0.18
	4	0.15	0.15	0.15	0.10	0.16	0.13
	5	0.15	0.15	0.15	0.12	0.19	0.16
	6	0.15	0.15	0.15	0.10	0.17	0.13

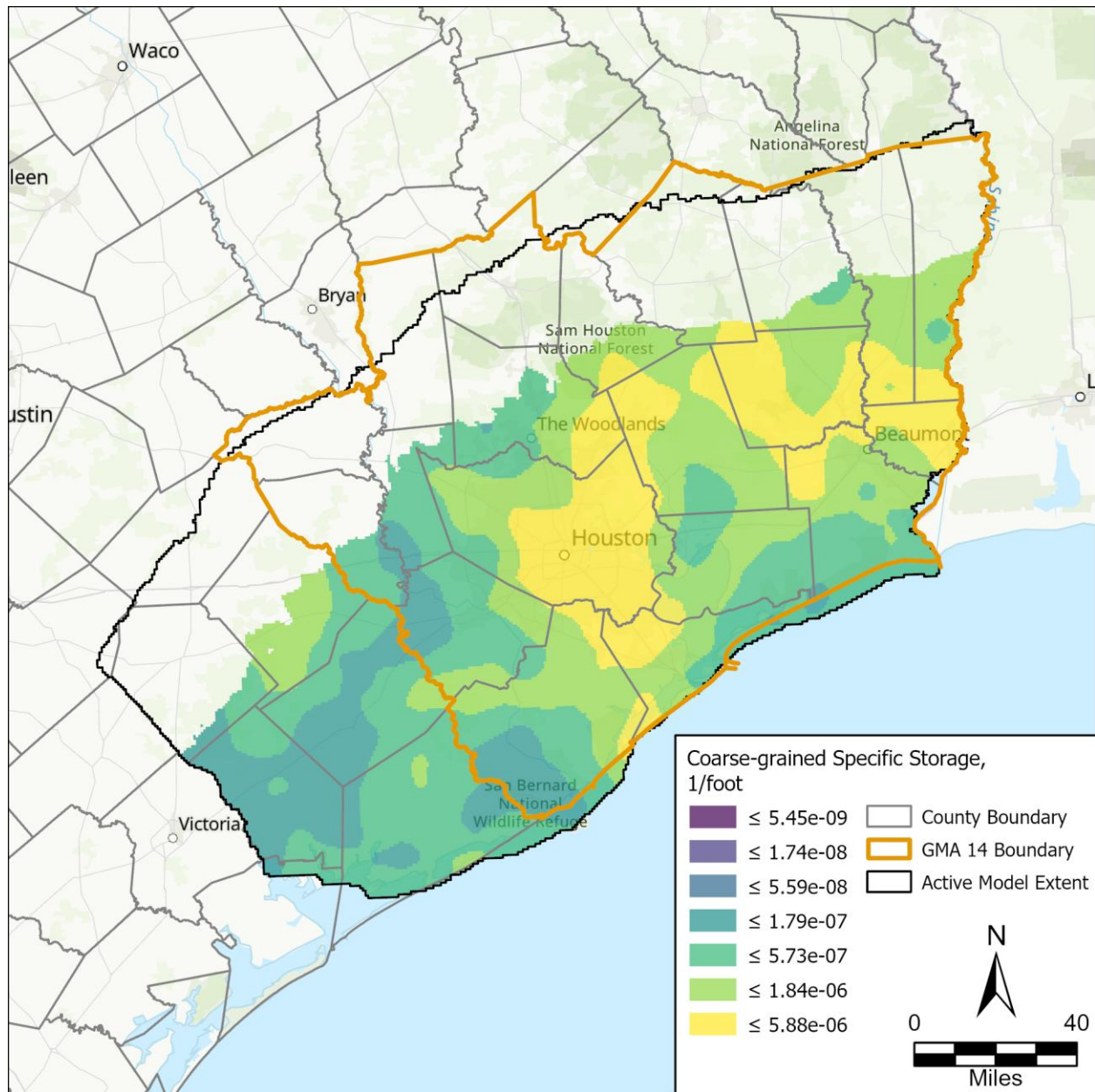


Figure 82. Layer 2 (Chicot Aquifer) calibrated coarse-grained elastic specific storage.

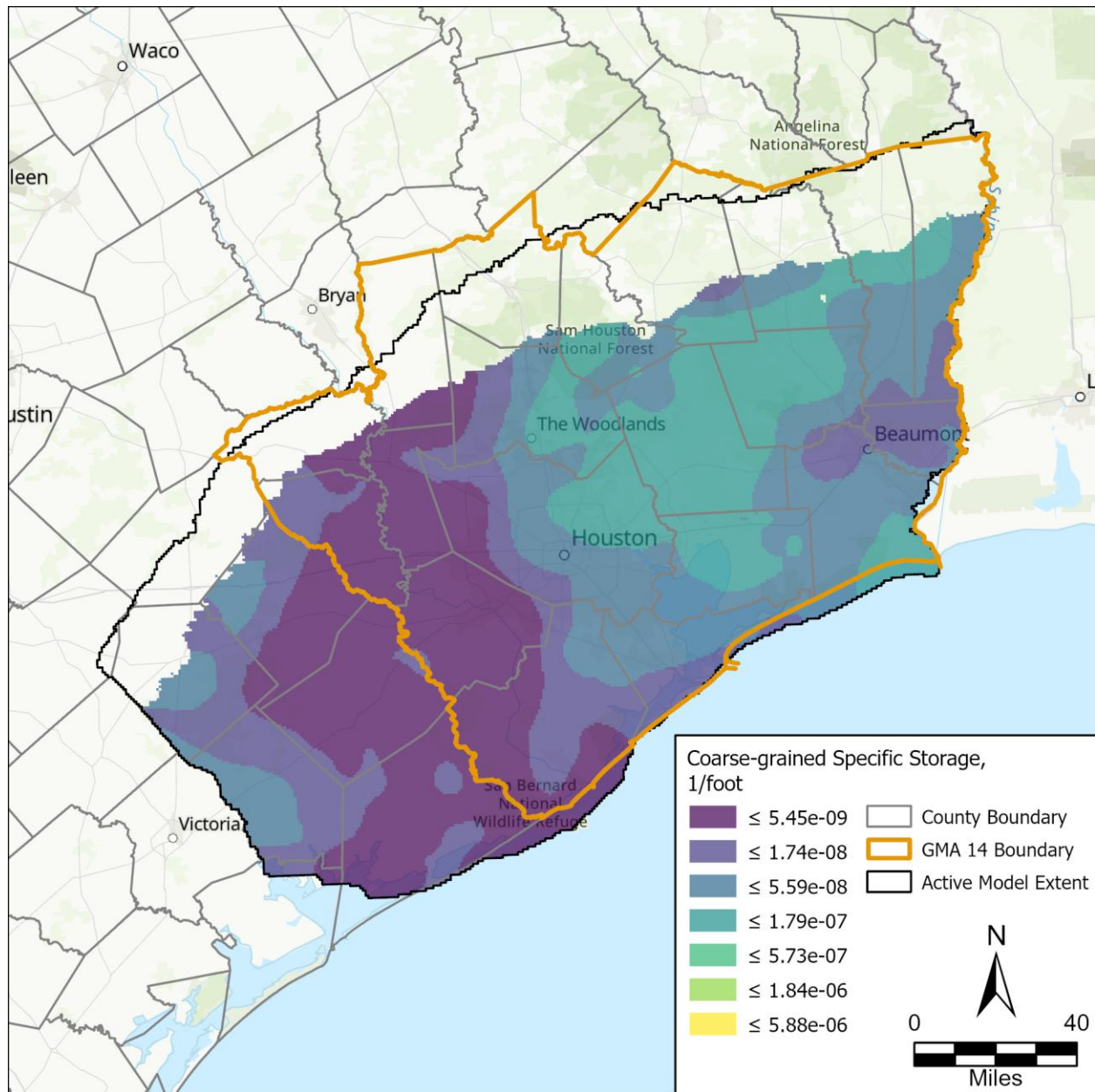


Figure 83. Layer 3 (Evangeline Aquifer) calibrated coarse-grained elastic specific storage.

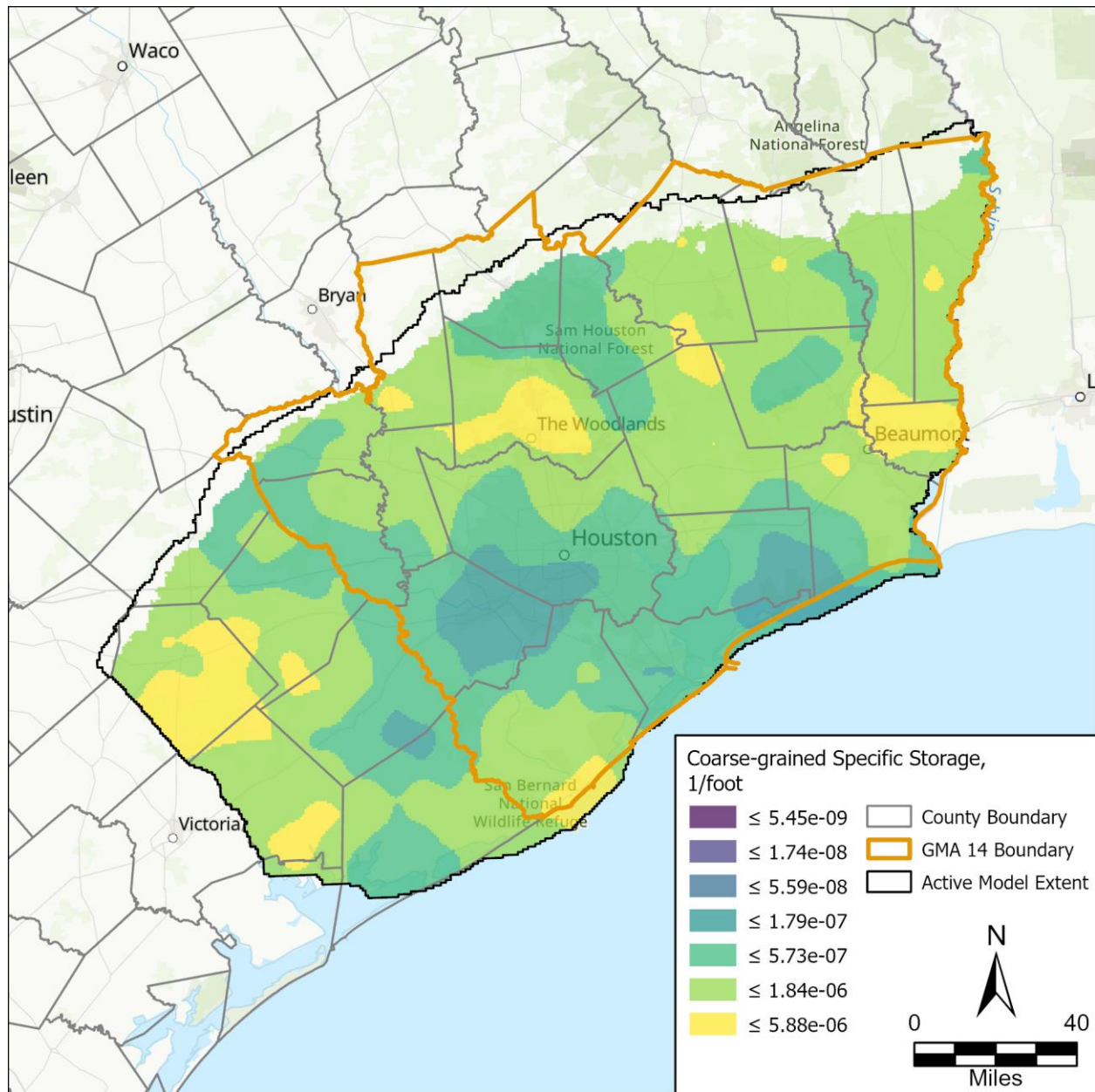


Figure 84. Layer 5 (Jasper Aquifer) calibrated coarse-grained elastic specific storage.

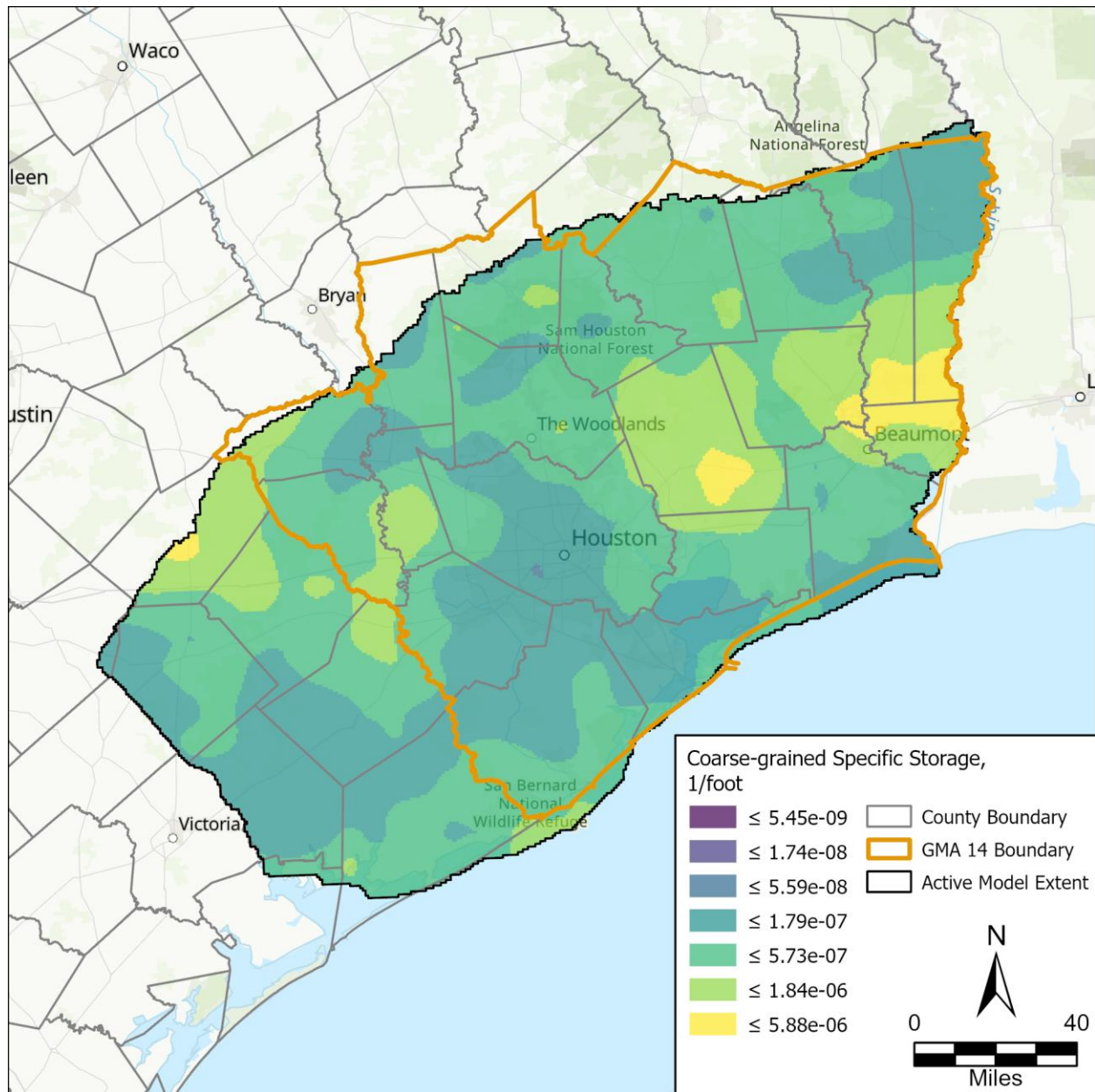


Figure 85. Layer 6 (Catahoula Aquifer) calibrated coarse-grained elastic specific storage.

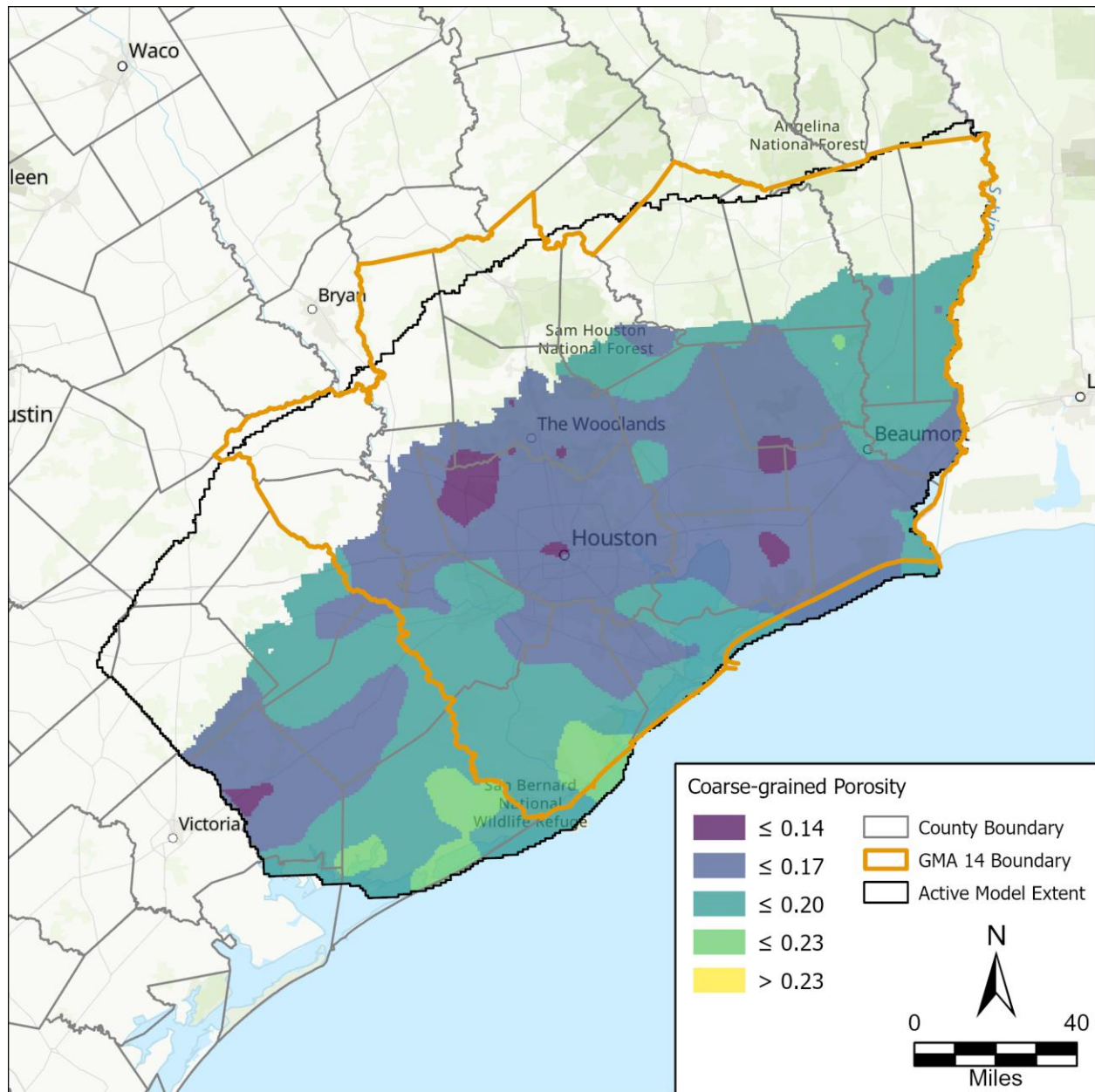


Figure 86. Layer 2 (Chicot Aquifer) calibrated coarse-grained porosity.

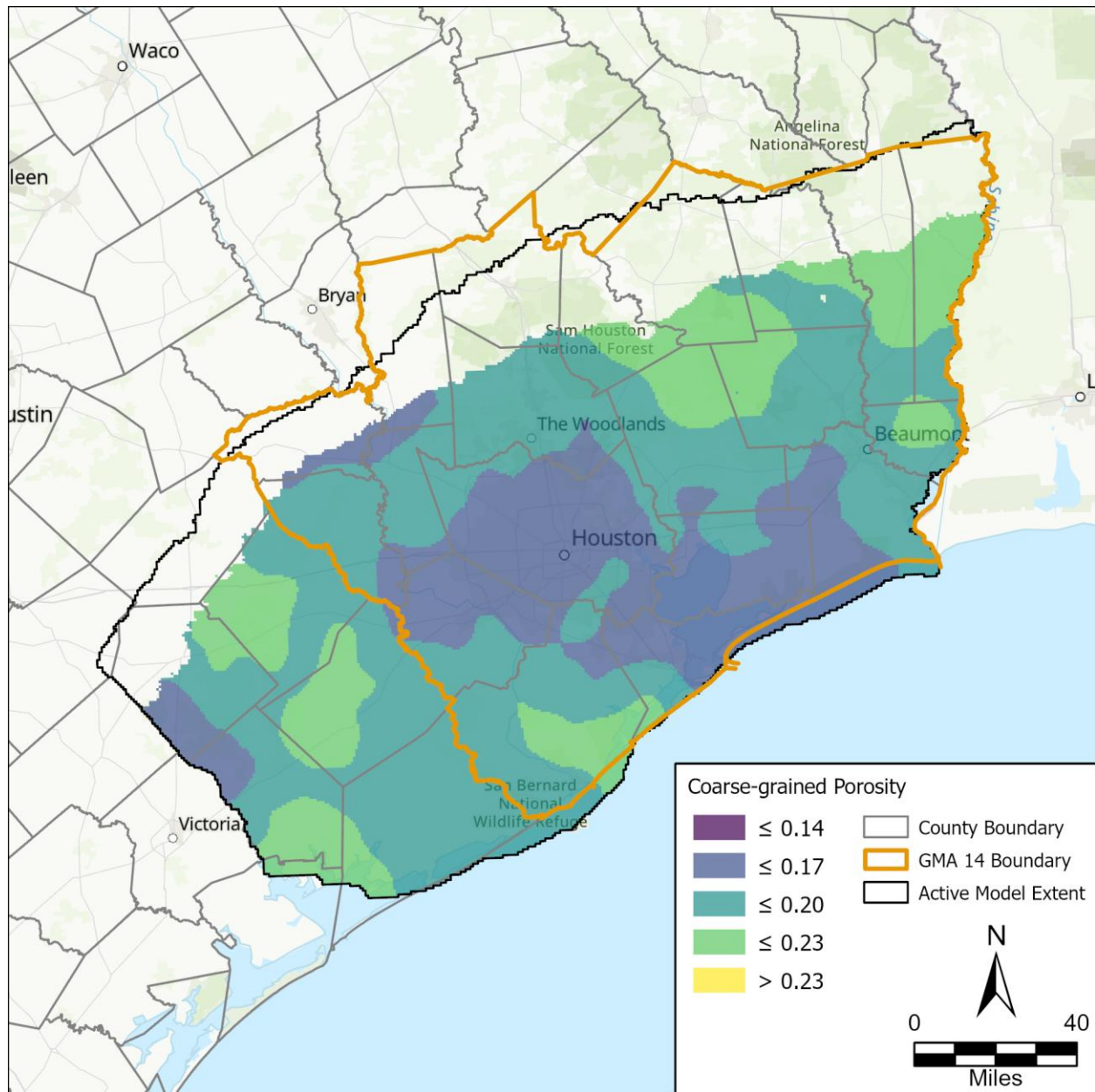


Figure 87. Layer 3 (Evangeline Aquifer) calibrated coarse-grained porosity.

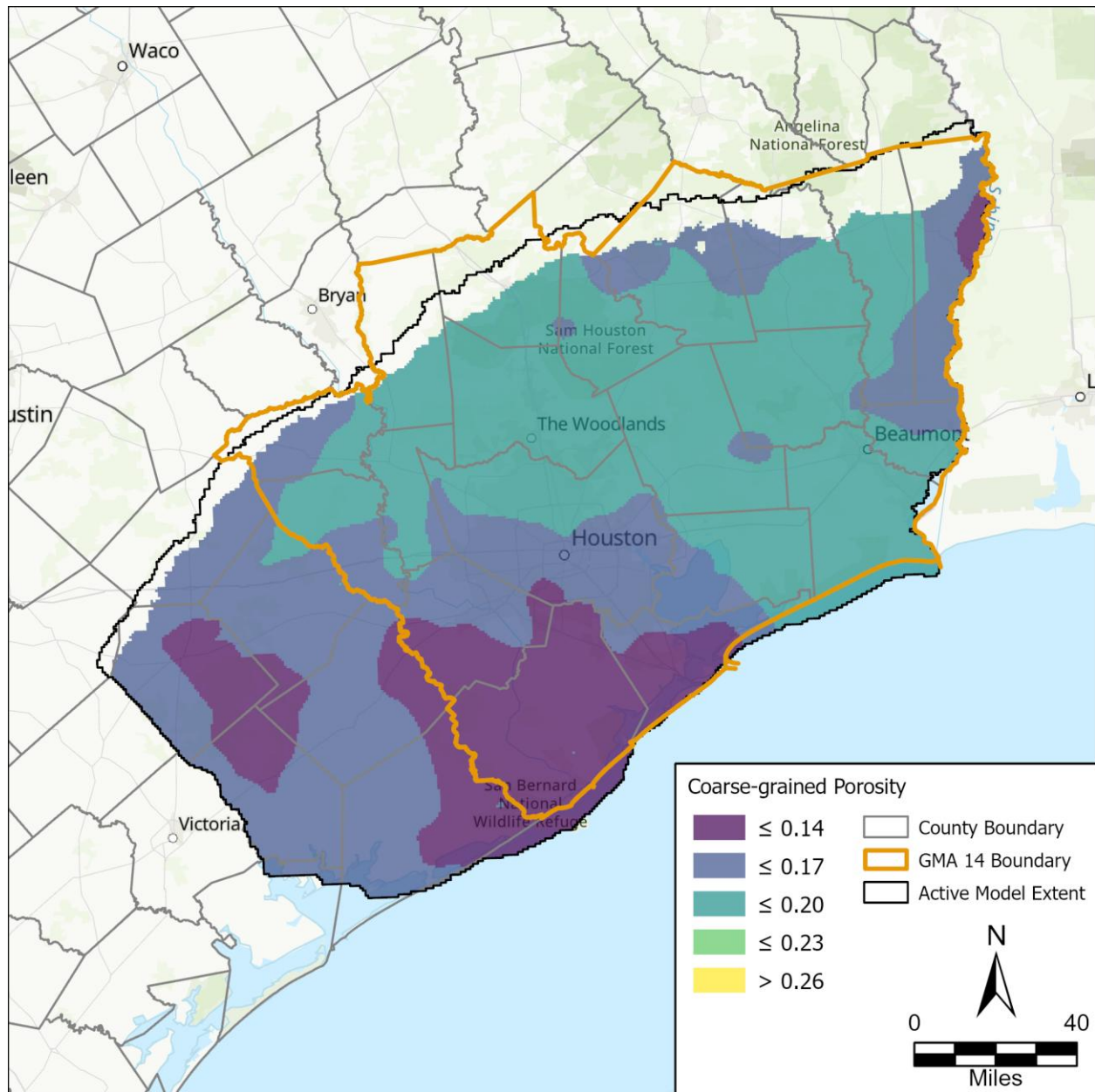


Figure 88. Layer 5 (Jasper Aquifer) calibrated coarse-grained porosity.

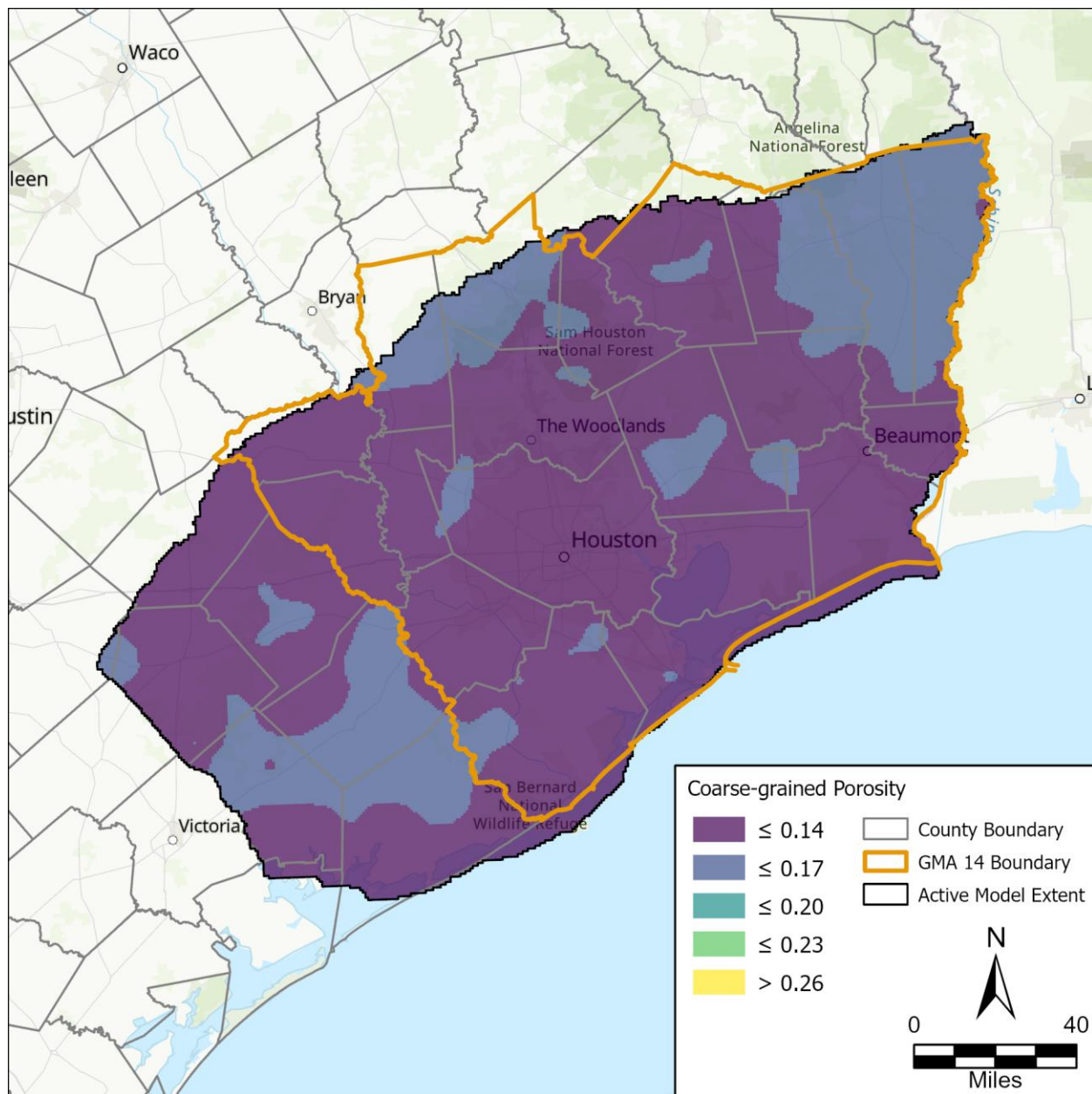


Figure 89. Layer 6 (Catahoula Aquifer) calibrated coarse-grained porosity.

4.1.5. Calibration of Boundary Conditions

We calibrated the GHB conductance using a model-wide constant which ranged from 0.1 to 10. The initial conductance value was 5.45 square feet per day and the calibrated value is 38.90 square feet per day. The GHB package simulated the flux between the model and the Gulf of Mexico. The increase in conductance during calibration allows for a less resistance flux between the model and the boundary.

We also calibrated the RIV conductance using a model-wide constant along with a cell-by-cell multiplier. The addition of the cell-by-cell multiplier allowed for different reaches of the river to vary in hydraulic conductance and thus adjust the surface water and groundwater interactions. The upper and lower limits of the multipliers were 0.1 to 10 with an ultimate upper and lower limit of 10 to 10,000 square feet per day. The initial value for the river conductance was 1,090 square feet per day for all river cells. The mean value for the calibrated base model was 2,216 square feet per day. Figure 90 illustrates the calibrated river conductance from the base model. The river conductance had the highest increases for segments of the Neches River, Brazos River, and Colorado River.

We calibrated recharge using a model-wide constant multiplier ranging from 0.75 to 1.25. Recharge is only applied to layer 1 (shallow aquifer system). Figure 91 illustrates the calibrated recharge for 2018. Recharge reached over 4 inches per year throughout the outcrop area with the largest concentration of high values in Taylor and Polk counties. Figure 92 shows the calibration recharge for the base model over time. Recharge is flat during the earlier years due to the stress periods covering multiple years (see Table 7).

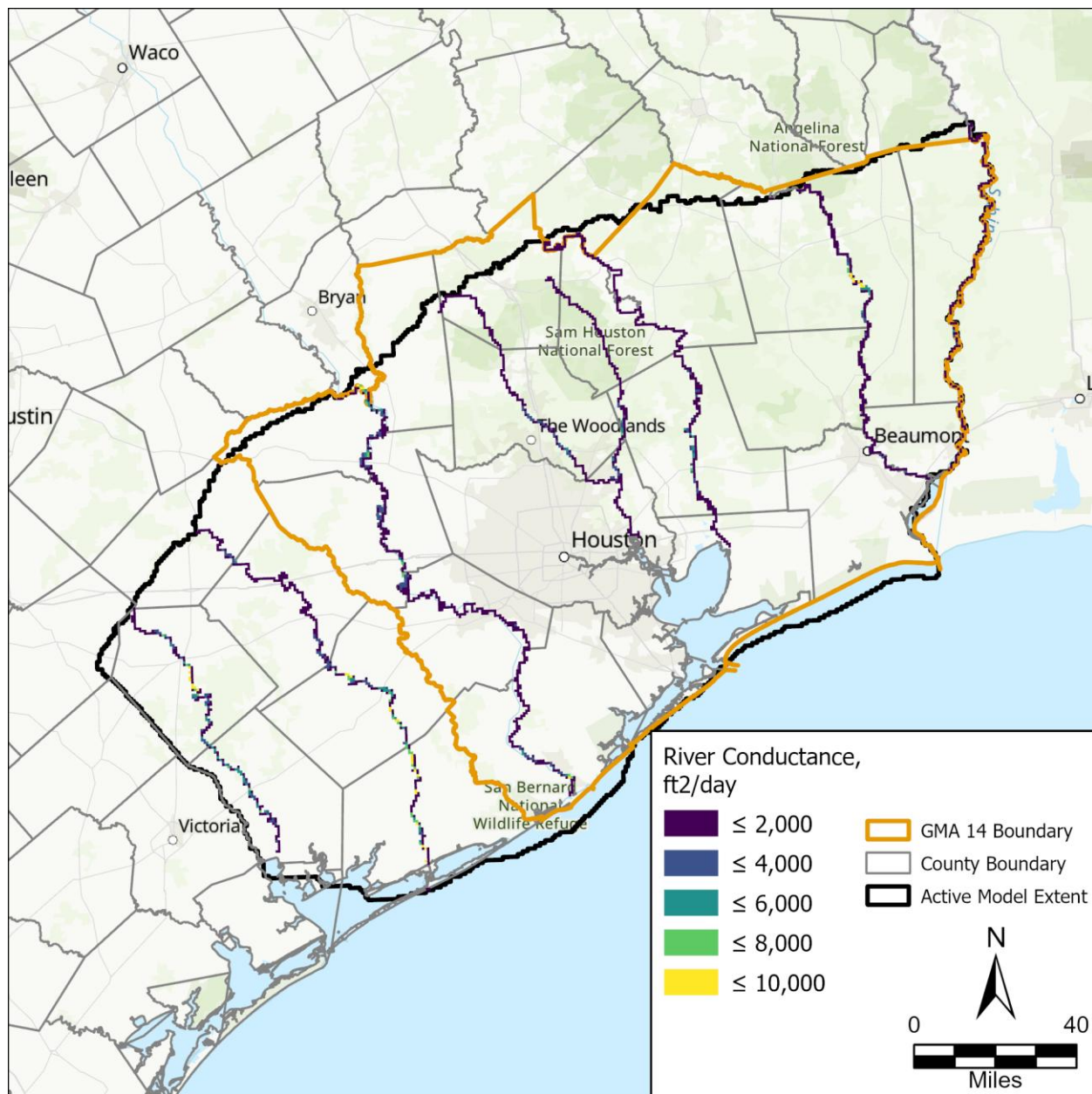


Figure 90. Calibrated river conductance.

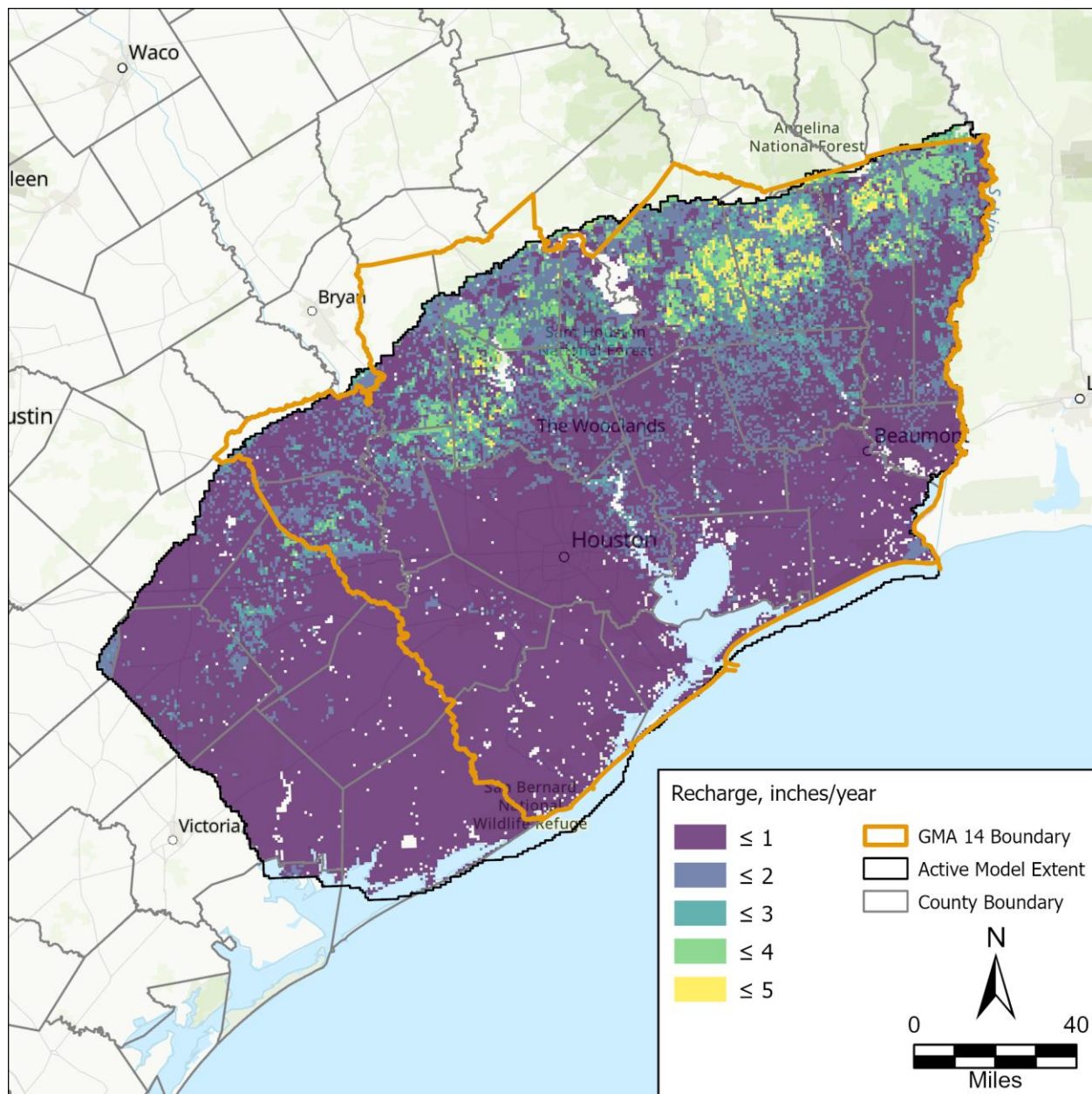


Figure 91. Layer 1 (Shallow Aquifer System) calibrated recharge.

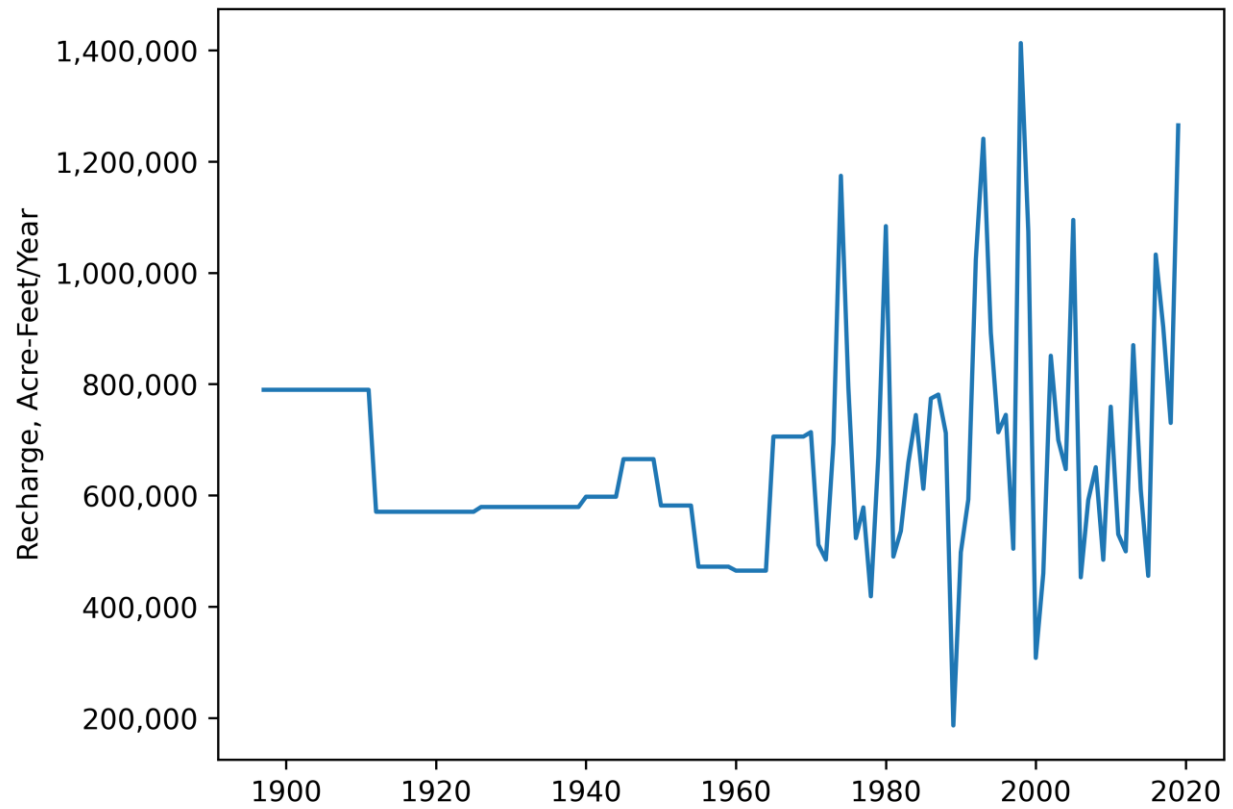


Figure 92. Calibrated recharge over time across the model.

4.2. Model Simulated Versus Measured Head

4.2.1. Water levels

We compared simulated and observed water levels to evaluate calibration results. Each calibration statistic starts with determining the residual for each target with the following equation:

$$r = target_o - target_s \quad \text{Eq. 15}$$

Where r is the residual, $target_o$ is the observation target value, and $target_s$ is the simulated target value. The residual for each target represents the difference between the observed and simulated value for that target. Using the residual, we apply the following equations to determine the Mean Error (ME), Mean Absolute Error (MAE), Root Mean Squared Error (RMSE), and Normalized RMSE (NRMSE):

$$ME = \frac{1}{N} \sum_{i=1}^N r_i \quad \text{Eq. 16}$$

$$MAE = \frac{1}{N} \sum_{i=1}^N |r_i| \quad \text{Eq. 17}$$

$$RMSE = \sqrt{\frac{1}{N} \sum_{i=1}^N r_i^2} \quad \text{Eq. 18}$$

$$NRMSE = \frac{1}{max_{target_o} - min_{target_o}} \sqrt{\frac{1}{N} \sum_{i=1}^N r_i^2} \quad \text{Eq. 19}$$

Where N is the number of targets. ME is the average difference between the observed and simulated values, indicating whether the model tends to overestimate (positive value) or underestimate (negative value) water levels. MAE measures the average magnitude of the residuals which provides an unbiased representation of model accuracy. RMSE takes the square root of the average of squared residuals making the metric more sensitive to higher residuals. The NRMSE takes the RMSE and divides by the range of observed values to evaluate the significance of RMSE to the range of observed values across the model domain. One calibration goal is to have an NRMSE less than 10 percent for each aquifer layer. Table 13 summarizes the GMA 14 Model calibration statistics for the water level targets.

Table 13. Water Level calibration statistics.

Layer	Number of targets	Mean Error, feet	Mean Absolute Error, feet	Root Mean Squared Error, feet	Range, feet	Normalized RMSE (%)
Chicot	17,634	4.1	31.3	40.9	621	6.6
Evangeline	10,627	15.3	49.5	61.3	851	7.2
Jasper	2,930	-19.1	42.2	57.5	622	9.2
Catahoula	914	-11.5	52.7	79.5	515	15.4
GMA 14 Model	32,105	5.3	38.9	51.5	937	5.5

Cross plots of the observed and simulated water level targets are illustrated in Figure 93 for each aquifer layer and Figure 94 for the entire model. The perfect fit line is represented as a black dotted line; the closer points are to the perfect fit line, the better the model fit though it is appropriate to have points distributed on either side of the line. As indicated with the mean error, the cross plots can show if the model produces over or under simulated water levels. Overall, the targets generally follow the perfect fit line except in deeper portions of the Jasper where water levels were biased to being simulated higher than observed.

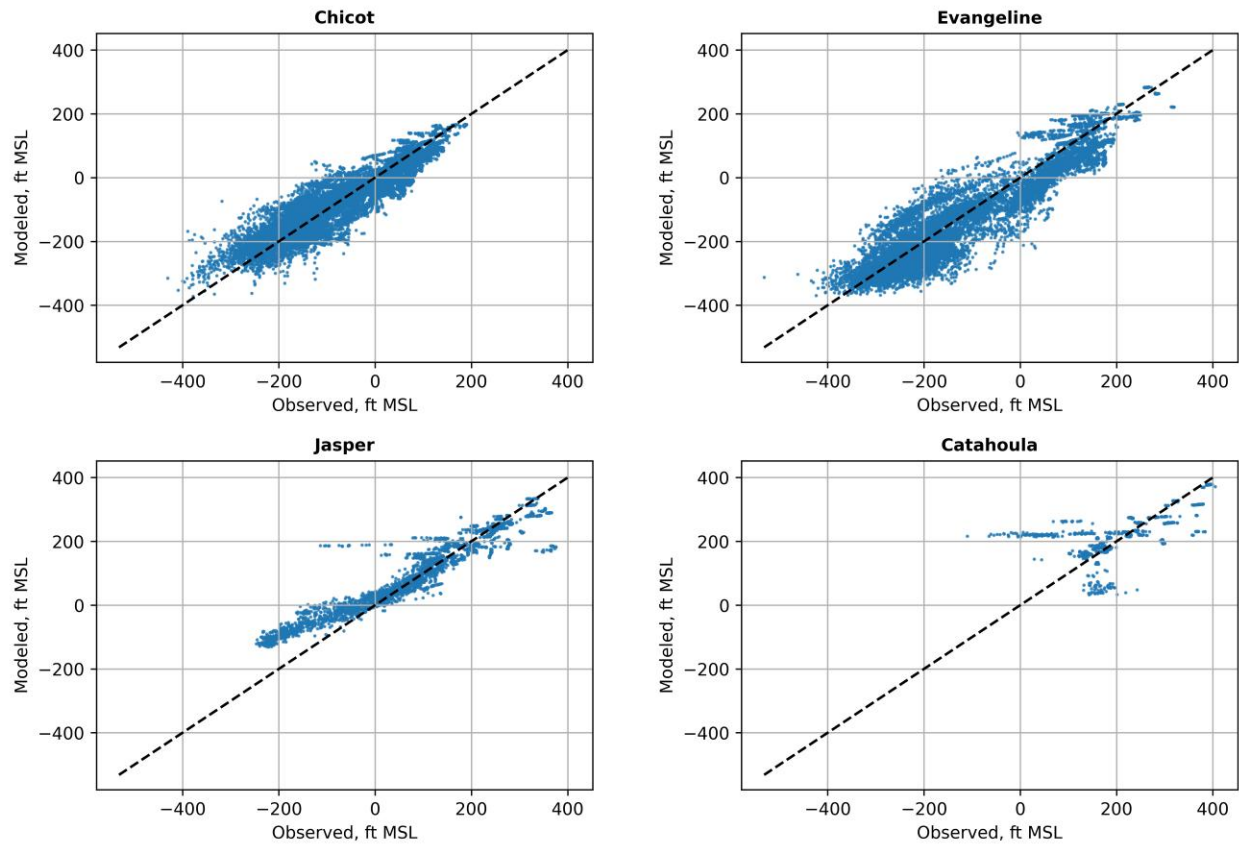


Figure 93. Measured versus modeled water level measurements for each layer.

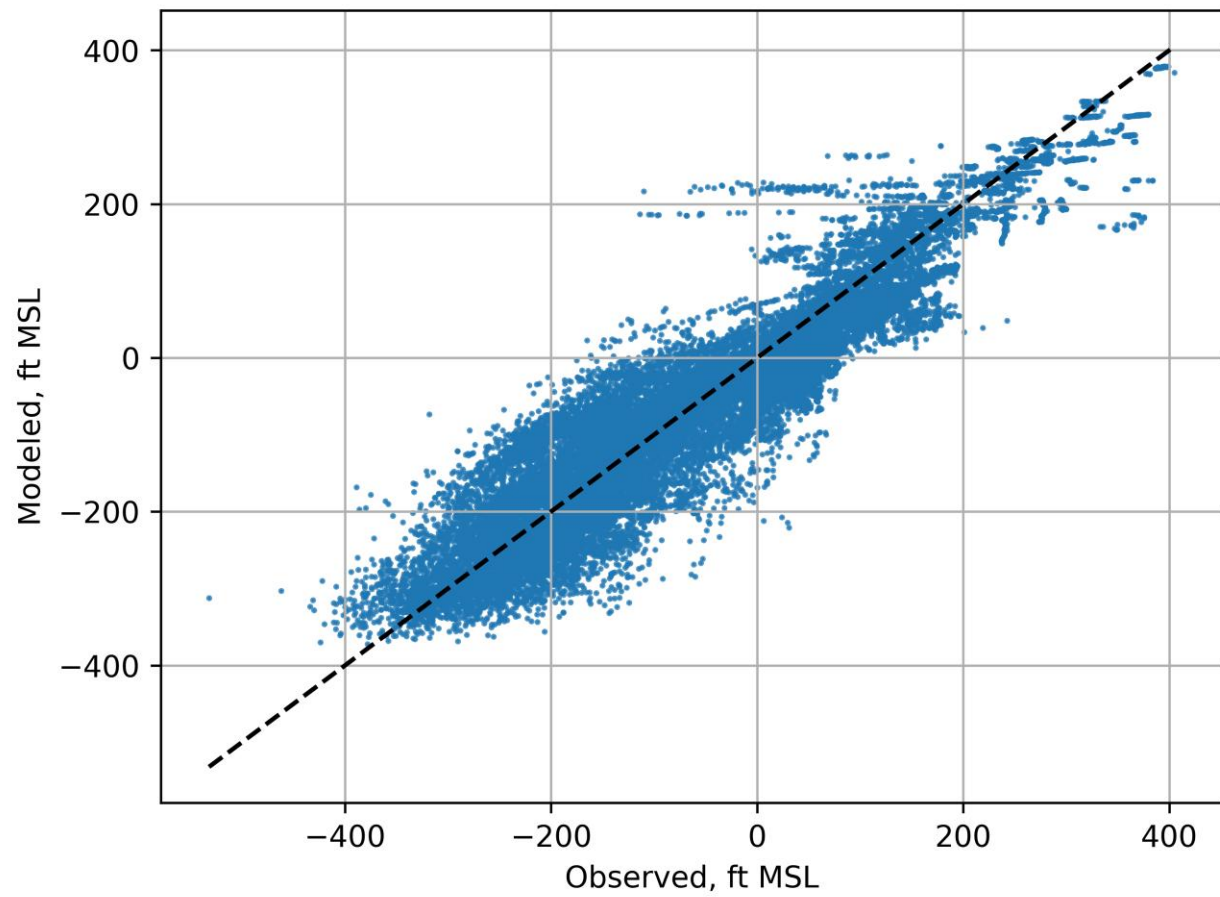


Figure 94. Measured versus modeled water level measurements for the Chicot, Evangeline, Jasper, and Catahoula layers.

4.2.2. Residual Distributions

Figures 95 through 98 illustrate the mean residual for each observation well by layer. The residual for each well was calculated by determining the average of all residuals throughout the history matching period for each well. Negative residuals indicate simulated water levels are greater than the observed water level (over simulated) and visa-verse for positive values (under simulated). The Chicot layer shows under simulated water levels in southwestern Harris County and Wharton County, and over simulated water levels in southeastern Harris County and The Woodlands area. Beyond these areas, simulated water levels were relatively unbiased.

Simulated water levels in the Evangeline layer were under simulated in western Harris County and southeastern Montgomery County and moving towards the western and southwestern region of the model. Over simulated water levels are in The Woodlands area in southern Montgomery County. Simulated water levels in the Jasper layer were over simulated in southern Montgomery and northern Harris Counties. The outcropping areas of the Jasper were unbiased. Within the Catahoula layer simulated water levels were under simulated in northern Montgomery County and unbiased throughout the outcropping areas.

Figures 99 through 102 illustrate the histograms of water level residuals for each aquifer layer. The ideal residual histogram would be normally distributed and centered around zero, indicating an unbiased distribution of residuals. The mean error on the histogram shows residual distribution bias. The Chicot layer water level residuals are normally distributed and have the least amount of bias with a mean error of 4.1 feet. The Evangeline layer water level residuals are also symmetrically distributed with a similar spread as the Chicot but with slightly higher frequencies near the tails. The Jasper layer water level residuals are symmetrically distributed with a few higher residuals in the -200 to -300 bins. The Catahoula layer water level residuals are less symmetrical with a left-skewed tail.

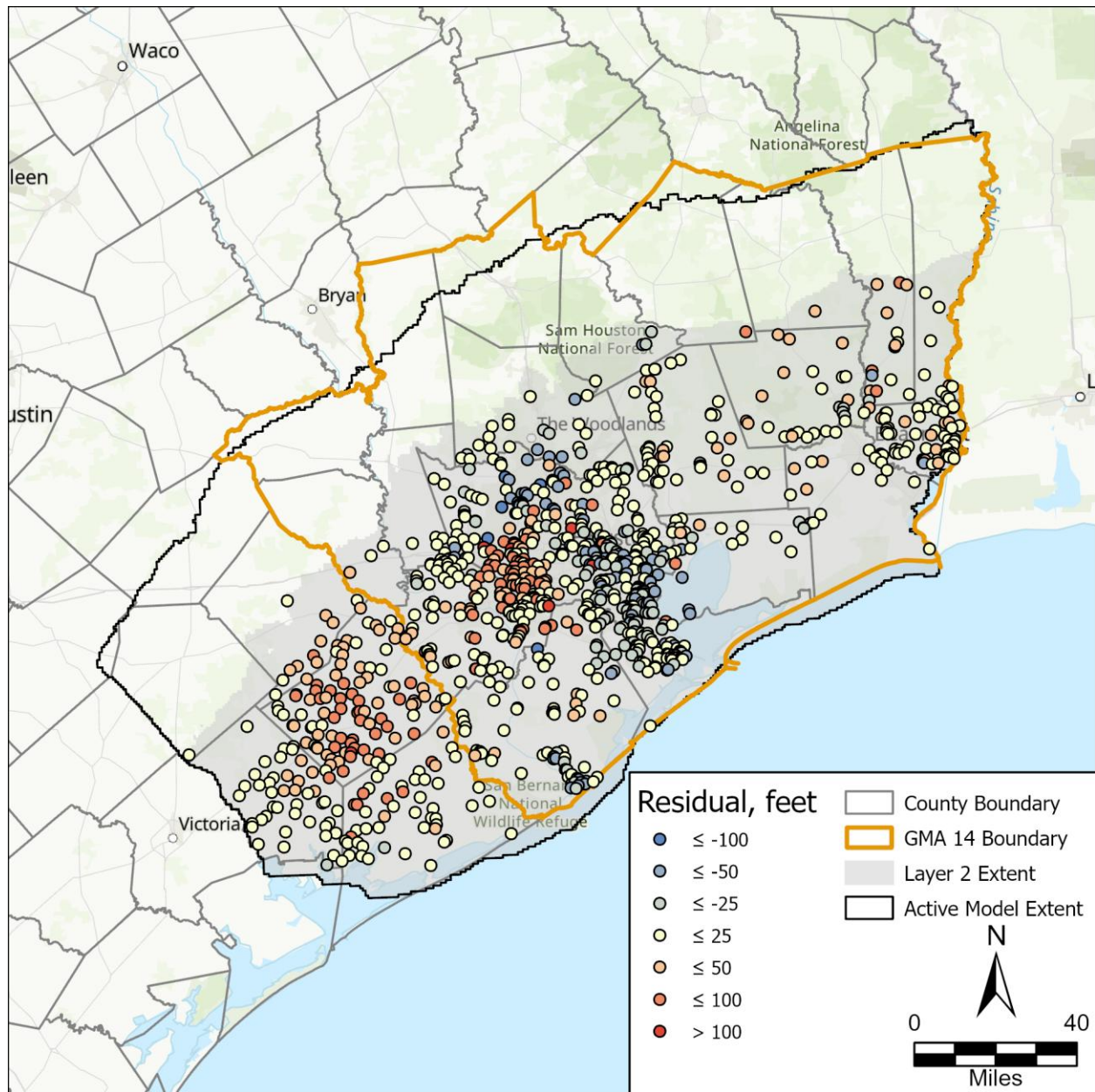


Figure 95. Layer 2 (Chicot Aquifer) mean residual by well.

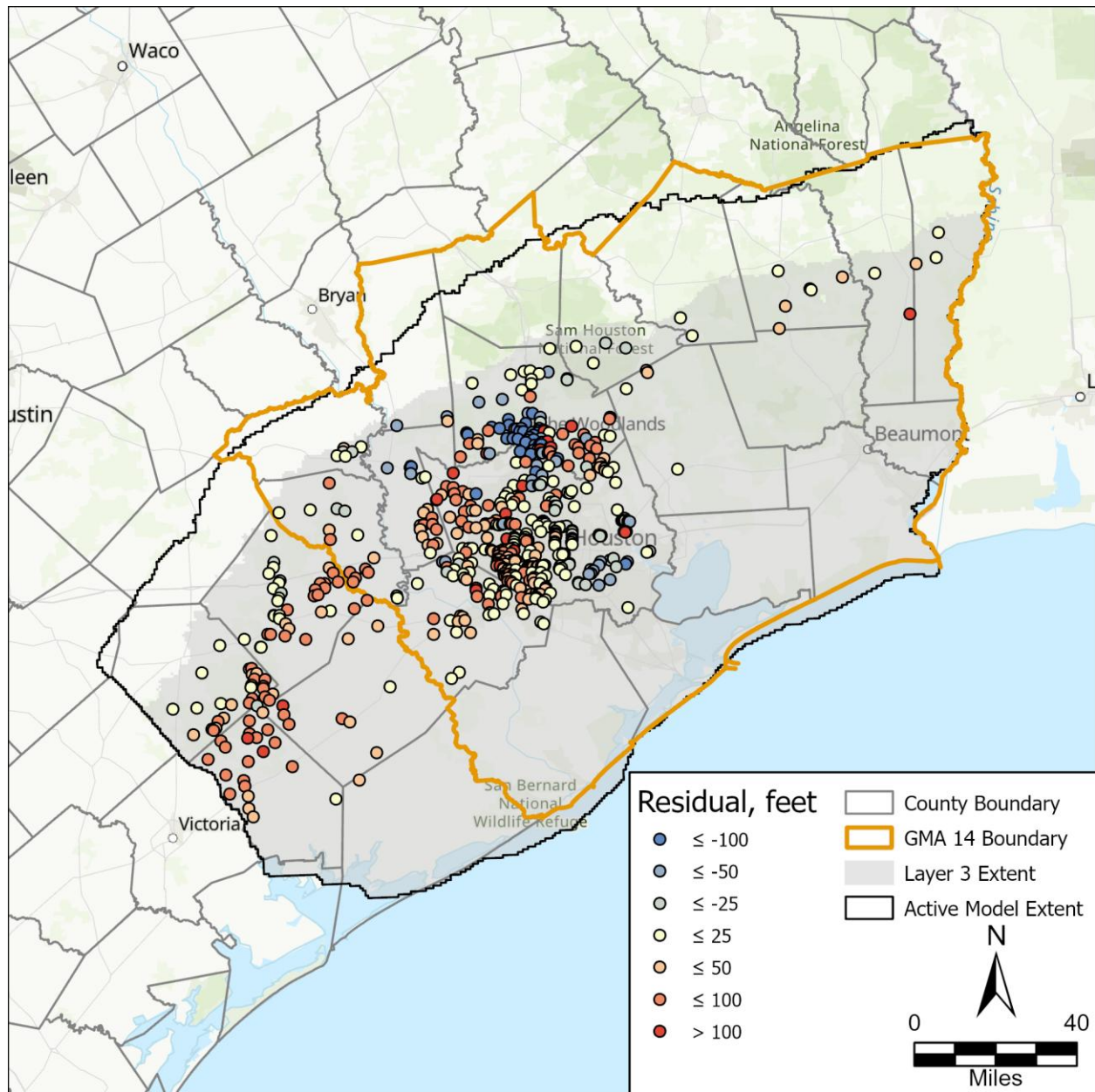


Figure 96. Layer 3 (Evangeline Aquifer) mean residual by well.

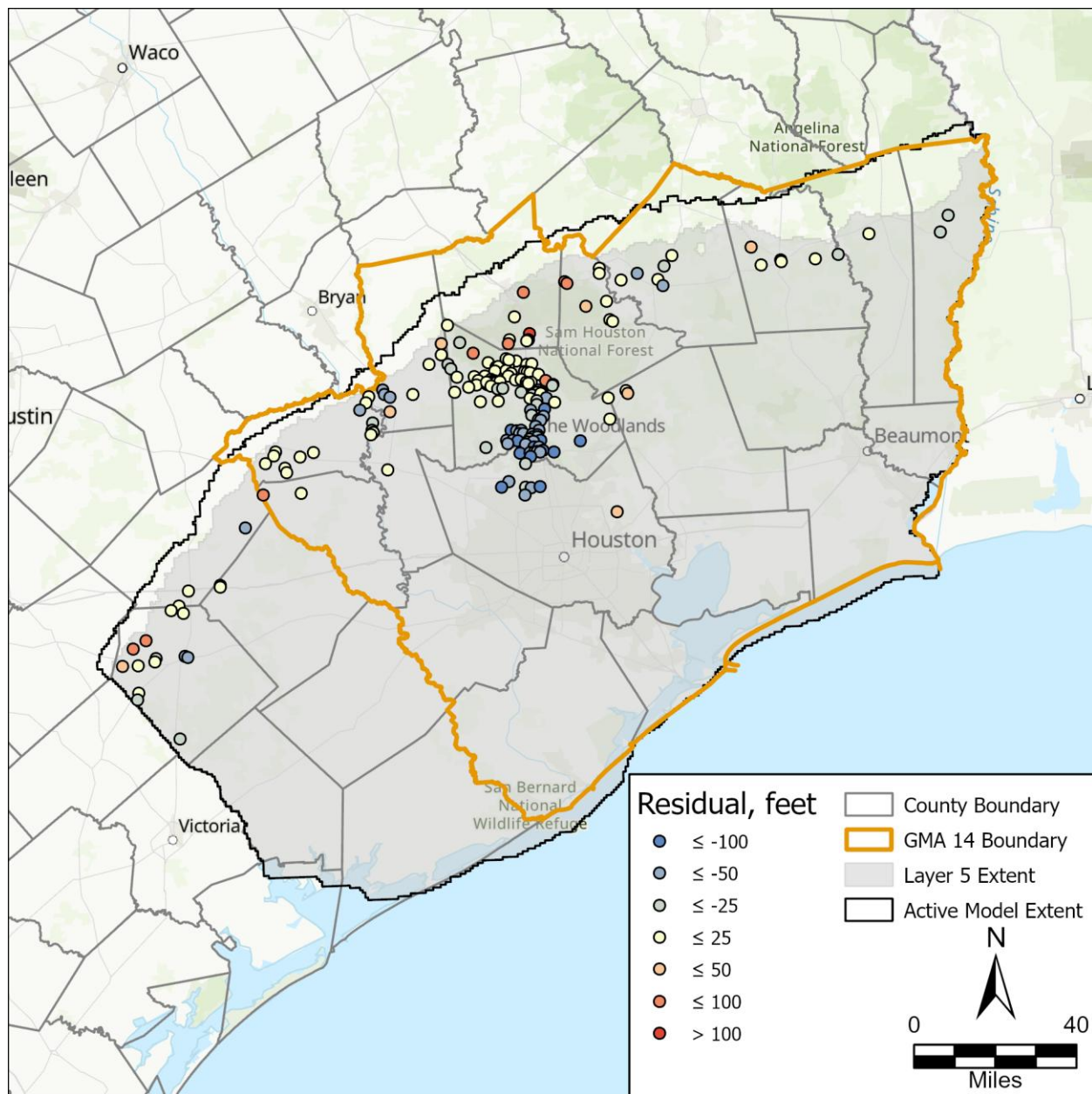


Figure 97. Layer 5 (Jasper Aquifer) mean residual by well.

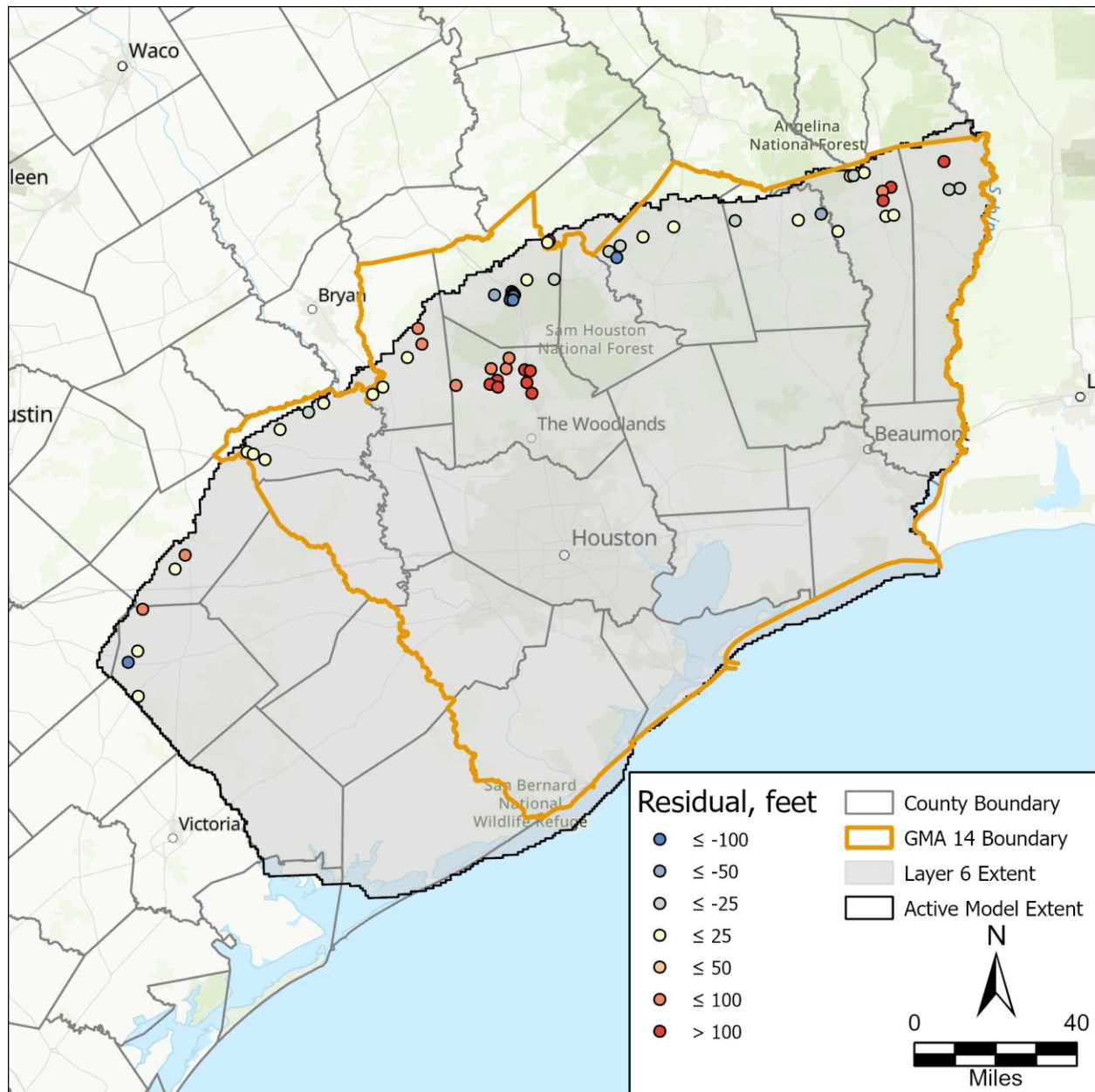


Figure 98. Layer 6 (Catahoula Aquifer) mean residual by well.

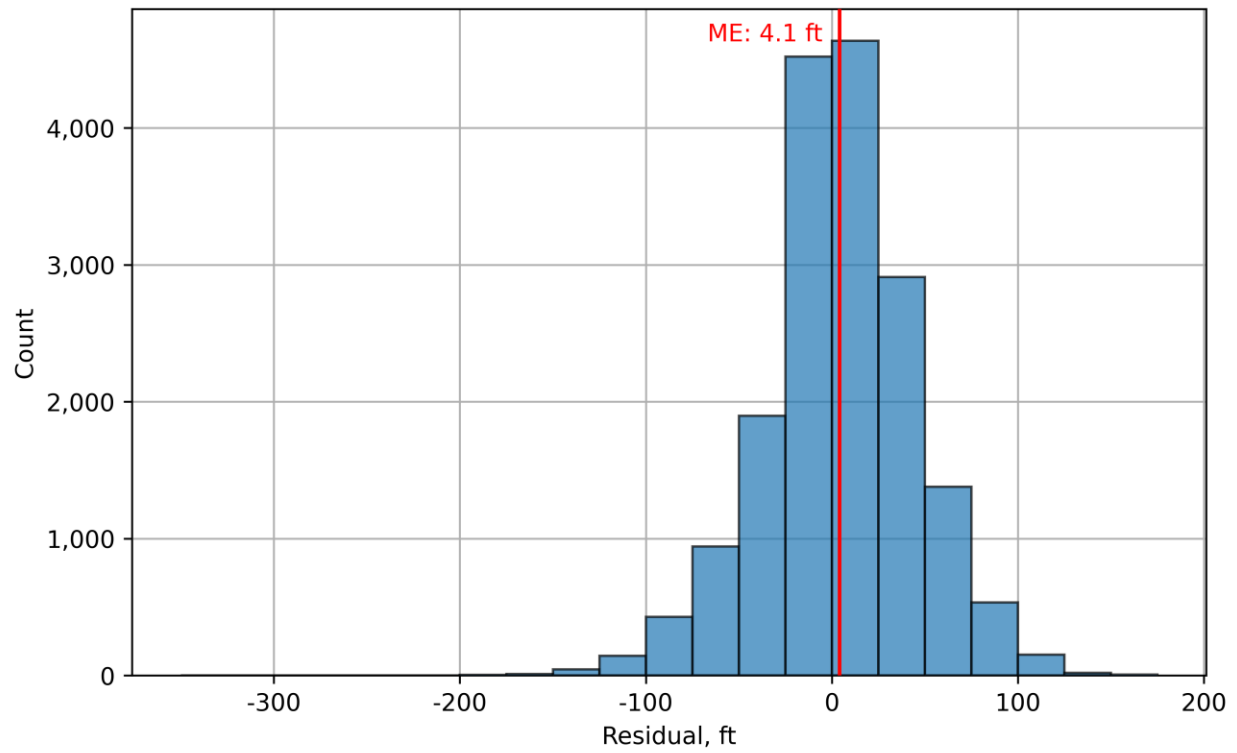


Figure 99. Layer 2 (Chicot Aquifer) residual histogram. ME = Mean Error.

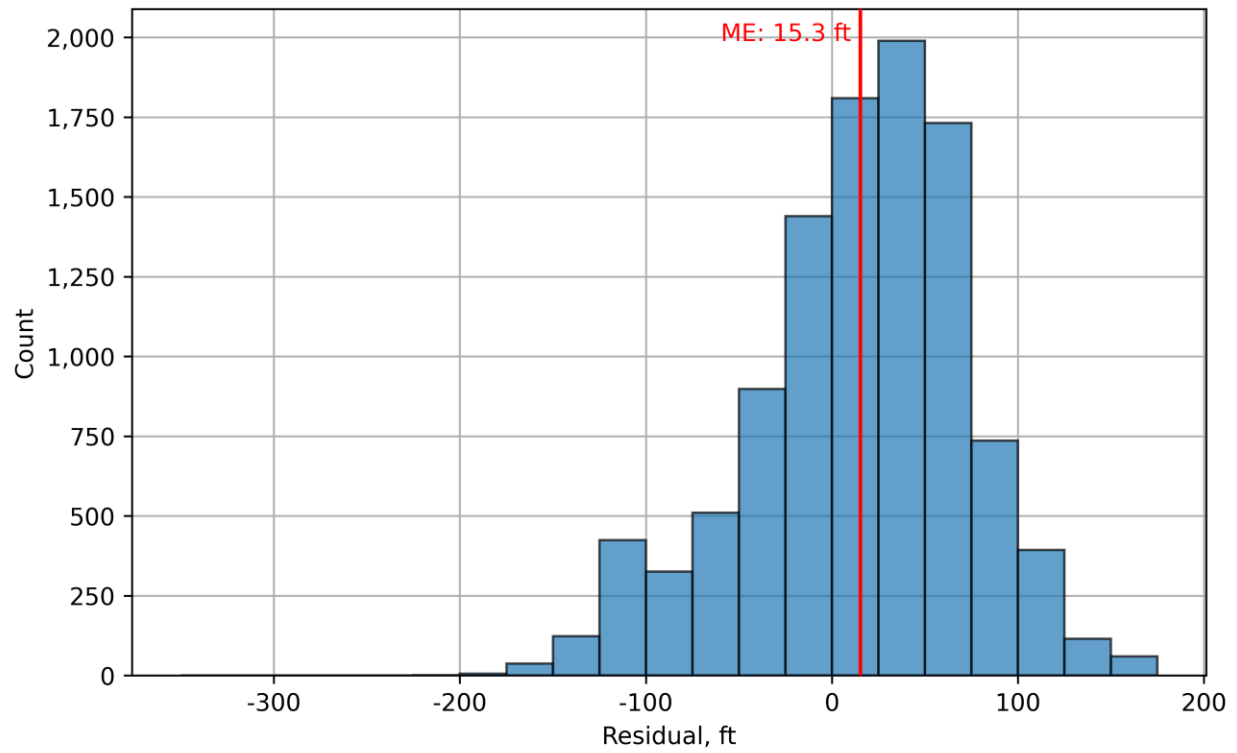


Figure 100. Layer 3 (Evangeline Aquifer) residual histogram. ME = Mean Error.

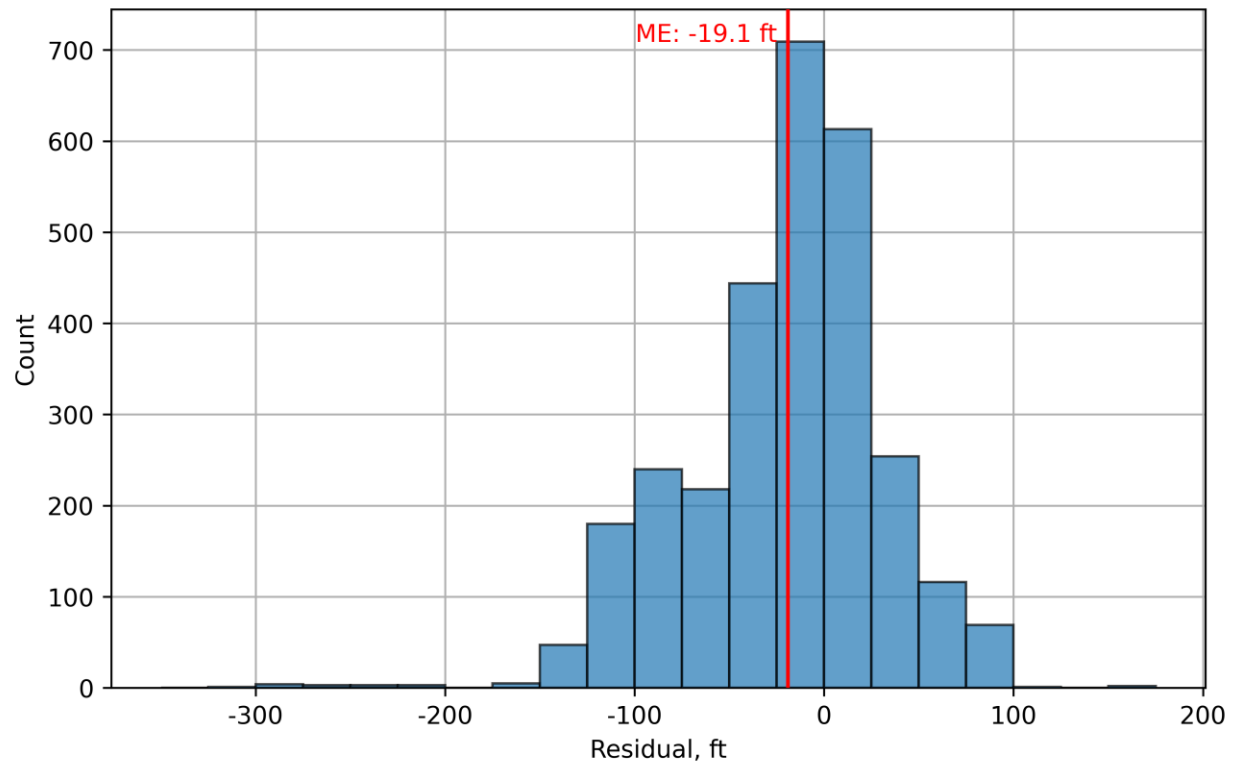


Figure 101. Layer 5 (Jasper Aquifer) residual histogram. ME = Mean Error.

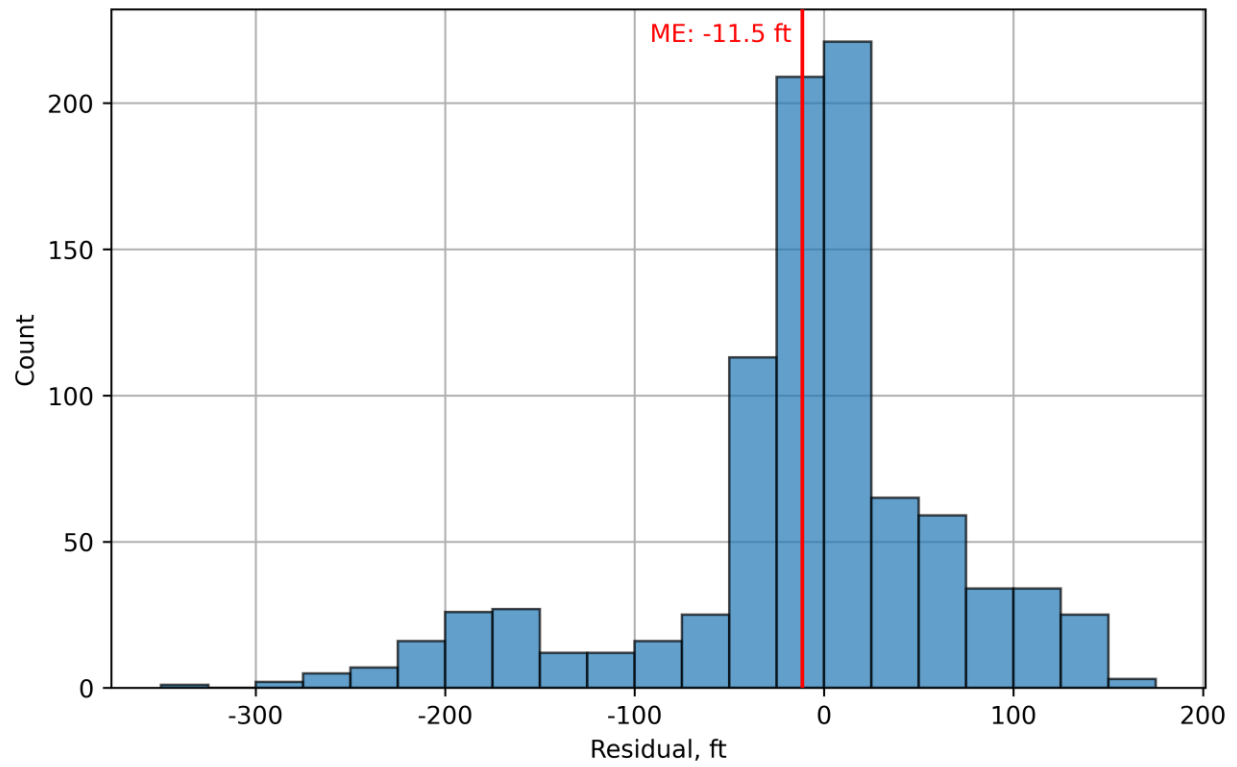


Figure 102. Layer 6 (Catahoula Aquifer) residual histogram. ME = Mean Error.

4.2.3. Water level hydrographs

Figures 103 through 105 show the simulated and observed hydrographs of the Chicot, Evangeline, and Jasper aquifers. The hydrographs indicate simulated trends are similar to observed trends throughout the model area. We also developed a series of hydrographs to compare simulated water levels with observed water levels from GULF-2023 and the GMA14 Model. Appendix 7 presents hydrographs for the Chicot, Evangeline, Jasper, and Catahoula aquifers.

The GMA 14 Model was able to capture the Chicot Aquifer observed water level trends throughout Harris County and the surrounding area. State Well Number 6514405 (see Figure 103) shows water levels were over simulated prior to 1970 but the trend is similar to the target values. After 1970, when pumping declined in the area, the simulated water levels rebounded in a similar manner to the observed values. In northern Harris County, State Well Number 6060103 (See Figure 103) was consistent with the observation values but was not able to fully capture the decreasing trend. Other areas of the model showed a similar pattern to the examples above and overall the observed water level trends were similar to the simulated trends.

Within the Evangeline Aquifer, State Well Number 6514405 (see Figure 104) was able to reflect observed water levels and both trends that were observed before and after 1970. Water levels were over simulated in southeast and southwest Montgomery County and under simulated in The Woodlands / Interstate 45 corridor area in south Montgomery County. However, the overall water level trends were similar between the observed and simulated values.

The Jasper simulated water levels throughout the outcropping area and into north Montgomery County (including the City of Conroe) had a similar water level and trends as the observation values. State Well Number 6045504 (see Figure 105) reflected the observation values and trends until about 2005 where water levels become over simulated.

The GMA 14 Model includes a larger groundwater level dataset than the GULF-2023 model. Additionally, no smoothing was applied to the GMA 14 Model water level targets, allowing the data to reflect more immediate groundwater responses compared to the smoothed GULF-2023 targets. As shown on the hydrographs in Appendix 7, while both models show similar groundwater level trends, the GMA 14 Model more accurately matches observed groundwater levels.

GMA 14 Groundwater Availability Model

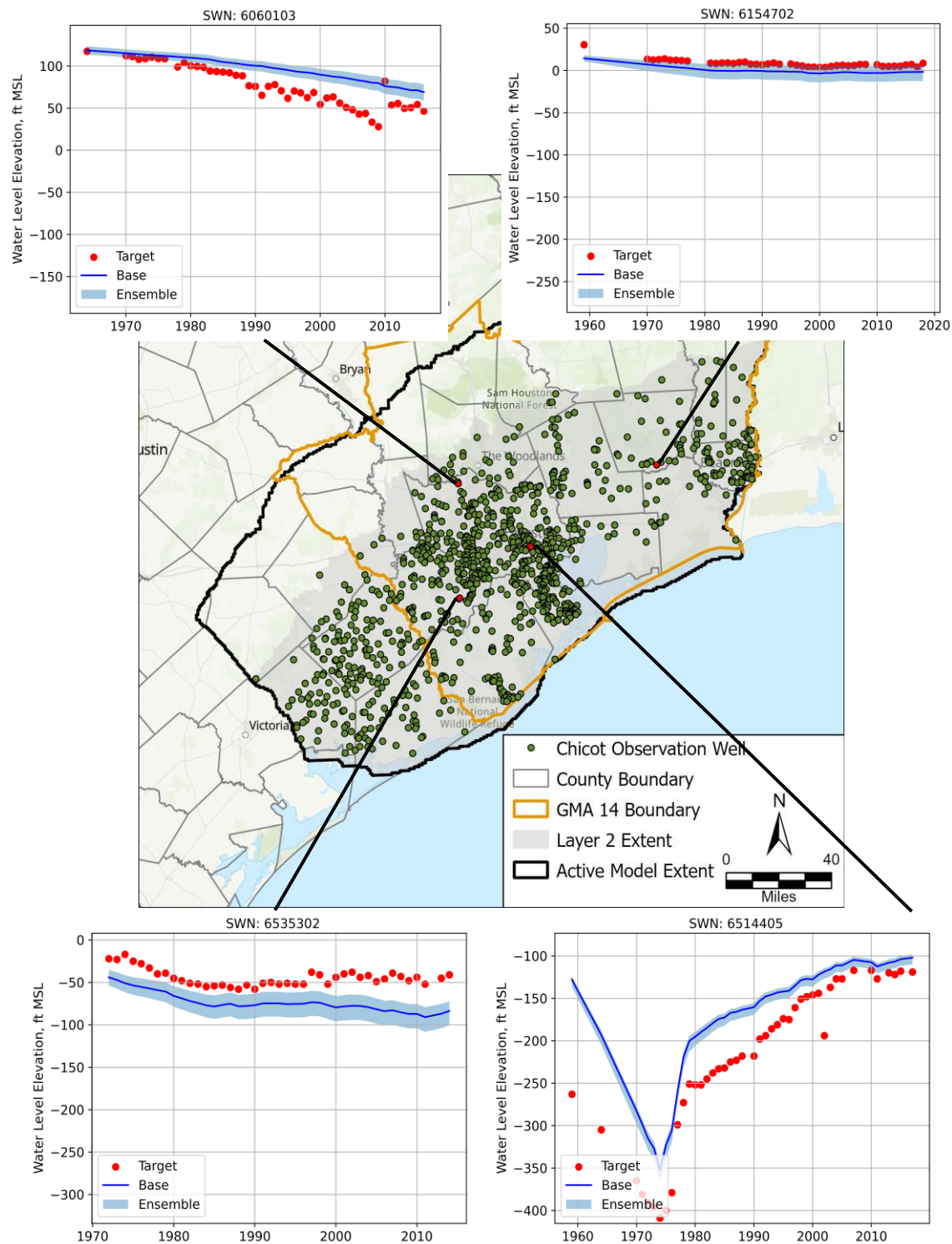


Figure 103. Layer 2 (Chicot Aquifer) simulated and observed hydrographs. SWN = State Well Number.

GMA 14 Groundwater Availability Model

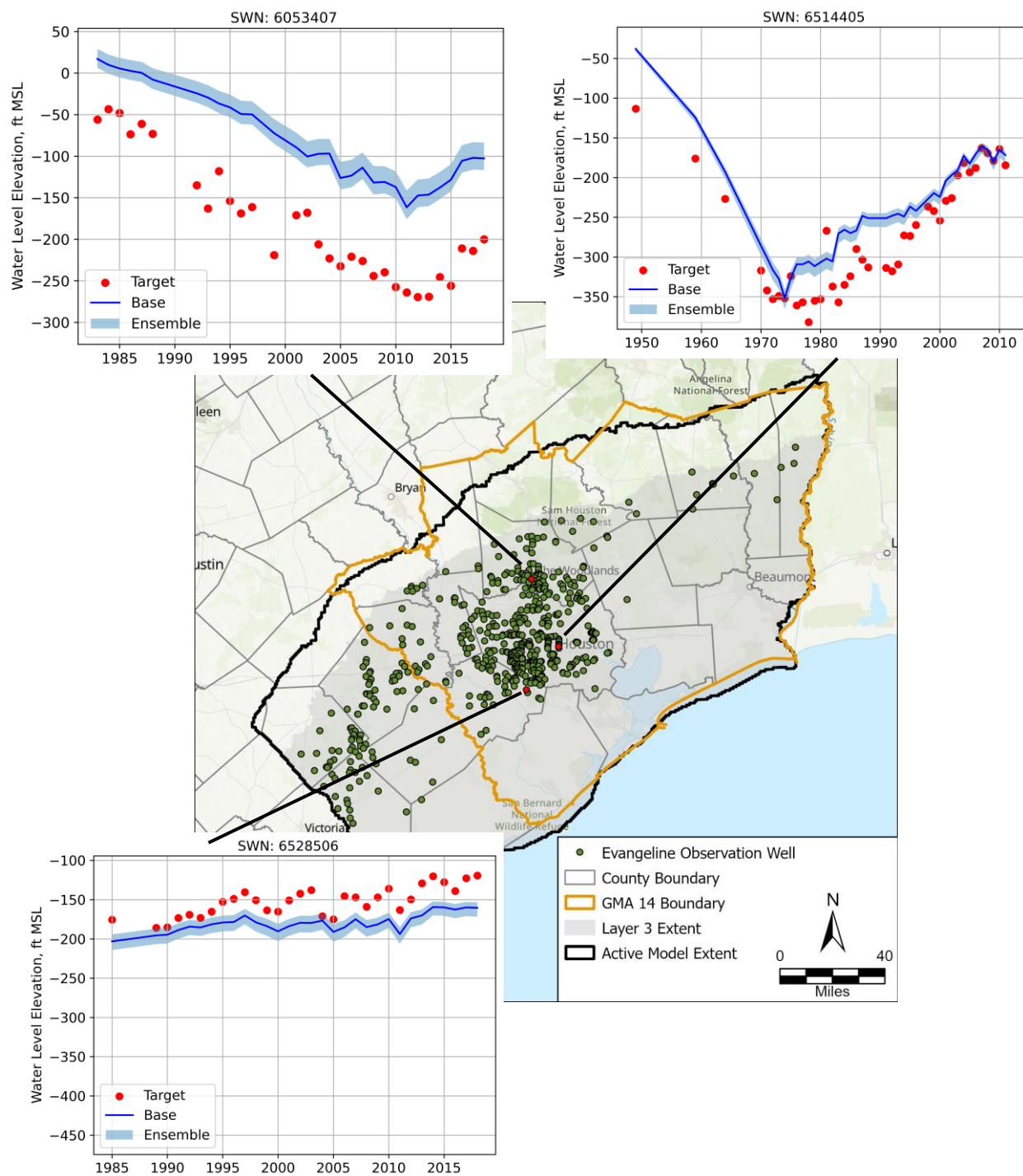


Figure 104. Layer 3 (Evangeline Aquifer) simulated and observed hydrographs. SWN = State Well Number.

GMA 14 Groundwater Availability Model

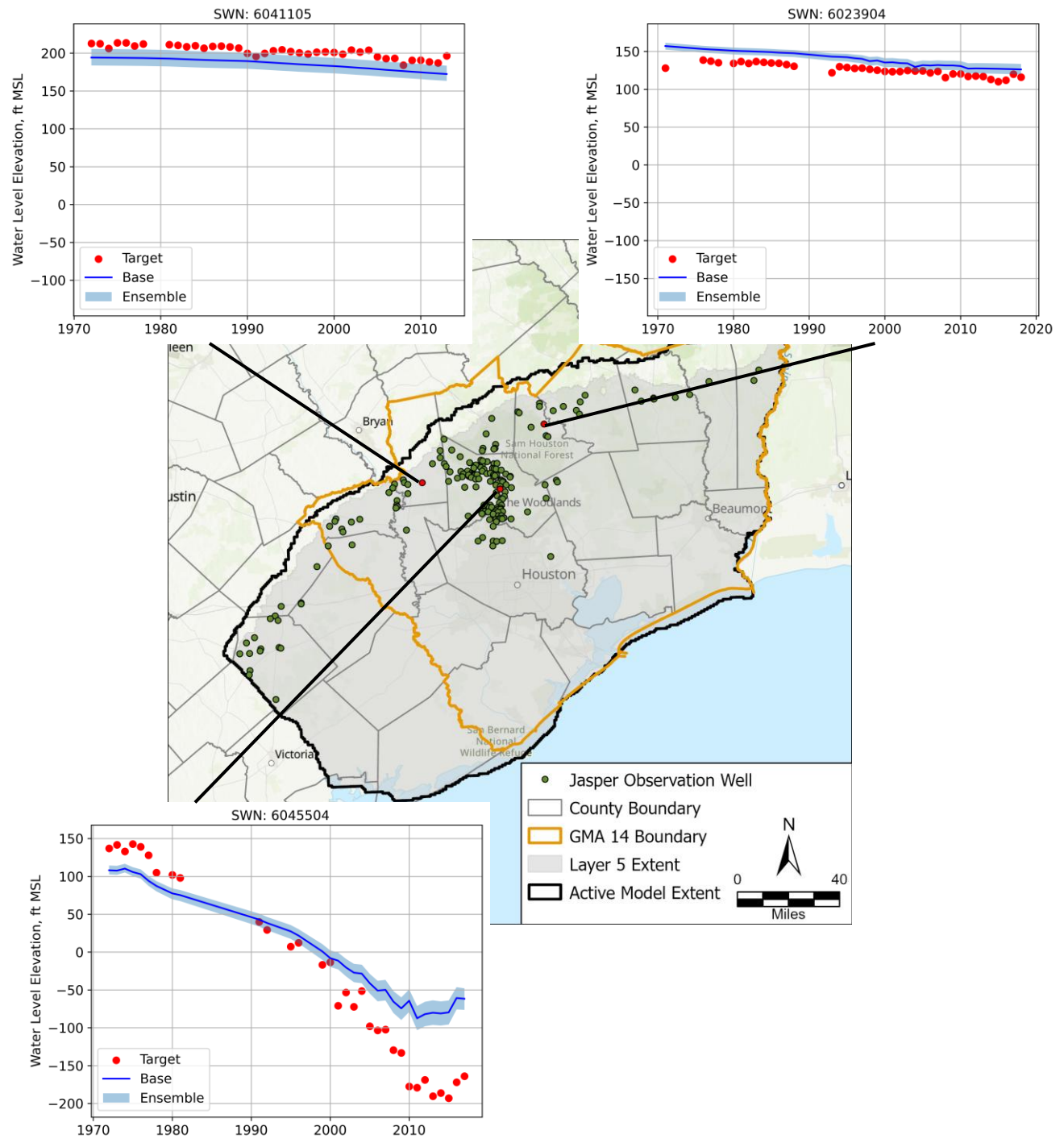


Figure 105. Layer 5 (Jasper Aquifer) simulated and observed hydrographs. SWN = State Well Number.

4.2.4. Simulated Water Levels

We prepared simulated water level contour plots for the aquifer layers to assess the flow regimes (Figures 106 through 109). Groundwater flows perpendicular to the water level contours. Regionally, the simulated water levels indicate groundwater flow is from outcropping areas in the northwest towards the Gulf of Mexico. Within the Chicot and Evangeline aquifers, there is a cone of depression focused around the Houston area, deviating groundwater from regional flow regimes towards the Houston area. The Jasper Aquifer shows a similar occurrence with groundwater being drawn to The Woodlands area.

Figures 110 through 113 illustrate the spatial distribution of the drawdown between the end of the predevelopment period (1896) and 2018. The drawdown cones focused around the Houston area in the Chicot and Evangeline. For the Jasper Aquifer, The Woodlands shows the most drawdown since the predevelopment period. The cone of depression regions reflects the pumping outlined in Section 3.5.

Figures 114 through 117 compare simulated and observed water level contours for 2018. Overall, flow patterns within the aquifer layers are similar for both simulated and observed water levels. Within the Chicot layer, the simulated water levels captured the cone of depression around the Houston area along with contours further up dip. Differences in the Chicot in the southwestern portion of the model reflect where water levels were under simulated. Similar to the Chicot, the GMA 14 Model captured the Houston and Montgomery area water levels for the Evangeline layer but the observations indicated more local drawdown from pumping centers. Water levels in the southwestern portion also were under simulated with the northeastern region being difficult to compare due to the lack of available data. The Jasper and Catahoula layers were both limited in the available observation data, but where data is available, the flow directions indicated by simulated water levels are similar to flow directions based on the observation data.

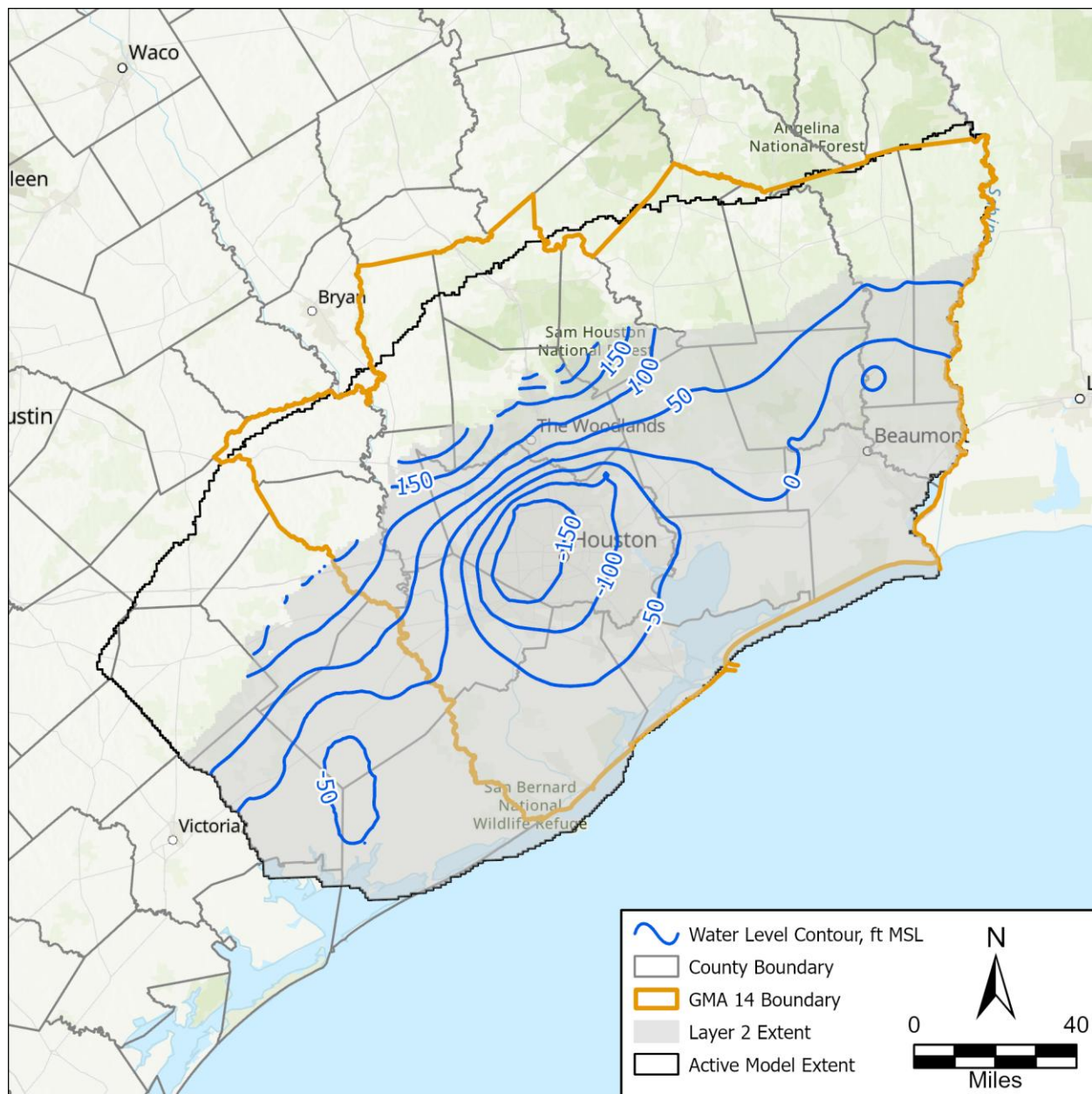


Figure 106. Layer 2 (Chicot Aquifer) simulated potentiometric surface for 2018.

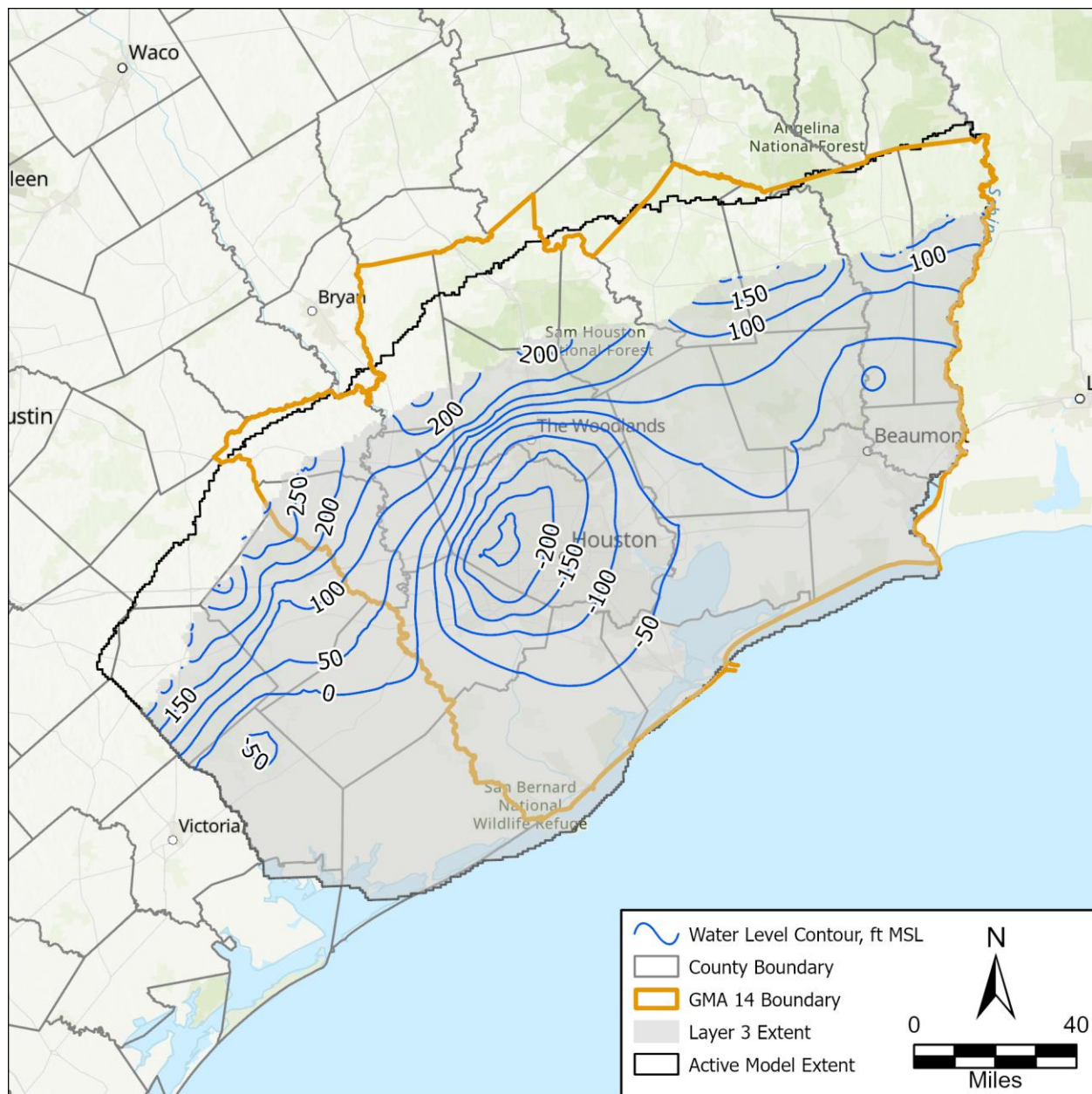


Figure 107. Layer 3 (Evangeline Aquifer) simulated potentiometric surface for 2018.

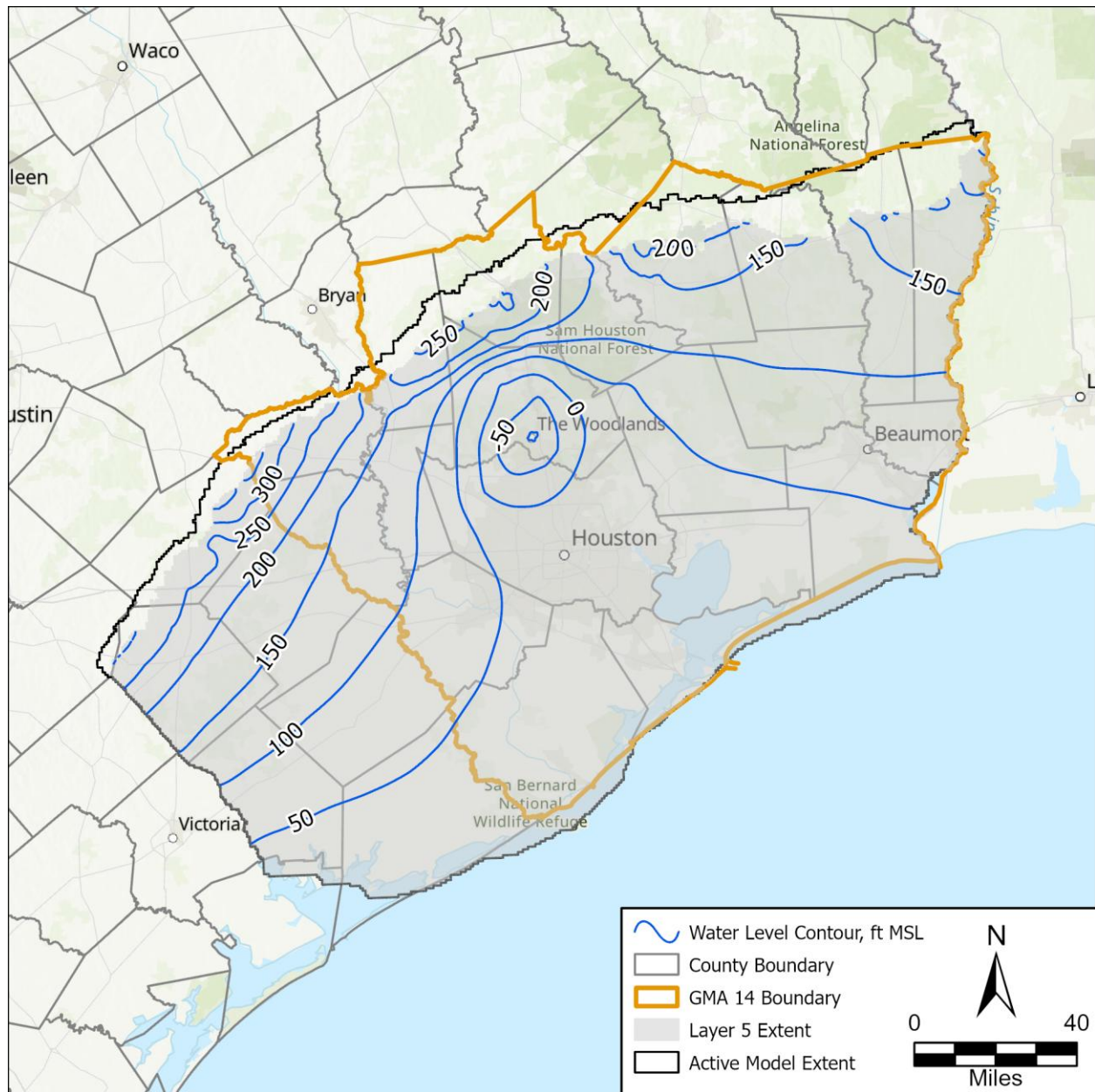


Figure 108. Layer 5 (Jasper Aquifer) simulated potentiometric surface for 2018.

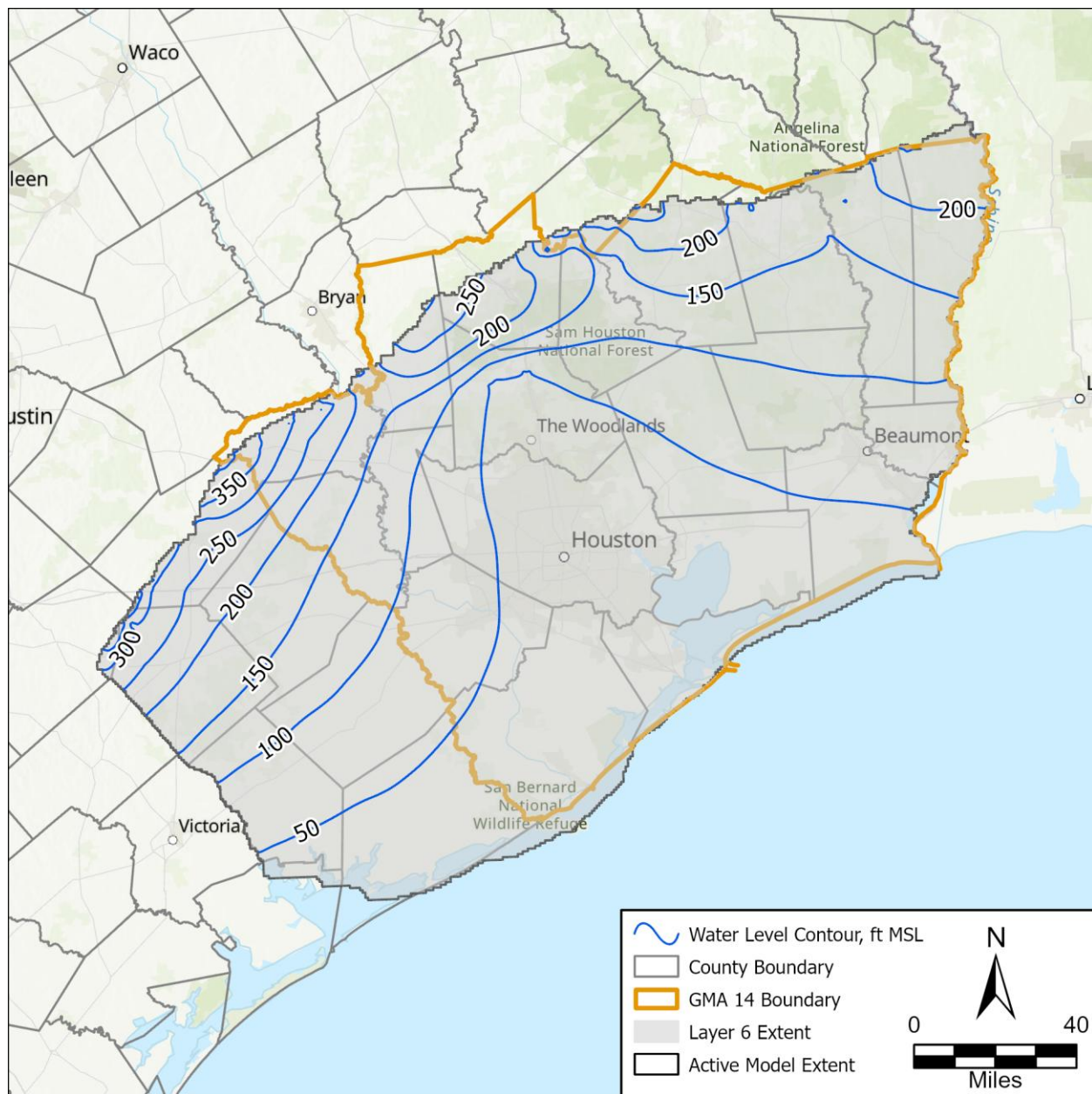


Figure 109. Layer 6 (Catahoula Aquifer) simulated potentiometric surface for 2018.

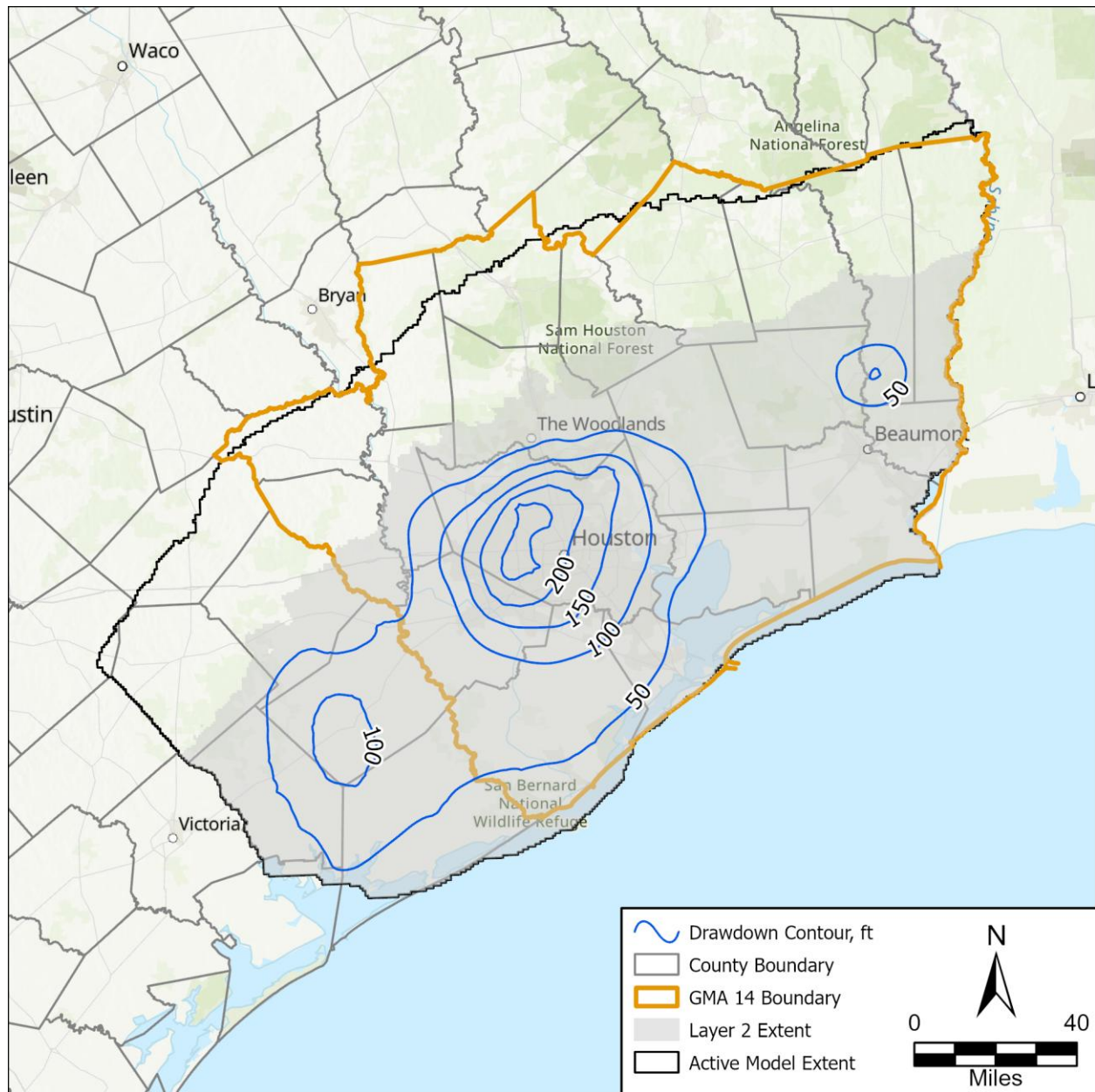


Figure 110. Layer 2 (Chicot Aquifer) simulated drawdown between predevelopment and 2018.

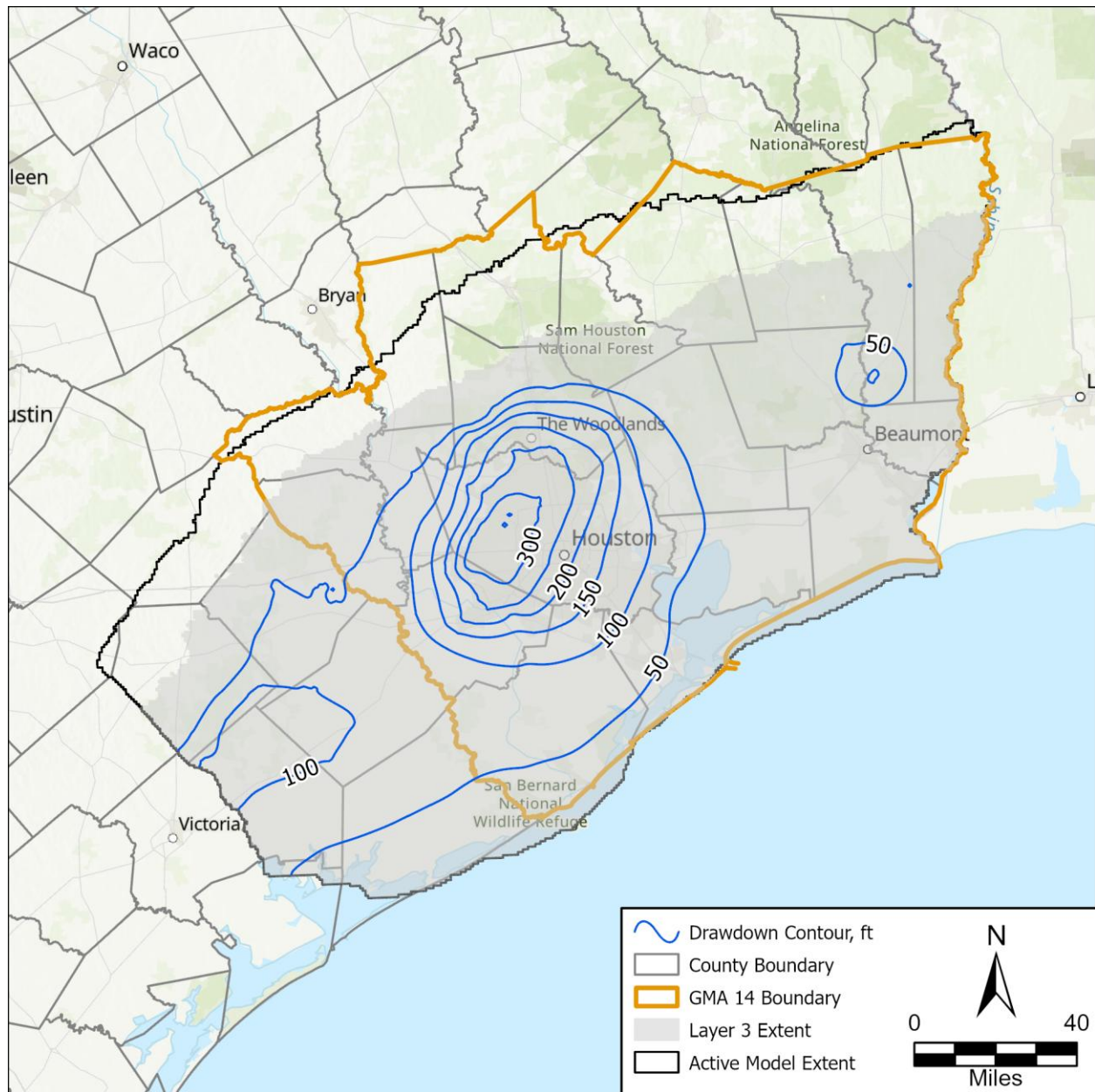


Figure 111. Layer 3 (Evangeline Aquifer) simulated drawdown between predevelopment and 2018.

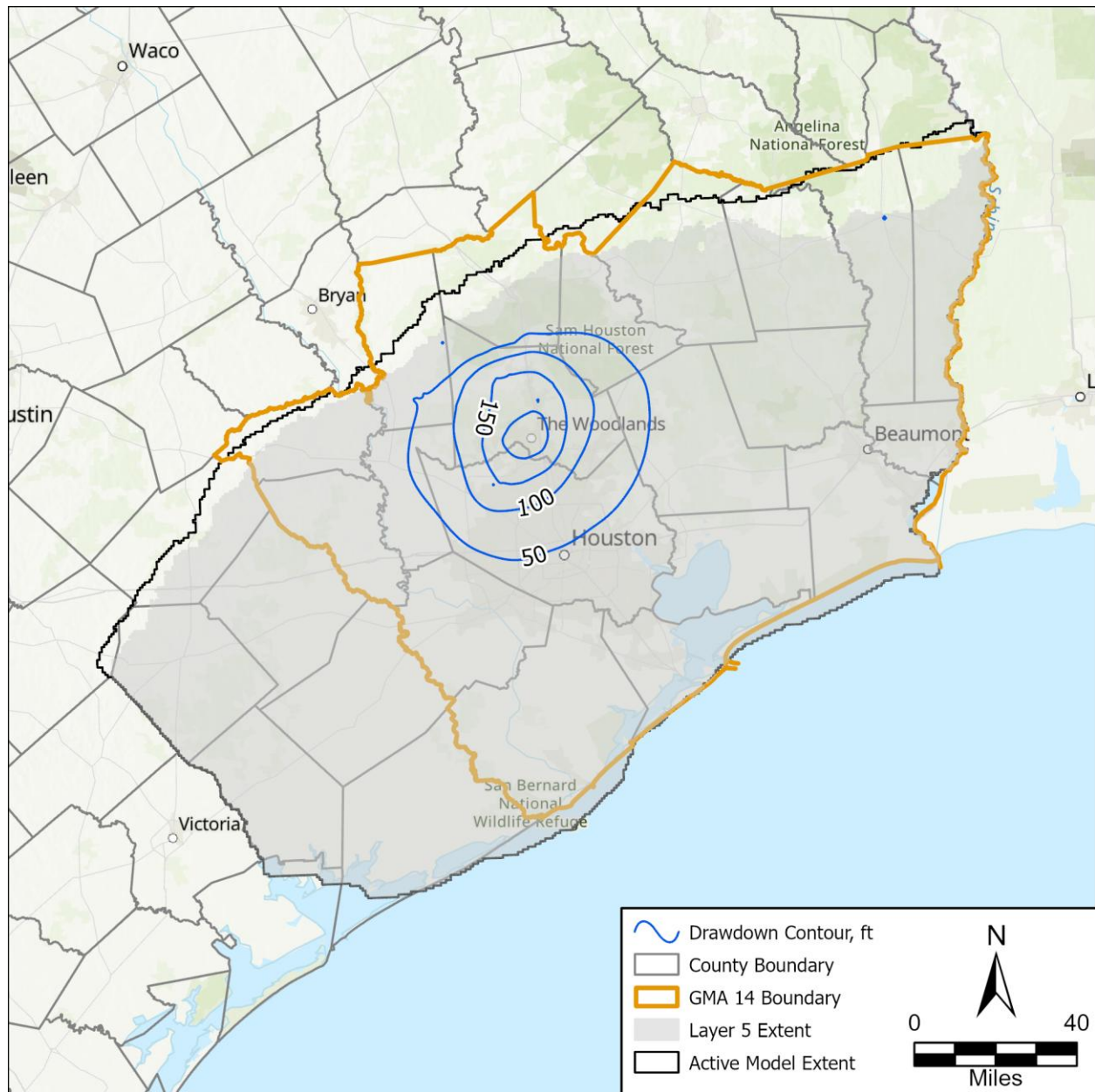


Figure 112. Layer 5 (Jasper Aquifer) simulated drawdown between predevelopment and 2018.

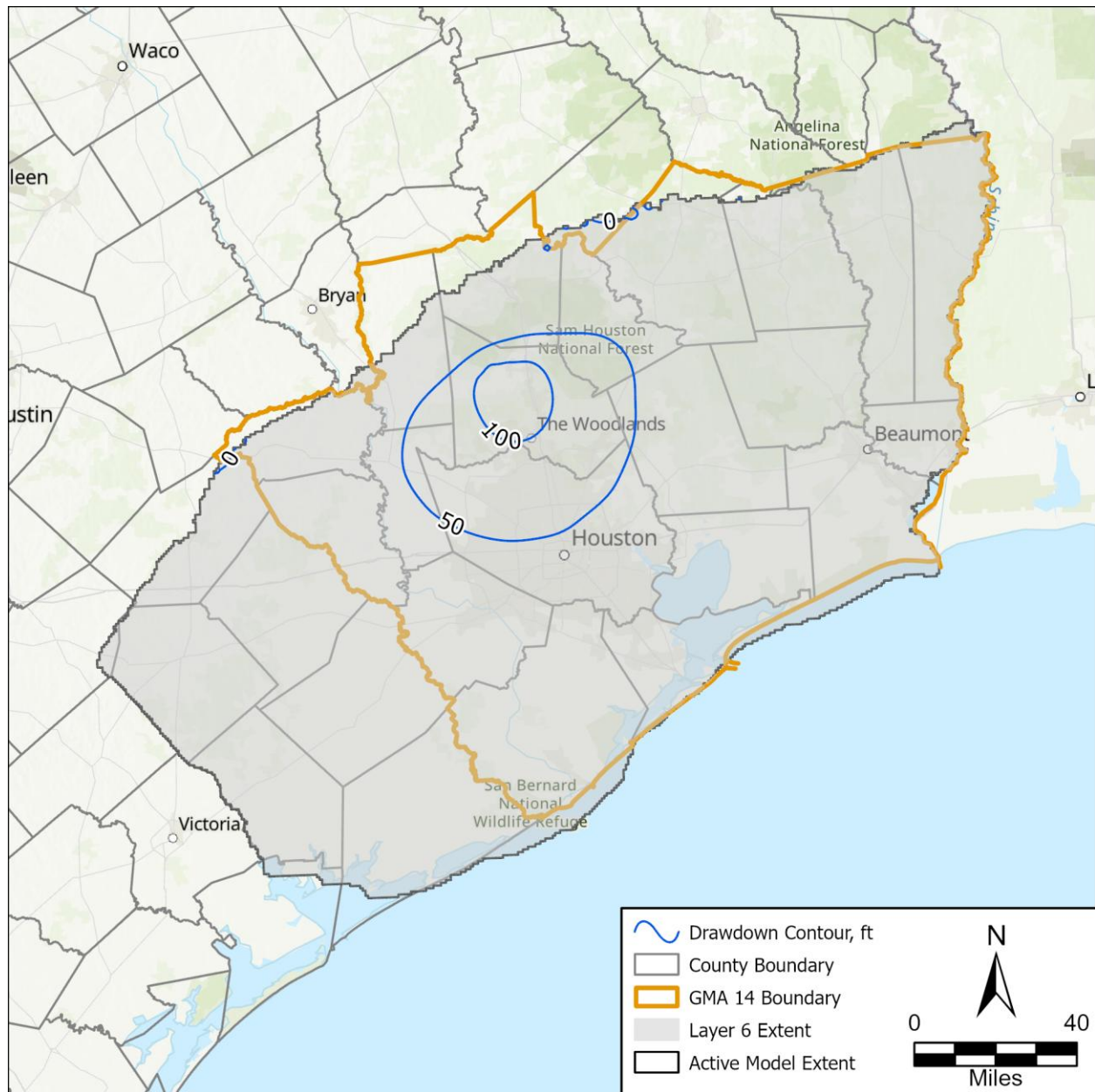


Figure 113. Layer 6 (Catahoula Aquifer) simulated drawdown between predevelopment and 2018.

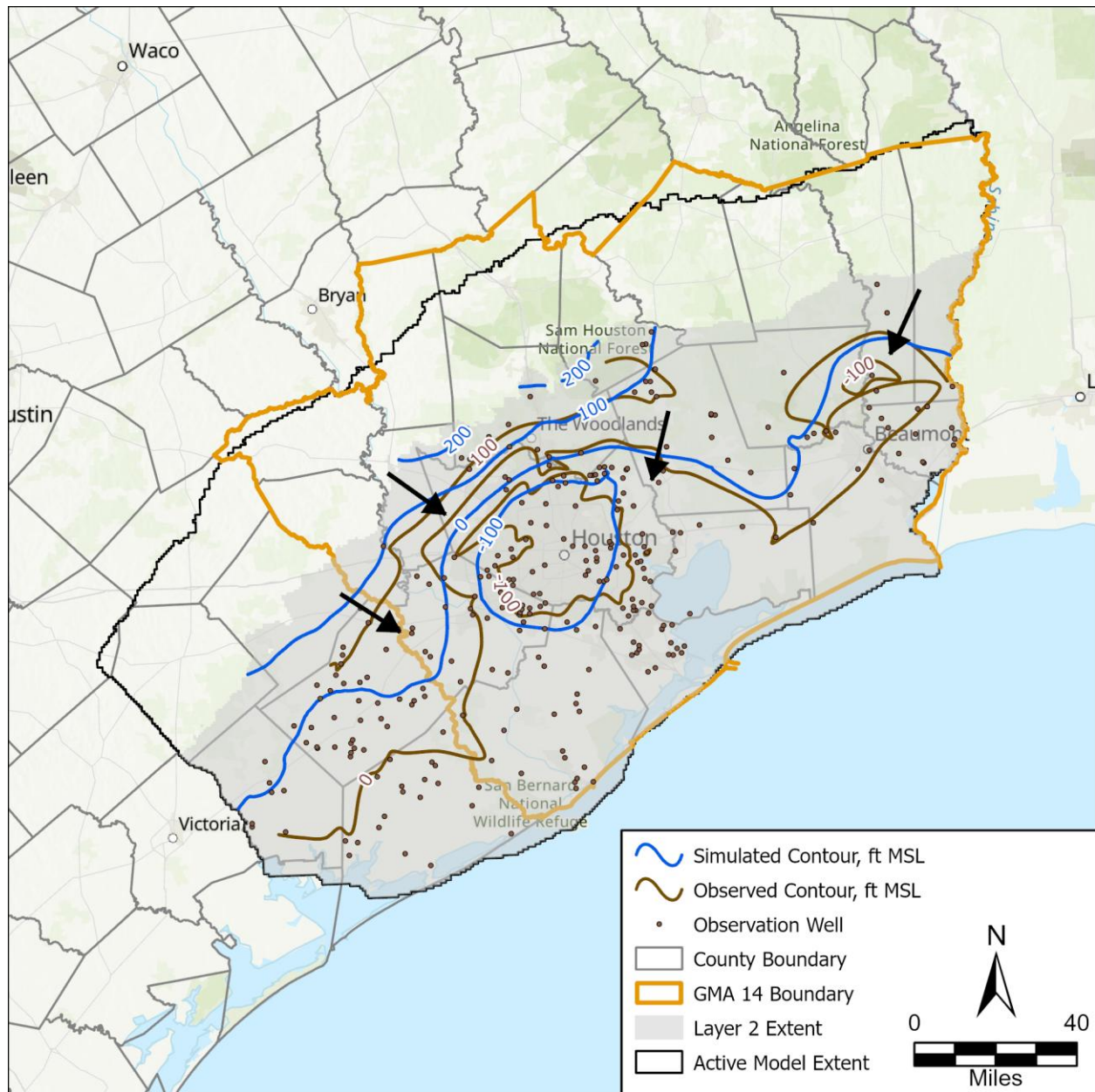


Figure 114. Layer 2 (Chicot Aquifer) simulated versus observed water levels. Arrows indicate approximate direction of regional flow.

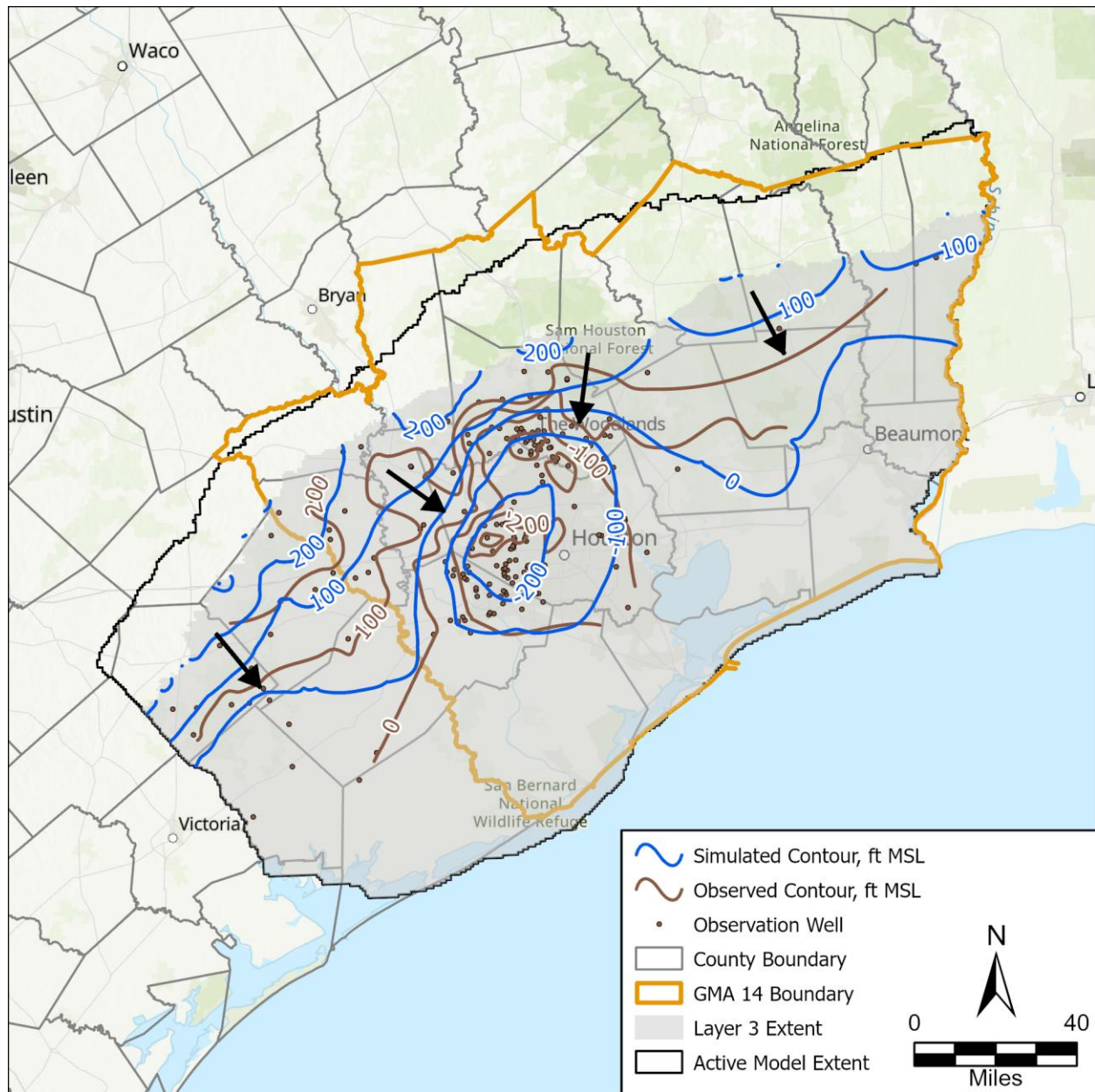


Figure 115. Layer 3 (Evangeline Aquifer) simulated versus observed water levels. Arrows indicate approximate direction of regional flow.

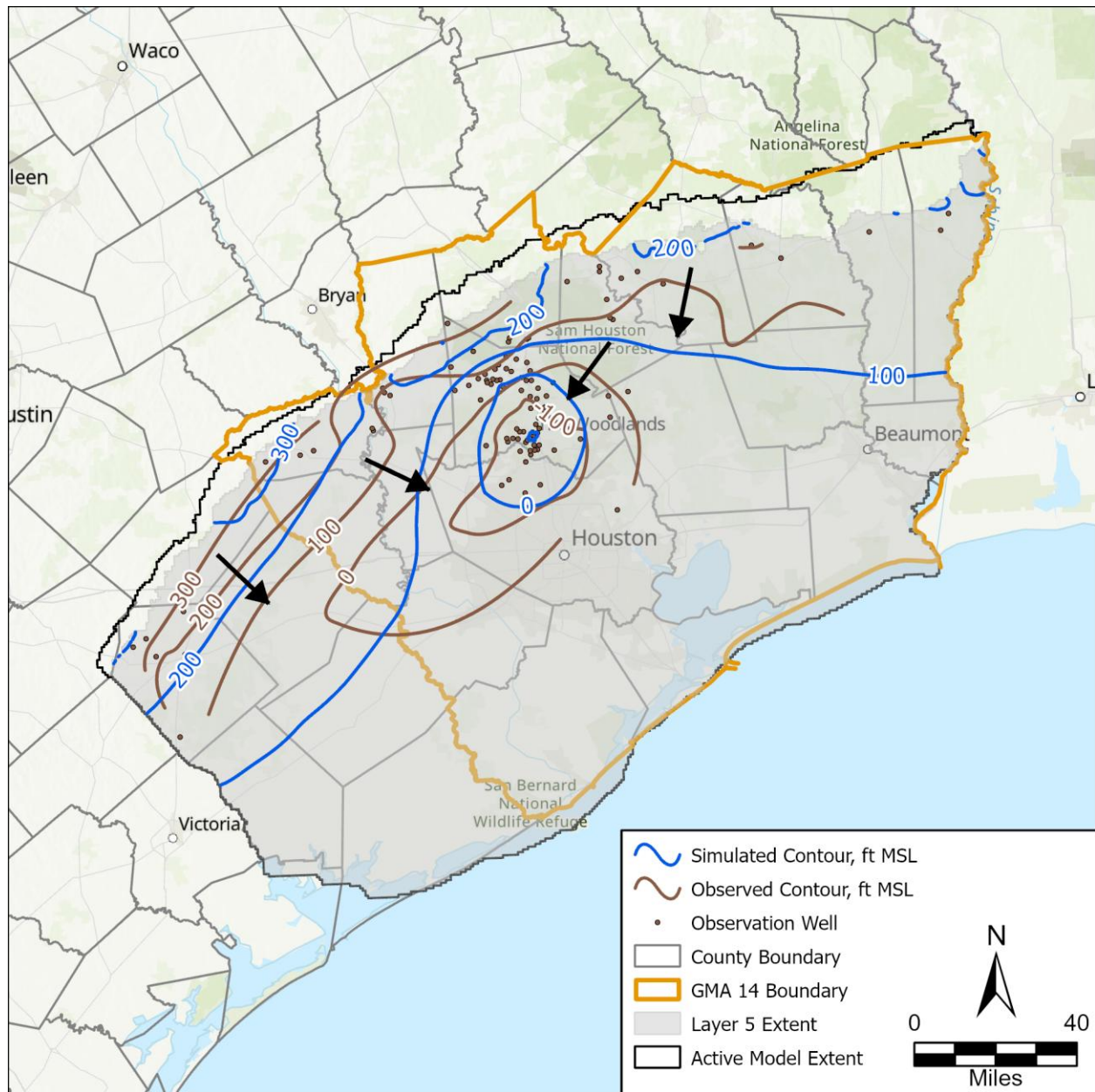


Figure 116. Layer 5 (Jasper Aquifer) simulated vs observed water levels. Arrows indicate approximate direction of regional flow.

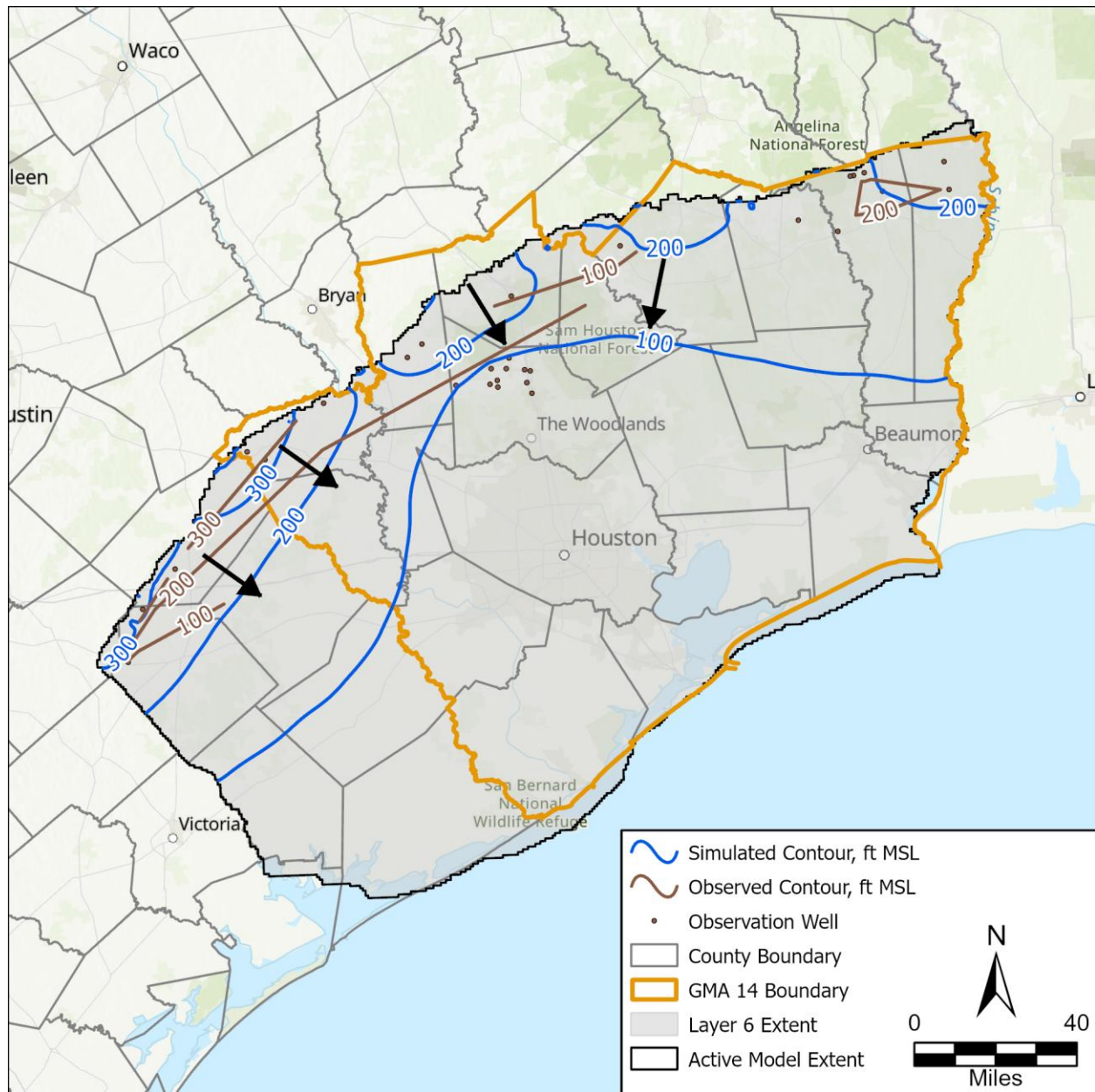


Figure 117. Layer 6 (Catahoula Aquifer) simulated vs observed water levels. Arrows indicate approximate direction of regional flow.

4.3. Model Simulated Versus Measured Compaction and Subsidence

4.3.1. Compaction and Subsidence

Table 14 summarizes the summary statistics for the compaction and subsidence targets. The calibration statistics are calculated with the same formulas outlined in Section 4.2. The Mean Residual of 0.03 feet indicates the GMA 14 Model simulated subsidence is unbiased. The Mean Absolute Residual is 0.17 feet indicating the magnitude of the residual was slightly over simulated. A Normalized RMSE less than 10 percent indicates a reasonable calibration which the GMA 14 Model achieved with a value of 3.85 percent.

Cross plots of the observed and simulated compaction and subsidence targets are illustrated in Figures 118 through 120 by station type. The perfect fit line is represented as the black dotted line in each plot with values closer to the perfect fit line indicating a perfect match between the observed and simulated value. As indicated with the mean error, the cross plots can show if the model produces over- or under- simulated compaction/subsidence.

The global positioning system (“GPS”) station targets generally surround and are close to the perfect fit line, indicating a good match between observed and simulated targets and that values are not bias in either direction. The simulated compaction from the extensometer stations was generally under simulated but followed the perfect fit line. Except for a few values, the benchmark station targets also surrounded the perfect fit line, indicating an unbiased fit between the simulated and observed targets. Figure 121 shows the simulated versus observed compaction and subsidence targets from all station types.

Table 14. Calibration statistics for compaction and subsidence targets.

Calibration Statistic	Value
Number of targets	2,551
Mean Residual, feet	0.03
Mean Absolute Residual, feet	0.17
Root Mean Squared Error, feet	0.32
Range, feet	8.27
Normalized RMSE (%)	3.85

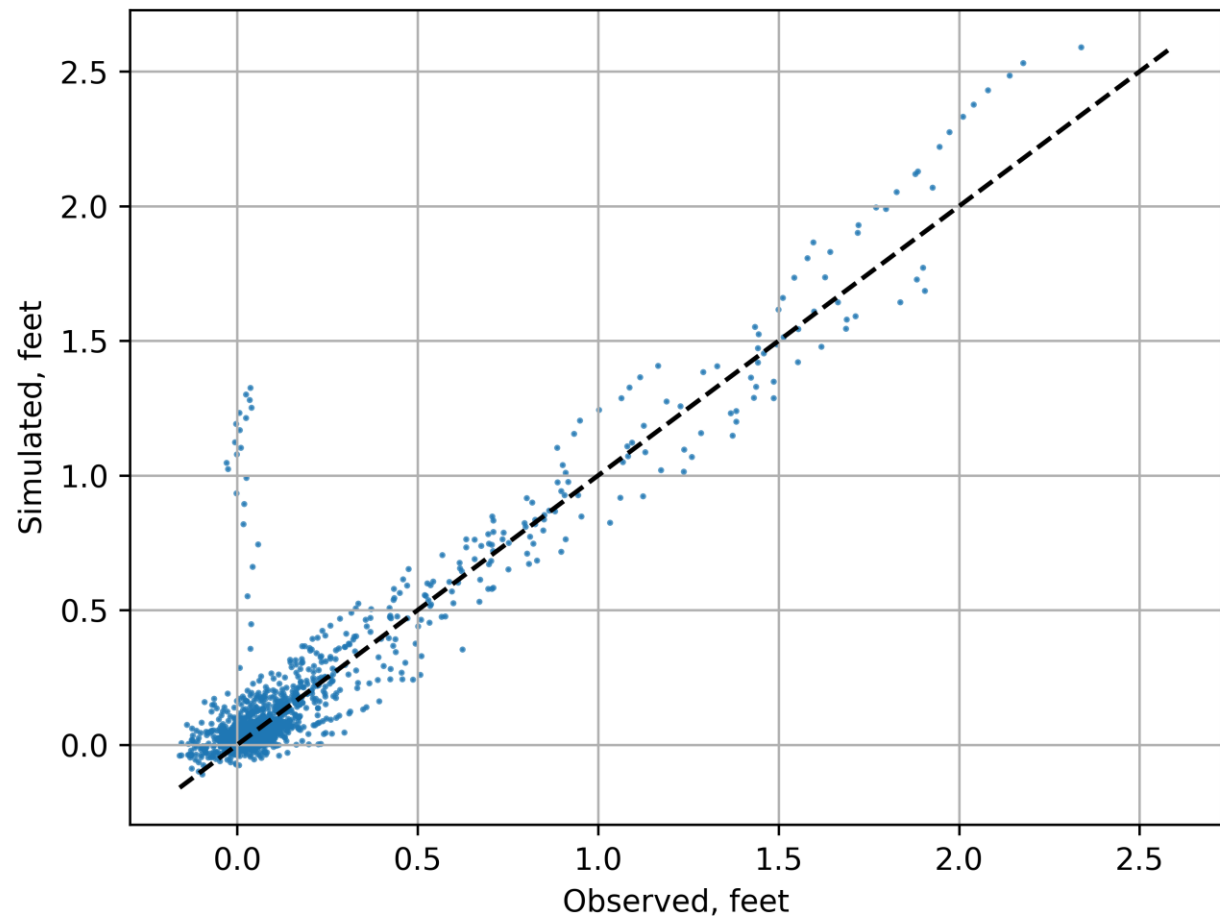


Figure 118. Observed versus simulated subsidence for global positioning system stations.

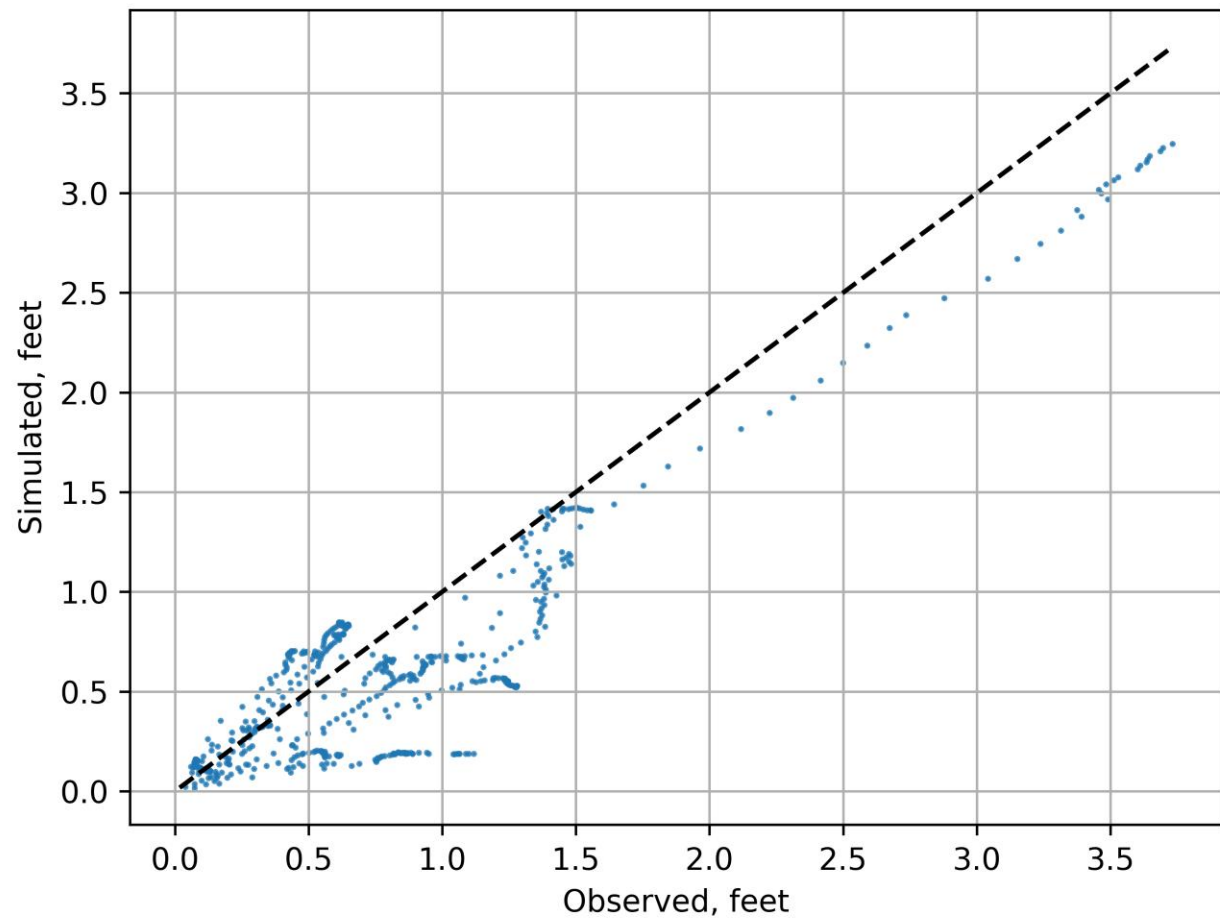


Figure 119. Observed versus simulated compaction for extensometer stations.

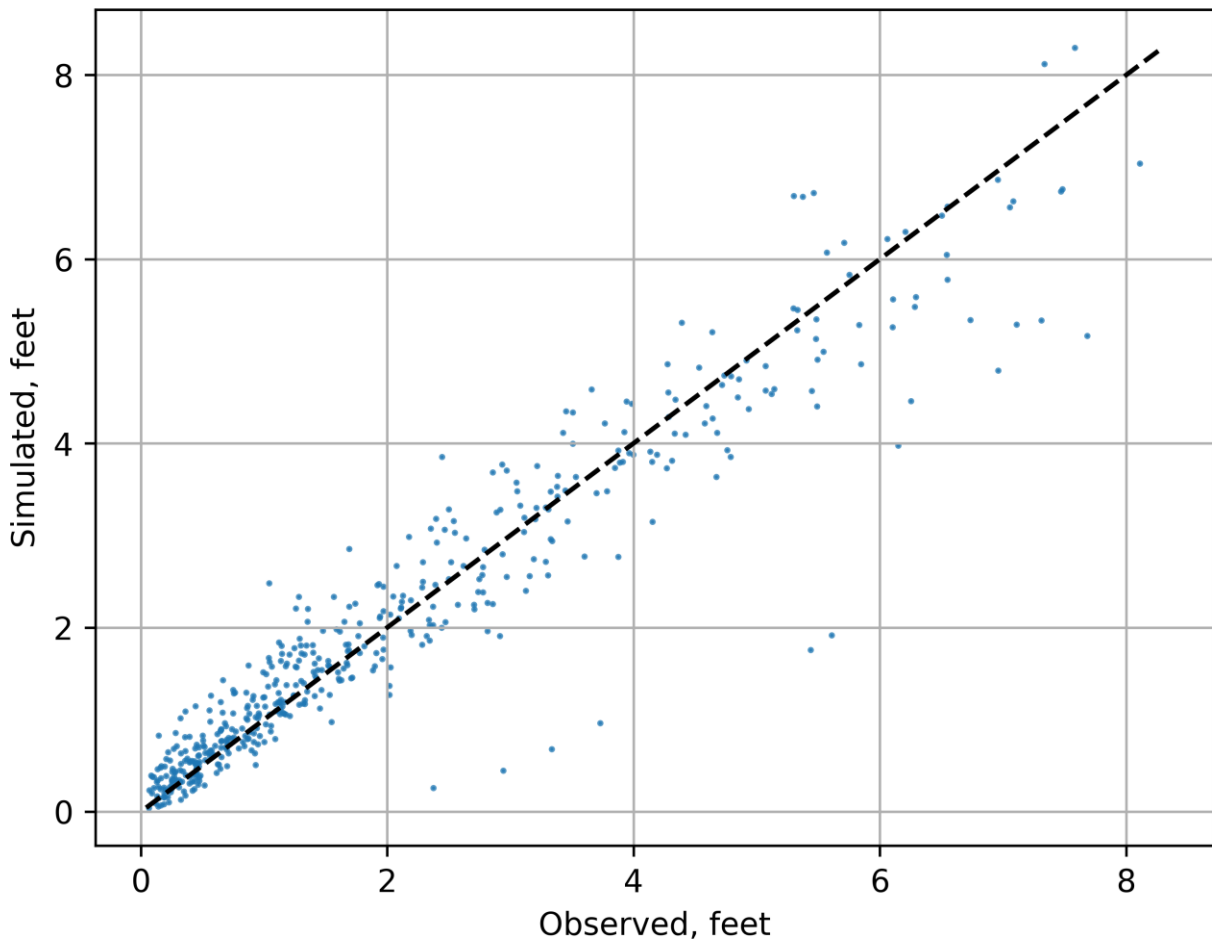


Figure 120. Observed versus simulated subsidence for benchmark locations.

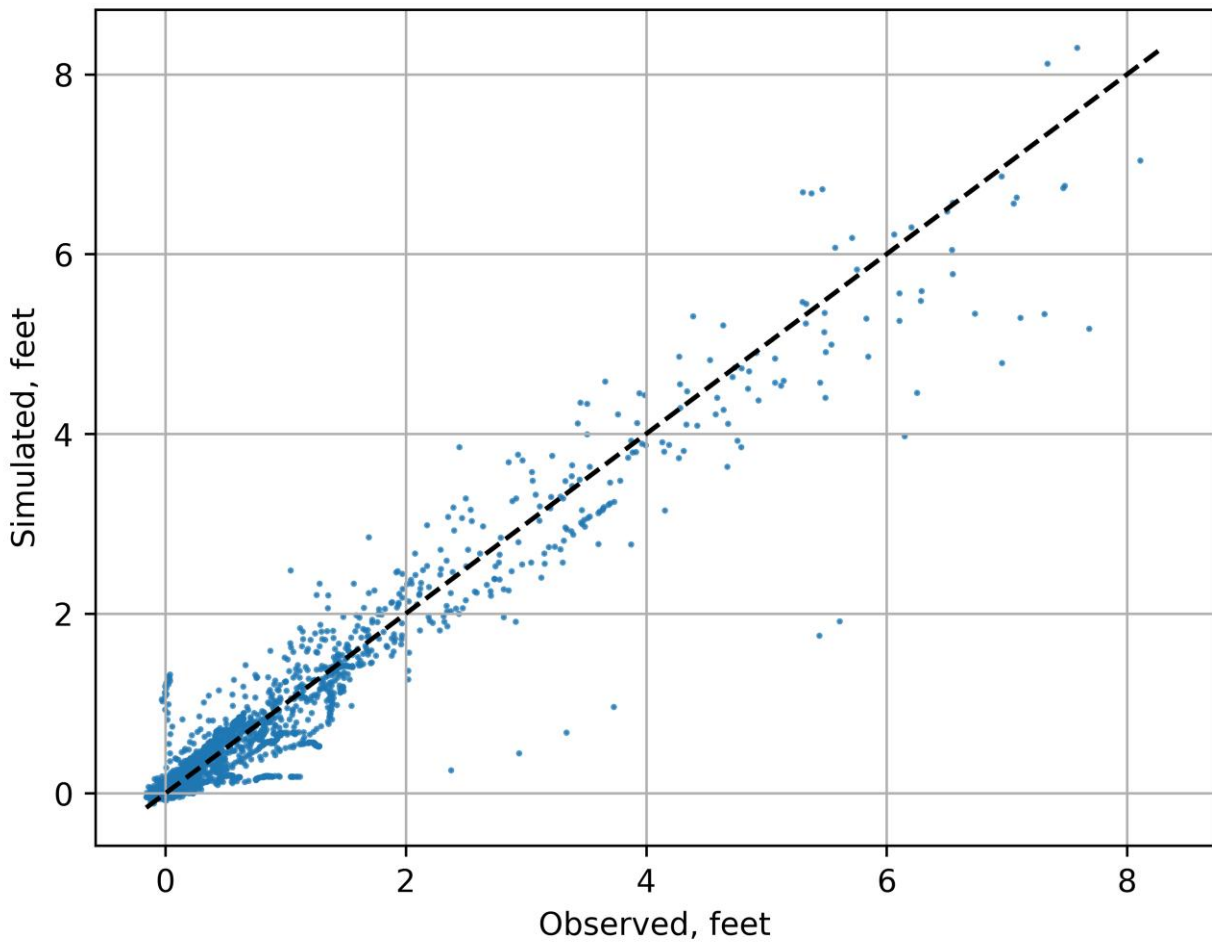


Figure 121. Observed versus simulated subsidence for all station types.

4.3.2. Residual Distribution

Figure 122 illustrates the spatial distribution of residuals for all compaction and subsidence target stations. The residuals for each station were averaged to get a mean residual per station. Overall, there is a similar amount of over simulated and under simulated mean residuals indicating no spatial bias in the simulated subsidence or compaction. Only areas with sufficient observed compaction or subsidence data can be evaluated for spatial bias. There is sparse compaction data beyond Harris County and the surrounding counties, so these areas were not evaluated.

Figure 123 illustrates the histogram of compaction and subsidence residuals for all stations. The ideal residual histogram would be symmetrical and centered around zero, indicating an unbiased distribution of residuals. Residuals were distributed around 0.03 feet with a symmetrical distribution indicating the simulated compaction and subsidence residuals were unbiased.

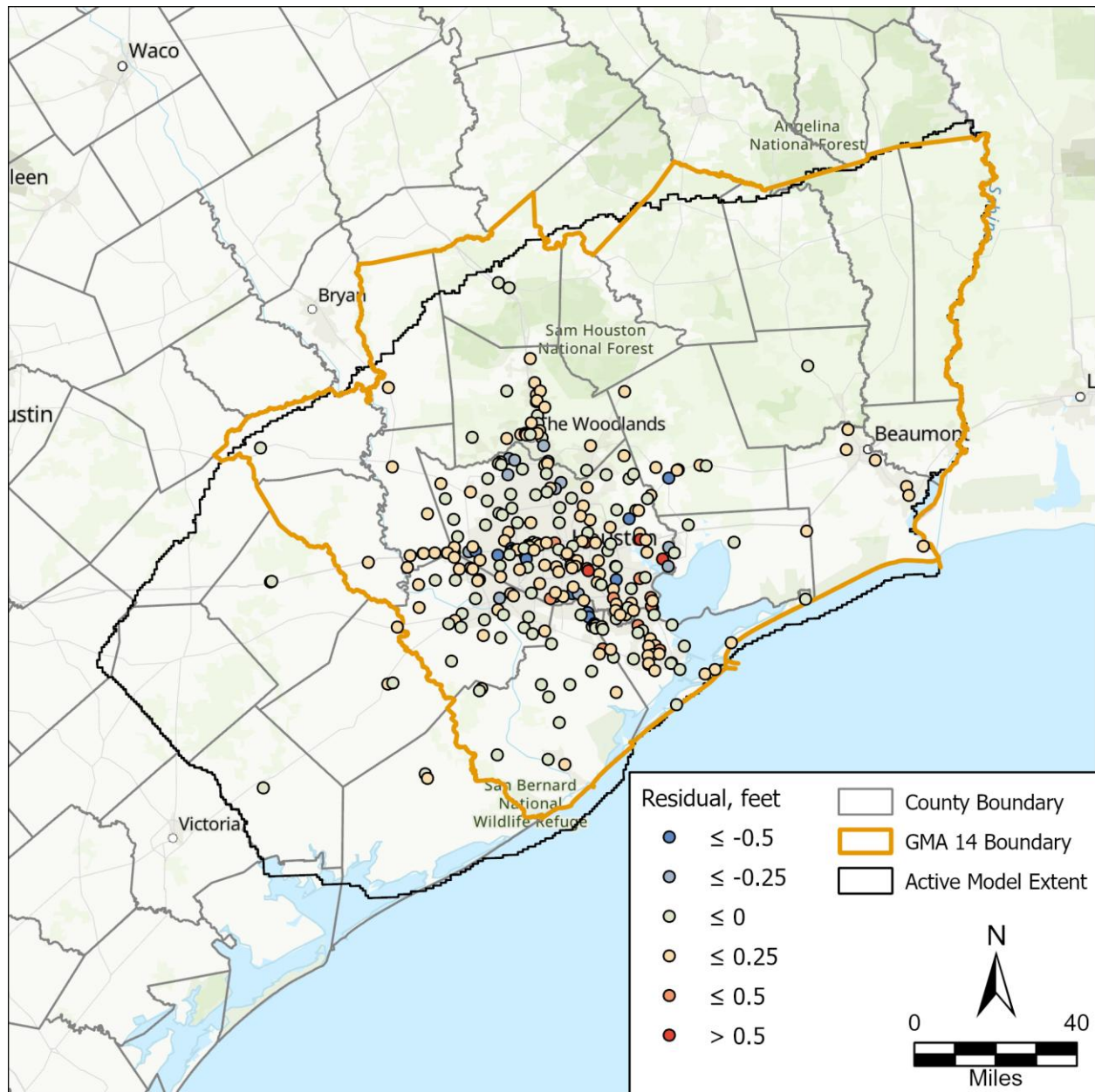


Figure 122. Compaction or subsidence mean residual by station.

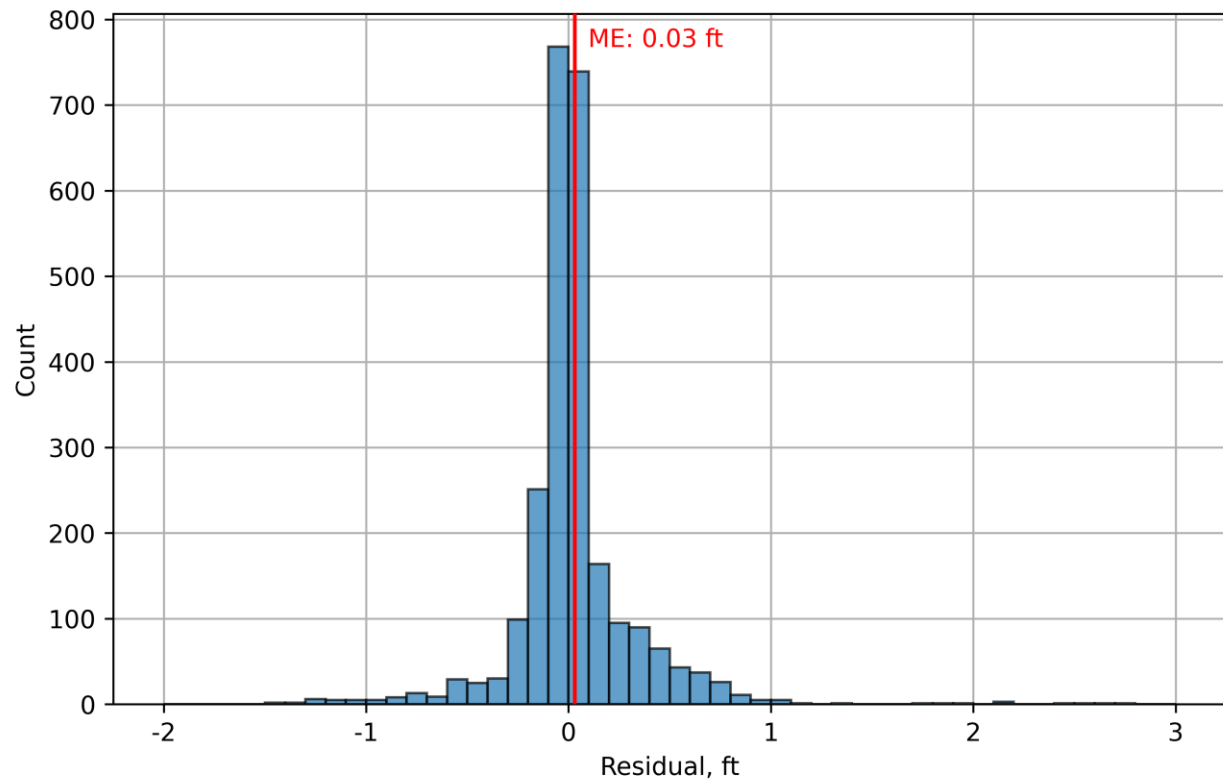


Figure 123. Residual histogram for compaction or subsidence targets. ME = mean error.

4.3.3. Compaction and Subsidence Time Series

Figure 124 show the subsidence and compaction time series of two extensometer sites and two global positioning system sites. The extensometer sites partially penetrate the Evangeline and are measuring compaction between the base of the extensometer and near land surface rather than subsidence as noted by the y-axis label. Since the global positioning system stations are recording land deformation, the y axis is labeled as subsidence. Appendix 8 contains time series charts of the measured and GMA 14 Model simulated compaction and subsidence.

The global positioning system site in northern Montgomery County matches the amount of observed subsidence and the long-term trends. Global positioning system site P014 also shows similar subsidence from the GMA 14 Model compared to the observed values. Both Extensometer sites under simulate the measured compaction.

Figure 125 illustrates GMA 14 Model results at four global positioning system stations in Montgomery and Harris counties. In central Montgomery County the GMA 14 Model under simulates the observed subsidence as shown for global positioning system station TXCN. At site P012, the model over simulates the observed subsidence while the two other stations show a relatively close match between observed and simulated subsidence.

Figure 126 illustrates GMA 14 Model results at three extensometers and one global positioning system station in Harris County. The measured versus simulated values at the extensometer stations illustrate how the GMA 14 Model over predicts in some areas and under predicts in others. Overall, the charts on Figure 125 and Figure 126 illustrate the minimal bias of the GMA 14 Model.

GMA 14 Groundwater Availability Model

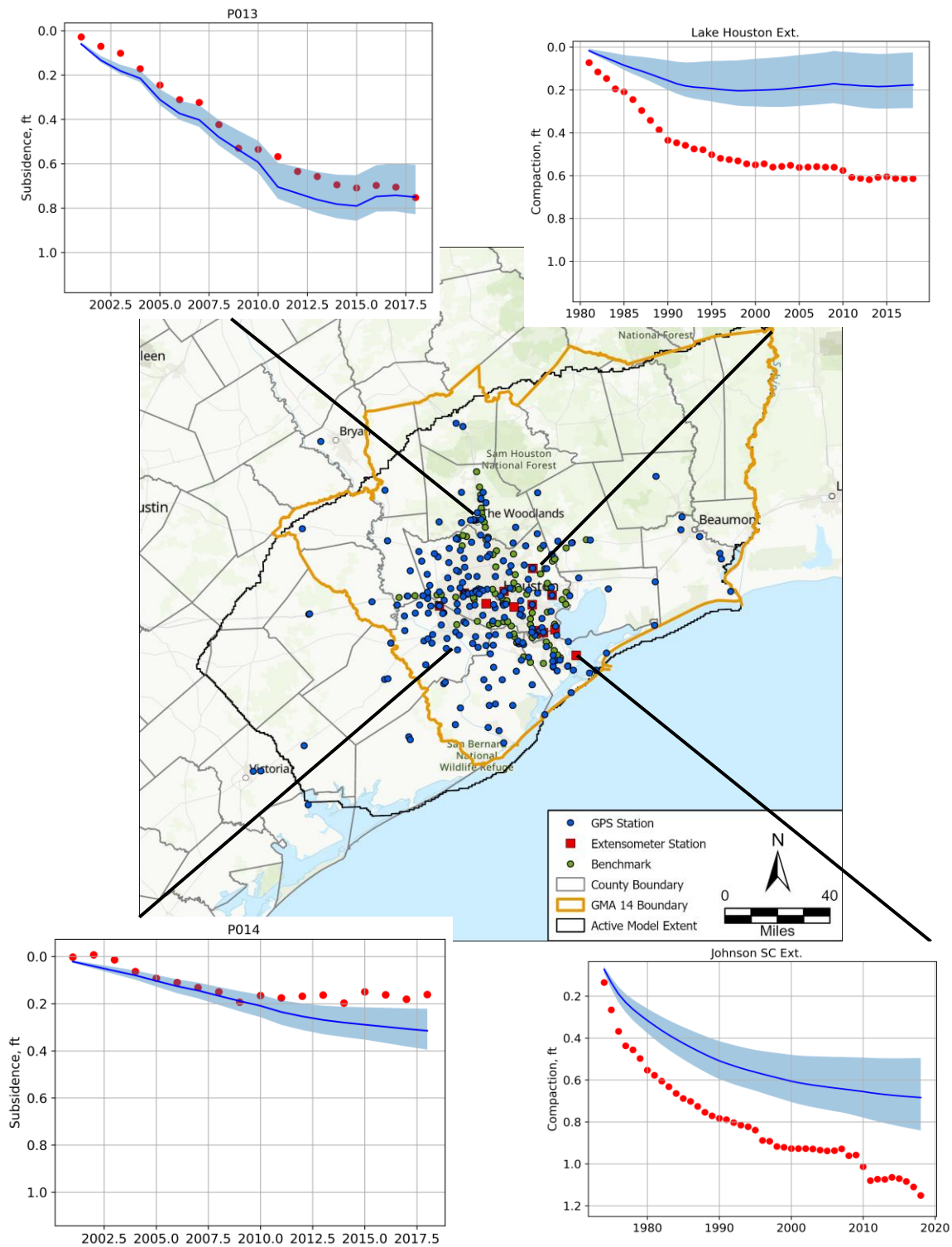


Figure 124. Compaction and subsidence simulated versus observed time series.

GMA 14 Groundwater Availability Model

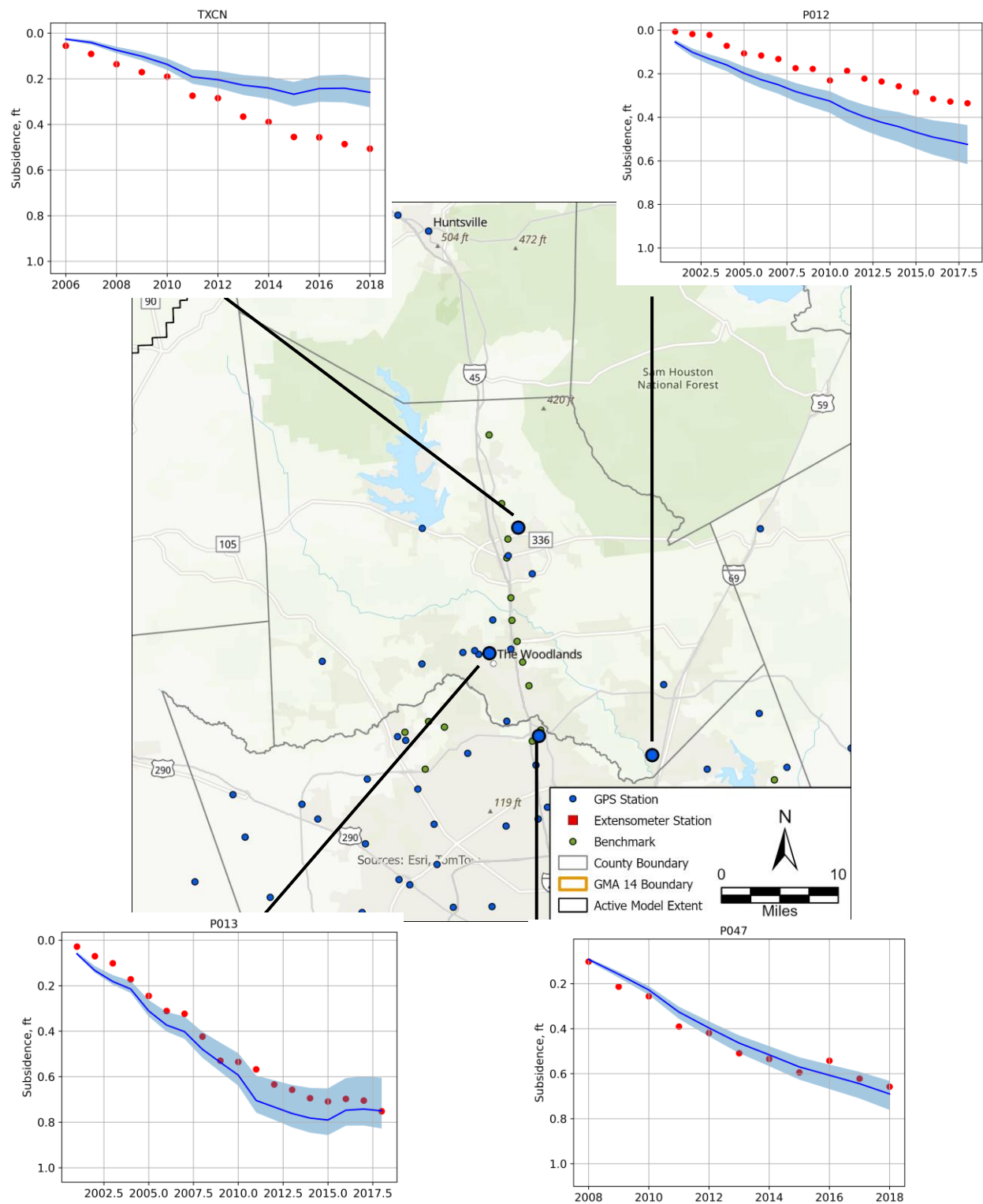


Figure 125. Subsidence simulated versus observed time series.

GMA 14 Groundwater Availability Model

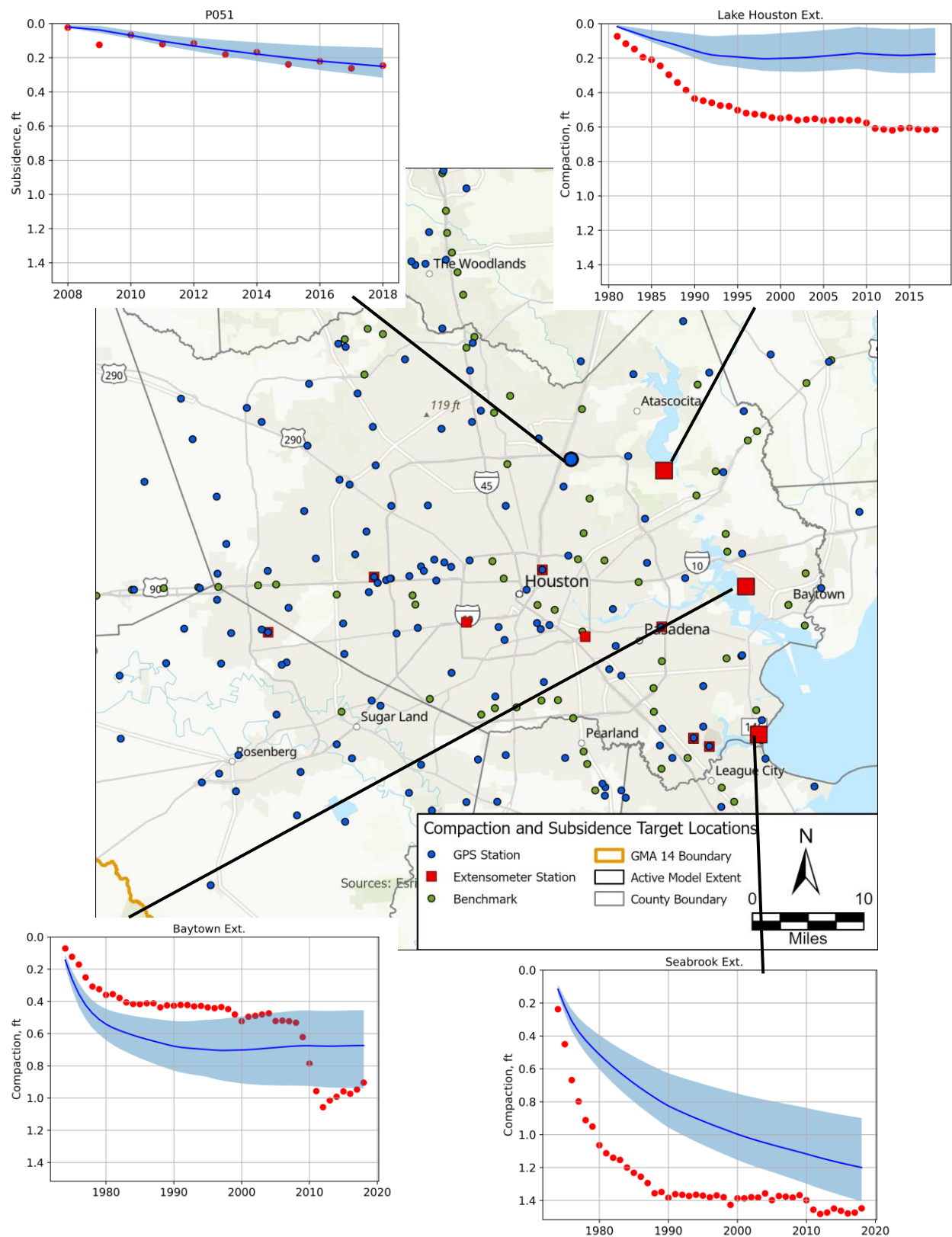


Figure 126. Compaction and Subsidence simulated versus observed time series.

4.3.4. Simulated Compaction and Subsidence

Figures 127 through 129 illustrate the compaction within the Chicot, Evangeline, and Jasper, respectively, from the end of predevelopment to 2018. The Burkeville and Catahoula layers did not have any compaction contours more than 0.5 feet and are not shown.

The simulated compaction within the Chicot was greatest around southeast Harris County reaching approximately five feet. The one-foot simulated compaction contours extend beyond Harris into neighboring counties. The GMA 14 Model also simulates compaction in the southwestern and eastern regions of model domain, but these areas did not have any benchmark or extensometer sites which were able to provide calibration data earlier than the global positioning system sites. The simulated compaction within the Evangeline centered around Harris County reaching a maximum of seven feet. The simulated compaction within the Jasper greater than 0.5 feet was contained within northern Montgomery County.

Figure 130 illustrates the subsidence due to all layers of the model from the end of predevelopment to 2018. The maximum simulated subsidence reaches approximately 10 feet in southeastern Harris County.

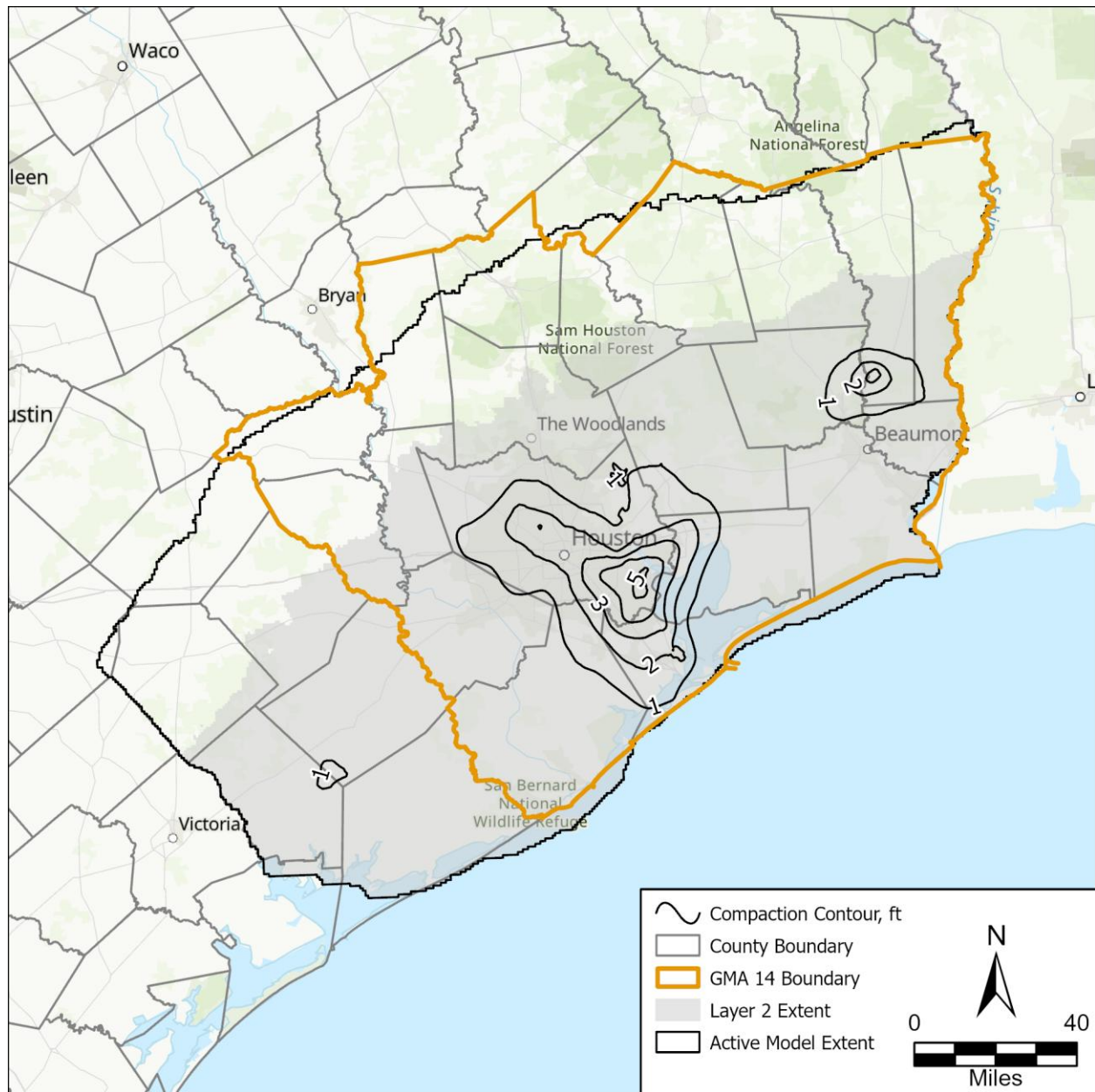


Figure 127. Simulated compaction from Layer 2 (Chicot Aquifer) between the end of predevelopment and the end of the calibration period (2018).

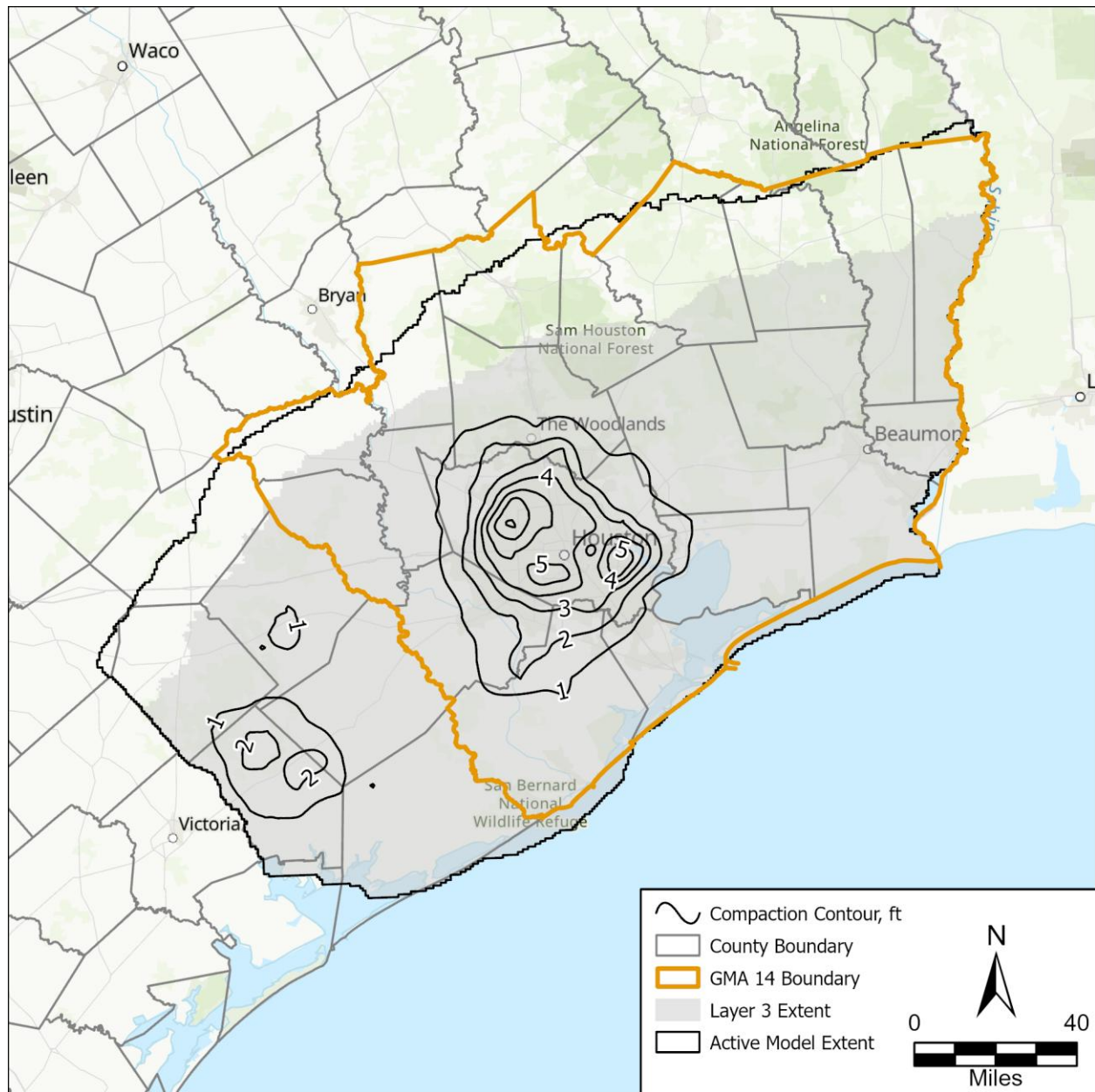


Figure 128. Simulated compaction from Layer 3 (Evangeline Aquifer) between the predevelopment period and the end of the calibration period (2018).

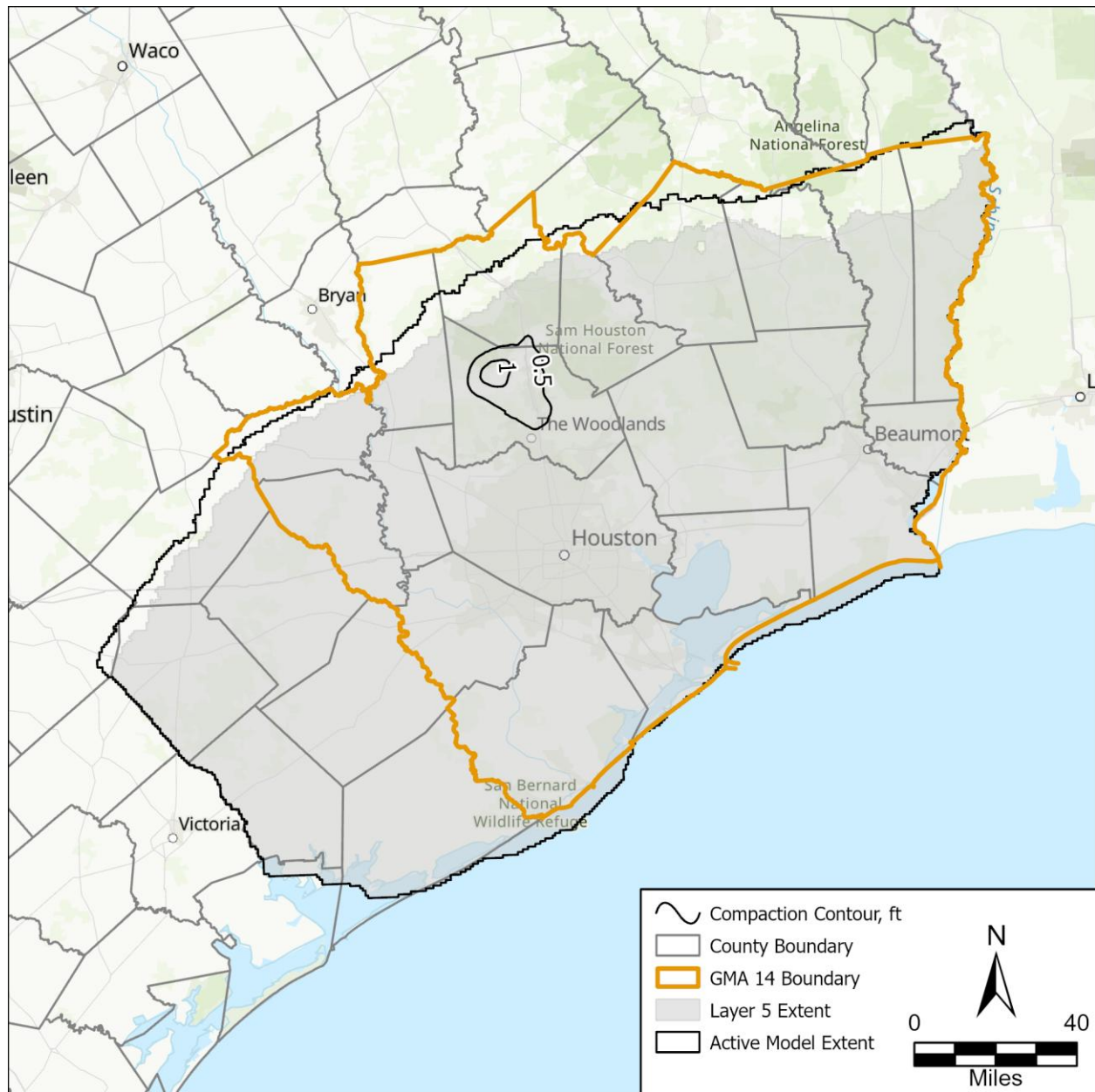


Figure 129. Simulated compaction from Layer 5 (Jasper Aquifer) between the predevelopment period and the end of the calibration period (2018).

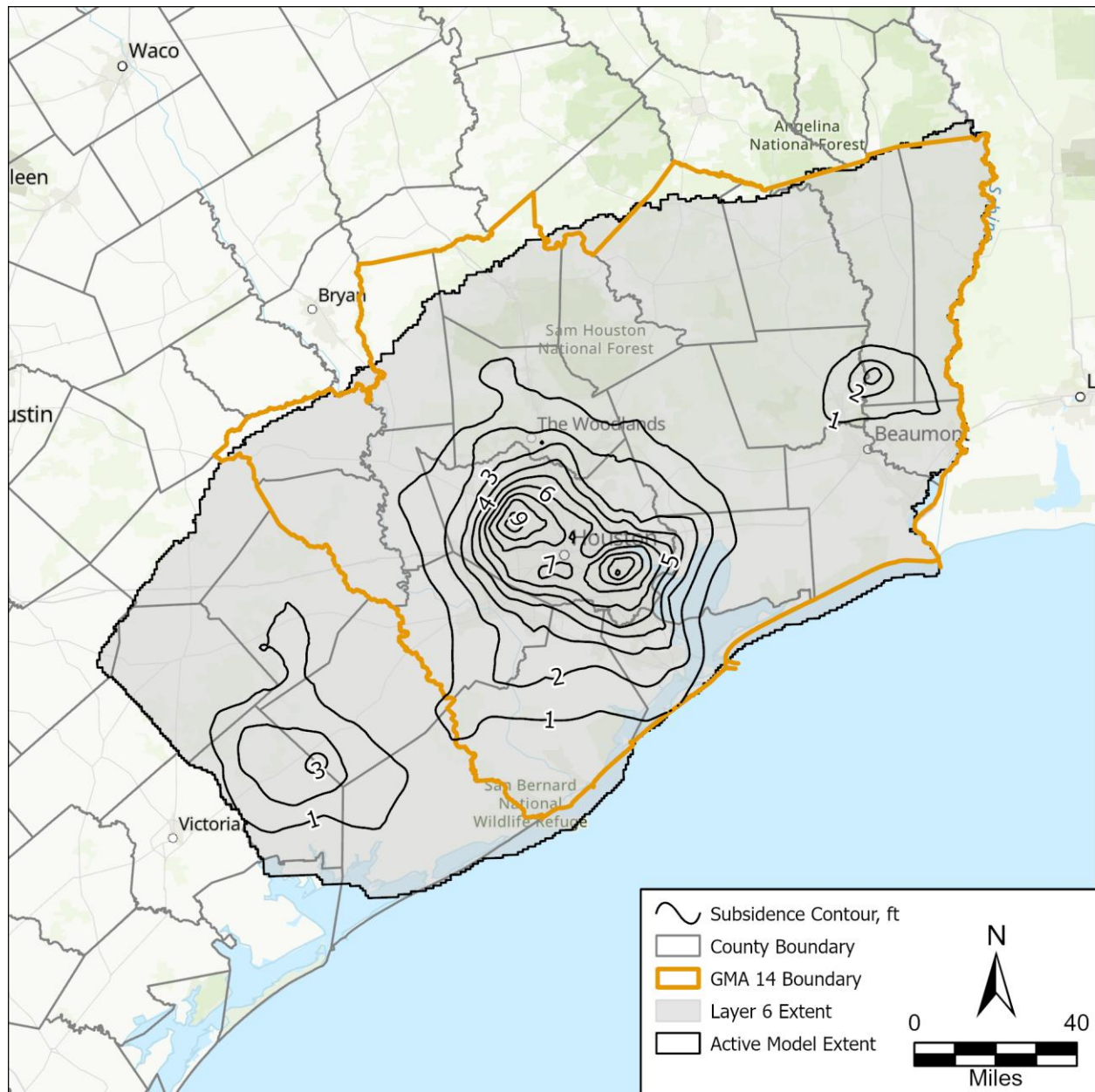


Figure 130. Simulated subsidence between the predevelopment period (1896) and the end of the calibration period (2018).

4.4. Simulated Water Budgets

We extracted the GMA 14 Model water budget results using ZONEBUDGET 6 (USGS, 2025b) and the cell-by-cell flows output from the model.

Table 15 summarizes the simulated water budget during steady state (that is, predevelopment) conditions. Table 16 summarizes the simulated net water budget during steady state conditions. Recharge contributed to the majority of the inflows to the model through layer 1. Recharge is only applied to layer 1 (shallow aquifer system) and thus is the only layer that receives recharge. Approximately 93 percent of the recharge that contributes to the shallow aquifer system exits the model via surface water simulated as drains and rivers. The remaining recharge, approximately 7 percent, contributes to layers 2 through 6. The outflow to rivers exceeded the inflow from rivers indicating that major rivers were gaining during the predevelopment period. Groundwater contributed to layers 2 through 6 then continue to deeper layers or contribute to the Gulf of Mexico through General Head Boundary cells. Layers 3 and 5, Evangeline and Jasper respectively, have a few wells and a minor amount of water is extracted through the well boundary condition. The percent difference between total inflows and total outflows is 0 percent indicating acceptable mass balance for the steady state GMA 14 Model.

Table 17 summarizes the simulated water budget for stress period 59 (2018) and Table 18 summarizes the simulated net water budget. Similar to the predevelopment period recharge was the major inflow component. Approximately 44 percent of recharge exited the model via surface water simulated with drain and river cells. Approximately 42 percent of the recharge contributed to layers 2 through 6, much higher than the 7 percent during the pre-development period. The inflow and outflows from rivers are similar, indicating that the major rivers are close to equilibrium with the groundwater system during 2018. Groundwater contributing to deeper layers is captured by wells with the Jasper and Catahoula also contributing to the Gulf of Mexico via general head boundary cells.

The storage component is divided into the contributions from coarse-grained material and fine-grained material (interbeds). The majority of the coarse-grained storage comes from areas with unconfined conditions which are most prevalent within the layer outcrops. As interbeds compact or expand, groundwater is released or added to interbed storage, respectively. The Chicot and Evangeline show the highest amount of groundwater released from interbed storage which is consistent with the majority of compaction occurring within these layers throughout the calibration period.

Table 15. Steady state simulated water budget by layer (values in acre-feet).

Budget Component	Layer 1	Layer 2	Layer 3	Layer 4	Layer 5	Layer 6	Total
<u>Inflows</u>							
Coarse-grained Storage	0	0	0	0	0	0	0
Interbed Storage	0	0	0	0	0	0	0
Water Compressibility	0	0	0	0	0	0	0
Wells	0	0	0	0	0	0	0
Drains	0	0	0	0	0	0	0
Rivers	5,768	0	0	0	0	0	5,768
General Head Boundary	1,207	268	269	0	0	0	1,744
Recharge	789,188	0	0	0	0	0	789,188
Vertical Leakage (Upper)	0	80,892	50,304	334	25,461	48,647	205,638
Vertical Leakage (Lower)	114,970	36,754	344	431	16,148	0	168,647
Total Inflows	911,133	117,914	50,917	765	41,609	48,647	1,170,985
<u>Outflows</u>							
Coarse-grained Storage	0	0	0	0	0	0	0
Interbed Storage	0	0	0	0	0	0	0
Water Compressibility	0	0	0	0	0	0	0
Wells	0	0	1,046	0	645	0	1,691
Drains	693,026	0	0	0	0	0	693,026
Rivers	46,268	0	0	0	0	0	46,268
General Head Boundary	4,178	7,952	8,869	462	14,533	19,723	55,717
Recharge	0	0	0	0	0	0	0
Vertical Leakage (Upper)	0	90,140	40,359	232	8,990	28,926	168,647
Vertical Leakage (Lower)	167,660	19,822	644	71	17,442	0	205,639
Total Outflows	911,132	117,914	50,918	765	41,610	48,649	1,170,988
Total In - Total Out	1	0	-1	0	-1	-2	-3
Percent Difference	0%	0%	0%	0%	0%	0%	0%

Table 16. Steady state net simulated water budget by layer (values in acre-feet).

Budget Component	Layer 1	Layer 2	Layer 3	Layer 4	Layer 5	Layer 6	Total
Coarse-grained Storage	0	0	0	0	0	0	0
Interbed Storage	0	0	0	0	0	0	0
Water Compressibility	0	0	0	0	0	0	0
Wells	0	0	-1,046	0	-645	0	-1,691
Drains	-693,026	0	0	0	0	0	-693,026
Rivers	-40,500	0	0	0	0	0	-40,500
General Head Boundary	-2,971	-7,684	-8,600	-462	-14,533	-19,723	-53,973
Recharge	789,188	0	0	0	0	0	789,188
Vertical Leakage (Upper)	0	-9,248	9,945	102	16,471	19,721	36,991
Vertical Leakage (Lower)	-52,690	16,932	-300	360	-1,294	0	-36,992

Table 17. Stress Period 59 (2018) simulated water budget by layer (values in acre-feet).

Budget Component	Layer 1	Layer 2	Layer 3	Layer 4	Layer 5	Layer 6	Total
<u>Inflows</u>							
Coarse-grained Storage	127,964	212,401	38,324	421	24,212	15,292	418,614
Interbed Storage	0	19,184	34,610	410	12,245	0	66,449
Water Compressibility	6	465	2,888	141	900	1,705	6,105
Wells	0	0	0	0	0	0	0
Drains	0	0	0	0	0	0	0
Rivers	26,716	0	0	0	0	0	26,716
General Head Boundary	3,493	14,705	14,665	0	0	0	32,863
Recharge	1,264,132	0	0	0	0	0	1,264,132
Vertical Leakage (Upper)	0	436,947	255,818	283	32,698	65,198	790,944
Vertical Leakage (Lower)	19,772	39,667	1,121	298	27,271	0	88,129
Total Inflows	1,442,083	723,369	347,426	1,553	97,326	82,195	2,693,952
<u>Outflows</u>							
Coarse-grained Storage	310,040	9,558	536	1	704	594	321,433
Interbed Storage	0	1,908	1,954	16	50	0	3,928
Water Compressibility	70	179	176	0	16	7	448
Wells	0	491,486	302,576	0	51,604	30,179	875,845
Drains	560,265	0	0	0	0	0	560,265
Rivers	25,414	0	0	0	0	0	25,414
General Head Boundary	1,264	0	0	396	11,250	15,270	28,180
Recharge	0	0	0	0	0	0	0
Vertical Leakage (Upper)	0	4,688	41,257	1,130	4,908	36,146	88,129
Vertical Leakage (Lower)	545,029	215,561	1,080	480	28,793	0	790,943
Total Outflows	1,442,082	723,380	347,579	2,023	97,325	82,196	2,694,585
Total In - Total Out	1	-11	-153	-470	1	-1	-633
Percent Difference	0%	0%	0%	-26%	0%	0%	0%

Table 18. Stress period 59 (2018) net simulated water budget by layer (values in acre-feet).

Budget Component	Layer 1	Layer 2	Layer 3	Layer 4	Layer 5	Layer 6	Total
Coarse-grained Storage	-182,076	202,843	37,788	420	23,508	14,698	97,181
Interbed Storage	0	17,276	32,656	394	12,195	0	62,521
Water Compressibility	-64	286	2712	141	884	1698	5,557
Wells	0	-491,486	-302,576	0	-51,604	-30,179	-875,845
Drains	-560,265	0	0	0	0	0	-560,265
Rivers	1,302	0	0	0	0	0	1,302
General Head Boundary	2,229	14,705	14,665	-396	-11,250	-15,270	4,683
Recharge	1,264,132	0	0	0	0	0	1,264,132
Vertical Leakage (Upper)	0	432,259	214,561	-847	27,790	29,052	702,815
Vertical Leakage (Lower)	-525,257	-175,894	41	-182	-1,522	0	-702,814

Figures 131 and 132 illustrate the transient simulated water budget and net water budget by component for the Chicot Aquifer. The major outflow component is pumping from wells which ramp up over time. With the increase in pumping there is an increase in cross formation flow from the shallow aquifer system with a portion of this flow continuing to underlying layers. Water released from storage also increases with increasing pumping where the majority is derived from coarse-grained storage. After the predevelopment period, the model contributes to the Gulf of Mexico but as pumping increases the flux transitions to the Gulf of Mexico contributing to the model.

Figures 133 and 134 illustrate the transient simulated water budget and net water budget by component for the Evangeline Aquifer. Similar to the Chicot, the water released from storage and the vertical leakage from the above layers increase over time with pumping. Since the underlying layer is the Burkeville, leakage from the lower units is insignificant.

Figures 135 and 136 illustrate the transient simulated water budget and net water budget by component for the Jasper Aquifer. Similar to the above layers, the vertical leakage from overlying and underlying layers increases along with water from storage as pumping increases. Unlike the above layers, the Jasper losses groundwater to the Gulf of Mexico throughout the entire calibration period.

Figures 137 and 138 illustrate the transient simulated water budget and net water budget by component for the Catahoula Aquifer. The major budget component over time is the vertical leakage to overlying layers. A minor amount of pumping is within the Catahoula but is mostly offset by the water released from storage due to a decline in water levels. The Catahoula also losses groundwater to the Gulf of Mexico throughout the calibration period.

Appendix 9 summarizes the simulated water budgets by county and aquifer and by Groundwater Conservation District and aquifer for each stress period.

GMA 14 Groundwater Availability Model

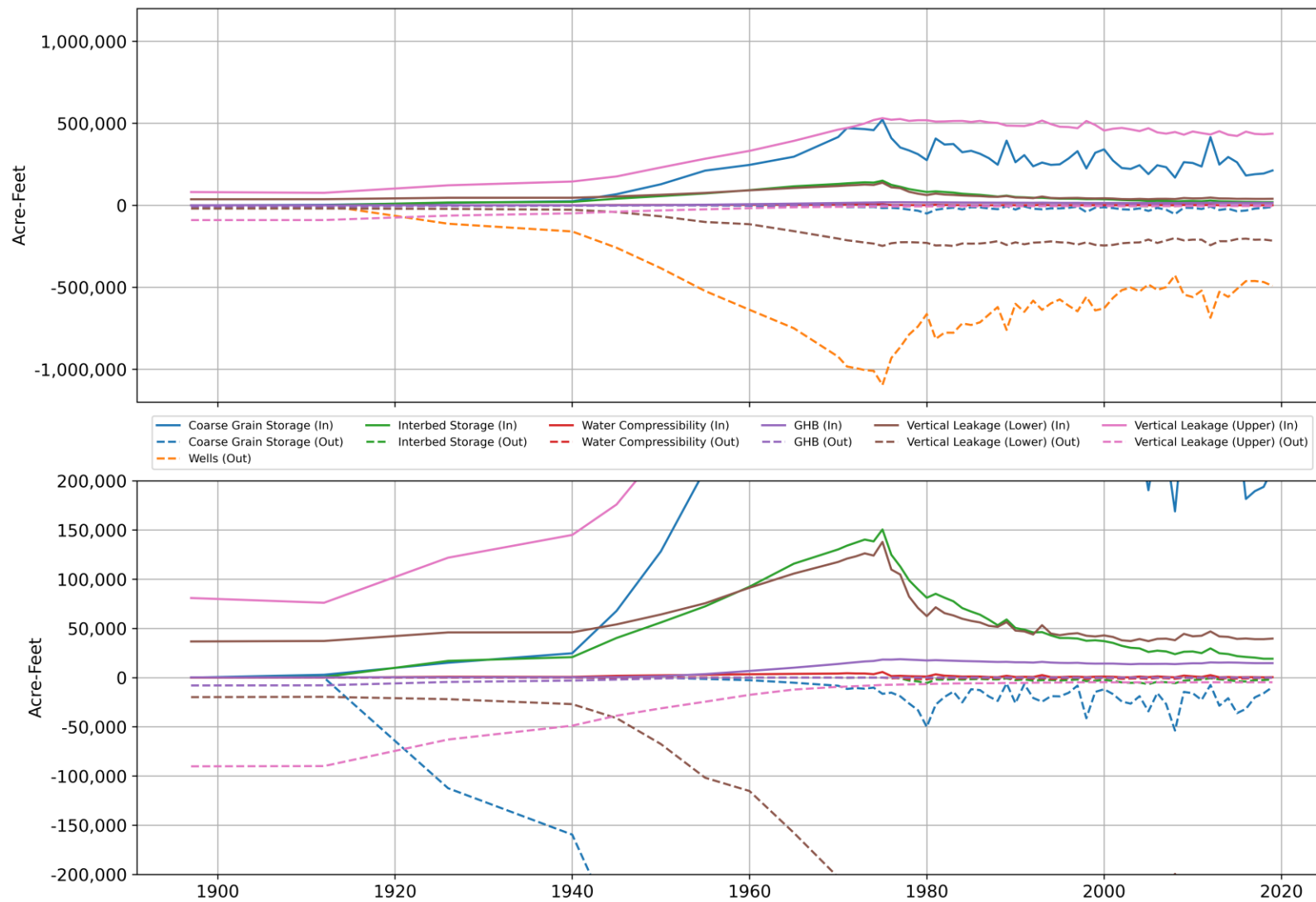


Figure 131. Layer 2 (Chicot) transient simulated water budget for the calibration period (1896 – 2018). Lower plot is zoomed in to visualize minor components of the simulated budget.

GMA 14 Groundwater Availability Model

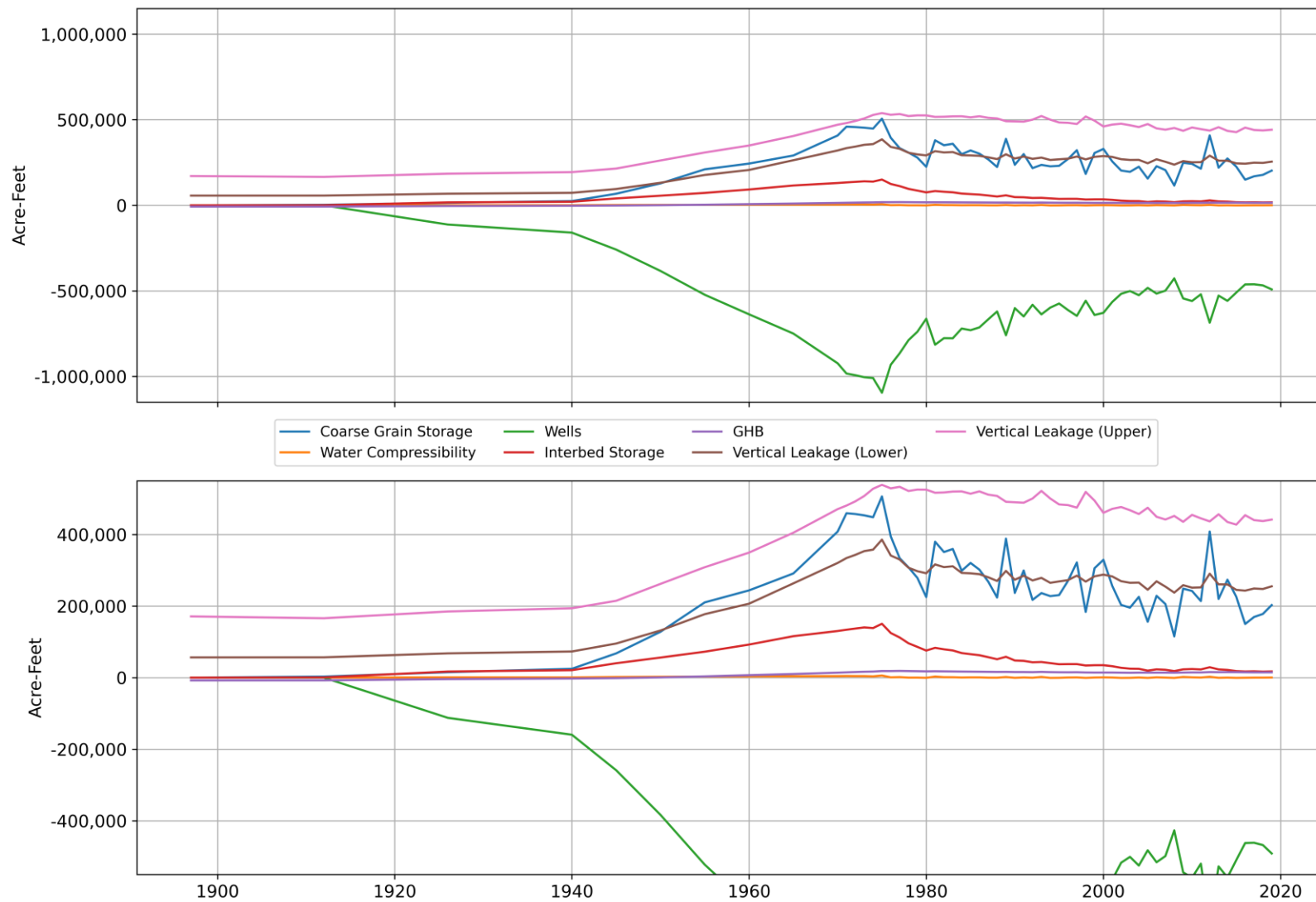


Figure 132. Layer 2 (Chicot) transient simulated net water budget for the calibration period (1896 – 2018). Lower plot is zoomed in to visualize minor components of the simulated budget.

GMA 14 Groundwater Availability Model

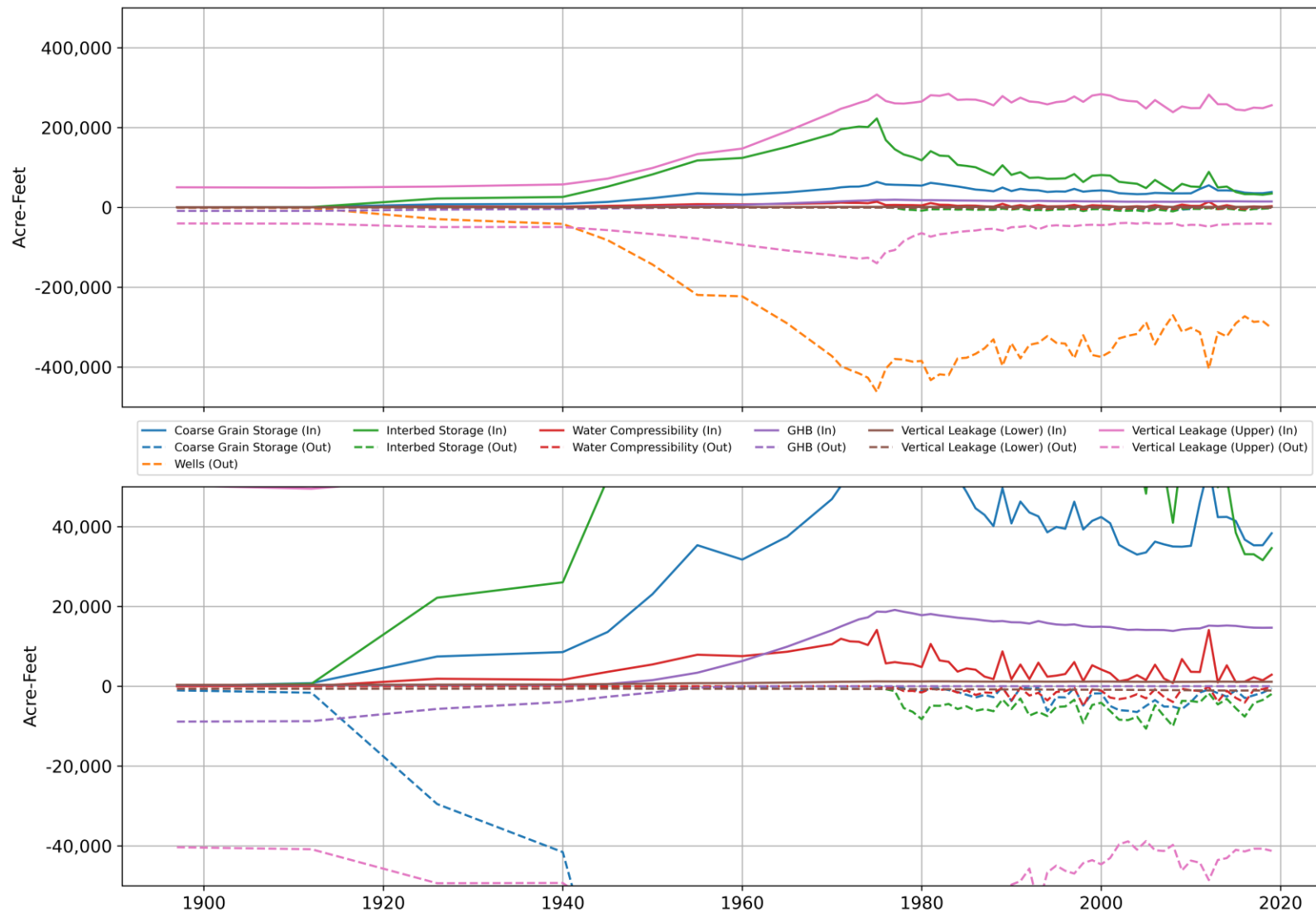


Figure 133. Layer 3 (Evangeline Aquifer) transient simulated water budget for the calibration period (1896 – 2018). Lower plot is zoomed in to visualize minor components of the simulated budget.

GMA 14 Groundwater Availability Model

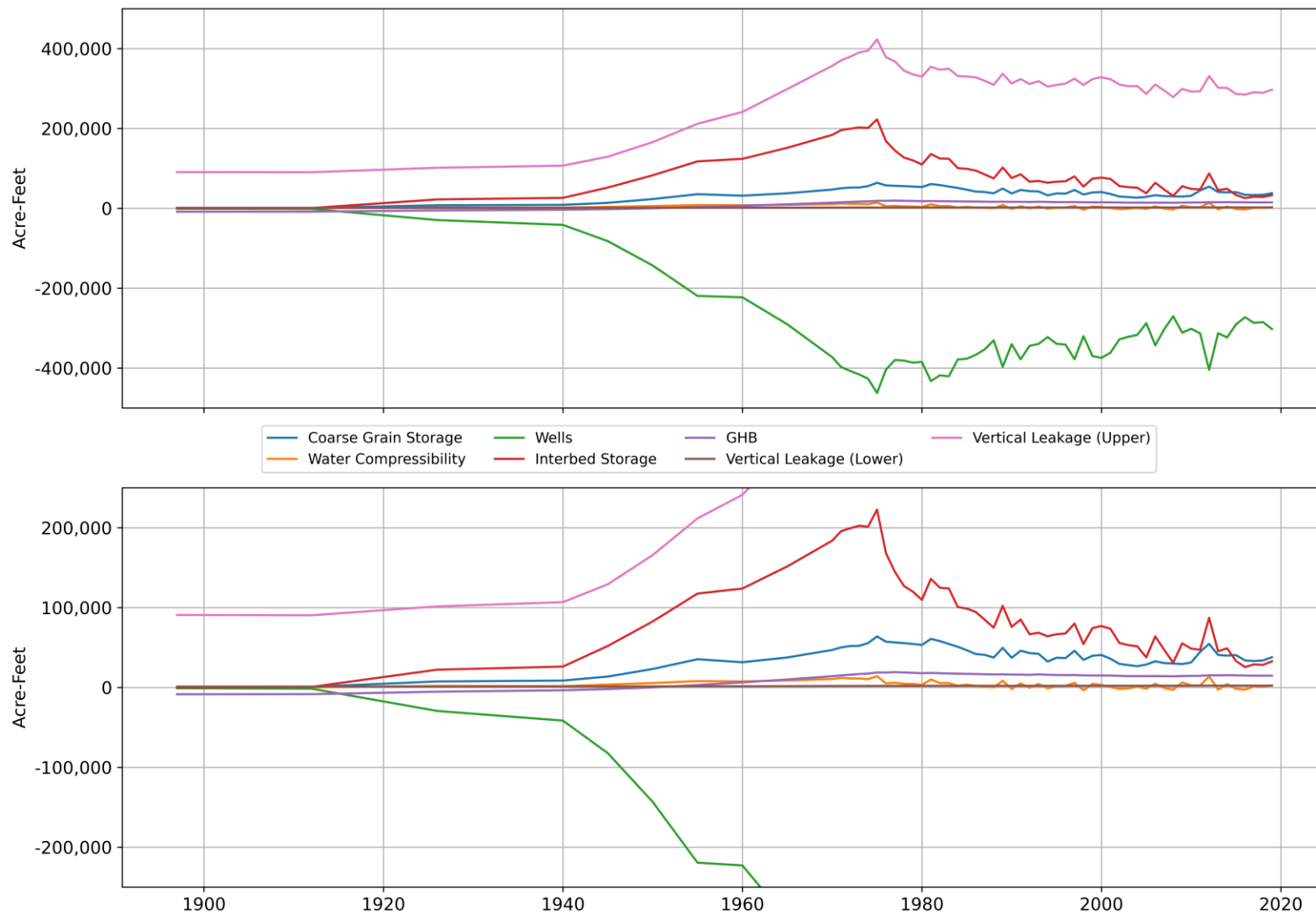


Figure 134. Layer 3 (Evangeline Aquifer) transient simulated net water budget for the calibration period (1896 – 2018). Lower plot is zoomed in to visualize minor components of the simulated budget.

GMA 14 Groundwater Availability Model

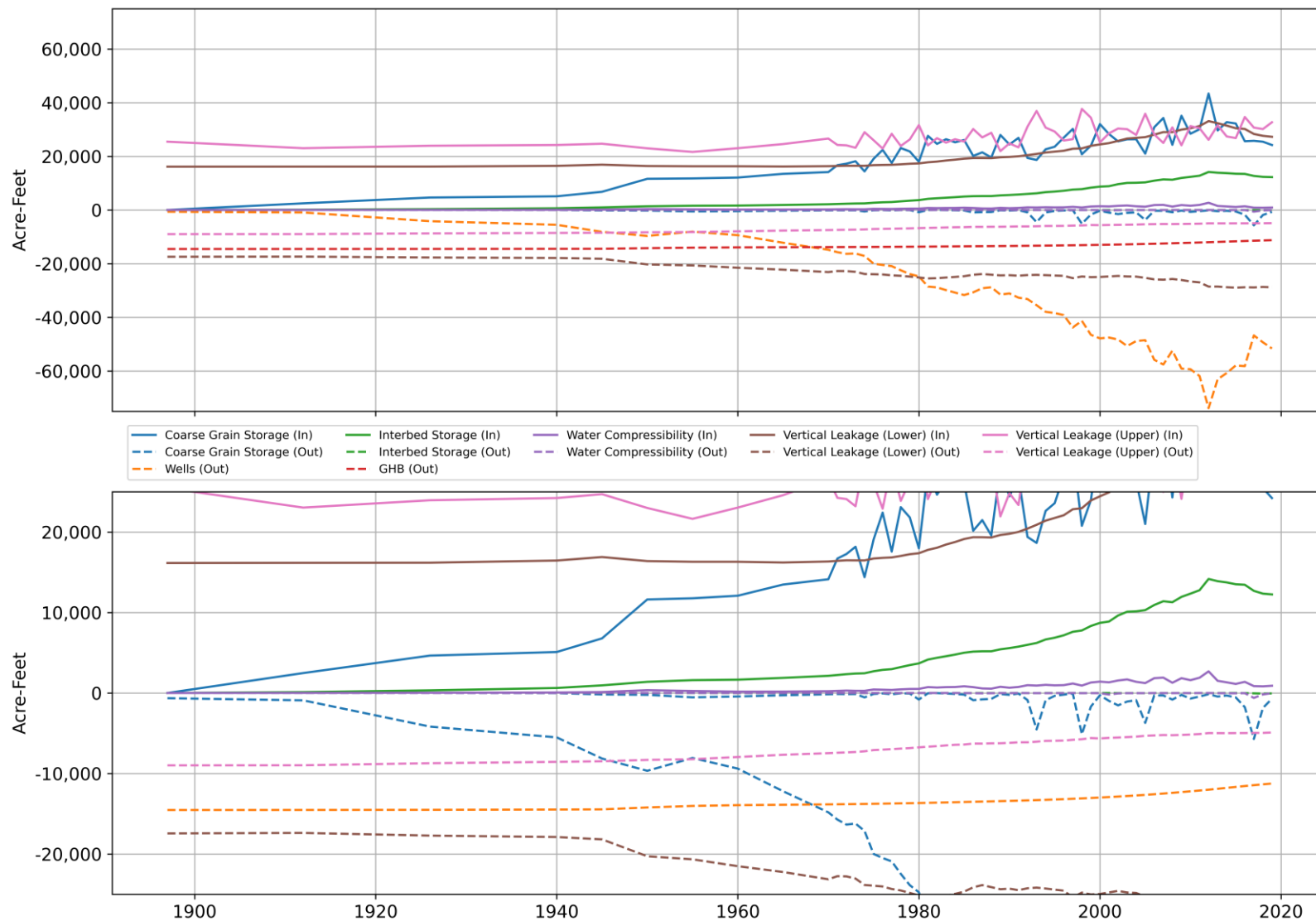


Figure 135. Layer 5 (Jasper Aquifer) transient simulated water budget for the calibration period (1896 – 2018). Lower plot is zoomed in to visualize minor components of the simulated budget.

GMA 14 Groundwater Availability Model

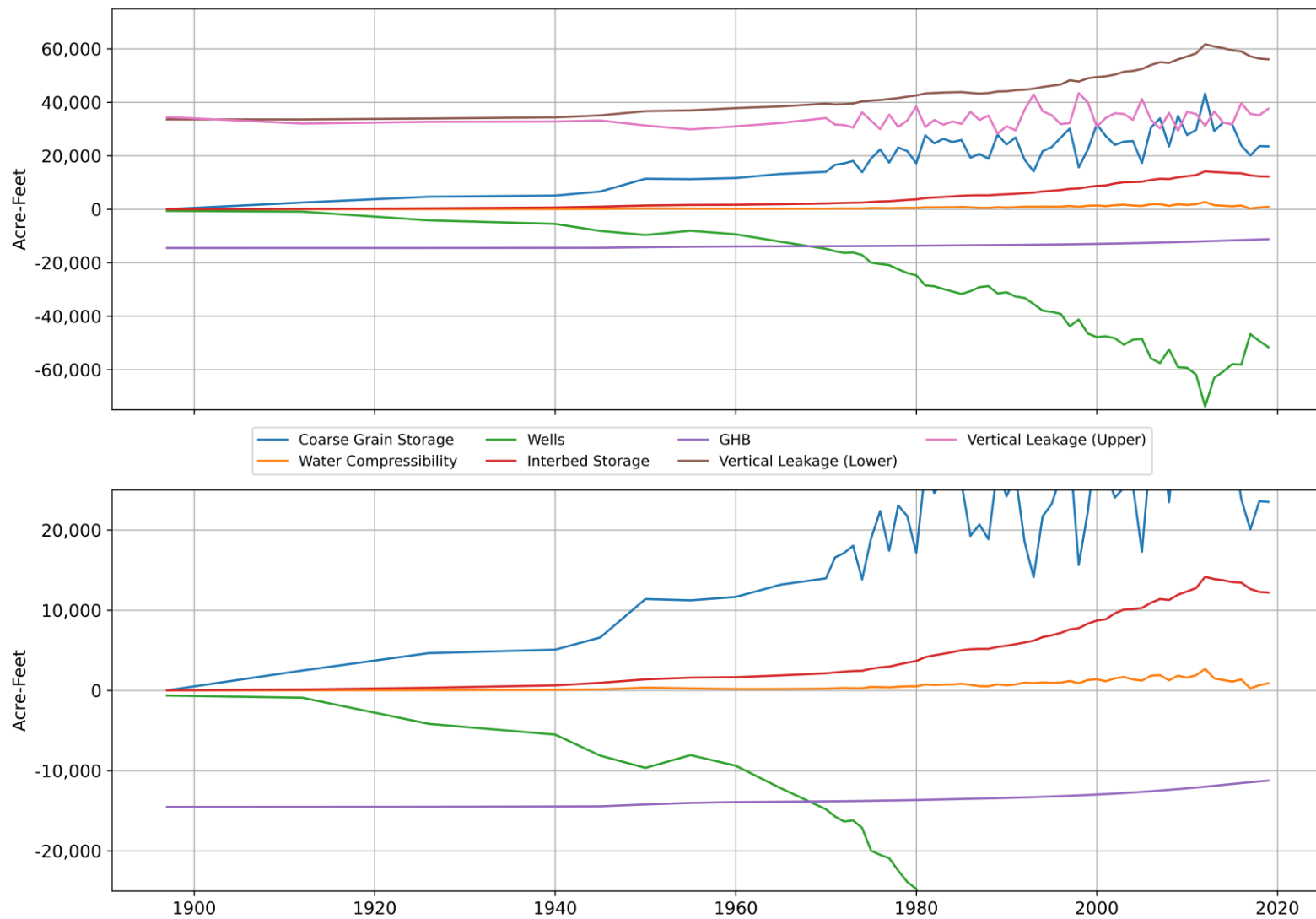


Figure 136. Layer 5 (Jasper Aquifer) transient simulated net water budget for the calibration period (1896 – 2018). Lower plot is zoomed in to visualize minor components of the simulated budget.

GMA 14 Groundwater Availability Model

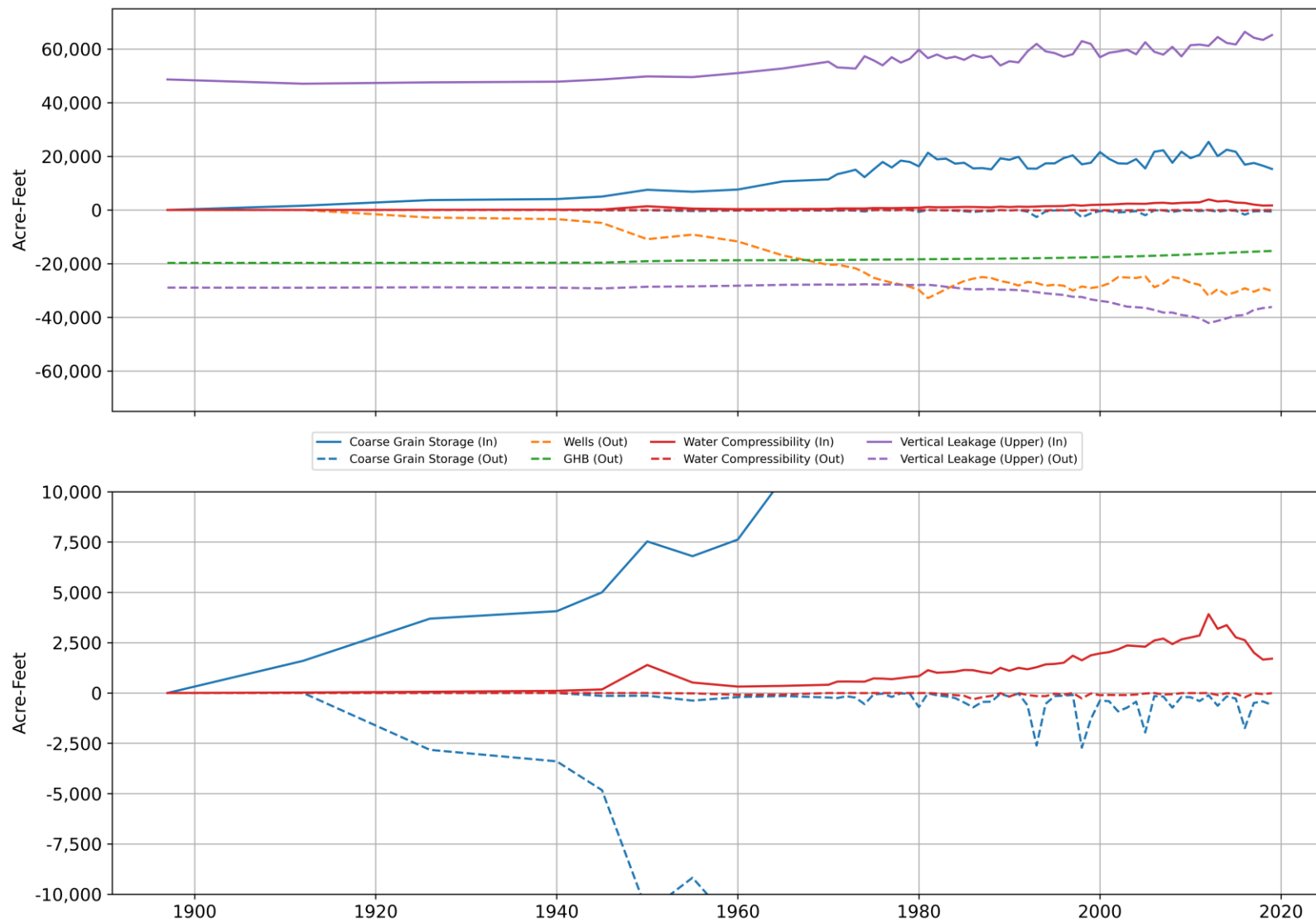


Figure 137. Layer 6 (Catahoula Aquifer) transient simulated water budget for the calibration period (1896 – 2018). Lower plot is zoomed in to visualize minor components of the simulated budget.

GMA 14 Groundwater Availability Model

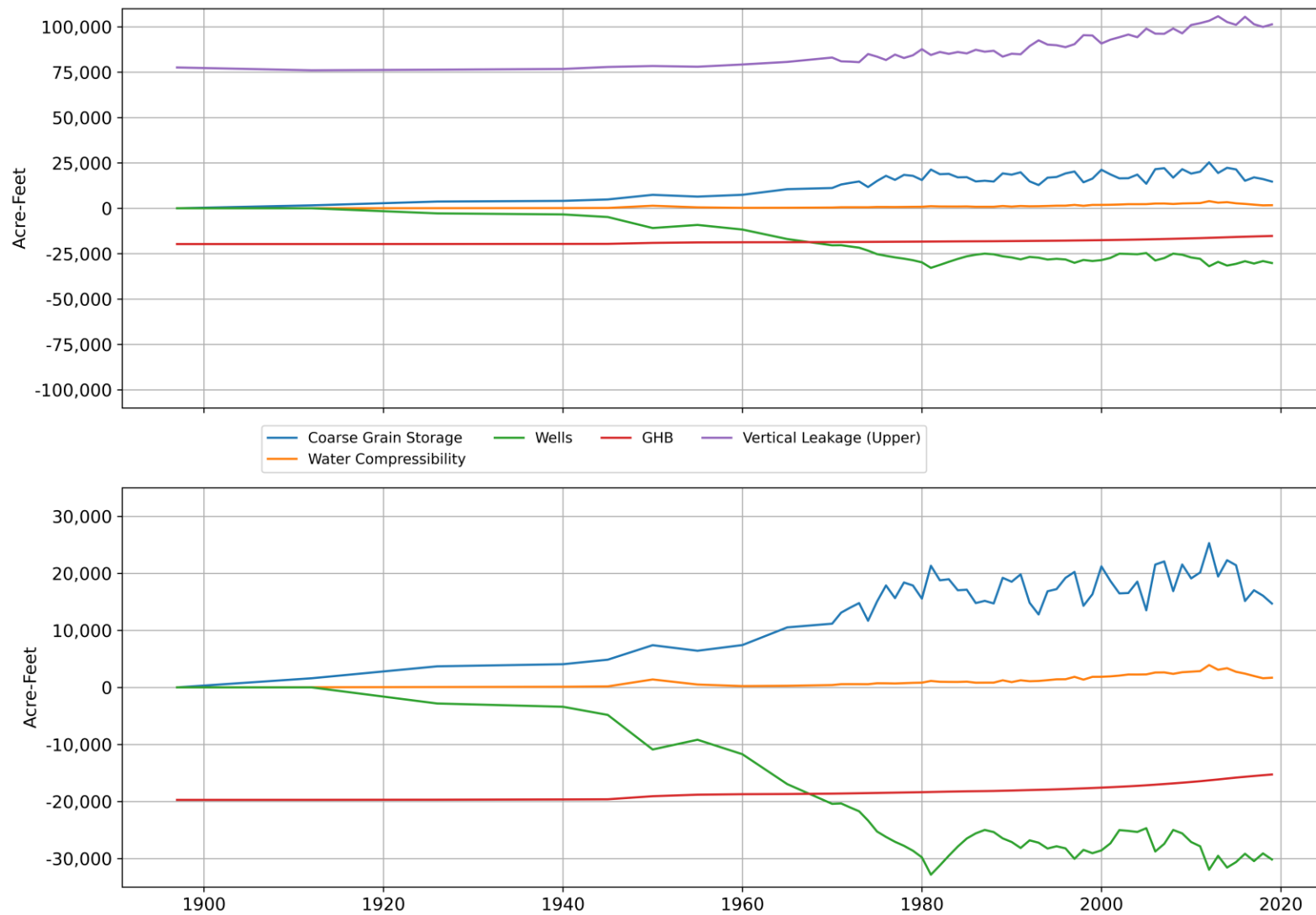


Figure 138. Layer 6 (Catahoula Aquifer) transient simulated water budget for the calibration period (1896 – 2018). Lower plot is zoomed in to visualize minor components of the simulated budget.

5. Model Limitations

We developed the GMA 14 Model as an update to GULF-2023 for Groundwater Management Area 14 joint planning purposes. As GULF-2023 is the current groundwater availability model of record, our approach was to use as much of the current model as possible so that TWDB review of the model would be expeditious, allowing Groundwater Management Area 14 to use the model for consideration of desired future conditions as part of the 2026 joint planning cycle. Many of the GULF-2023 limitations discussed by Ellis and others (2023) remain applicable. The following are additional, or expansion of, limitations applicable to both GULF-2023 and the GMA 14 Model.

5.1. Jasper Aquifer as a Single Layer

The Jasper Aquifer is a significant source of groundwater in Montgomery County. It is represented by a single layer in GULF-2023 (Ellis and others, 2023) and previous models of the Gulf Coast Aquifer System such as the Houston-Area Groundwater Model (Kasmarek, 2013). As described in Section 3.1.2, we did not alter the layer elevations from GULF-2023 for the GMA 14 Model. However, it is a common approach to separate the Jasper Aquifer into upper and lower units based on lithology (Keester and others, 2022).

Moderate to large capacity water wells screen sands of the upper Jasper Aquifer throughout Montgomery County and in parts of north and northwest Harris County. As discussed in Lone Star Groundwater Conservation District's Phase 2 Subsidence Study, there is more sand available for well screening in the upper Jasper Aquifer compared to the lower Jasper Aquifer (Keester and others, 2022). The lower Jasper Aquifer consists of mostly clay with interbedded sand through most of Montgomery County and into north Harris County.

As described above, the conceptual model for the Jasper is that it is two distinct hydrostratigraphic units. Kelley and others (2018) recognized this conceptual model in the Jasper model they developed for the Harris-Galveston Subsidence District. By simulating the Jasper as a single layer, the clays of the lower Jasper Aquifer are more directly affected in the model simulation than is expected to actually occur. Rather than only the top of the lower Jasper being affected through leakage to the upper Jasper, all clays of the lower Jasper are assumed to be affected by pumping in the upper Jasper when the Jasper is a single layer. As such, compaction results for the Jasper when simulated as a single layer may be greater than may actually occur.

5.2. Compaction and Subsidence Data Availability

We based the initial parameterization of the CSUB package on the depth-dependent compaction parameters developed from five sites in the greater Houston area (see Figure 7). The southeast Harris County and Fort Bend County sites only analyzed Chicot and Evangeline core samples. The Lone Star Groundwater Conservation District Porter site analyzed core samples from the Chicot, Evangeline, Burkeville, and Jasper. The limited compaction parameter data from each layer limits our ability to develop a robust spatially variable representation of the parameters affecting the simulation of subsidence. This limitation is particularly applicable to the Burkeville and Jasper where data are only available for a single location. In addition, since the compaction parameter data is only available within the greater Houston area, simulated compaction results decrease in reliability beyond the greater Houston area.

We used compaction and subsidence targets from global positioning system, benchmark, and extensometer sites during calibration to improve the model fit. Most of the compaction and subsidence stations are within the greater Houston area (see Figure 46). Beyond the greater Houston area, only global positioning system targets are available. The earliest global positioning system stations beyond the greater Houston area were installed in the early-2000s with most of the stations installed after 2010. The benchmark data set provides data going back to the 1930s and extensometers began providing data in the mid to late 1970s. Benchmark and extensometer datasets provide long-term trends and observations to help improve the model during calibration of early simulation years. Due to the limited subsidence observation data prior to 2010 beyond the greater Houston area, the long-term simulated subsidence results in the outer portions of the GMA 14 Model area are less reliable.

5.3. Subsidence District Groundwater Pumping

We did not modify pumping in counties within subsidence districts modified as part of the GMA 14 Model. We understand the subsidence district regulatory plans are in place and were developed in part using pumping data that is included in GULF-2023. However, a review of the GULF-2023 pumping distribution within the counties with subsidence districts, particularly the north and west parts of Harris-Galveston Subsidence District Regulatory Area 3, could help improve the performance of future groundwater flow models developed for the region.

6. Summary and Conclusions

One purpose for updating GULF-2023 to the GMA 14 Model was to create a groundwater availability model for the purpose of joint planning. GULF-2023 issues identified by Groundwater Management Area 14 members were a primary driver for undertaking the model update. The GMA 14 Model meets goals of correcting the compaction and subsidence package, incorporating new data for the compaction properties of the Gulf Coast Aquifer System, more reasonable matching aquifer testing data, and creating a more manageable model.

Conceptual model updates focused on aquifer transmissivity, groundwater pumping, and compaction. We incorporated previously unpublished pumping test results for transmissivity to define the parameter for the aquifer layers. Our approach diverged from GULF-2023 and resulted in an improved correlation between measured and modeled transmissivity values.

For groundwater pumping, we elected to rely on the estimates of groundwater production despite uncertainty that may be in some values. We did not allow the model to modify pumping during the calibration. Our approach diverged from GULF-2023 where Ellis and others (2023) allowed pumping values to change and results in historical pumping amounts that are consistent with the TWDB Water Use Survey.

For compaction, we incorporated the data collected from 18 core samples collected by the Lone Star Groundwater Conservation District. We incorporated lab results from testing of these core samples with the data from Gabrysch and Bonnet (1974; 1976a; 1976b). Porosity, compression index, and recompression index data from the core analyses were relatively consistent with previous investigations. However, the vertical hydraulic conductivity values from the newly collected core were about 10 times less than the previous investigations. The lower vertical hydraulic conductivity suggests the compaction may be slower than previously thought.

We incorporated the new conceptual model information into the GMA 14 Model. We used PEST++ (White and others, 2020) to support our calibration of the model. Specifically, we used the iterative ensemble smoother approach to generate an ensemble model. One advantage of this approach is the generation of multiple model realizations along with the base model. The resulting model calibration indicated a model with minimal bias in simulating water level decline and compaction.

Water level and subsidence trends are matched well with the GMA 14 Model. Both the decline in water level during periods of high groundwater use and subsequent recovery of water levels are simulated with the model. Overall, the model appears to be well suited for use by Groundwater Management Area 14 for joint planning.

7. Future Improvements

One improvement for the GMA 14 model would be the representation of the Jasper Aquifer as at least a two-part system. Dividing the Jasper would allow for a more practical approach to simulating groundwater pumping and subsidence in the upper part of the Jasper Aquifer where the pumping occurs. Having a lower Jasper layer available for model simulations is also important as the potential for future brackish groundwater development continues to increase.

In addition to production wells being located in the upper Jasper, on geophysical logs, there are distinct differences in the electrical resistivity signatures of the upper Jasper Aquifer and lower Jasper Aquifer sands. The water contained within the lower Jasper Aquifer sands is often brackish with higher concentrations of chloride and total dissolved solids. In addition, elevated concentrations of fluoride, methane gas, and/or hydrogen sulfide are common. The water quality and hydraulic property differences between the upper and lower Jasper are more than sufficient to justify dividing the Jasper Aquifer model layer.

Our work also identified some areas where pumping could be updated. Pumping is a difficult, but very important, value to determine for a groundwater model. A future improvement could involve updating the pumping distribution where it remains uncertain in some areas the model, particularly in northwest Harris County.

Another improvement would be the development of local sub-models for the Groundwater Management Area 14 members that is informed by the regional model. These local models would allow for the rapid incorporation of new aquifer data collected as part of district groundwater management. In addition, the local models could more easily serve district needs for permitting evaluations.

8. Acknowledgements

The authors appreciate the support of the Lone Star Groundwater Conservation District who recognized the importance of this model for Groundwater Management Area 14 joint planning efforts. Along with the Lone Star Groundwater Conservation District, we also appreciate the support and contributions from Bluebonnet Groundwater Conservation District, Brazoria County Groundwater Conservation District, Lower Trinity Groundwater Conservation District, and Southeast Texas Groundwater Conservation District toward the development of the GMA 14 Model. We also thank the Texas Water Development Board and U.S. Geological Survey for the collection and hosting of a wealth of hydrogeologic data for the Gulf Coast Aquifer System.

9. References

- Asquith, G. and Gibson, C., 1982, Basic Well Log Analysis for Geologists - AAPG Methods in Exploration Series Number 3: Tulsa, OK, The American Association of Petroleum Geologists,
- Bear, J., 1979, Hydraulics of Groundwater: Mineola, New York, Dover Publications, Inc., 569 p.
- Das, B.M., 2010, Principles of Geotechnical Engineering (7th ed.): Cengage Learning,
- Drabek, C. and Keester, M.R., 2023, Comments on the GULF-2023 model – Draft Model Files and Report: Comments submitted to the TWDB on behalf of the Lone Star Groundwater Conservation District, 31 p.
- Eaton, B.A., 1972, The effects of Overburden Stress on Geopressure Prediction from well logs: Journal of Petroleum Technology, v. 24, p. 929-934, 10.2118/3719-PA.
- Eaton, B.A., 1995, How to Use Drilling Petrophysical Data in Prospect Evaluation: World Oil Conference by SPE.
- Ellis, J.H., Knight, J.E., White, J.T., Sneed, M., Hughes, J.D., Ramage, J.K., Braun, C.L., Teeple, A., Foster, L., Rendon, S.H., and Brandt, J., 2023, Hydrogeology, Land Surface Subsidence, and Documentation of the Gulf Coast Land Subsidence and Groundwater-Flow (GULF) Model, Southeast Texas, 1897-2018, US Geological Survey Professional Paper 1877: 432 p.
- Espey, Huston, and Associates, Inc., 1982, Phase II—Water Management Study - Appedix B - PRESS Model Documentation: Prepared for Harris–Galveston Coastal Subsidence District, 9 p.
- Furnans, J., Keester, M., Pedrazas, M., Wong, S.S., Fullmer, T., Goswami, R., Mohandass, U.J., Thornhill, M., Seeger, E., and Sutherland, M., 2022, Estimation of Groundwater Pumping Volumes, Locations, and Aquifers for West Texas: Prepared for Texas Water Development Board under Contract Number 2048302456, 898 p, http://www.twdb.texas.gov/publications/reports/contracted_reports/index.asp.
- Gabrysch, R.K. and Bonnet, C.W., 1974, Land-Surface Subsidence in the Area of Burnett, Scott, and Crystal Bays Near Baytown, Texas: U.S. Geological Survey Water-Resources Investigations Report 74-21, 48 p.
- Gabrysch, R.K. and Bonnet, C.W., 1976a, Land-surface subsidence at Seabrook, Texas: U.S. Geological Survey Water Resources Investigation, 53 p.

- Gabrysch, R.K. and Bonnet, C.W., 1976b, Land-surface subsidence in the area of Moses Lake near Texas City, Texas: U.S. Geological Survey Water-Resources Investigation 76-32, 42 p.
- George, P.G. and Mace, R.E., 2011, Aquifers of Texas: Report 380.
- Granato, G.E., 2006, Kendall-Theil Robust Line (KTRLLine—version 1.0)—A visual basic program for calculating and graphing robust nonparametric estimates of linear-regression coefficients between two continuous variables: U.S. Geological Survey Techniques and Methods 4-A7, 31 p.
- Hoffman, J., Leake, S.A., Galloway, D.L., and Wilson, A.M., 2003, MODFLOW-2000 Ground-Water Model—User Guide to the Subsidence and Aquifer-System Compaction (SUB) Package: U.S. Geological Survey, Open-File Report 03—233, 46 p.
- Hughes, J.D., Leake, S.A., Galloway, D.L., and White, J.T., 2022, Documentation of the Skeletal Storage, Compaction, and Subsidence (CSUB) Package of MODFLOW 6: U.S. Geological Survey Techniques and Methods, Book 6, Chapter A62, 57 p, <https://doi.org/10.3133/tm6A62>.
- Imhanzuaria, D.E. and Bello, K.O., 2019, Evaluation of Poisson's Ratio Range for Fracture Pressure Gradient (FPG) Prediction for Niger Delta Formation: Nigerian Journal of Technology, v. 38, no. 3, p. 628-635, <http://dx.doi.org/10.4314/njt.v38i3.13>.
- Jiangtao Li, L.Z.H.G.J.Z.Z.D.X.L.H.W.C.Z.P.T., 2022, Unraveling elastic and inelastic storage of aquifer systems by integrating fast independent component analysis and a variable preconsolidation head decomposition method: Journal of Hydrology, v. 606, no. 127420, p. 11.
- Jorgensen, D.G., 1980, Relationships between basic soils-engineering equations and basic ground-water flow equations: U.S. Geological Society Water-Supply Paper 2064: 40 p.
- Kasmarek, M.C., 2013, Hydrogeology and Simulation of Groundwater Flow and Land-Surface Subsidence in the Northern Part of the Gulf Coast Aquifer System, Texas, 1891-2009: U.S. Geological Survey Scientific Investigations Report 2012-5154, 55 p.
- Keester, M., 2024, GULF 2023 Model CSUB Package Update for the GMA 14 Model: Presentation to Groundwater Management Area 14 dated May 14, 2024, 18 p.

- Keester, M., Drabek, C., Thornhill, M., and Beach, J., 2022, Phase 2 Subsidence Investigations: Report prepared for the Lone Star Groundwater Conservation District, 66 p.
- Keester, M.R., Drabek, C., Thornhill, M., and Beach, J., 2022, Phase 2 Subsidence Investigations: Report prepared for the Lone Star Groundwater Conservation District: 66 p.
- Kelley, V., Deeds, N., Young, S.C., Pinkard, J., Sheng, Z., Seifert, J., and Marr, S., 2018, Subsidence Risk Assessment and Regulatory Considerations for the Brackish Jasper Aquifer - Harris-Galveston and Fort Bend Subsidence Districts: Report prepared for Harris-Galveston Subsidence District and Fort Bend Subsidence District, 69 p.
- Langevin, C.D., Hughes, J.D., Banta, E.R., Niswonger, R.G., Panday, S., and Provost, A.M., 2017, Documentation for the MODFLOW 6 Groundwater Flow Model: U.S. Geological Survey Techniques and Methods, book 6, chap. A55, 197 p.
- Langevin, C.D., Hughes, J.D., Provost, A.M., Russcher, M.J., Niswonger, R.G., Panday, S., Merrick, D., Morway, E.D., Reno, M.J., Bonelli, W.P., Boyce, S.E., and Banta, E.R., 2025, MODFLOW 6 Modular Hydrologic Model version 6.6.1: U.S. Geological Survey Software Release, 10 February 2025, <https://doi.org/10.5066/P9FL1JCC>.
- LBG-Guyton Associates and Intera, 2012, Catahoula Aquifer Characterization and Modeling Evaluation in Montgomery County: Modeling report prepared for Lone Star Groundwater Conservation District.
- Leake, S.A. and Galloway, D.L., 2007, MODFLOW Ground-Water Model—User Guide to the Subsidence and Aquifer-System Compaction Package (SUB-WT) for Water-Table Aquifers: U.S. Geological Survey, Techniques and Methods 6–A23, 42 p.
- Leake, S.A. and Prudic, D.E., 1991, Documentation of a Computer Program to Simulate Aquifer-System Compaction Using the Modular Finite-Difference Ground-Water Flow Model: U.S. Geological Survey, Techniques of Water-Resources Investigations 06-A2, 68 p.
- Seifert, Jr., W.J., 2017, Task 3 Technical Memorandum Regarding Future Groundwater Availability: Technical Memorandum prepared by LBG-Guyton Associates for Task 3 of the Lone Star Groundwater Conservation District Strategic Water Resources Planning Study, 53 p.

- Song, S., Bai, L., and Yang, C., 2022, Characterization of the Land Deformation Induced by Groundwater Withdrawal and Aquifer Parameters Using InSAR Observations in the Xingtai plain, China: remote sensing, v. 14, no. 4488, p. 19.
- Terzaghi, K., 1925, *Erdbaumechanik auf bodenphysikalischer Grundlage*: Vienna, Austria, Deuticke, 399 p.
- Terzaghi, K., Peck, R.B., and Mesri, G., 1996, *Soil Mechanics in Engineering Practice* (3rd ed.): John Wiley & Sons,
- Tiab, D. and Donaldson, E.C., 2016, Effect of Stress on Reservoir Rock Properties (Chapter 9) in *Petrophysics - Theory and Practice of Measuring Reservoir Rock and Fluid Transport Properties*: (4th) New York, Elsevier, 483-582 p.
- U.S. Geological Survey, 2025a, MODFLOW 6 – Description of Input and Output: Version mf6.6.1, 370 p, 10.5066/F76Q1VQV.
- U.S. Geological Survey, 2025b, ZONEBUDGET for MODFLOW 6: Version mf6.6.1 — February 10, 2025, 7 p.
- White, J.T., Hunt, R.J., Fienen, M., and Doherty, J.E., 2020, Approaches to Highly Parameterized Inversion: PEST++ Version 5, a Software Suite for Parameter Estimation, Uncertainty Analysis, Management Optimization and Sensitivity Analysis: U.S. Geological Survey Techniques and Methods 7C26, 52 p, 10.3133/tm7C26.
- Young, S.C. and Draper, C., 2020, The Delineation of the Burkeville Confining Unit and The Base of the Chicot Aquifer to Support the Development of the Gulf 2023 Groundwater Model: Report prepared for Harris-Galveston Subsidence District and Fort Bend Subsidence District, 27 p, <https://hgsubsidence.org/science-research/district-research/>.
- Young, S.C., Kelley, V., Deeds, N., Knox, P., Budge, T., Baker, E., Galloway, B., and Dutton, A., 2006, A Site Conceptual Model to Support the Development of a Detailed Groundwater Model for Colorado, Wharton, and Matagorda Counties: Prepared for LCRA, 304 p.
- Zhang, J. and Yin, S., 2017, Real-Time Pore Pressure Detection: Indicators and Improved Methods: *Geofluids*, v. 2017, no. Article ID 3179617, p. 1-12, <https://www.hindawi.com/journals/geofluids/2017/3179617/>.